Nova shells as a diagnostic tool for the physics and evolution of cataclysmic variables

LIENTUR CELEDÓN PICHÚN

Supervisor: Dr. Claus Tappert (UV)

Internal reviewer: Dr. Catalina Arcos (UV)

External reviewer: Dr. Alessandro Ederoclite (CEFCA)

Tesis para optar al grado de Doctor en Astrofísica

Instituto de Física y Astronomía

Facultad de Ciencias

Universidad de Valparaíso

September, 2025

Valparaíso, Chile.

"You should be smiling, too
Aren't you excited?
Aren't you happy?
You are going to be free"

This thesis is solely my own composition,
except where specifically indicated in the text.

Total or partial reproduction, for scientific or academic purposes,
is authorised, including a bibliographic reference to this document
and to the published articles.

Lientur Celedón
September, 2025
Valparaíso, Chile.

Acknowledgements

To my family, friends, and colleagues. You made these four years truly great.

LC acknowledge economic support from ANID-Subdireccion de capital humano/doctorado nacional/2022-21220607, European Southern Observatory, and Universidad de Valparaíso beca FIB.

Abstract

Nova eruptions are a recurrent phenomenon in the lifetime of Cataclysmic Variables, playing a crucial role in their evolution. A classical nova eruption occurs on the surface of a white dwarf (WD) once a critical amount of hydrogen has been accreted, releasing a significant amount of energy during the process. As a consequence, the luminosity of the system increases significantly in a short amount of time before starting to fade slowly, originating what is known as a nova eruption light curve. An additional consequence of the nova eruption is the ejection of the accreted material into the interstellar medium, forming a nebular remnant around the system known as a nova shell. It has been widely assumed that the properties of these nova shells, such as their axial ratio, expansion velocity, and ejected mass, are directly correlated to the mass of the underlying WD. This makes nova shells excellent diagnostic tools for our understanding of the physical processes that dominate the ejection mechanisms during a nova eruption.

The usual study of nova shells involves the use of narrow-band (NB) photometry and long-slit (LS) spectroscopy, which, when combined, can provide a precise, although incomplete, characterisation of the expanding shell. A better approach is to use integral-field spectroscopy, which gives a complete characterisation of the shell's geometry and kinematics. In this thesis, for the first time, an in-depth analysis of nova shells using the Multi-Unit Spectrograph Explorer (MUSE), an integral-field spectrograph, is carried out. Data for a total of 21 nova shells with ages between 26 and 120 years have been collected over several observation cycles, allowing for the detection of a nova shell around 17 systems, yielding the largest sample of nova shells observed with MUSE to date.

The analysis of the shells involves creating passband photometry from the datacube to address the shell geometry, creating channel and velocity maps to determine the kinematics of the ejecta, and combining this information to obtain the 3D geometry of the nova shell. The results emphasise the significant advantages that IFS observations have over the classical combination of NB images and LS spectroscopy. A first

case that showcases this was the study of the old shell around RR Pic (Nova Pictoris 1925), which was observed mainly in the Hα, Hβ, and [OIII] λ 5007 Å lines. The images and kinematics confirmed that the shell is composed of an equatorial ring that contains $\sim$ 99% of the Hα flux, and the rest corresponds to filaments expanding in the polar direction. The 3D reconstruction of the shell shows that hydrogen and oxygen emissions occupy different spatial positions, revealing the differences in the gas density across the shell.

Within the selected sample of nova shells, a small group shows asymmetric ejecta, which defies the usual ejection mechanisms in nova shells. The first of these asymmetric shells was discovered around V1425 Aql (Nova Aquila 1995). From the MUSE data, it was concluded that the hydrogen shell consists of an approximately spherical shell, while the asymmetric ejecta traced by the oxygen forbidden emission possesses an arc-shaped geometry that surrounds the hydrogen shell. The origin of the asymmetry in these shells is far from clear, but it may have significant implications for our understanding of the ejection mechanisms. In addition to the particular analysis of these two individual nova shells, the number of detected shells allows for a quantitative analysis of the data. For the 17 shells, Hα images were obtained from the datacube to study the geometry of their shells. An ellipse was fitted to each one to obtain the semi-major and semi-minor axes, from which the axial ratio of the shell can be derived. This parameter was compared against the white dwarf masses extracted from the literature. No correlation was found, likely due to the uncertainties involved in the determination of the masses. The results of this thesis have been published in two articles in a refereed journal, with a third one being planned for the near future. They highlight the advantages and capabilities for the study of nova shells using MUSE, encouraging the rest of the community to use similar instruments and techniques.

Contents

Chapter 1

Introduction

Nova shells are nebular structures of high interest for the study of the interstellar medium (ISM) and stellar evolution. They are the remnants of a nova eruption: a transient phenomenon that occurs when a white dwarf (WD) has accreted from its companion star the amount of matter required to reach the critical pressure to ignite the hydrogen on its surface. This phenomenon is typical of cataclysmic variables (CVs) and, to a lesser extent, in symbiotic binaries. The eruption is powerful enough to expel part of the white dwarf crust and the accreted matter into the ISM, but not powerful enough to destroy the WD. Thus, nova eruptions are a recurring phenomenon in the lifetime of cataclysmic variables, and they play a crucial role in their evolution. By studying the nova shell, a nebular structure formed from the material expelled from the system during the nova eruption, it is possible to gain insight into the physical processes that occur during the nova eruption itself. There are several questions regarding the nova shells and their evolution: how much mass is ejected? What is the chemical composition of the ejecta? When does it start to decelerate? How does it interact with the ISM? For how long will it be detectable by our instruments? To answer these questions, several works have been carried out using photometry and spectroscopy since the first days after the nova eruption, while others focus on the shell structure decades after the eruption. In this section, I will introduce the reader to the basic concepts to understand CVs and their evolution, how nova eruptions occur and how they depend on the CV's physical properties, and finally, how nova shells are formed, what can be

learned from them, and the different challenges we face to have a complete picture of the phenomenon.

1.1 Basic concepts

To properly introduce CVs to the reader, it is necessary to explain first some general terms relevant to the field of binary stars, and in particular, to the field of interacting binary stars. If two stars in a binary system orbit each other at large distances, they will hardly interact with each other, and each one will evolve as a single star. But if they are close enough, they will interact with their companion, affecting the evolution of both stars. This leads to very interesting phenomena such as synchronisation of the periods, mass transfer, and accretion disc formation, among others. This makes interacting binaries excellent testbeds for many astrophysical phenomena and theories.

Many of these phenomena are revealed by the study of the emission lines in CVs, either by allowed transitions such as the Balmer lines, revealing the behaviour of the accretion disc around the WD, or by the forbidden transitions that appear in low-density environments such as the expanding ejecta after a nova eruption. To better understand the physics behind the formation of these kinds of emission lines, a brief summary is provided at the end of this section.

1.1.1 Roche lobe

One of the most basic but important concepts is the Roche lobe, named in honour of the French mathematician Edouard Roche, who studied the potential experienced by a massless particle in a binary system. For simplicity, the problem was reduced to a binary with a circular orbit, and a corotating frame with the centre at the position of the most massive star with a mass m_1. In this corotating frame, the less massive star (whose mass is m_2) is fixed at the position (x,y,z)=(1,0,0). The potential Φ that a massless particle experiences in this frame is the sum of the gravitational potentials of both stars plus the rotational potential due to the orbital motion, and it can be written as:

$$\Phi_{\rm n} = \frac{2}{(1+q)\,r_1} + \frac{2\,q}{(1+q)\,r_2} + (x - \frac{q}{1+q})^2 + y^2, \tag{1.1}$$

where $\Phi_{\rm n}$ is the normalized potential defined as $\Phi_{\rm n} = -2\Phi/G(m_1+m_2)$, with G the gravitational constant. The parameter q is called the mass ratio of the system, and

it is defined as m_2/m_1, with $m_2 < m_1$, and x and y are points in the space defined by the reference frame (Hilditch, 2001).

The potential given by Equation 1.1 can be solved for any point in the space, allowing us to calculate different surfaces of equipotentials around the stars. An example of different equipotential surfaces seen in the orbital plane of the binary ($z = 0$) for a binary system with $q = 0.2$ is presented in Fig. 1.1. An equipotential surface of particular importance is the so-called Roche lobe, which corresponds to the '8'-shape that surrounds both stars. A particle will be gravitationally bound to a star only if it is inside its respective lobe. Thus, the Roche lobe defines a maximum size for the star in which its different components (atoms, ions, electrons, etc) are gravitationally bound to it. It is worth noting that the shape of this lobe is not spherical but a teardrop shape instead. This leads up to the use of the effective radius $r_{\rm L}$ to characterise the size of the Roche lobe, which is defined as the radius of a sphere that has the same volume as the Roche lobe. A good approximation for $r_{\rm L}$ as a function of q and the orbital separation a in a binary system was provided by Eggleton (1983), which is valid for all values of q:

$$r_{\rm L} = \frac{0.49\, a\, q^{2/3}}{0.69\, q^{2/3} + \ln(1 + q^{1/3})}, \tag{1.2}$$

The size of the Roche lobe is proportional to the orbital separation, making it more likely that one of the components fills its Roche lobe if the system has a short orbital period. This allows us to classify binary systems depending on whether or not a star (or both of them) has filled its Roche lobe: if neither of the stars has filled its Roche lobe, we classify the system as a detached system, if only one of the stars is filling its Roche lobe we classify it as a semi-detached, and if both stars are filling their Roche lobe simultaneously we classify it as a contact system.

The Roche lobe not only defines the limits of a star, but also an important point called the inner Lagrangian point $\rm L_1$. This is an unstable equilibrium point located between the stars and connecting the Roche lobes of both stars. A particle that is located at this point and experiences a perturbation, due to a pressure change, for example, will be pushed away from the $\rm L_1$ point and will start to fall into the Roche lobe of one of the stars. This phenomenon is of particular importance in semi-detached systems, as it allows mass transfer to occur from the star that fills its Roche lobe to its companion, in a process called Roche lobe overflow.

On the x-axis that connects both stars (Fig. 1.1), there are two other points of unstable equilibrium denoted as Lagrangian points $\rm L_2$ and $\rm L_3$ located behind the stars.

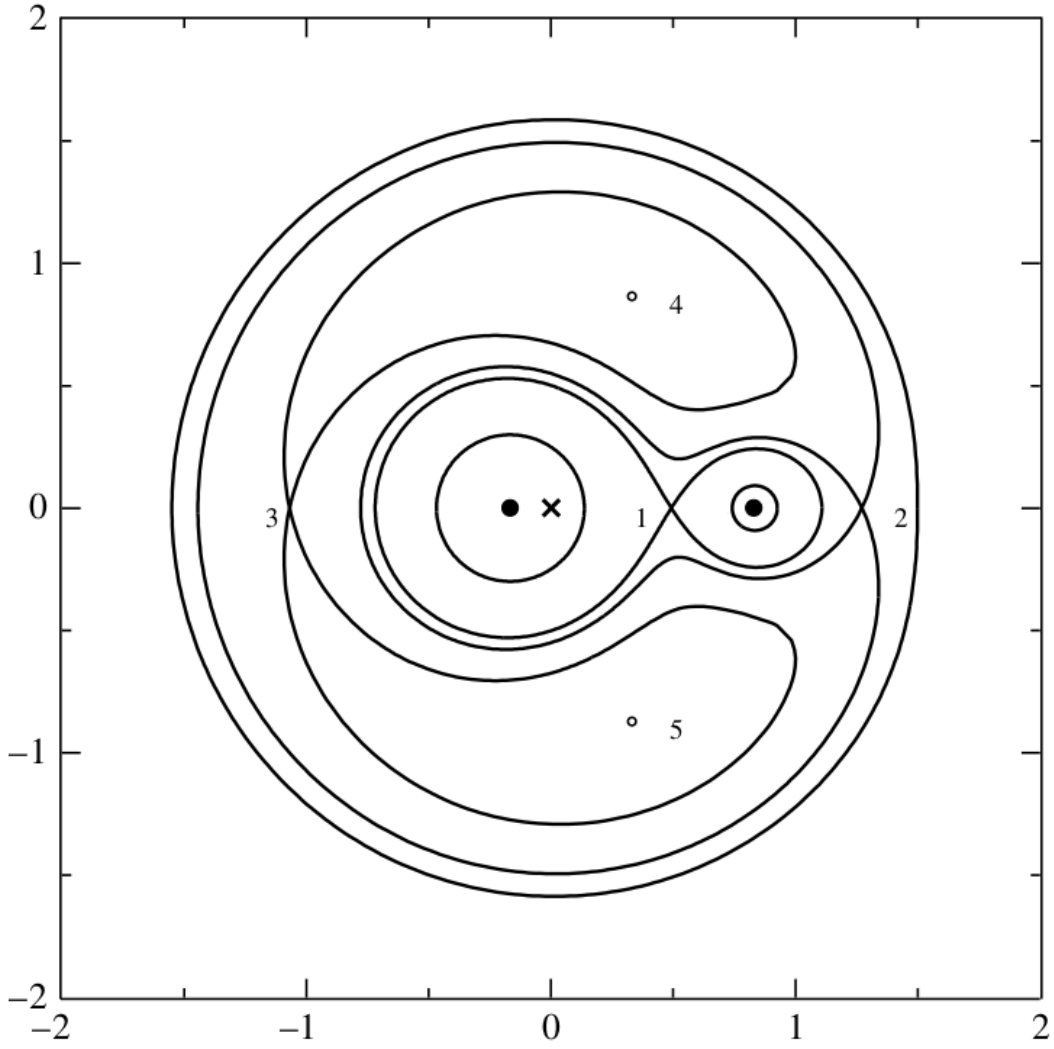

Figure 1.1: Cross-section of equipotential surfaces in the orbital plane of a binary system with $q = 0.2$. Several equipotential surfaces are drawn, including the Roche lobes of each star, which are marked with black circles. The locations of the different Lagrangian points are indicated with numbers from 1 to 5, while the centre of mass of the system is denoted with a black x. Adapted from Fig.3 of Carroll & Ostlie (2017).

A particle that reaches one of these two points may be able to leave the binary system. In contrast with these Lagrangian points, the Lagrangian points L_4 and L_5 correspond to regions of stable equilibrium instead.

1.1.2 Circularisation and synchronisation

In a close binary system, the tidal friction exerted between stars is significant, and it can alter both the rotation of the stars and the system's orbit. The tidal dissipation, the loss of energy due to the tidal friction mechanisms, is characterised by two different mechanisms: equilibrium and dynamical tides. The equilibrium tides refer to the hydrodynamical equilibrium resulting from the deformation of the star from the gravitational pull of its companion, while the dynamical tides involve tidal dissipation via the excitation of stellar oscillations originating from the tidal potential (Zahn, 1975, 1989). The main tidal dissipation mechanism will depend on whether the stars have a convective (CE) or radiative (RE) envelope. Secular equations that show the evolution of the orbital parameters (orbital separation a, eccentricity e, and angular velocity of the stars ω) can be provided once the main tidal dissipation mechanism is clear (Zahn, 1977; Hilditch, 2001).

For CE stars, the most efficient mechanism for energy dissipation is the turbulent friction that originates from equilibrium tides within the envelope of the star. The secular equations governing the evolution of the orbital parameters in this case were provided by Zahn (1977). These equations show that the system will evolve towards an equilibrium when the star's rotational period matches the system's orbital period. This phenomenon is known as synchronisation of the orbital period. As the system synchronises, the eccentricity will start to decrease, and the system will evolve towards a circular orbit. This phenomenon is called circularisation of the orbit.

The timescales for these two phenomena to occur, synchronisation ($t_{\rm sync}$) and circularisation ($t_{\rm circ}$), strongly depend on the orbital period, with reference time scales for $t_{\rm sync}$ and $t_{\rm circ}$ of 10^4 and 10^6 years, respectively, for a binary system with $q = 1$ and $P = 1\,\mathrm{d}$. Changing the orbital period to $10\,\mathrm{d}$ leads to time scales of 10^8 and 10^{11} years instead, thus showing the strong dependence on the orbital period (Zahn, 1977).

A similar exercise can be done for stars with RE. In this case, the main mechanism for tidal dissipation is by radiative damping of internal oscillations inside the stars. These oscillations can be related to g-mode or f-mode pulsations as they are amplified by the tidal forces exerted by the companion star. Similar to the case of CE stars, for

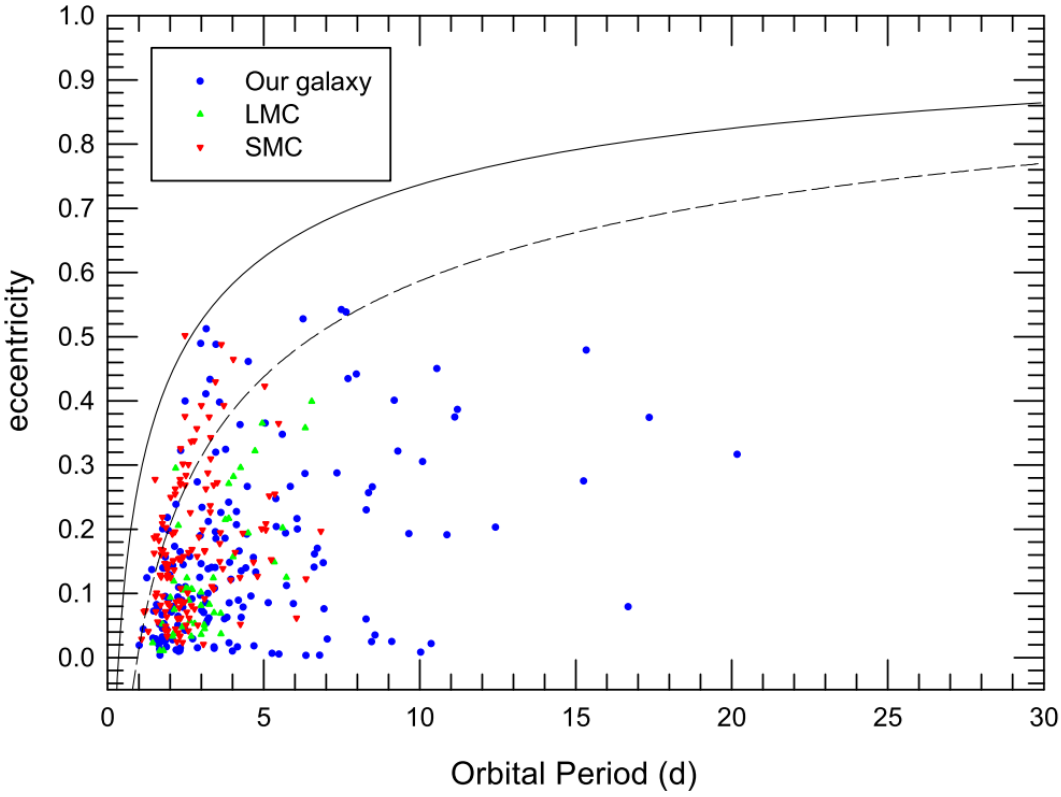

Figure 1.2: Eccentricity vs orbital period for a collection of eclipsing binaries from the Milky Way, and from the Large and Small Magellanic Clouds. The data show that systems with shorter orbital periods have orbits closer to circular, while theoretical upper limits for this distribution are presented with solid and dashed lines. Original from Fig.5 from Kim et al. (2018).

RE stars, the synchronisation time is significantly shorter than the circularisation time, and strongly dependent on the orbital period of the system (Tassoul, 1987, 1988).

In both cases, CE and RE, $t_{\rm sync}$ and $t_{\rm circ}$ are strongly correlated with the orbital period of the binary; thus, we should expect to see a higher fraction of circularised and synchronised systems among binaries with short orbital periods. And this is what we observe. In Fig. 1.2, the eccentricity of a collection of eclipsing binaries is plotted against their respective orbital period. The data clearly show how binaries with shorter orbital periods present lower eccentricities, that is, circular orbits.

1.1.3 Mass transfer and accretion disc formation

In a semi-detached system, one of the stars is in contact with its Roche lobe. This allows matter to fall from this star to the companion through the Lagrangian point L_1 in a process called mass transfer. The process affects the binary in several ways, including changes in the mass ratio of the stars, rejuvenation of one component, changes in the orbital parameters, and accretion disc formation, among other phenomena.

In response to the mass loss, the star's radius will be adjusted to recover its equilibrium. The star's reaction is characterised by different timescales: dynamical ($\sim$hours), thermal ($\sim 10^7$ years), and nuclear timescales ($\sim 10^9$ years). Additionally, a change in the mass ratio of the system will occur as a consequence of the mass transfer, affecting the size of the Roche lobe of the donating star in the process, according to Equation 1.2 (Sect. 1.1.1). The dominant timescale that determines the mass transfer rate $\dot{M}$ will depend on the changes in the radius of the donor star R and the size of the Roche lobe in response to the mass loss.

If the Roche lobe shrinks more quickly than the star can adjust its radius on dynamical timescales, the star can no longer remain in hydrostatic equilibrium. In this situation, $\dot{M}$ will be high ($\sim 10^{-5} - 10^{-4}$ $M_\odot$ yr^{-1}), limited only by the sonic flow of the gas when passing through L_1. If the Roche lobe shrinks slowly enough to allow the star to recover its hydrostatic equilibrium, mass transfer on thermal and nuclear timescales can still occur. In the case of thermal equilibrium, the star must increase its radius on longer time scales to balance the energy produced in the core and the energy radiated. If this increase is faster than the shrinking of Roche lobe size, then the mass transfer will occur on thermal timescales, which allows lower $\dot{M}$ than in the dynamical case ($\sim 10^{-7} - 10^{-6}$ $M_\odot$ yr^{-1}). Lastly, if the star manages to regain its thermal equilibrium, mass transfer can occur only because of the expansion of the star due to stellar evolution, or by a gradual decrease in r_L such as that caused by angular momentum loss. In this nuclear timescale, $\dot{M}$ will be relatively low ($\sim 10^{-11} - 10^{-8}$ $M_\odot$ yr^{-1})(Hjellming & Webbink, 1987; Hilditch, 2001).

As the mass transfer process takes place, the mass ratio of the stars will change. Because the angular momentum of the system must be conserved, the orbital separation will adjust accordingly to the change in mass ratio, affecting the binary's orbital period. The fractional change of the orbital period, $\dot{P}/P$, in a binary system experiencing a mass transfer process can be expressed as:

$$\frac{\dot{P}}{P} = -\frac{\dot{M}_{\rm D}}{M_{\rm D}}\left[3 - 3\beta\frac{M_{\rm D}}{M_{\rm G}} - (1-\beta)\frac{M_{\rm D}}{M_{\rm G}+M_{\rm D}} - 3(1-\beta)\alpha\frac{M_{\rm G}}{M_{\rm G}+M_{\rm D}}\right] + 3\frac{\dot{J}}{J}, \quad (1.3)$$

Where $\dot{M}_{\rm D}$ is the mass transfer rate from the donor star; $M_{\rm G}$ and $M_{\rm D}$ are the masses of the gainer and donor stars, respectively; and α and β are parameters that indicate the amount of matter accreted by the gainer and the amount of angular momentum loss carried out by the material leaving the system, respectively. The term $\dot{J}/J$ indicates the fractional change of angular momentum by other sources such as magnetic braking (Verbunt, 1993, , see Sect. 1.2.1). The simplest case to consider is when all the matter lost by the donor star is accreted by the gainer star and there is no loss of angular momentum, that is, $\beta = 1$, $\alpha = 0$, and $\dot{J} = 0$. This case is called the conservative mass transfer regime, and the expression for $\dot{P}/P$ is reduced to:

$$\frac{\dot{P}}{P} = -3\dot{M}_{\rm D}\frac{(M_{\rm G} - M_{\rm D})}{M_{\rm G}M_{\rm D}}. \quad (1.4)$$

We can see that the sign of the period fractional change will depend on the mass difference between the donor and gainer star. If the donor star is more massive, as we should expect in the first phase of mass transfer, the orbital period will decrease. This trend will continue until q reverses, and the gainer star becomes the more massive component in the system. In a full conservative mass transfer regime where the donor star is the less massive component in the system, the orbital period will always increase, and with it, the Roche lobe size of the components. If the increase in the radius of the donor star is smaller than the increase in its Roche lobe size, the mass transfer will eventually stop as the donor star loses contact with its Roche lobe.

When we consider mass loss from the system and loss of angular momentum, Equation 1.3 becomes more complicated as the parametrisation of α, β, and $\dot{J}$ becomes non-trivial, but in general, the decrease in orbital period will be greater when compared with a conservative mass transfer. The orbital period may continue to decrease even after the reverse in q.

The mass transfer process may have other consequences in addition to the change in orbital period and mass ratio of the components. It may cause an increase in the angular momentum of the accreting star or lead to the formation of an accretion disc around it. It depends on the radius of the accreting star and the angular momentum carried by the material leaving the donor star. The latter will prevent the material from falling directly into the gainer star, and instead, it will form a stream of matter characterised by a circularisation radius, $r_{\rm circ}$, which is defined as the radius for which

its Keplerian orbit has the same angular momentum as the particle that is falling from L_1 (Frank et al., 2002), and can be approximated by:

$$r_{\rm circ}/a = (1+q)(0.5 + 0.227 \log q)^4. \tag{1.5}$$

If the radius of the accreting star is larger than $r_{\rm circ}$, the stream will impact directly onto its photosphere, increasing its angular momentum. This led the accreting star to rotate at very high velocities. However, in most cases, this will not be the case, and an accretion disc will be formed around the accreting star. This disc will start as a ring with radius $r_{\rm circ}$, but due to the differences in velocity, both thermal and Keplerian, the particles within this ring will experience shear viscosity. The net effect of this viscosity is to transport angular momentum from the inner to the outer parts of the ring, spreading it towards inner and outer radii and creating a proper accretion disc around the accreting star.

The potential energy released by the falling material allows accretion discs to be one of the most energetic structures in the universe, particularly when formed around a compact object like a WD, a neutron star, or a black hole. To illustrate this, let's consider a flow of particles with a mass flow rate $\dot{M}$ that comes from infinity into the accretion disc, which rotates with Keplerian velocity ($\Omega^2 = GM/R^3$). The potential energy of the flow is converted into kinetic energy, which eventually transforms into heat and is radiated as energy. In that case, we can see that the energy released by the accretion disc, $L_{\rm disc}$, corresponds to:

$$L_{\rm disc} = \left(\frac{1}{2}\Omega^2 R^2 - \frac{GM}{R} \right) \dot{M} = \frac{GM\dot{M}}{2R}, \tag{1.6}$$

where M and R are the mass and radius of the accreting object (Frank et al., 2002). It is easy to see that compact objects accreting at high rates can host very luminous accretion discs.

An additional implication of Equation 1.6 is that the released energy is proportional to $\dot{M}$, thus for large $\dot{M}$ we can have luminosities large enough so that the radiation pressure exerted over the accreting matter surpasses the gravitational potential of the accretor. This defines a maximum luminosity for which accretion can take place, the Eddington luminosity $L_{\rm Edd}$. For the case of the pure ionised hydrogen, this limit corresponds to:

$$L_{\rm Edd} = \frac{4\pi GMm_{\rm p}c}{\sigma_{\rm T}} \approx 1.3 \times 10^{38} \, (M/{\rm M}_\odot) \, {\rm erg \, s^{-1}}, \tag{1.7}$$

where $m_{\rm p}$ corresponds to the mass of the proton, c the speed of light, and $\sigma_{\rm T}$ the Thomson cross section for the electron (6.7×10^{25} cm^2).

1.1.4 Formation of emission lines

Accretion discs are characterised at optical wavelengths by the presence of emission lines superimposed on a continuum. Both the emission lines and the continuum slope can provide us with information about the underlying system and disc. Besides the accretion discs, other structures related to the binary system, such as a circumstellar disc that surrounds the binary system, wind blowing from a giant star within the system, or material ejected from the system during an energetic event, to mention some possibilities, may originate emission lines of different kinds. Therefore, it is important to understand how these different emission lines are formed and what the different processes involved.

Both in stars and discs, the continuum emission observed can be approximated by a black-body emission (or by the contribution of several such sources). Black bodies are theoretical bodies that absorb all the radiation they receive, to subsequently re-emit it following the well-known Planck function:

$$B_\lambda(T) = \frac{2hc^2}{\lambda^5}(e^{\frac{hc}{\lambda kT}} - 1)^{-1}, \tag{1.8}$$

where B_λ is the specific intensity at wavelength λ, h the Planck constant, c the speed of light, k the Boltzmann constant, and T the temperature of the black body. The total emission radiated by a black body scales significantly with the temperature, as depicted in Fig. 1.3, where B_λ is presented for three different black bodies with temperatures of 2 000, 6 000, and 12 000 K. The figure also shows that the wavelength corresponding to the maximum of the emission, $\lambda_{\rm max}$, is inversely proportional to the temperature, which is known as the Wien law.

On the other hand, emission lines are produced when an electron that occupies a high-energy level within an atom (an excited population) jumps to a lower energy level in a process called spontaneous emission. This generates a photon with a specific wavelength, corresponding to the energy between levels (h/λ). Spontaneous emission occurs naturally and randomly with a probability per unit of time that is specific for each transition, and it is represented by the Einstein coefficient $A_{\rm ul}$, where the subscript stands for the upper and lower energy levels. However, several other factors play a role in the formation of spectral lines.

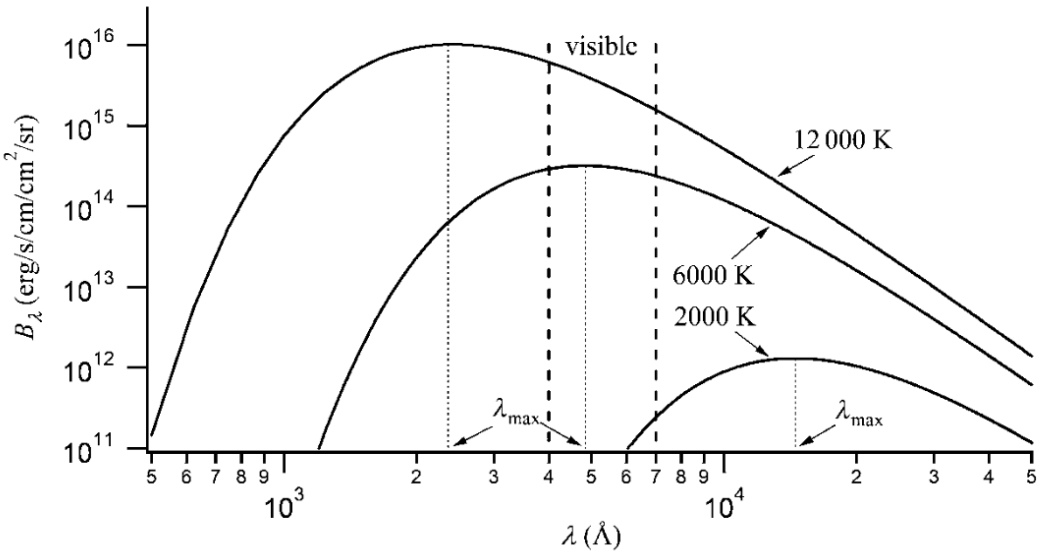

Figure 1.3: Black-body emission as a function of wavelength for three different temperatures: 2 000, 6 000, 12 000. The λ_{max} associated with each temperature is presented. Original from Figure 1.2 from LeBlanc (2010).

To begin with, it is necessary to start populating the excited level in question. This can be done by a source that emits photons with a specific energy, which are then absorbed by the electrons in the atom, pushing them to higher energy levels. Another possibility is to populate the excited levels of an atom by collisions with other particles. During these collisions, part of the kinetic energy is transferred to the electron, allowing it to populate more energetic levels.

In the case of an emitting source, the most common thing is to approximate the radiation to the black body emission, $B_\lambda(T)$. The radiation field must be strong enough to emit sufficient photons with energy h/λ to populate the upper levels of the atom in question, but weak enough to avoid an excessive ionisation of the population, which prevents the formation of spectral lines. In the case of excitation by collisions, key factors are the electron density and temperature. In this case, the energy carried out by the electrons in the environment (which is given by the electron temperature of the gas) can be absorbed by the electron bound to the atom if the energy corresponds exactly to h/λ, in that way populating the upper levels (a process called collision excitation). However, and similar to the case of B_λ, an equilibrium must be reached in which the energy and number of collisions (which is related to the electron density of the gas) must be high enough to populate the levels while also avoiding the ionisation

of the atoms.

Once the upper energy levels of an atom start to be populated, the spontaneous emission process will produce photons with wavelength λ. However, if $A_{\rm ul}$ is low, the high-energy population may be depopulated via collisions instead. This creates a differentiation between allowed and forbidden transitions, in which the former have large enough $A_{\rm ul}$ values so they can occur in environments of high density, while the latter can only decay via spontaneous emission in environments of low density where collisions are rare. To distinguish forbidden from allowed transitions, they are denoted with two square brackets, as [NII] λ 6584 Å.

In the case that the excitation is purely by collision, and the density is low enough to allow all the atoms to deexcite by spontaneous emission only, it is possible to determine the electron temperature and density of the gas by comparing the ratios of certain transitions of different elements. Certain atoms have excited levels that are accessible within the range of expected energies in the gas, but also have a significant difference between their energies (of the order of kT). In these cases, the ratio between these two transitions is sensitive to the electron temperature of the gas rather than its density. Some examples are [OIII] $(j\lambda4959 + j\lambda5007)/j\lambda4363$ and [NII]$(j\lambda6548 + j\lambda6584)/j\lambda5755$, where j denotes the emissivity of each transition. On the other hand, some atoms have transitions with similar energies, which makes their population level insensitive to the electron energy. The strength ratio between these transitions, however, differs for environments of high and low density, which makes them good indicators of the electron density of the gas. Some examples are [SII]$j\lambda6716/j\lambda6731$ and [OII]$j\lambda3726/j\lambda3729$. These diagnostics are useful for studying extended sources like planetary nebulae (see for example, Mari et al., 2023; Konstantinou et al., 2025), but also for unresolved ejecta like the one originating after a nova eruption (e.g. Harvey et al., 2023). A more detailed explanation of the different diagnostic lines, their physics behind, and how they can be utilised to determine the physical properties of the regions that originated them is beyond the scope of this manuscript, but the reader can refer to the books Osterbrock & Ferland (2006) and Draine (2011).

1.2 Cataclysmic variables

Cataclysmic variables (CVs) are binary systems composed of a white dwarf (WD) and a low-mass main-sequence star (secondary or donor star) with short ($\sim$hours) orbital periods, implying that their orbits are circularised and synchronised (Sect. 1.1.2). In these systems, the main-sequence star is actively transferring matter to its WD companion via Roche lobe overflow, forming in most cases an accretion disc around the WD (Sect. 1.1.3). The interaction between the star, the WD, and the accretion disc leads to a significant variability in CVs, and makes them excellent laboratories for studying a diverse range of astrophysical phenomena related to accretion processes across the entire electromagnetic spectrum, from radio to γ-rays.

An artistic representation of a classical CV is presented in Fig. 1.4. The image depicts the main-sequence star (red) actively transferring matter to its WD companion (white). The falling matter forms an accretion disc around the WD (blue), which can be subject to instabilities depending on the mass transfer rate from the secondary star. These instabilities translate to variations in the brightness of the disc, which are reflected in a variable light curve of the system.

Additional flavour can be added when we consider that some WDs are magnetic. The magnetic field disrupts the innermost parts of the accretion disc, affecting its configuration, funnelling the accretion towards the magnetic poles of the WD. This allows the appearance of other phenomena, such as synchrotron or X-ray emission. In the most extreme cases, the magnetic fields totally prevent the formation of an accretion disc around the WD.

The rate at which the WD accretes material from its main-sequence companion gives rise to nova eruptions: powerful and sudden ignition of the hydrogen accumulated over the WD surface (Sect. 1.3). The energy released by these eruptions increases the brightness of the system by several magnitudes, ejects material into the ISM, forming nova shells (Sect. 1.4), and affects the properties of the system (at least for a time). These nova eruptions do not destroy the WD or disrupt the system, allowing for successive cycles of eruptions with time scales of $\sim 10^4$ years. They play a significant role in the evolution of CVs by being the main source of mass loss from the system.

CVs also provide important clues for stellar astrophysics, as their evolution is also deeply related to the phenomena of magnetic braking and gravitational wave radiation (Sect. 1.2.1). As is the case for many other binary systems containing a compact object with a short orbital period, CVs originate (mainly) from binary systems that ex-

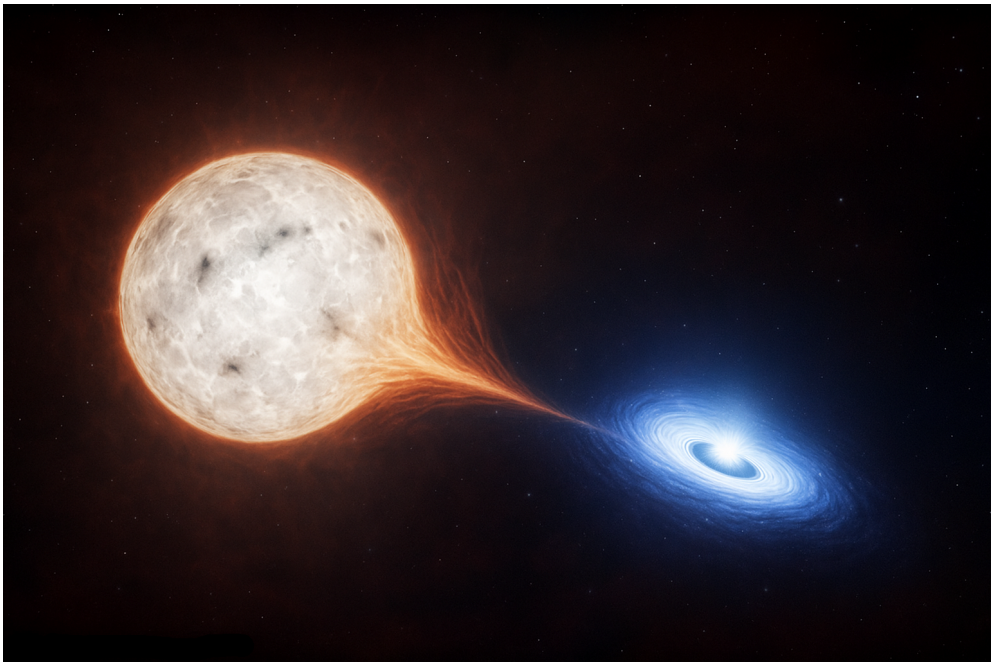

Figure 1.4: An artistic representation of a classical CV. The image depicts a low-mass main-sequence star transferring matter to a WD companion via Roche lobe overflow. The image was created using ChatGPT.

perienced a post-common envelope phase. Their future, on the other hand, is linked to brown dwarf stars orbiting cool WDs. A complete review of CVs is beyond the scope of this thesis, but I invite the reader to check out the work of Warner (1995) or Hellier (2001) for a more in-depth study.

1.2.1 Origin and evolution of CVs

Like many other binary systems involving compact objects in short orbital periods, CVs are born after a common envelope phase of a progenitor system (Ivanova et al., 2013). The original progenitors of CVs would have been composed of an intermediate-mass star and a low-mass companion in a wide orbital period. After the most massive star reaches its red giant phase, its radius becomes large enough to engulf its companion, significantly reducing the orbital separation due to the friction between the outer layers of the giant star and the companion. Eventually, the outer layers of the giant star are ejected into the ISM, leaving only a WD as a remnant. In most cases, the resulting WD will host a carbon-oxygen (CO) core, but more massive WDs hosting oxygen-neon (ONe) cores, or less massive WDs with helium (He) cores, may also be

formed. In any case, the less massive star survives, and the system is now composed of the WD and a low mass companion in a short orbital period, which is usually referred to as a post-common envelope binary (PCEB).

After a PCEB is born, its evolution will be deeply dictated by the angular momentum loss (AML) from the system. The main source of AML in PCEBs and CVs of long (> 3 h) period is the magnetic braking (MB) effect (Verbunt & Zwaan, 1981). This phenomenon is the result of the charged particles being carried out by the stellar wind from the companion star that happens to be locked in the magnetic lines of the secondary while leaving the system. As they are locked with the magnetic lines, they carry the angular momentum of the secondary with them, which is eventually lost once the particles decouple from the magnetic lines. In single stars, this AML is reflected in an increase in their rotational period, but in tidally locked binary stars, this is not possible. An increase in the rotational period of a tidally locked star would imply an increase in its orbital separation a, as $P_{\rm rot} = P_{\rm Kep} \propto a^{3/2}$. In binary systems, most of the angular momentum of the system is in their orbit, which is $\propto a^{1/2}$, with the rotation of the stars contributing minimally. Thus, in tidally locked binary systems, the AML by MB is not extracted from the star but from the binary orbit instead, resulting in a steady reduction of the binary separation (Warner, 1995; Hilditch, 2001). Once the orbital separation has decreased enough, the secondary star will be in touch with its Roche lobe and mass transfer via Roche lobe will take place. This will make the PCEB be considered as a proper CV.

The distribution of orbital periods of CVs shows a sharp decline in the number of systems with orbital periods between $\sim 2-3$ hours. This gap in the orbital distribution, which is referred to as the period gap of CVs, is presented in Fig. 1.5, which shows the orbital period distribution of non-magnetic CVs from the Ritter & Kolb (RK) catalogue (Ritter & Kolb, 2003). The most accepted explanation for the period gap is a disruption of MB at these orbital periods (Rappaport et al., 1983; Spruit & Ritter, 1983). As the system evolves, the constant loss of angular momentum from the system causes the orbital period to decrease until it reaches $\sim$3 hours. At this orbital period, the secondary star has lost enough mass to become fully convective, producing a reconfiguration and disruption of its magnetic field, and thus, of MB. Without the AML by MB, the Roche lobe will stop shrinking, the secondary can readjust to achieve its equilibrium, the system will detach, mass transfer will stop, and the accretion disc will be disrupted. This will cause the CV to become a detached system, much fainter and difficult to observe.

Although MB is not efficiently operating anymore, there are other sources of AML to consider, such as gravitational wave radiation (GWR, Paczyński, 1967). Analogous to the radiation produced by accelerated charged particles, particles with mass radiate energy when they are under acceleration, like in a binary system, for instance. This energy is radiated as oscillations of the space-time carrying out angular momentum from the system with them. The efficiency of GWR in binaries strongly depends on the masses of the components and the orbital separation, being more efficient for massive components in short orbital periods. Therefore, even when MB is not operating, GWR will cause AML from the system, which eventually will cause the orbit to shrink. Once the CV reaches an orbital period $\sim$ 2 hours, the secondary will be in touch again with its Roche lobe, restarting the mass transfer, reactivating the accretion disc around the WD, and making the CV detectable again. The mass transfer rate (and in consequence, their brightness) for CVs that evolved past the period gap is considerably lower than for systems above it, resulting in intrinsically fainter objects that are consequently harder to detect.

In addition to the period gap, Fig. 1.5 also reveals another feature of CVs: the period minimum. As the CV crosses the period gap and its orbital period continues decreasing, the secondary star will continue losing mass. This will continue until the secondary can not support hydrogen burning in its core and becomes a brown dwarf. A brown dwarf is a degenerate object that is supported by electron-degeneracy pressure, and the response of a degenerate object to mass loss is an increase in its radius, contrary to the behaviour of normal stars. On the other hand, an increase in the radius of the companion star implies an increase in the orbital period; thus, the CVs will start to return towards longer orbital periods. These systems are known as period bouncers, and they define a minimum orbital period for the secular evolution of CVs (Patterson, 1998).

It is expected that most of the CVs are period bouncers that have evolved beyond the minimum period. This is because the evolution of CVs is directly related to the effects of AML, which are stronger for systems above than below the period gap. In consequence, CVs spent most of their lifetime below the gap, a large fraction of it as period bouncers. Theoretical works have established that the minimum period should be located at $\sim$70 min (Kolb & Baraffe, 1999), and that $\sim$99% of all CVs should be located below the period gap, $\sim$70% of them corresponding to period bouncers (Kolb, 1993). These predictions are in strong discrepancy with the results of magnitude-limited surveys, such as the R&K catalogue (Fig. 1.5). These surveys show a similar number of

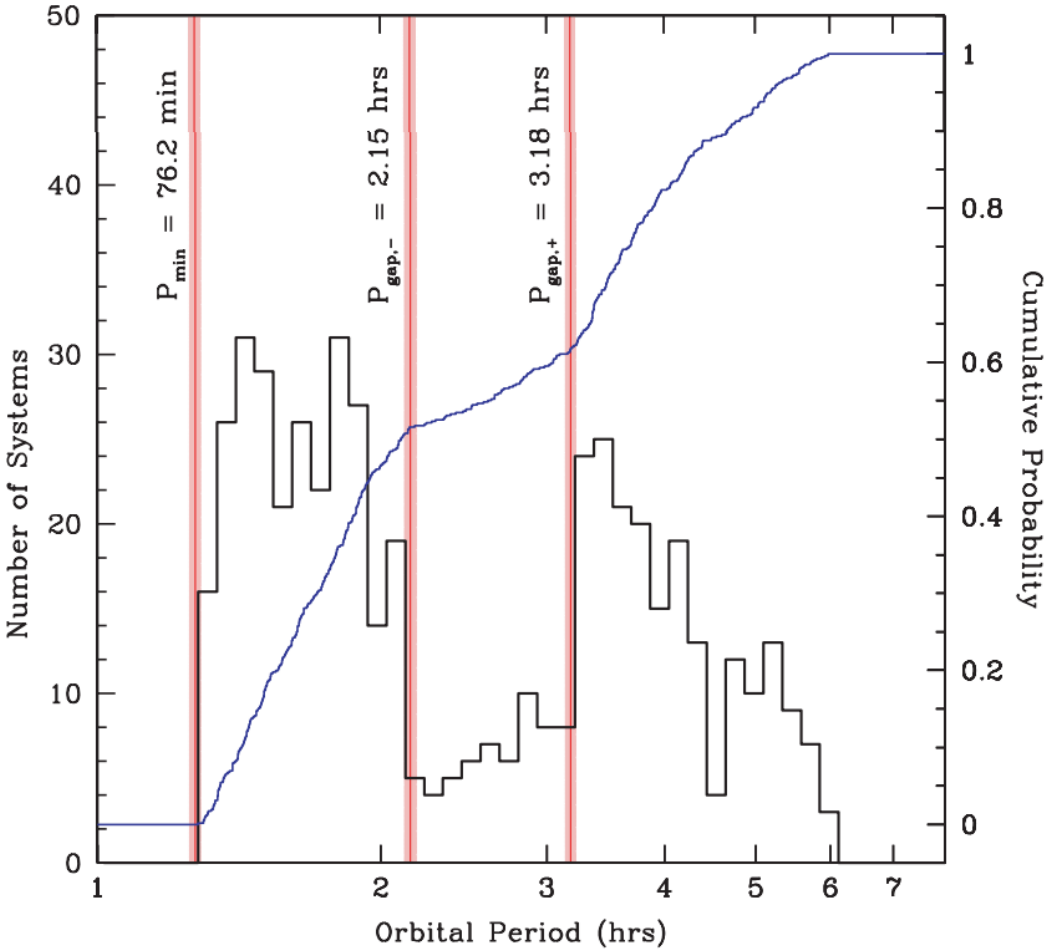

Figure 1.5: Discrete (black) and cumulative (blue) distribution of the orbital periods of CVs. The data was obtained from the R&K catalogue (Ritter & Kolb, 2003). The location of the period minimum and the edges of the period gap determined by the authors are marked with vertical red lines. Although the release of the most recent survey has left the presented distribution outdated, it serves well the purpose of illustrating the limits of the period gap as well as the period minimum (see text for details). Original from Fig.4 of Knigge (2006).

systems above and below the gap, and a period minimum that is higher than the predicted value (∼76 min according to Knigge (2006)). The discrepancy in the number of systems above and below the gap is expected, as systems below the gap have lower accretion rates, thus lower luminosities, making them more difficult to detect and undersampled in a magnitude-limited survey. This undersampling was alleviated by the results from the Sloan Digital Sky Survey, which reveal a higher number of CVs below than above the gap, and a spike of systems between $\sim 80-86$ min, associated with the period minimum (Gänsicke et al., 2009). On the other hand, the distribution derived from volume-limited samples shows many more CVs below than above the gap, but still not enough to reconcile it with the theoretical predictions (Pala et al., 2020; Inight et al., 2021). It has been proposed that an additional (hypothetical) mechanism of AML of unknown origin operates below the gap in addition to GWR. This extra AML is, in theory, able to explain the location of the period minimum and the dearth of period bouncers by causing some system to merge (Inight et al., 2023b).

Lastly, it is worth noting that the previous results are valid only for non-magnetic CVs. For the magnetic CVs, the period gap is not evident, and this is attributed to a less efficient MB because of the interaction between the magnetic lines of the WD and the secondary itself (Inight et al., 2023a; Schreiber et al., 2024).

1.2.2 Subtypes of CVs

CVs are subclassified depending on their $\dot{M}$ and on the strength of the WD's magnetic field. These two parameters are the origin of significant differences among CVs, which are then translated into their light curves and spectra. A scheme of the different CV subtypes and classifications is presented in Fig. 1.6. Starting with $\dot{M}$, CVs can be subclassified as dwarf novae (DNe) and nova-likes (NLs) for low and high $\dot{M}$, respectively. On the other hand, a distinction can be made between systems hosting magnetic WDs, as intermediate-polars (IPs) or polars, depending on whether the magnetic field is strong enough to partially or totally disrupt the accretion disc around the WD.

Non-magnetic WDs

The DNe are CVs that have low $\dot{M}$. This causes their accretion disk to be cold and faint, but more importantly, it gives rise to outbursts: short (∼days) and small ($\Delta m \sim 3-5$ mag) increases in the luminosity of the system. An outburst originates

as a result of thermal instabilities within the disc. The amount of material accreted by the WD is directly proportional to the disc's viscosity, which is directly proportional to the disc's temperature. If the viscosity of the disc is low, the rate of material accreted by the WD may be lower than the mass transfer rate from the secondary, resulting in material piling up in the disc. This leads to an increase in the disc's surface density, which is reflected in its opacity and temperature. This results in a sudden growth of the disc's viscosity, which leads to an increment in the disc's size and luminosity, that is, an outburst. This stage lasts until the disc is depleted and returns to its quiescence stage (Shakura & Sunyaev, 1973; Osaki, 1974; Balbus & Hawley, 1991). Some systems may also present superoutbursts, similar in brightness to normal outbursts but of significantly longer duration. The origin of these superoutbursts can also be found in the accretion disc, although in these cases they originate from a precessing accretion disc whose radius is close to the tidal radius (Vogt, 1982; Whitehurst, 1988). The superoutburst will last until the disc is truncated below the tidal radius and stop precessing, causing the system to return to its quiescent stage. During its quiescence stage, the spectra of DNe are dominated mainly by Balmer emission lines originating in the accretion disc, a continuum characterised by a flat slope resulting from the low temperature of the disc, while sometimes the secondary dominates the spectrum at redder wavelengths. During the outburst, the spectrum is dominated by the accretion disc.

Nova-likes, on the other hand, are CVs that have a high enough $\dot{M}$ so that their accretion disc can be in a stable high-temperature state. The high $\dot{M}$ allows for steady accretion discs that experience much less variability than their DNe counterparts. Still, some NLs can present changes in luminosity by jumping from high to low states with a difference in magnitude of $\sim 2-3$ mag if their $\dot{M}$ is relatively low (see for example, the VY Scl subclass Warner & van Citters, 1974). They are more luminous than DNe and their spectra show a blue continuum with comparatively weak emission lines of H and He originating from the accretion disc.

Magnetic WDs

Additional complexity can be added when we consider the strength of the WD magnetic field. Most of the CVs host WDs with no significant magnetic fields. In those cases, the weak (or nonexistent) magnetic field allows the accretion disc to reach the

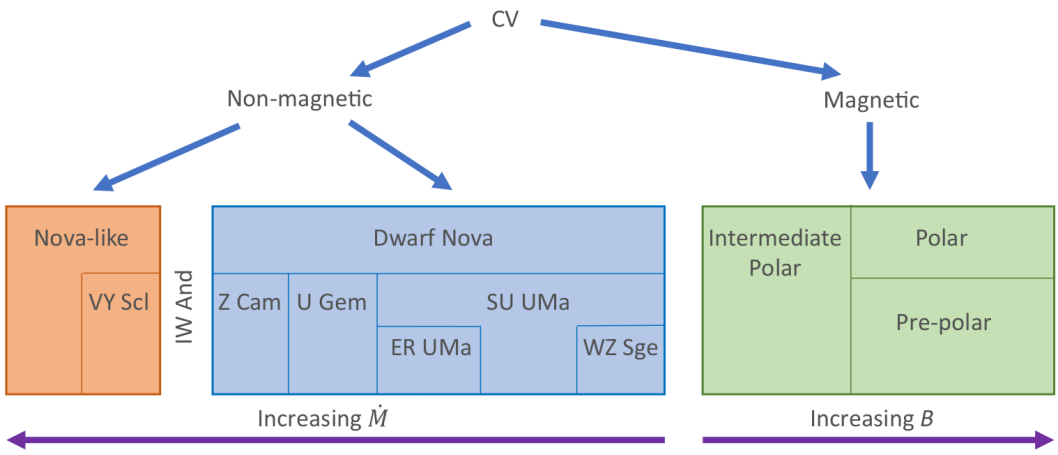

Figure 1.6: Scheme of the different CV subtypes, including DNe, NLs, IPs, and polars. Original from Fig.1 of Inight et al. (2023a).

boundary layer of accretion [1] around the WD within the orbital plane. Some systems, however, host WD with a magnetic field strong enough ($1 - 10$ MG) to disrupt only the inner parts of the accretion disc by forcing the ionised particles to follow the magnetic lines when they reach the Alfvén radius: the radius at which the magnetic energy density equals the kinetic energy density in a plasma (Davidson, 2001). These systems are called intermediate polars (IPs), with the prototype system being DQ Her. The accretion in IPs differs from the usual non-magnetic CV as the accreted material is forced to follow the magnetic lines originating from the WD, from the accretion disc onto the magnetic poles. The shock region generated by the infalling material reaches high enough temperatures to ionise helium, giving rise to HeII emission lines, a common feature of IPs. From this shock region, X-rays may also be detected, from which the spin of the WD can be measured.

The Alfvén radius is proportional to the square of the magnetic field of the WD, and therefore, for WDs with very high magnetic fields (> 10 MG), their Alfvén radius may be larger than their $r_{\rm circ}$ (see Sect. 1.1.3). If this is the case, the accreted material can not form an accretion disc around the WD and instead is funnelled directly towards the magnetic poles. These extreme systems are called 'polars' or AM Her CVs, by their prototype system. In contrast to IPs, the WD is synchronised (its rotational period matches its orbital period) as a result of the interaction between its magnetic field and

[1]The transferred material does not fall directly onto the surface of the WD. The material in the accretion disc needs to lose additional energy to match the angular velocity of the surface of the compact object. This takes place via a boundary layer.

the one from the secondary, exerting an additional torque on the WD. Their spectra may also present, in addition to hydrogen emission, synchrotron emission originating from the ionised particles trapped in the magnetic lines, X-ray and HeII emission from the shock-heated impact zone around the accreting WD's magnetic pole, Zeeman splitting, and polarised light reason for which they are called 'polars'.

1.3 Nova eruptions

When a WD has accreted the matter required to reach the critical pressure to ignite hydrogen into helium, a thermonuclear runaway is triggered on its surface's bottom layer, initiating what is called a nova eruption. This is a transient phenomenon that can last hundreds of days, and where the brightness of the system can increase up to 16 mag before declining. The energy released during the eruption is insufficient to destroy the WD or disrupt the systems, and after a time, the CV will return to its quiescent state, restarting the transfer of matter from the companion to the WD, and therefore, the cycle. Thus, nova eruptions are a cyclic phenomenon in CVs, playing a crucial role in their evolution as they are the main source of mass loss from the system. However, the short-term effects of the eruption on the CV are still under debate.

1.3.1 Thermonuclear runaway

As a WD accretes matter, this starts to accumulate onto its surface. The accreted matter is usually mainly hydrogen coming from a companion star, either by Roche lobe overflow or by stellar winds. As the hydrogen accumulates on the surface, the pressure at the bottom layer of this hydrogen material starts to increase significantly, leading to a degeneration of the matter. In a degenerate matter, the pressure and temperature are decoupled in its equation of state; thus, the material can not expand in response to a sudden increase in its temperature until a critical temperature value is reached (the Fermi temperature). Therefore, once the pressure and temperature of the bottom layer reach the critical pressure $P_{\rm crit} \approx 2 \times 10^{19}$ dyn cm^{-2} (MacDonald, 1983) to ignite the hydrogen into helium, the material can not expand in response, leading to a sudden detonation of the remaining hydrogen layer across the whole WD's surface. This process is referred to as a thermonuclear runaway (TNR). After a couple of minutes, the temperature of the gas reaches the Fermi temperature and starts to expand, putting an end to the TNR (Starrfield et al., 1972; José, 2012; Starrfield et al., 2016).

The TNR is powered first by *p-p* chain and *pep* reactions (Starrfield et al., 2009) and then by the hot CNO cycle (José, 2012; Starrfield et al., 2016). The C, N, and O required to sustain the CNO cycle come mainly from the deeper layers of the WD, reaching the surface via Kelvin-Helmholtz instabilities, with only a minor fraction coming from the accreted material (José, 2012). In the cold CNO cycle, a constant delivery of protons is required to keep the cycle ongoing. In normal star core conditions, an equilibrium exists between the rate of proton captures and beta decay of the elements, which allows

a sustained cycle in time. During a TNR, however, the number of available protons is significantly higher than in normal star cores, thus breaking the aforementioned equilibrium, leading to the hot CNO cycle instead. This leads to the formation of different isotopes and elements, as the atoms capture a proton before they can decay. As the TNR suddenly stops, the cycle is interrupted, leaving behind isotopes that are not commonly found in other transients or stars. Nova eruptions are believed to be the main source of ^{7}Li, ^{13}C, ^{15}N, and ^{17}O among others in the galaxy (Gehrz et al., 1998; Starrfield et al., 2016, 2020, 2024).

It is worth mentioning that the previous discussion is based on the assumption of a symmetric and spherical TNR, which is not necessarily true in all cases. It has been proposed that localised TNR may take place in certain systems (Shara, 1982; Orio & Shaviv, 1993). The origin of these localised TNRs could be the material accreted and funnelled by magnetic fields, pointed out as a possible explanation for micro-novae, shorter and significantly less energetic events than classical novae (Scaringi et al., 2022a,b).

Mass of the WD

From a physical point of view, the most critical parameter to characterise a TNR in terms of energy released is the mass of the accreting WD. The TNR will start once the pressure in the hydrogen bottom layer reaches a critical value, $P_{\rm crit}$, given by:

$$P_{\rm crit} = \frac{G M_{\rm WD} M_{\rm env}}{4\pi R_{\rm WD}}, \tag{1.9}$$

where G is the universal gravitational constant, $M_{\rm WD}$ and $R_{\rm WD}$ are the mass and radius of the accreting WD, and $M_{\rm env}$ is the mass of the accreted envelope (Fujimoto, 1982). Equation 1.9 reveals the strong dependence of $P_{\rm crit}$ required to ignite a TNR of the accreting WD (Gehrz et al., 1998). Furthermore, as the mass and radius of a WD follow a tight relation, the previous equation implies that the amount of accreted material can be written solely as a function of the WD mass. As WDs are supported by electron degeneracy pressure, it follows that $R_{\rm WD} \propto M_{\rm WD}^{-1/3}$, thus Equation 1.9 can be rewritten as:

$$M_{\rm env} \propto M_{\rm WD}^{-4/3}. \tag{1.10}$$

This implies that the material required to trigger a TNR is inversely proportional to the mass of the WD. Simulations have shown that other factors like the WD tem-

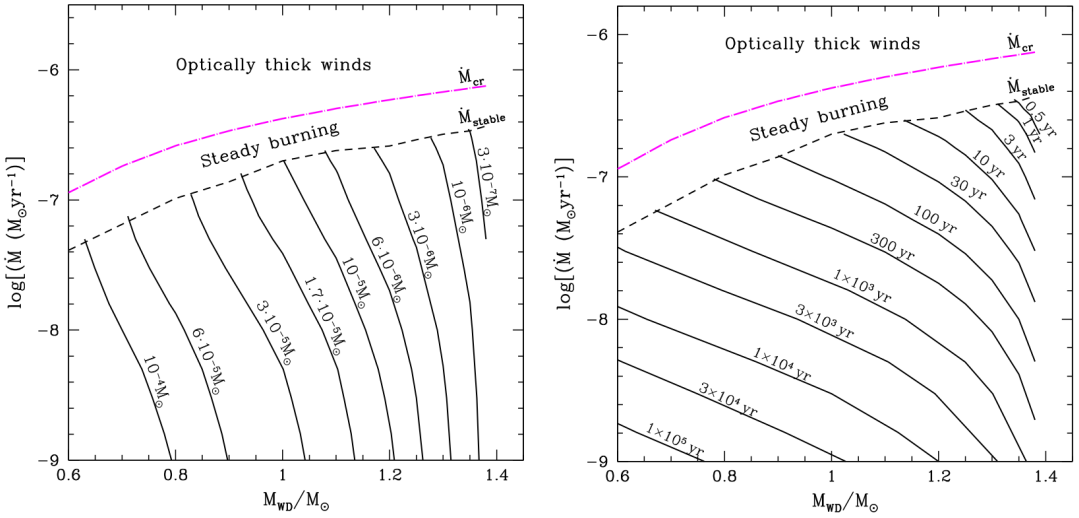

Figure 1.7: Critical $M_{\rm env}$ required to trigger a TNR. Left panel: isomasses of $M_{\rm env}$ in the $M_{\rm WD} - \dot{M}$ plane. Right panel: same as left panel but for equi-recurrence periods instead of $M_{\rm env}$. In both cases, the minimum ($\dot{M}_{\rm stable}$) and maximum ($\dot{M}_{\rm crit}$) limits for a steady burning of hydrogen on the WD surface are marked with dashed lines. Adapted from Figs. 3 and 6 of Kato et al. (2014).

perature or the chemical composition of the accreted material play a minor role in the required amount of $M_{\rm env}$ when compared with the WD mass (Kato et al., 2014; Starrfield et al., 2020, 2024). Thus, Equation 1.10 may serve as a good approximation to reality.

Recurrence times

The time required for the WD to accrete the critical $M_{\rm env}$, usually denoted as the recurrence time $t_{\rm rec}$, depends on the $\dot{M}$ value. Systems hosting more massive WDs and accreting at higher $\dot{M}$ will reach the critical $M_{\rm env}$ much faster than those systems with less massive WDs and lower $\dot{M}$. Fig. 1.7 shows the results of simulations aimed to characterise the shortest recurrence time possible as a function of $M_{\rm WD}$ and $\dot{M}$ (Kato et al., 2014). The left panel of Fig. 1.7 shows different isomasses in the $M_{\rm WD}$-$\dot{M}$ plane. These isomasses correspond to the $M_{\rm env}$ required to trigger a TNR, whose values range from $\sim 10^{-7}$ $M_\odot$ for the most massive WD accreting at the highest rates, up to $\sim 10^{-4}$ $M_\odot$ in the case of the less massive and slowest accreting WD. The figure also highlights the position of a stable and critical $\dot{M}$. The $\dot{M}_{\rm stable}$ corresponds to the lowest accretion rate required to have a steady burning of hydrogen onto the WD's

surface, that is, the hydrogen is immediately fused into helium. This implies that no TNR is possible above this $\dot{M}_{\rm stable}$ limit and instead, a steady growth of the WD occurs. The other limit of interest is defined by the $\dot{M}_{\rm critical}$ line, which corresponds to the limit where the Eddington luminosity is reached, preventing further accretion onto the WD (see Sect. 1.1.3).

On the other hand, these isomasses can be converted to equi-recurrence times (right panel of Fig. 1.7). We can see that the $t_{\rm rec}$ can be as short as $\sim$ 1 year, while for other conditions it can reach up to $\sim 10^5$ years. Observationally, the shortest observed $t_{\rm rec}$ is $\sim$ 1 year (Darnley et al., 2014), while several others present $t_{\rm rec}$ of decades (e.g. RS Oph with $t_{\rm rec}$ $\sim$15 years, Montez et al., 2022). This allows us to classify nova eruptions based on their recurrence time, with those systems that have $t_{\rm rec}$ short enough for us to record at least two eruptions as recurrent novae (RNe), and those systems for which we have recorded only one eruption as classical novae (CNe). Although this classification is merely observational, it is useful to distinguish systems with massive WDs accreting at high rates (RNe) from more common CVs (lower WD mass and accretion rates). There are several candidates to RNe for which we have recorded only one eruption, but a confirmation of their recurrence nature will be possible within the next decades (Pagnotta & Schaefer, 2014). This will increase the number of confirmed RNe with time, but for the vast majority of CVs, their recurrence times are too large ($> 10^3$ years), so observing a second nova eruption will not be possible.

1.3.2 Observations of nova eruptions

Nova eruptions have been observed across the entire electromagnetic spectrum, either using photometric and spectroscopic observations. For a long time, these observations focused on the optical part of the spectrum, revealing the complex evolution of nova eruptions through their light curve and spectra. Their light curves present a significant variety of morphologies, including differences in the amplitude of their maximum and the speed at which they evolve. Multi-wavelength analysis indicates additional variation of the photometric colour of the nova eruption, revealing the variation in temperature and density of the ejecta, as well as other processes that may take place, like dust and grain formation. Spectroscopic studies, on the other hand, have shed light on the properties of the ejected material, including its composition and velocity. Observations at different times after the eruption show how the spectra vary with time, unveiling the temperature and density evolution within the ejecta, revealed

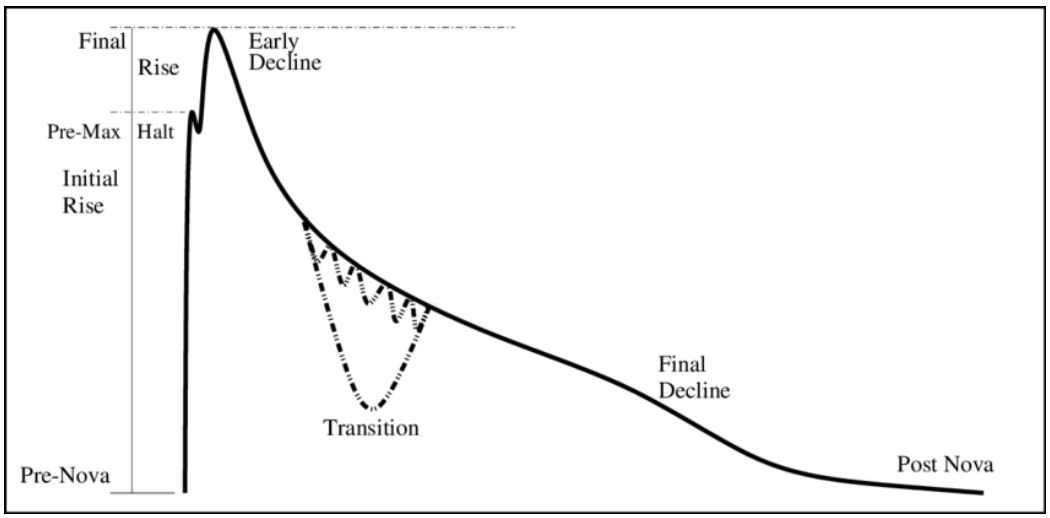

Figure 1.8: Illustrative example of an optical nova light curve. The different stages of an eruption, including the pre-nova, the initial rise, the maximum, and the posterior decline, are presented. A more detailed explanation of each phase is presented in the main text. Adapted from Fig.1 of McLaughlin (1943).

by the changes in the number and strength of emission lines of forbidden and allowed transitions. The spectral profiles, in particular the Hα, reveal clumpy ejecta and evidence for several ejections of material during the nova eruption. In recent years, the evolution of nova eruptions has been revealed by wavelengths beyond the optical range: γ-rays and X-rays at high energies; infrared, submillimeter, and radio at lower energies. Observations at these wavelengths show a complex picture, including shocks produced by the collision of several ejecta and expanding lobes of material.

Photometric observations

Nova eruptions are usually discovered immediately after the eruption, as the brightness of the system increases by several (8-16) magnitudes (e.g. Duerbeck, 1987a). Thus, the most common kind of observations we have for nova eruptions are light curves. In many cases, the system was too faint ($\gtrsim$20 mag) to be detected prior to the eruption, which, in combination with the fast increase of brightness, causes the ascending part of the light curve to be rarely recorded, although the number of ascending light curves has increased in the last years thanks to the growth number of fast-response surveys (Aydi et al., 2024). The posterior phases of the light curve, corresponding to the maximum and its subsequent decline, are usually recorded in their entirety.

As an illustrative example, a generic nova light curve is presented in Fig. 1.8, which

shows the main stages of a nova eruption. Starting from the pre-nova phase, which corresponds to the system just before the TNR takes place, it follows the initial and fast rise. In some systems, the brightness increase halts before reaching the maximum, giving origin to a pre-maximum stage. After reaching the maximum, the brightness will decrease during the posterior decline until reaching the post-nova stage. In some systems, a dip is observed in the months after the eruption, which is denoted as a transition stage, and it is usually attributed to the formation of dust in the ejecta (see for example, Chong et al., 2025).

The previous scheme, however, may be deceptive as it can suggest a common behaviour for all nova light curves. The reality is more complex, with nova light curves showing a variety of morphologies, which can be characterised in terms of several observables such as the amplitude of the eruption, how fast it declines from its maximum, and its overall shape. One of the usual ways to subclassify light curves of nova eruptions is by how fast they decline. This is usually parameterised using a $t_{\rm n}$ parameter, which expresses the number of days it took for the light curve to decrease its brightness n magnitudes from its maximum. Some studies prefer the use of t_3 to characterise the speed of the decline in nova eruptions (e.g. Schaefer, 2022; Santamaría et al., 2025), while other prefer the use of t_2 (e.g. Aydi et al., 2024; Chong et al., 2025) or t_1 (for example, Kasliwal et al., 2011). In some cases, as could be an extra-galactic nova, for example, the post-nova is too faint to be detected one or two magnitudes fainter than the maximum. In these cases, the use of t_1 or t_2 is the only available option. The use of t_n led to a general classification and differentiation between fast novae with t_n in the range of days and weeks, and slow novae for which t_n can reach hundreds of days.

The determination of the time of the maximum is not trivial, though. The light curves of nova eruptions present a variety of morphologies, with only a handful of them showing a clear and unique maximum. Most of them present several local maxima, plateaus, and/or jittering that complicate a clear identification of the maximum, and thus the t_n parameter.

This variety of morphologies in the light curves was classified by Strope et al. (2010), who grouped the light curves of 93 eruptions according to the features they present. The authors considered seven different light curve morphologies: flat (F), cusped (C), jitters (J), plate (P), oscillations (O), smooth (S), and dips (D), each one with their own characteristic morphology. The prototypes for these light curve classifications are shown in Fig. 1.9. These morphological varieties reflect the diverse processes

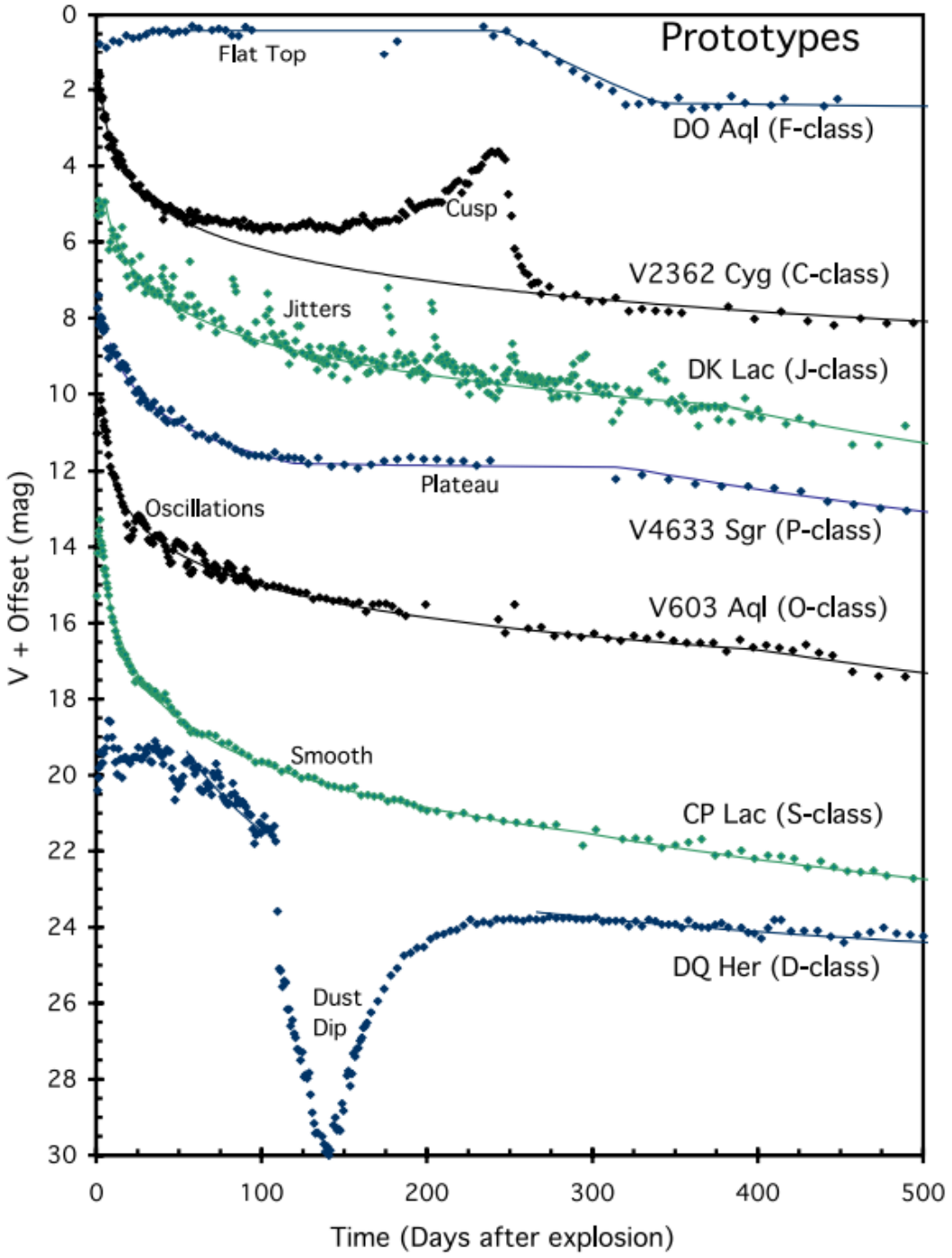

Figure 1.9: Examples of the different morphologies of light curves of novae. It shows the prototypical morphologies for the light curve classification proposed by Strope et al. (2010). Original from Fig.2 of Strope et al. (2010).

that play a role during a nova eruption, encoding important physics behind them.

Similarly, there have been attempts to use nova eruptions as standard candles, in a manner similar to supernovae. The idea is that the maximum amplitude reached by the nova eruption and the speed at which it fades from its maximum are directly correlated to the WD's mass. Therefore, a correlation should exist between these two parameters, which is known as the maximum-magnitude-rate-of-decline (MMRD; Arp, 1956; della Valle & Livio, 1995; Della Valle & Izzo, 2020). The MMRD relation has been calibrated using galactic novae, providing a well-established anticorrelation between the absolute maximum of the nova eruption and t_3 (see for example, Selvelli & Gilmozzi, 2019). On the other hand, the population of novae observed in different galaxies present a different behaviour with respect to the galactic novae (Kasliwal et al., 2011; Shara et al., 2017a). These differences, together with the variety of nova light curves, show the complexity behind the physics of nova eruptions and how different parameters, such as WD temperature, metallicity, or accretion rate, play a significant role during the nova.

Additional information about the nova eruption and the subsequent ejecta arises from the study of colour during the decline phase of the light curve. Analysing the evolution of the nova light curve in different filters allows us to clarify some of the observed properties. For example, multi-wavelength studies of the fading of nova eruptions reveal the presence and formation of dust in the months after (e.g. Evans & Gehrz, 2012; Chong et al., 2025), a characteristic attributed to the diminishment in the flux observed in D-type nova light curves.

Spectroscopic observations

The information provided by their light curves, although very valuable, is insufficient to comprehend the totality of the physical processes that operate during the eruption. Thus, it is also necessary to follow the eruption with spectroscopic observations, as they can reveal additional information that the light curves can not. However, spectroscopic observations are not exempt from challenges. The observations of the ascending phase, often called 'pre-maximum phase', are difficult if the nova evolves fast, thus causing an observational bias towards the slowest novae during this phase (Aydi et al., 2020, 2024). Nevertheless, observations during and after the maximum are usually obtained, allowing us to draw a common picture of novae evolution during this phase.

These observations reveal an overabundance of heavy elements such as carbon,

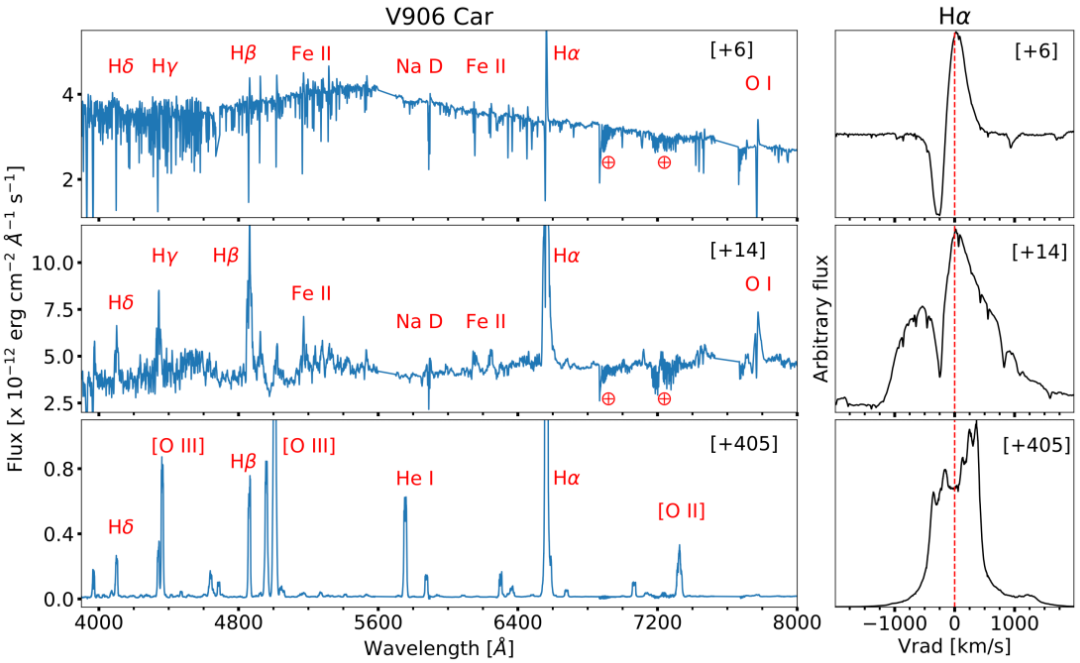

Figure 1.10: Spectral evolution of V906 Car (Nova Carinae 2018). Each panel in the left column show a spectrum at a different epoch, with the days after the eruption for each spectrum denoted within square brackets. The right column shows a zoom to the Hα profile. After the eruption, the spectra transition from a pseudo-stellar phase characterized by a P-Cygni profile (top panel) to an 'Orion' spectrum starting to be dominated by emission lines and the appearance of fast components (mid panel), and finally to a nebular spectrum dominated only by emission lines of the fast component observed in allowed and forbidden transitions (bottom panel). Adapted from Fig.4 of Chomiuk et al. (2021).

oxygen, nitrogen, or neon, among others (e.g. McLaughlin, 1943; Gehrz et al., 1998; Downen et al., 2013; Chomiuk et al., 2021). These elements can not be generated by the TNR, therefore implying a drag mechanism that extracts these elements from the WD core and ejects them during the nova eruption. The velocity at which these elements are ejected is indicated by the full-width at half maximum (FWHM) of their spectral profiles. The ejecta is not composed of a single shell expanding uniformly, but of a complex series of ejections with different ejection velocities $v_{\rm ej}$. The FWHM of a line provide an approximation to this range of velocities, with $v_{\rm ej}$ varying between a few hundred to thousands of km s^{-1} (e.g. Gehrz et al., 1998; Darnley et al., 2016). These observations also support the theory that states that RNe should host more massive WD, having higher $v_{\rm ej}$ and eject less material than their classical counterparts (Schaefer, 2010; Pagnotta & Schaefer, 2014).

Another interesting aspect of the study is the evolution of the overall spectra as the nova eruption evolves and fades. The spectral profile in general, and the Hα line in particular, shows significant changes before, during, and after the maximum brightness of the nova. The spectral evolution of the nova eruption of V906 Car (Nova Carinae 2018) is presented in Fig. 1.10 as an example of the overall evolution observed in novae (Aydi et al., 2020; Chomiuk et al., 2021). Absorption and emission lines for several elements are present in the spectra, including but not limited to He, Fe, and N. These lines were observed to differ significantly for different novae, leading to a spectral differentiation between 'He/N' and 'FeII' novae (Williams, 1992, 2012). Besides the differences in the elements, 'He/N' novae show faster (FWHM$>$ 2 500 km s^{-1}) ejecta dominated by P-Cygni profiles, while 'FeII' novae show slower ejecta (FWHM$<$ 2 500 km s^{-1}) with flat profiles instead. In some cases, the spectra show characteristics of both classes, even evolving from one to another. Supported by follow-up spectroscopy of 10 different novae from as early as pre-maximum, Aydi et al. (2024) provided evidence to claim that the 'He/N' and 'FeII' classifications are no more than different phases of an overall universal evolution of the spectra in novae. They proposed that virtually all novae follow an 'He/N', 'FeII', and 'He/N' evolution before reaching the nebular phase, attributing the previous differentiation to the time the spectra were observed.

During the first 'He/N' phase, the ejecta is hot and dense, allowing the appearance of high-excitation lines like HeI or NIII. This stage is fast ($\sim$hours-days) and therefore usually missed. As the ejecta expands, it cools, permitting the formation of less energetic lines such as FeII. This phase is reached near the maximum of the optical light, and is usually denoted as the 'iron-curtain' or 'pseudo-photospheric' phase (top and middle panel in Fig. 1.10). As the ejecta continue expanding, their density decreases, and the gas starts to become optically thin. This allows the energetic photons from the hot WD to ionise the gas, and the reappearance of high-excitation lines. This lasts until the totality of the ejecta has become optically thin, leading to the emergence of nebular lines (the nebular phase, bottom panel of Fig. 1.10).

In addition to the mentioned evolution, the Hα profile also shows an interesting evolution during nova eruptions. This is shown in the right column of Fig. 1.10. The first spectrum shows the Hα before the nova light curve reached its maximum, showing a P-Cygni profile, characteristic of mass loss from the system, with $v_{\rm ej} \lesssim 1000$ km s^{-1}. After the nova eruption reaches its maximum, the spectrum starts to transition to a middle point between a stellar atmosphere and a nebular phase. During this

transition stage, a fast component ($v_{ej} \gtrsim 1000$ km s^{-1}) starts to appear and dominates Hα, where the P-Cygni profile appears superimposed on this new fast component (middle panel of Fig. 1.10). Lastly, several months after the eruption, and when the spectrum has reached its nebular phase, the Hα profile shows no traces of the former P-Cygni profile and instead is dominated by the fast component observed after the maximum. This evolution of the spectrum continuum and the Hα profile has been observed in many different novae (McLaughlin, 1943; Aydi et al., 2020, 2024).

The universality of the observed evolution of the spectrum, and particularly in the Hα profile, led Aydi et al. (2020) to propose a universal ejection mechanism for nova eruptions, in which a first slow component is ejected, likely to have a preference for the orbital plane of the binary. This slow component is responsible for the P-Cygni profile. Before reaching the maximum brightness, at least one additional component is ejected from the system at higher velocities. This fast ejecta will catch the first and slower ejecta, producing shocks that powered the luminosity near the maximum brightness of the nova eruption. The fast component soon starts to dominate the Hα profile, until eventually the P-Cygni profile disappears and only the fast component remains, as shown in the bottom spectra of Fig. 1.10.

Novae across the electromagnetic spectrum

In addition to the observations in the optical part of the spectrum, novae have also been observed emitting X-rays and γ-rays, as well as in the infrared and radio ranges of the electromagnetic spectrum. A schematic summary of the different emissions at different wavelengths is presented in Fig. 1.11, including the time scales and the main event that dominates the emission.

During the first seconds of the TNR, material is dragged from the WD interior due to the appearance of Kelvin-Helmholtz instabilities (José, 2012; Casanova et al., 2016). As the material expands and reaches the 'fireball' phase, it was proposed that a strong and rapid flash in the UV/X-ray should dominate the nova spectrum. The expected short duration of this phase ($\sim$hours) makes it usually go undetected. The first observational confirmation of this phase was provided for the nova of YZ Ret (Nova Reticulum 2020), where a strong X-ray emission lasting < 8 hours was detected 11 hours before the optical peak (König et al., 2022).

As the nova reaches its peak in the optical wavelength in the hours and days after the TNR, the eruption is dominated by the presence of a slow outflow from the system (Sect. 1.3.2). When the fast flow starts to dominate, shocks are expected to

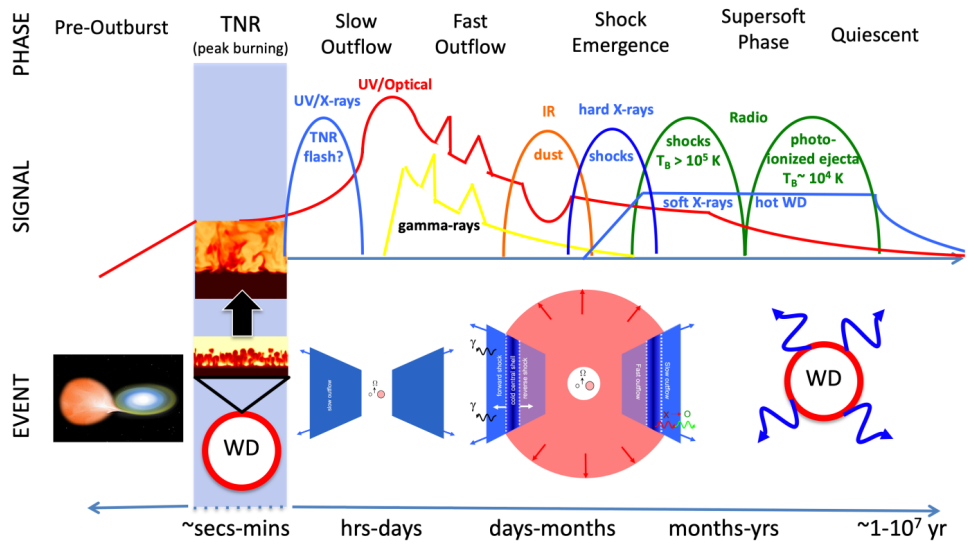

Figure 1.11: Summary of the different emissions expected during a nova eruption for different time scales. The energy released at different wavelengths during the different phases of a nova eruption is presented, with the proposed event that dominates the emission presented in the row below. Original from Fig.1 of Chomiuk et al. (2021).

generate as a result of the collision between these two ejecta. As the fast ejecta collide with the slow ejecta, it accelerates the ionised particles, which gives rise to magnetic turbulence behind the shock, originating thermal and non-thermal emission. The detection of γ-rays in classical novae was considered unlikely until the first confirmation by Ackermann et al. (2014). Since then, several observations of novae have revealed the presence of γ-rays of several GeV of non-thermal origin (Ackermann et al., 2014; Martin et al., 2018). It is generally accepted that these high-energy photons have a hadronic origin, resulting from the collision of high-energy protons, rather than a leptonic one, which originates from the inverse Compton scattering (see Chomiuk et al., 2021, and references therein).

On the other hand, a correlation between the γ-ray and optical luminosity has been observed in some novae showing quasi-simultaneous ($\sim$hours difference) peaks in both light curves, as was observed during the nova eruption of V906 Car (Nova Carina 2012; Fig. 1.12). It is assumed that the origin of this correlation lies in the reprocessing of the high-energy photons that originate the γ-ray emission, and its subsequent reemission into optical wavelengths. It is expected that this correlation is universal to all novae; however, only a handful of them have been detected in γ-rays. This imposes an upper limit to the common γ-ray flux emitted during a nova

eruption (Chomiuk et al., 2021).

In the months and years after following the TNR, X-rays, both soft and hard, can be detected. Soft X-rays are detected weeks to months after the nova eruption, once the column density of the ejecta has decreased enough for these photons to reach us. They originate from a steady burn of hydrogen on the WD's surface following the nova eruption, a process that can last months, and it is referred to as the super-soft source phase. On the other hand, hard X-rays originate from the shock resulting from the colliding ejecta. In this case, the origin of this emission is thermal, resulting from the high temperature of the shocked plasma. There is a general delay between the detection of soft and hard X-rays, with the latter being detected later. This is attributed to the lag between the super-soft phase and the collision between ejecta, but could also be due to the decrease in column density of the ejecta as time passes by (Chomiuk et al., 2014, 2021).

At radio wavelengths, novae are detected as a result of non-thermal synchrotron emission during the months and years after the optical peak. As the shocks boost the magnetic turbulence of the plasma, relativistic electrons are trapped, gyrating within these magnetic fields. This radio emission is detected in the weeks and months after the TNR, reaching a peak and then decreasing. An example of a nova light curve seen in radio emission is presented in Fig. 1.13. The figure shows the radio light curve of V1324 Sco (Nova Scorpius 2012), which presents two distinctive peaks. The first one is associated with non-thermal emission originated by shocks, while the second originates from thermal emission from the expanding ejecta (Chomiuk et al., 2021). The non-thermal peak observed during the first days of the nova eruption can rival the thermal peak observed later, while in other cases the non-thermal peak is more subtle than the following thermal peak (Chomiuk et al., 2021).

A particular advantage of observing nova shells at longer wavelengths is that we can achieve resolutions of the order of milliarcseconds, either at millimetrical (e.g. Diaz et al., 2018) or radio (e.g. Chomiuk et al., 2014) wavelengths. These observations have revealed clumpy structures originating from free-free thermal emission and synchrotron radiation. In the particular case of V959 Mon (Nova Monoceros 2012), an apparent shift in the position angle of the expanding ejecta was observed at radio wavelengths (Chomiuk et al., 2014). This result was interpreted as evidence for multiple ejecta, where a slow component was ejected first in the orbital plane, followed by a subsequent, faster ejecta that expanded preferentially across the poles of the binaries. The slow ejecta is a direct consequence of the nova eruption, while the radiation of

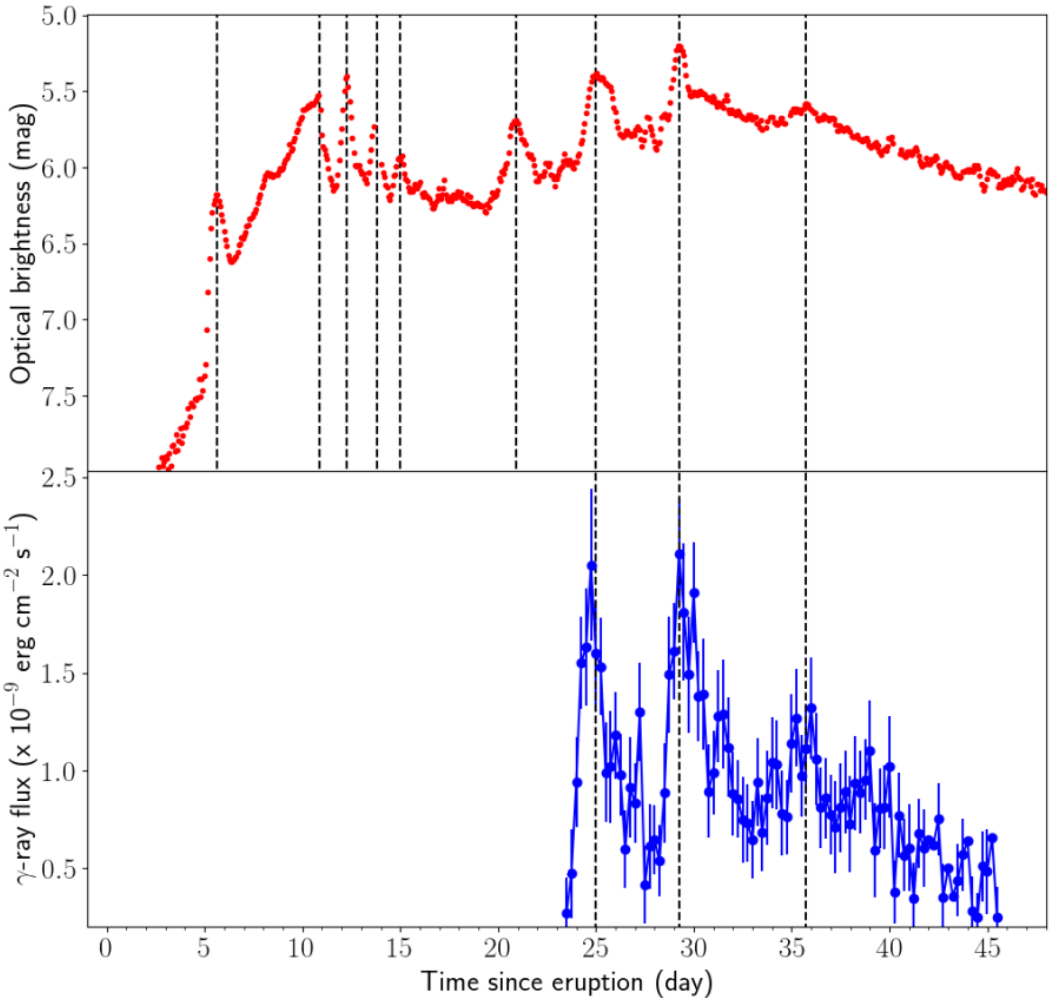

Figure 1.12: Optical (red) and γ-ray (blue) light curves of V906 Car (Nova Carina 2018), showing simultaneous peaks between both light curves. This supported the idea that the luminosity in nova eruptions is powered by shocks between different ejecta. Adapted from Fig.2 of Aydi et al. (2020).

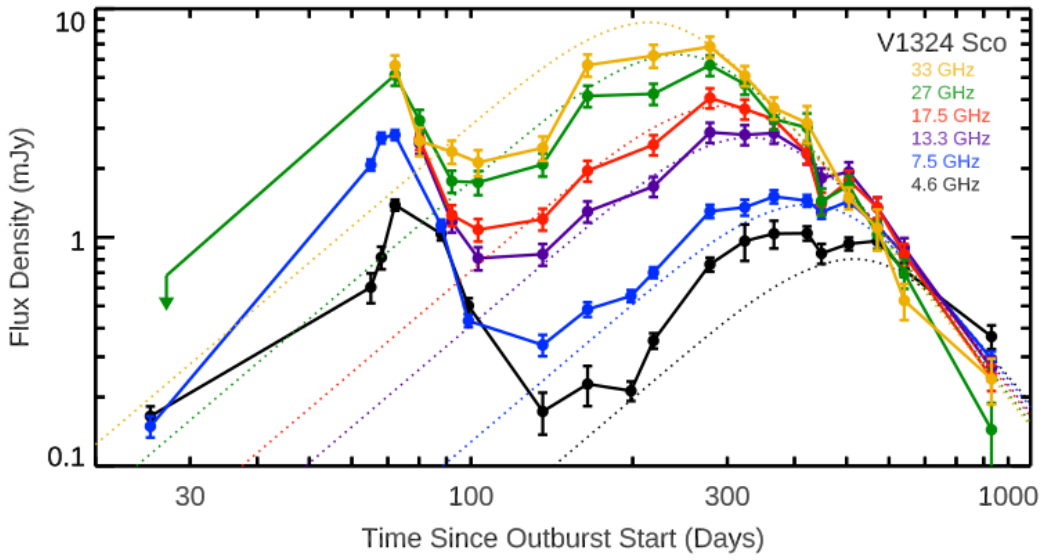

Figure 1.13: Radio observations of V1324 Sco (Nova Scorpius 2012) at different frequencies reveal two prominent peaks. The first peak is associated with non-thermal synchrotron emission, while the second can be modelled as thermal emission from an expanding ejecta (colour dashed lines). Adapted from Fig.12 of Chomiuk et al. (2021).

the hot WD powers the fast ejecta that appears later. The apparent shift in the position angle of the ejecta originates when the faster ejecta start to dominate the thermal emission, giving the impression that the position angle of the ejecta has changed by 90°. When this fast ejecta starts to fade away, due to the cooling of the WD, the apparent position angle returns to its original value. An artistic representation of this phenomenon is presented in the bottom panels of Fig. 1.14. This interpretation offers additional support to the idea that nova eruptions are characterised by several ejecta (see Sect. 1.3.2).

1.3.3 Consequences for the CV

Nova eruptions play a crucial role in the lifetime of CVs, as they act as the main source of mass loss. However, it is not clear if the WD has a net growth of mass after the eruption. Clarifying this topic will have significant implications for the characterisation of the population of supernova Ia progenitors and the evolution of CVs themselves. In addition to the mass loss from the system, it has been proposed that other parameters may be affected by the nova eruption. For example, it has been speculated that angular momentum may be extracted from the system, or that the mass transfer may

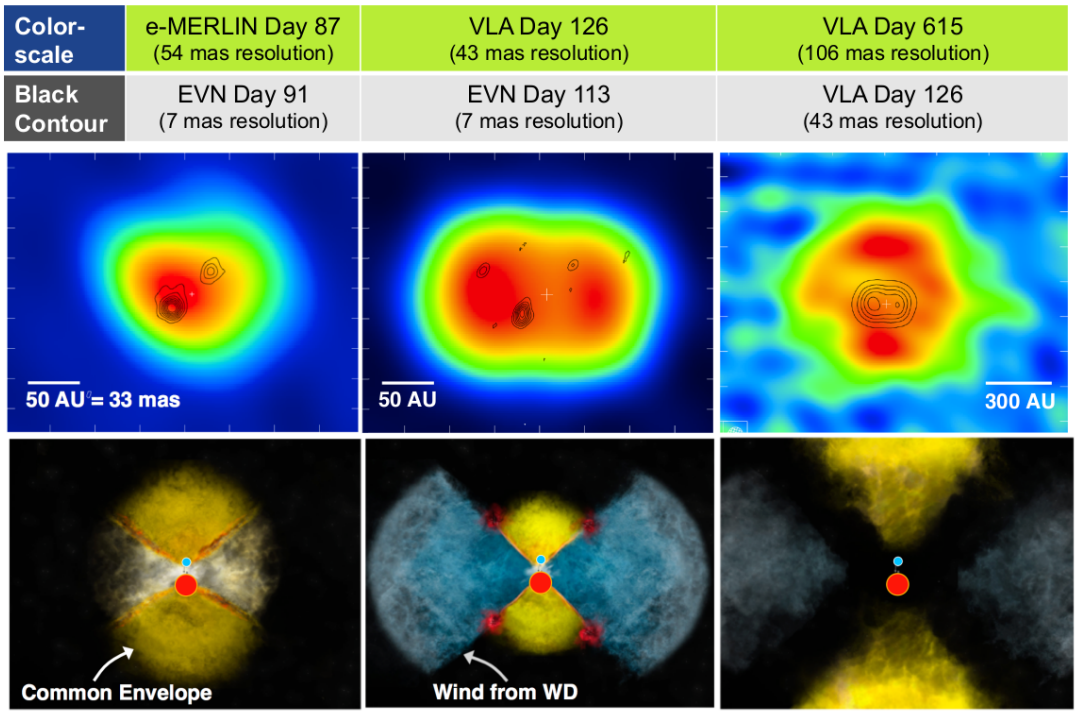

Figure 1.14: Radio imaging of V959 Mon (Nova Monoceros 2012) months after the nova eruption. Lower resolution images revealed the radio surface brightness of the expanding ejecta, while higher resolution observations allowed the identification of several knots of synchrotron emission. Top panels: Radio images of the ejecta a different epochs and with different instruments. Bottom panels: artistic representation of the expanding ejecta, including the slow (yellow) and fast (blue) components, as well as the regions of interaction between them that originate the synchrotron emission (red). Original from Fig.6 of Chomiuk et al. (2021).

increase as a result of the nova.

Growth of WD mass

Although it is widely accepted that nova eruptions are the main source of mass loss from the CV, it is still debated whether the WD experiences a net growth of its mass as a consequence of these eruptions. If this were the case, CVs could be potential precursors of supernovae Ia, as long as the system's conditions allow the growth of the WD until the Chandrasekhar mass ($\sim$ 1.4 $M_{\odot}$). Although this idea is supported by simulations (e.g. Hillman et al., 2016; Starrfield et al., 2020, 2024), it is in direct contrast with the observational evidence. Recent studies have shown that there are no significant differences in the masses of CVs above (younger, less evolved) and below (older, more evolved) the period gap (Pala et al., 2022, , see Sect 1.2.1). Therefore, it is concluded that the WDs do not gain any significant mass during the nova eruption process. This implies that virtually all the mass accreted by the WD during the inter-nova periods is expelled to the ISM during the eruption. This evidence provides a strong argument against the idea that CVs are progenitors of supernova Ia.

Frictional angular momentum loss

Together with the loss of mass, there is a potential loss of angular momentum from the system after the nova eruption. An additional source of the AML has been proposed to exist during nova eruptions in the form of a mini common-envelope phase, where the friction between the expanding ejecta and the secondary star produces a frictional AML. The strength of this potential source of AML is inversely proportional to the velocity of the ejecta (Schenker et al., 1998), and in consequence, to the mass of the WD. This phenomenon was pointed out as the possible physical reason behind the empirical consequential AML used by Schreiber et al. (2016), which acts stronger for systems hosting low-mass WDs. The inclusion of this empirical consequential AML in binary population models leads to these low-mass WDs systems to merge, solving several discrepancies between models and observations (see Sect. 1.2.1). Thus, the frictional AML appears as a potentially relevant source of AML during nova eruptions.

Hibernation theory

Nova eruptions have been proposed to have additional consequences for the CV besides the potential frictional AML. The most immediate consequence is the heating

of the WD, which can reach temperatures of $\sim 10^6$ K. The now hotter WD irradiates the secondary star, which may drive it out of its thermal equilibrium. As a result of this, an expansion of the secondary atmosphere and the subsequent increase in $\dot{M}$ is expected. This phase of higher $\dot{M}$ could last several millennia, forcing the system to appear as a nova-like system during this time.

The aforementioned consequence is the basis for the so-called hibernation theory. This theory, proposed by Shara et al. (1986), says that after the WD cools and the secondary returns to its equilibrium size, $\dot{M}$ will decrease. Furthermore, the mass lost during the nova eruption should produce an increase in the orbital separation, thus increasing the Roche lobe of the secondary star. The hibernation model proposes that the combination of these factors causes the $\dot{M}$ to decrease significantly in the centuries/millenia after the eruption, reaching values incompatible with the presence of an accretion disc, the main source of optical light in CVs. In consequence, the brightness of the system will decrease by several magnitudes, thus becoming harder to detect and classify as a CV. With time, the AML loss due to MB and GWR causes the system to shrink its orbital separation, the secondary gets in touch with its Roche lobe again, and the mass transfer is resumed. The CV appears visible again, and the overall cycle between nova eruptions is resumed. The hibernation model was proposed as an explanation for the discrepancies between theory and observations at that time, when the models predicted the presence of many more CVs than the number of observed ones. However, modern surveys significantly reduced these discrepancies (see Sect. 1.2.1), making the hibernation model unnecessary. Even further, measurements of the orbital period of CVs before and after experiencing a nova suggest that the orbital period of CVs may decrease. Photometric collection of different systems from several sources (from photo-electric plates to modern CCDs) reveals a mixed behaviour in the orbital period evolution, with some systems showing a decrease while others show the opposite (Schaefer, 2023, 2024), while the hibernation model predicts that the period should only increase. These results, in particular those that show a decrease in the orbital period, are a strong argument against the hibernation model.

Even when the hibernation model is not necessary, the effects that the nova eruption may have on the CV's properties are unclear, leading to a refinement of the model. Motivated by the coexistence of NLs and DNe (CVs with high and low $\dot{M}$, see Sect 1.2.2) within the same orbital periods (Knigge et al., 2011), Hillman et al. (2020) aimed to study the evolution of CVs via simulations that consider the different possible effects that novae have, such as irradiation and mass loss. Their results show a

variable $\dot{M}$ during the inter-novae period, where it starts high, then decreases until it reaches a minimum before starting to increase again in preparation for a new eruption. These same simulations show that mass-transfer rates consistent with a hibernation of a CV ($\sim 10^{-12} - 10^{-13}$ $M_\odot$ yr^{-1}) can only be reached by CVs with short periods (below the period gap) and low mass ($\lesssim 0.3\,M_\odot$) companions. According to these results, most CVs above the period gap should experience mild variations in their $\dot{M}$ during the internova period, resulting in a NL-DN-NL cycle.

1.4 Nova shells

The material ejected during the nova eruption forms a nebular structure around the system called a nova shell. The ejected material will expand freely after the eruption for at least a century, and potentially be detectable even a millennium after the eruption. The geometry of these nova shells is revealed after they have expanded enough to be resolved by some of the different available instruments. They appear as complex structures with several components, including equatorial rings, filaments, and clumpy structures. Nova shells are observed mainly as Hα emitters, and in many cases, emission corresponding to the forbidden lines of [NII] and [OIII] can also be detected. The allowed and forbidden emissions usually present spatial differences, which are indicative of the differences in density across the whole shell structure. The origin of these differences and the observed geometries might be found in the nova eruption itself, as it is unlikely that the shells experienced any kind of interaction with the ISM during the first decades of expansion. Thus, studying nova shells can provide insights into the physics of nova eruptions themselves.

1.4.1 Observations of nova shells

The most common way of observing nova shells is by using narrow-band (NB) photometry centred at the Hα+[NII] and/or [OIII] wavelengths. There are several studies that have used this technique to observe a single or several shells, with some of the largest collections presented in the works of Gill & O'Brien (1998), Downes & Duerbeck (2000), and more recently, Santamaría et al. (2025). In each one of these investigations, the authors provided NB photometry of several ($\sim$dozens) nova shells. This technique has the advantage that it can provide a fast characterisation of the spatial properties of nova shells, revealing that they tend to show prolate geometries with complex structures like rings, filaments, and clumps within them. One of the most famous nova shells is the one around the system GK Per (Nova Per 1901). An Hα+[NII] NB image of this shell is presented in Fig. 1.15, revealing the different knots and filaments that compose this shell, the reason for which is also known as the 'firework nebula'. By comparing images taken at different epochs, it is possible to determine the expansion rate of the shell. For the case of GK Per, it has been found that the different knots across the shell are continuing to expand freely, without showing evidence of deceleration (Liimets et al., 2012). A similar case of a clumpy shell is the expanding ejecta around V5668 Sgr (Nova Sagittarius 2015), for which millimetric ob-

servations with the Atacama Large Millimeter Array $\sim$ 2.5 years after the eruption revealed at least 36 individual knots. These results indicate that at least some shells present clumpy ejecta since very early stages.

The spatial information obtained from NB images can be complemented with the use of long-slit (LS) spectroscopy. This technique provides spectroscopic information along a slit, thus also providing some spatial information in the process. The information obtained from this technique allows for a characterisation of the spatio-kinematics of the expanding shell. Several works have employed this technique (See for example Santamaría et al., 2022b; Tappert et al., 2023). As an example of a nova shell observed with LS spectroscopy, the spectra corresponding to the nova V1425 Aql (Nova Aql 1995) are presented in Fig. 1.16. The shell is detected as a series of ellipses surrounding the system, which appears as a continuum flux. Each ellipse corresponds to a unique emission line, from which we can measure its spatial extension across the slit from the spatial (y-) axis, as well as its expansion velocity, thus characterising the kinematics of the shell within the slit.

The combination of NB images and LS spectroscopy can be used to model the geometry of the expanding shell. However, because the slit covers only a fraction of the total spatial extension of the shell, the derived kinematics of the ejecta must be extrapolated if the goal is to obtain a complete spatio-kinematic model of the shell. This can be done using specialised software such as `Shape` (Steffen et al., 2011). The results indicate that nova shells are usually consistent with ellipsoidal geometries (Santamaría et al., 2022b).

More recently, people have been realising the advantages that integral field spectroscopy (IFS) offers for the study of this kind of object. IFS observations provided spectroscopical (therefore kinematic) information across its entire field of view. This allows for a complete characterisation of the spatial and kinematic properties of a nova shell, being a major improvement compared with the LSS technique. On the other hand, if the spectral range of the IFS allows for the detection of two or more lines, an image of the shell for each one of these lines can be obtained, effectively obtaining a multi-wavelength image of the shell. The several advantages and capabilities of IFS data for the analysis of nova shells have been demonstrated in the studies of the systems of QU Vul (Santamaría et al., 2022a), T Pyx (Izzo et al., 2024; Santamaría et al., 2024), and FH Ser (Guerrero et al., 2025). In all of these works, the IFS data allowed the authors to reconstruct the geometry of the expanding shell, and similar to the case of NB images and LS spectroscopy, the results are consistent with ellipsoidal geometries.

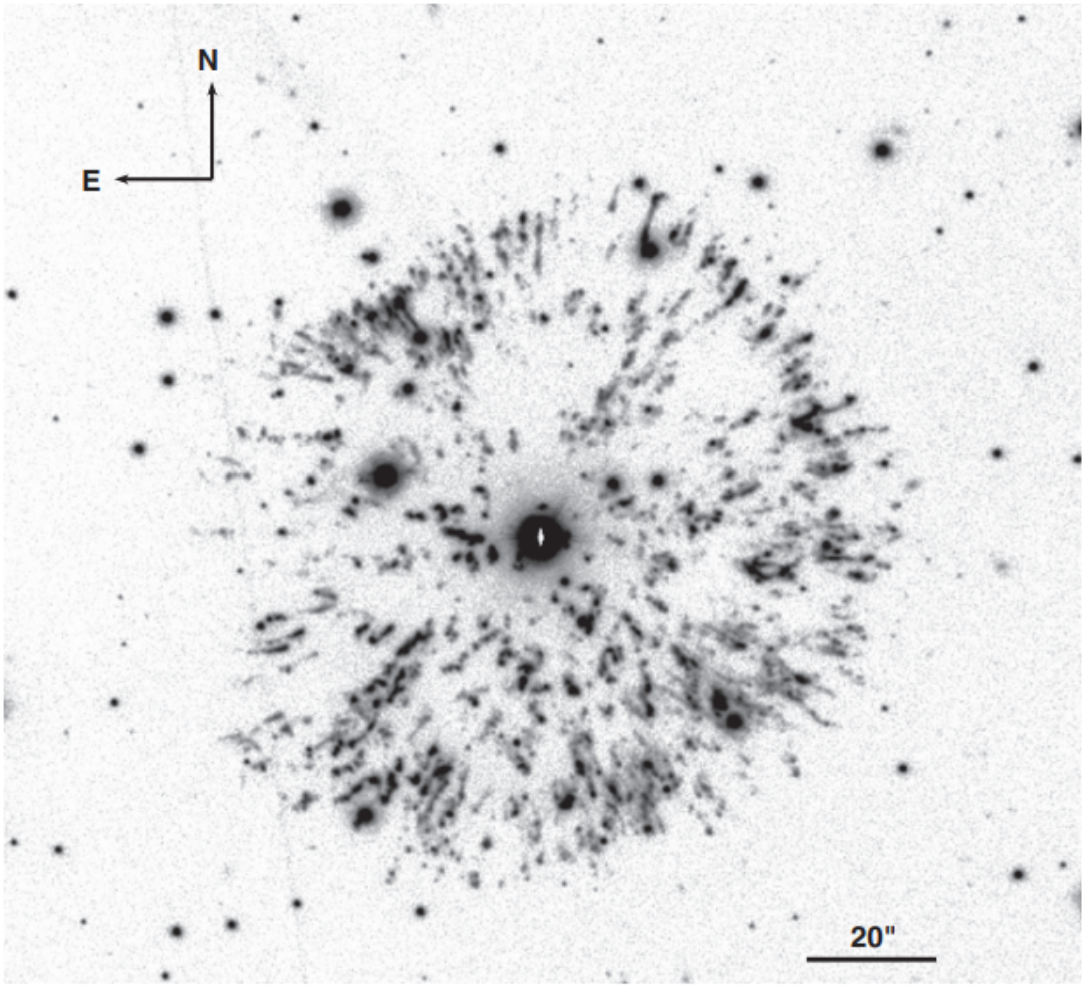

Figure 1.15: Hα+[NII] NB image of the nova shell around GK Per (Nova Persei 1901) as it was observed in 2007. NB image provides a complete characterisation of the spatial extension of the shell and its different components, being this case a shell consisting of several knots and filaments. From images obtained at different epochs, it is possible to determine the proper motion of the different knots, thus characterising the expansion of the shell with time. Original from Fig.1 of Liimets et al. (2012).

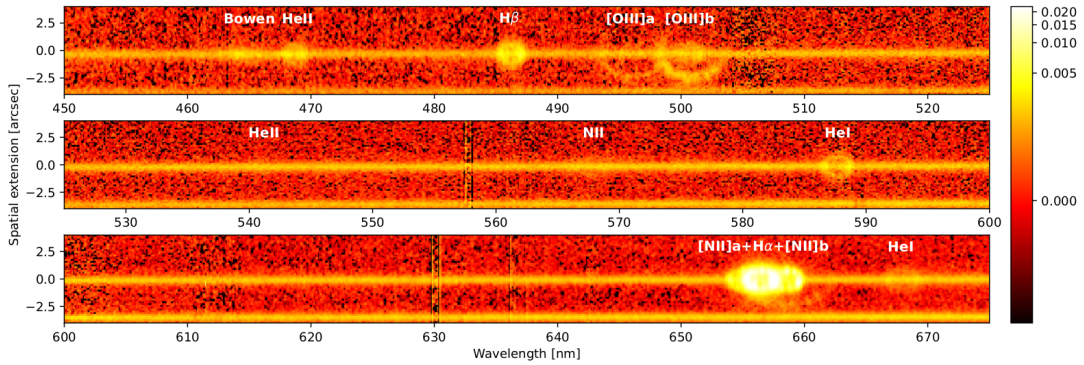

Figure 1.16: LS spectroscopy of V1425 Aql (Nova Aquila 1995), revealing the presence of the nova shell as a series of ellipses in the figure, one for each line. The combination of the spectral and spatial information provided by this technique allows for a different characterisation of the nova shell than only using NB photometry. Original from Fig.2 of Tappert et al. (2023).

1.4.2 Ancient shells and super-remnants

Nova shells are found around CVs that have been observed to erupt as a nova. However, there are cases where a nova shell is found around systems for which no nova eruption has been recorded. These shells are referred to as ancient nova shells and play a significant role in our understanding of the evolution of nova shells and the effect that nova eruptions have on CVs.

The first ancient nova shell was discovered around the DN Z Cam with an estimated age of the shell of ∼2 000 years (Shara et al., 2007, 2012b, 2024b). The shell is fragmented and composed of several arcs of material, of which the most notable is the arc to the southwest of the system due to its higher flux. An even fainter and larger shell was recently detected by the Condor Array Telescope (Lanzetta et al., 2023; Shara et al., 2024b). This discovery implies that nova shells can still be detected several hundred years after the nova eruption that originates them, allowing us to better study the effects of the interaction between the expanding shell and the surrounding ISM.

After Z Cam, several other ancient shells have been discovered or recatalogued such as V1315 Aql (Sahman et al., 2015, 2018), V341 Ara (Castro Segura et al., 2021), SY Cnc (Bond et al., 2024), CRTS J054558.3+022106 (Miszalski et al., 2016), AT Cnc (Shara et al., 2012a), IPHASX J210204.7+471015 (Guerrero et al., 2018), IGR J1401-4306 (Potter & Buckley, 2018) and one in the globular cluster M22 (Göttgens et al., 2019).

In the cases when the physical parameters of the CV that likely originated the ancient shell are determined with confidence, a variety of CV classes are revealed,

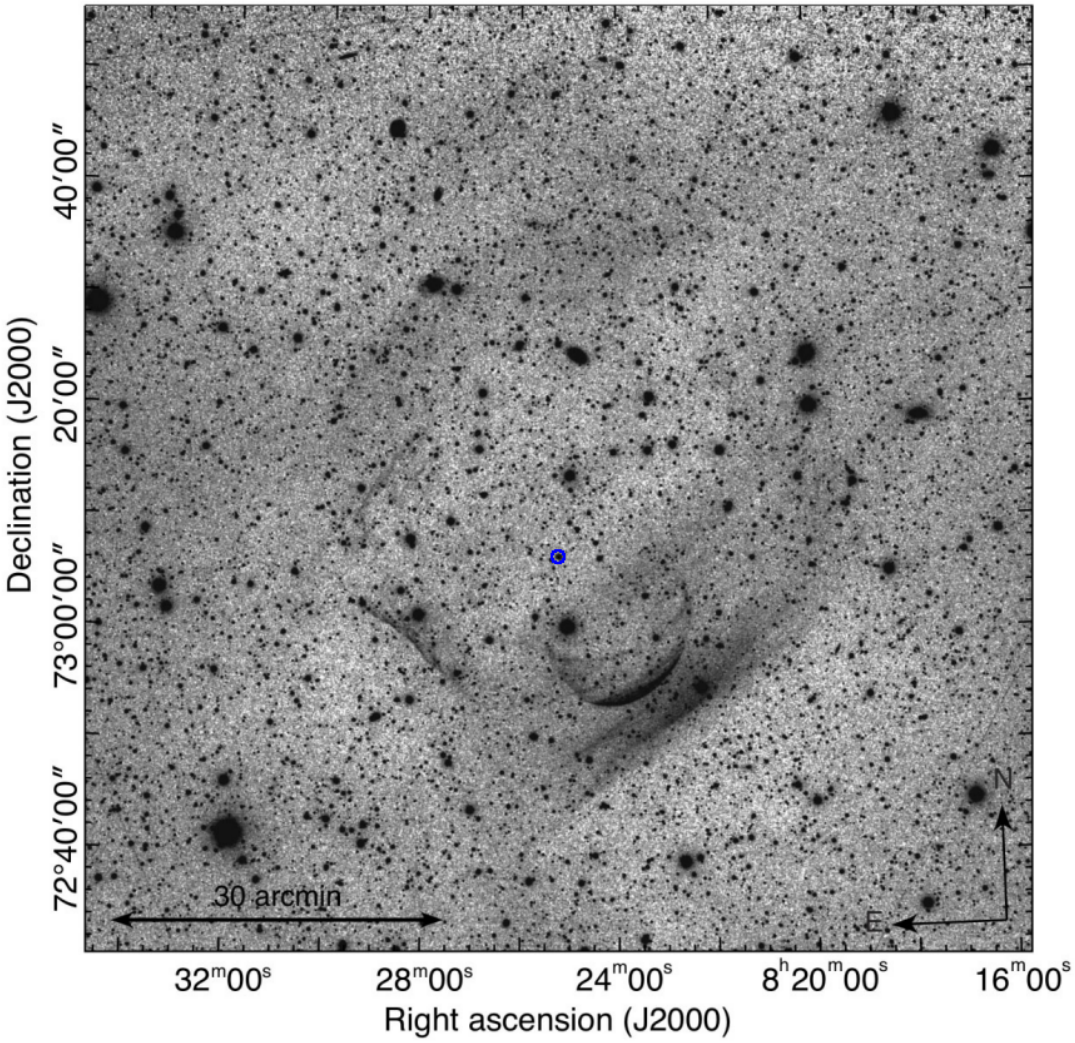

Figure 1.17: The ancient shell around Z Cam as seen in Hα+[NII]. The shell is composed of several arcs that together form a fragmented shell. The position of Z Cam is marked with a blue circle. Adapted from Fig.3 of Shara et al. (2024b).

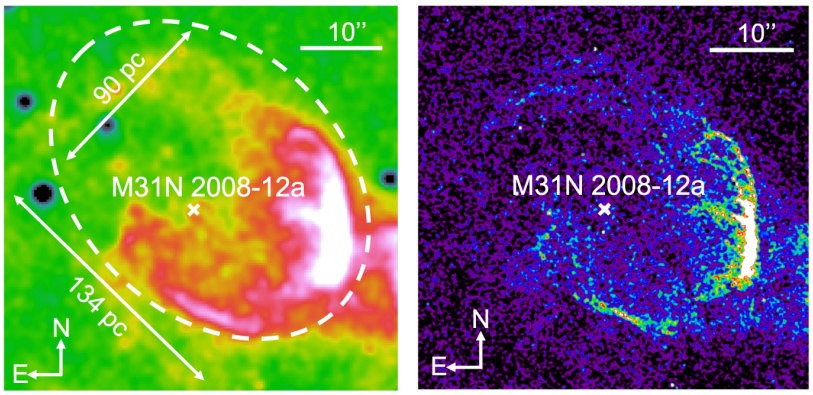

Figure 1.18: The NSR around 12a. Left: Ground-based observations using an Hα+[NII] narrow-band filter with its continuum subtracted. The dimensions of the NSR are provided. Right: HST Hα+[NII] image of the NSR. The high resolution of the HST allows for a better appreciation of the fragmented nature of the NSR. Adapted from Fig.1 of Darnley et al. (2019).

including NLs, DNe, and IPs. In principle, the observation of NLs and DNe argues against the classical hibernation scenario, which states that after a nova eruption, the CV should start to slowly evolve into a DN in the subsequent centuries. It is expected, according to this scenario, that the population of CVs hosting ancient shells should be dominated by DNe. However, the sample is too small to draw any meaningful conclusions. Other parameters like the system age, orbital period, or the strength of the field of a magnetic WD may have a role in the appearance of the CV after the nova eruption.

The analysis of the shells themselves shows that they are usually fragmented, indicating strong interaction with the surrounding ISM. The expansion velocities of these shells are also low compared with younger shells (see for example Z Cam with a $v_{exp} < 138$ km s^{-1} Shara et al., 2012b), which has been proposed as evidence that nova shells decelerate at certain point during its expansion. How and when is not clear, but the information provided by ancient shells may help us to clarify these questions. In the same line, many of these shells present bow-shock regions (e.g. V341 Ara Castro Segura et al., 2021), the result of the interaction between the expanding ejecta and the surrounding ISM. Thus, ancient nova shells present themselves as exceptional laboratories to also study the interaction with the ISM.

In recent years, another kind of shells that surpass the ancients in terms of spatial extension and age have begun to be discovered. These structures have been called nova super-remnants (NSR), with the prototype for them being the one around the

RN M 31N 2008-12a (12a to abbreviate). 12a is an exceptional RN located in the Andromeda galaxy with a recurrence time of ∼1 year. Deep Hα images revealed that it is located inside an ellipsoidal structure of $0\overset{'}{.}3 \times 0\overset{'}{.}2$, which translates into a physical size of 67 pc × 45 pc (Darnley et al., 2015). The size of the structure is too large to have been generated by a single nova eruption, and so it was proposed that it is the result of successive eruptions during a significant period of time. This idea was supported by hydrodynamical simulations that simulate 100 000 yearly eruptions, concluding that similar structures to the one observed in the 12a NSR can be formed (Darnley et al., 2019). By extrapolating the results of the simulations to the observations, the authors conclude that 12a should have been erupting constantly during the last 6×10^6 years to reach its current size. From these same simulations, the mass of the NSR was estimated to be ∼17 $M_\odot$, composed almost entirely of material swept up from the ISM.

The discovery of the NSR around 12a motivated the search for similar structures around galactic RNe, and they have been found around the suspected RN KT Eri (size ∼ 50pc Shara et al., 2024a) and the confirmed RN T CrB (size ∼ 30pc Shara et al., 2024c). The discovery of these NSR opens the door for studying how the ejecta of recurrent novae stack with each other, the effect that they have on the surrounding ISM, and how their luminosity and morphology look at these late stages, providing a new facet in the study of nova shells.

1.4.3 Evolution of nova shells

Nova shells are structures that evolve on human timescales; thus, we can see how they change their properties with time. The most evident change is in the size of the shell as it expands and reveals its geometry. There are plenty of examples of images of nova shells at different epochs that reveal how they expand: GK Per (Nova Persei 1901, Liimets et al., 2012); RR Pic (Nova Pictoris 1925, Duerbeck, 1987c; Gill & O'Brien, 1998); and DQ Her (Nova Hercules 1934, Williams et al., 1978; Santamaría et al., 2022b), to give some examples. From there, we can learn if they expand freely or if their geometry is somehow affected during their expansion into the ISM.

To answer the first question, it is necessary to observe the same shell at different epochs, identify features within the shell, like clumps or the semi-major axis, and then compare the angular size of these structures. This simple technique will provide us with information about the expansion rate of the shell, as long as the filters used for the images are similar. A pioneering work was the one carried out by Duerbeck

(1987b) who observed the shells around V603 Aql, V476 Cyg, DQ Her, and GK Per and compared their sizes with previous photographic observations. He found evidence for deceleration and concluded that nova shells decrease their expansion rate by half (half-lifetime) every $\sim$ 65 years. His results, however, were refuted later by Santamaría et al. (2020), who analysed a small sample of five nova shells with ages between 50 and 130 years: DQ Her, FH Ser, T Aur, V476 Cyg, and V533 Her. The authors in this case did not find any evidence for deceleration, even in the two systems that were also analysed by Duerbeck (1987b). In consequence, the half-lifetime of nova shells and the role of the ISM in their evolution are not settled.

From a theoretical point of view, it is expected that the shell expands freely until it drags a significant ($\sim M_{\rm ej}$) amount of mass from the ISM. At this point, the shell will start to expand adiabatically, giving rise to the so-called Sedov-Taylor phase, before entering the 'snowplough' phase where it starts to cool while conserving its momentum as it expands. Lastly, once the shell decelerates until reaching an expansion velocity comparable to the speed of sound of the ISM, the shell will start to dissolve and merge with the surrounding ISM. The details of these different phases have been deeply studied for the case of Supernova remnants (see Draine, 2011, and references therein for a detailed explanation), but the same physics may be applied to nova shells as follows.

During the first phase of expansion (free-expansion phase), the material ejected by the nova eruption expands at velocities much higher than the isothermal sound speed of the ISM, $c_{\rm s} = (kT/\mu)^{1/2} \approx 10 - 100$ km s^{-1} (where k is the Boltzmann constant, T the temperature of the gas, and μ its mean molecular weight), dragging the surrounding ISM material with the ejecta. As the surrounding medium does not decelerate the material, the shell expands linearly (or freely) with time, that is, is radius $r_{\rm shell}$ increases linearly with time: $r_{\rm shell} = v_{\rm ej} t$, where $v_{\rm ej}$ is the initial velocity of the ejecta and t is the time since the ejection. This phase will continue until the ejecta has dragged a mass comparable to the mass of the initial ejecta $M_{\rm ej}$. Assuming a spherical expanding ejecta into a medium with uniform density $\rho_{\rm ISM}$, we can estimate the time this phase lasts:

$$M_{\rm ej} = \frac{4\pi}{3} \rho_{\rm ISM} r_{\rm shell}^3 = \frac{4\pi}{3} \rho_{\rm ISM} (v_{\rm ej} t)^3, \tag{1.11}$$

and from Equation 1.11 it follows:

$$t = \frac{1}{v_{\rm ej}} \left(\frac{3}{4\pi} \frac{M_{\rm ej}}{\rho_{\rm ISM}} \right)^{(1/3)}. \tag{1.12}$$

Using some standard values for nova shells: $M_{\rm ej} = 10^{-5}$ M$_\odot$, $v_{\rm ej} = 1000$ km s^{-1}, and a value of 0.1 $n_{\rm H}$ cm^{-3} for $\rho_{\rm ISM}$, we can see that the free expansion phase can easily last $\sim$ 100 years. As the mass dragged by the shell reaches $M_{\rm ej}$, the expansion becomes adiabatic and the free-expansion phase ends. In this new phase, usually called the Sedov-Taylor phase[2] (Sedov, 1959; Taylor, 1950), the expansion of the shell is now governed only by its conservation of energy. We can assume that most of the energy of the shell is in the form of kinetic energy, thus:

$$E \approx \frac{1}{2} M_{\rm shell} v_{\rm shell}^2 = \frac{1}{2} \frac{4\pi}{3} \rho_{\rm ISM} r_{\rm shell}^3 v_{\rm shell}^2, \tag{1.13}$$

where $M_{\rm shell}$, $v_{\rm shell}$, and $r_{\rm shell}$ refer to the mass, expansion velocity, and radius of the expanding shell at a given time t, respectively. Because the total energy of the system is conserved, Equation 1.13 implies that $v_{\rm shell} \propto r_{\rm shell}^{-3/2}$ (under the assumption of a constant ISM density). This leads to the differential equation:

$$\frac{d}{dt} r_{\rm shell} = r_{\rm shell}^{-3/2}, \tag{1.14}$$

whose solution gives:

$$r_{\rm shell} \propto t^{2/5}, \;\; v_{\rm shell} \propto t^{-3/5}. \tag{1.15}$$

We can see that during the Sedov-Taylor phase, in contrary to the free-expansion phase, the ejecta decelerates with time. Once the radiative cooling in the shell has become significant, the assumption of conservation of energy does not apply anymore, and the shell enters a new phase: the 'snowplough' phase. This phase is characterised by the conservation of momentum instead of energy. Following the same procedure as for the Sedov-Taylor phase, we obtain:

$$\frac{d}{dt} p = \frac{d}{dt} \left(\frac{4\pi}{3} \rho_{\rm ISM} r_{\rm shell}^3 v_{\rm shell} \right) = 0, \tag{1.16}$$

from which follows $dr_{\rm shell}/dt \propto r_{\rm shell}^{-3}$, whose solution corresponds to:

$$r_{\rm shell} \propto t^{1/4}, \;\; v_{\rm shell} \propto t^{-3/4}. \tag{1.17}$$

[2]In honour of the scientists who independently described this expansion phase.

Compared with the Sedov-Taylor phase, the snowplough phase shows only a slightly steeper decline in $v_{\rm shell}$. The snowplough phase will continue until $v_{\rm shell} \sim c_{\rm s}$. At this point, the material of the shell will start to dissolve and mix with the ISM, implying the end of the shell.

The previous analysis considered several simplifications that are far from reality, such as uniform and spherical expansion of the shell, and a uniform surrounding ISM. Still, it provides a rough idea of the evolution we should expect to observe in nova shells. Up to date, we have only observed nova shells expanding freely without evident signals of deceleration, with the possible exception of IPHASX J210204+471015 (Santamaría et al., 2019). Even for ancient shells, whose low expansion velocity indicates that they already experienced a deceleration process, there are no studies that show how they currently expand. The lack of observational evidence of how shells decelerate prohibits us from testing whether the aforementioned scenario is correct. This uncertainty has implications for the determination of the age of ancient shells, for which it is not clear if the measured expansion velocities at present are representative of their past expansion (see for example the case of AT Cnc; Shara et al., 2012a)

Another point of the evolution of nova shells to consider is the evolution in luminosity and emissivity. As the shell expands, the density and temperature will vary, thus affecting the strength of the different emission lines within the shell. Observational efforts have been made to clarify the overall luminosity evolution of nova shells, first by Downes et al. (2001) and then by Tappert et al. (2020). In both works, the authors analysed the published measured fluxes of several nova shells at Hα and [OIII]λ5007Å at different times after the eruption, which, combined with reported distances, allow the authors to study the luminosity of the shells as a function of the time since the eruption, $L_{\rm shell}(t)$. The overall results show that many shells present a constant luminosity during the first ∼hundred of days after the nova eruption, but all present a main decline in the years and decades after eruption, where $\log(L_{\rm shell}) \propto t^n$, with $n \sim -3$. The inclusion of ancient shells (see Sect. 1.4.2) in the analysis by Tappert et al. (2020) indicates a tentative valley of constant luminosity in the century after the eruption.

The physical interpretation for each one of these stages is as follows: during the first weeks, the shell is optically thick, thus the number of atoms contributing to the emission is limited. As the shell expands, its density decreases, and with it, the number of available atoms to contribute within the same volume. This is compensated at the early stages by the fact that the shell becomes optically thinner, therefore, increas-

ing the available atoms in the line of sight, resulting in the flat slope observed at early stages. However, once the shell has become optically thin in its totality, there is no other factor to counter the decrease in density (which is proportional to t^{-3} assuming a free expansion of the shell), and the shell enters the main decline phase. The last stage of a tentative constant luminosity for ancient shells could be explained by the expected braking of the shell by the ISM interaction, which may inject additional energy into the shell, compensating for the decrease in density of the shell.

1.4.4 Correlation between shell and CV

One of the unsolved problems regarding nova shells is how they correlate to the properties of the nova eruption that originates it, and to the CV itself. Clarifying this topic would help to understand the physical processes that shape the nova shell during the nova eruption itself. The most basic parameter to obtain from a nova shell is its aspect (also known as axial) ratio, defined as the ratio between its major and minor axes. This can be easily obtained once the shell has expanded enough to be resolved using NB imaging (Sect. 1.3.2).

The aspect ratio can then be compared against basic parameters of the nova, such as its t_3 value or the velocity expansion of the ejecta, either derived by spectroscopic studies or deduced from the expansion of the shell in the plane of the sky. Several works have focused on correlating these parameters, finding evidence for a correlation between the aspect ratio and the t_3 parameter, that is, those shells associated with nova eruptions with lower t_3 (fast novae) tend to present more spherical shells (lower aspect ratio values) (Slavin et al., 1995; Santamaría et al., 2022b). Fig. 1.19 shows the axial ratio of several shells as a function of t_3, showing a strong correlation for the works of Slavin et al. (1995) (top panel) and Santamaría et al. (2022b) (middle panel) In the most recent compilation of nova shells by Santamaría et al. (2025), however, this correlation appears less evident than in the previous studies (bottom panel of Fig. 1.19), which may indicate underlying processes that are not being properly considered.

It has been proposed that the origin of this correlation lies in the 'mini common-envelope' phase that the ejecta experience during the nova eruption. An ejecta expanding faster will also evolve faster, presenting smaller t_n values compared to slower ejecta. As they expand, they will interact with the secondary star, transferring some angular momentum from the binary to the ejecta. The higher the amount of angular momentum transferred, the more prolate the geometry of the ejecta will be. In conclu-

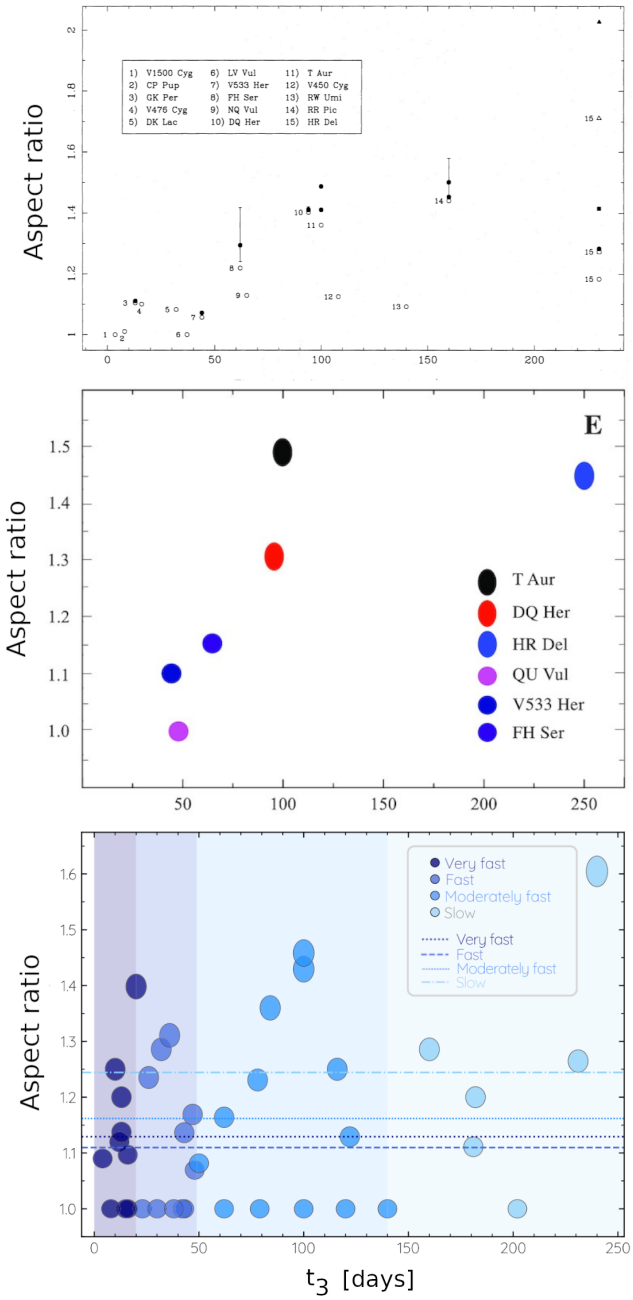

Figure 1.19: Aspect ratio versus the t_3 value from different works. Top panel: The results from Slavin et al. (1995) for a sample of 15 nova shells. Middle panel: The results from Santamaría et al. (2022b) for a sample of 6 nova shells. Bottom panel: The results from Santamaría et al. (2025) for a large sample of 60 nova shells. The results from Slavin et al. (1995) and Santamaría et al. (2022b) show a strong correlation between the aspect ratio of nova shells and the t_3 value associated with their nova eruption. The larger sample of Santamaría et al. (2025) does not show this correlation as evident as the previous works. Figure adapted from Fig.8 of Slavin et al. (1995), Fig.7 of Santamaría et al. (2022b), and Fig.13 of Santamaría et al. (2025).

sion, faster ejecta will have less time to interact in this 'mini common-envelope' phase, leading to more spherical geometries (Slavin et al., 1995).

The previous studies are limited by the nature of NB images, which can only measure the projected shell. Depending on its inclination, the projected geometry of a shell may present significant differences in axial ratio with respect to its real value. It is necessary to have a technique that allows us to overcome these projection effects to determine the true axial ratio of the shell, and IFS observations stand out as a potential technique to overcome this challenge.

In addition to the observational efforts, there have been studies aiming to characterise the role of the binary components in the shape of the expanding ejecta. Hydrodynamical simulations have confirmed that a faster ejecta experience less deformation from their original spherical shape and that clumpy structures arise naturally when considering Rayleigh-Taylor instabilities (Lloyd et al., 1997), while the rotation of the WD appears to play a significant role in the formation of tropical rings within the nova shell (Porter et al., 1998).

1.5 Aim of this thesis

There are several questions regarding the geometry of nova shells: What are the processes that shaped them? How does their expansion affect their geometry? What is the role of the ISM in this process? This thesis focuses on shedding light on these questions by studying the geometry and kinematics of several nova shells. To achieve this, this thesis aims to utilise data from the Multi-Unit Spectrograph Explorer (MUSE), an integral field spectrograph located at the Paranal Observatory. This is the first time that this instrument has been used for this scientific purpose.

All of the nova shells in the sample have been previously observed, which makes it possible to study their evolution by comparing the current observations with the past ones. This will allow us to provide compelling evidence about the deceleration and faintness of nova shells with time. Even further, the characterisation of the expanding ejecta, geometrically and kinematically, can be used as a diagnostic tool for our understanding of the physics of nova eruptions. It would be possible to test the different relations between the ejecta and the properties of the nova eruption and the CV that the theory predicts. It is expected that, at the end of this thesis, our knowledge of nova shells has improved, either for individual shells and for the population in general.

CHAPTER 2

Data acquisition

The data employed in this thesis correspond to several datacubes from the Multi-Unit Spectrograph Explorer (MUSE), an integral field spectrograph that offers exceptional capabilities for the study of extended sources thanks to its capacity to provide image and spectroscopic data in a single observation. Despite these advantages, before the start of this project, no published study of nova shells using MUSE data was available, although this changed with the analysis of the shell around the RN T Pyx (Izzo et al., 2024; Santamaría et al., 2024). One of the goals of this thesis is to provide the first analysis of nova shells using MUSE data, for which a total of 21 different shells were observed between the years 2021 and 2024. This translates into a significant increase in the number of available shells observed using IFS. The analysis of the data included the development of `Python` scripts using the diverse libraries available for the analysis of astronomical images and spectroscopic data.

2.1 Multi-Unit Spectroscopic Explorer

The work of this thesis is based mainly on observations done with the Multi-Unit Spectroscopic Explorer (MUSE; Bacon et al., 2010) placed at the Very Large Telescope (VLT) from the European Southern Observatory (ESO). MUSE is an Integral Field Spectrograph (IFS) covering the electromagnetic spectrum from the visual (465 nm) to the near-infrared (930 nm) with a spectral resolution of 1.25 Å (spectral resolving power

$R \sim 2\,600$ at Hα). The instrument's capabilities make it an ideal tool for the observation of extended sources like nova shells, and its wavelength coverage will allow us to study the main lines observed in these kinds of objects, such as [OIII] λ5007 Å or Hα.

The science output of MUSE is called a datacube: it has two spatial dimensions (right ascension and declination) plus one spectral dimension, which makes it different from images (two dimensions) and spectra (one dimension), and so the nomenclature differs with respect to these two other cases. The equivalent of a pixel in the spatial coordinates is called a spaxel, and it contains a spectrum at that exact coordinate. On the other hand, at each pixel in the spectral dimension, the datacube hosts an image of the field at that particular wavelength, which is referred to as a slice of the datacube. Lastly, the small component of the datacube is called a svoxel, which corresponds to a pixel of a slice image.

MUSE has several possible observing configurations. When observing in its standard observation wide-field mode (WFM), it provides a field of view of 1×1 arcmin^2 with a spatial resolution of 0.2×0.2 arcsec^2 per spaxel. Besides the WFM, MUSE also offers the possibility to observe using its narrow-field mode (NFM), in which the field of view is limited to 7.5×7.5 arcsec^2 and its resolution increases up to 0.025×0.025 arcsec^2 per spaxel. Similarly, its spectral range can vary depending on the mode of use. In its nominal mode (N), the wavelength range goes from 480 to 930 nm, but this range can be increased when observing in its extended mode (E), which covers from 465 to 930 nm. The disadvantage of the extended mode is that light from the second-order grating diffracts and contaminates the red part of the spectra at wavelengths longer than 790 nm. Lastly, the instrument can benefit from the use of adaptive optics (AO) to improve the natural seeing of the sky. This, however, has the disadvantage that the wavelength region between 580 and 596 nm is lost due to the saturation produced by the sodium lasers.

2.2 Data reduction and processing

The raw output from MUSE consists of the output of 24 different integral field units (IFUs), which need to be properly treated, reduced, and calibrated before obtaining a single MUSE science datacube. This is done using the data processing pipeline for MUSE data implemented in the ESO Recipe Execution Tool (*EsoRex*; Weilbacher et al., 2016, 2020). In a nutshell, *EsoRex* is divided into two parts; the first one applies the standard reduction to each one of the 24 IFUs, including bias, flat, wavelength calibra-

tion via arc-lamps and line spread function models, twilight illumination, and basic astrometry. The second stage consists of the calibration of the IFUs using standard flux and extinction tables, the removal of telluric and Raman lines (in the case of NFM observations), a correction of the atmospheric dispersion, and a refinement of the astrometry before combining the 24 IFUs to obtain a single science datacube. Even after the calibration process, some artefacts may remain in the datacube, including ghosts, straylights, ferry wheels, bad pixels, low-sensitivity regions, and fringing. Many of these artefacts are more evident in NFM observations rather than WFM.

The computational cost of reducing and calibrating a MUSE datacube is significantly high, prohibiting the processing of the raw data in a personal laptop or the IFS's[1] cluster. Therefore, for this study, we rely on the science products provided by ESO, that is, the reduced datacubes resulting from *EsoRex* with its standard configuration setup. For some of the targets (Section 2.3), several observations were carried out. The resulting datacubes of these observations were combined into a single one to increase the S/N of the nova shell. The combination of the datacubes, as well as the general analysis through this thesis, is done using the MUSE Python Data Analysis Framework, MPDAF, a Python library developed by the MUSE consortium (Bacon et al., 2016). The MPDAF library provides several useful methods and classes to deal with MUSE data, not limited only to datacubes but also for images and spectroscopic data.

The first step in the analysis of the datacubes is to check their astrometry, as they may present shifts of a couple of arcsecs. For that purpose, the position of the field stars present in the cube is compared against Gaia DR3 (Gaia Collaboration et al., 2016, 2023) data to apply the correction required to remove the astrometric shift if present. The position of the stars in the field is determined by creating a bandpass image from the datacube using the transmission of the i_SDSS filter. This bandpass image is given to Sextractor to determine the pixel and WCS position of the stars present in the field, which is then compared against the WCS positions according to Gaia DR3. This comparison allows us to determine the astrometric shift present in the datacube, and we can correct it by modifying the respective WCS headers. Once the astrometry is corrected, the datacubes can be combined into a single one using a sigma clipped mean process implemented in MPDAF. Additionally, if the extinction to the target is known, we can correct the flux values stored in the datacube accordingly. This is done by applying the Fitzpatrick reddening law (Fitzpatrick, 1999), which is implemented in the

[1]Instituto de Física y Astronomía

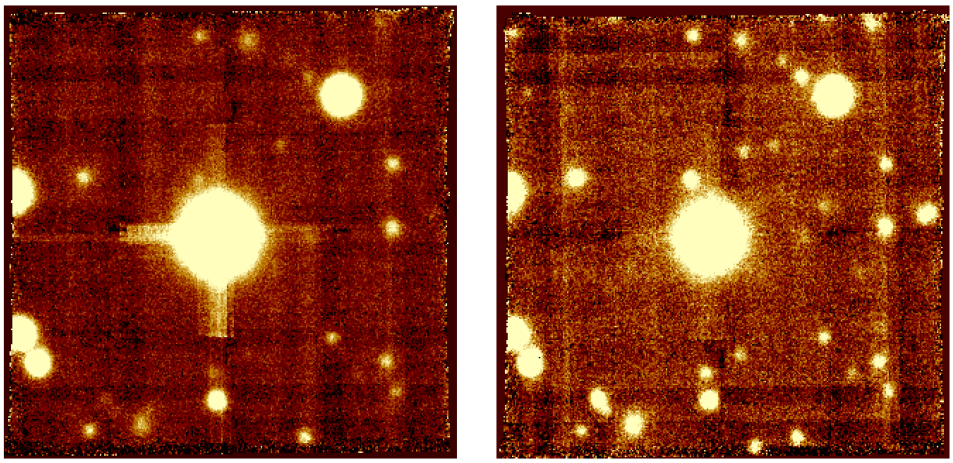

Figure 2.1: Example of the artefacts presented in the MUSE datacubes. The datacube of HR Del is presented for $\lambda = 550 - 600$ nm (left) and $\lambda = 850 - 900$ nm (right). The pattern drawn by the position of the 24 individuals' IFUs is more evident at redder wavelengths, while the 'blooming-like' effect is more distinctive at blue wavelengths due to HR Del being more luminous at bluer wavelengths. Both images are presented using a logarithmic scale between the quantiles 0.025 and 0.975.

`PyNeb` `Python` package (Luridiana et al., 2015). The resulting datacubes suffer from some of the artefacts previously mentioned, particularly a strong 'blooming-like' effect observed at bright stars, for which the separation between IFUs becomes evident. In the red parts of the spectrum ($\lambda > 750$ nm), a small fringing effect can be observed in some datacubes. As an example, Fig. 2.1 shows the artefacts observed at blue and red wavelengths for the datacube corresponding to the system HR Del.

2.3 Target selection

In total, 20 different classical post-novae were observed with MUSE between 2021 and 2024 in five different observing programmes. Most of these programmes were filler ones, which means that the observations were carried out in sky conditions that were not the most optimal ones. This may have implications for the quality of the flux of some datacubes. In addition to these CNe, the available archival data of MUSE observations of the RN T Pyx were included in the sample.

In the following, a brief description of the different systems is provided:

DO Aql

The nova eruption of DO Aql (Nova Aquila 1925) was discovered on September 8, 1925 (Wolf, 1925). Its light curve, characterised by a flat plateau before diminishing, showed a maximum increase in brightness of 8.7 mag. More interestingly, its t_3-time was 900 days, which makes it the slowest recorded nova (Duerbeck, 1987a; Strope et al., 2010). DO Aql is an eclipsing system with an orbital period of 0.167762 d ($\sim$ 4 h) (Shafter et al., 1994; Kreiner, 2004). The light curve of the system in quiescence presents an eclipse, which is preceded by a gradual obscuration of the light (Shafter et al., 1994). Its shell was first imaged by Harvey et al. (2020) using an Hα+[NII] NB filter, revealing an elongated shell with a PA of 98° without evident structures within it. From the parallax expansion method, the authors determined a distance of 6.7$\pm$3.5 kpc to the system. On the other hand, the distance derived from the *Gaia* DR3 parallax (0.348$\pm$0.180 mas), corresponds to 2580^{+1440}_{-450} pc (This work; Table 2.2), 4350^{+1200}_{-650} pc (Bailer-Jones et al., 2021), and 3150^{+1700}_{-600} pc (Schaefer, 2022).

V1229 Aql

Nova Aquila 1970 was discovered by Honda et al. (1970) in April 1970, reaching a magnitude $\sim$ 6.6 mag in the visual band. The light curve of the nova eruption showed a fast ($t_3 = 32$ d) and steep decline before reaching a plateau after $\sim$ 80 days after the eruption. It was classified as a member of the P sub-class by Strope et al. (2010).

Its shell was first detected by Cohen (1985), showing a radius of 0.7 arcsec, from which an expansion rate of 0.05 arcsec yr^{-1} was derived, and an expansion velocity of 575 km s^{-1} based on spectroscopic data. The shell was imaged again by della Valle & Duerbeck (1993) who observed a spherical shell with radius 1.59$\pm$0.13 arcsec, implying an expansion rate of 0.072$\pm$0.007 arcsec yr^{-1}. Based on the observed profile of Hα+[NII], the authors argued in favour of a shell consisting of a ring expanding at $\sim$ 750 km s^{-1} and with an inclination of 27°.

V1425 Aql

The nova eruption of V1425 Aql (Nova Aquila 1995) was first observed on February 2, 1995, and reached a maximum brightness of 8 mag (Nakano et al., 1995). A light curve analysis of the system shortly after the nova eruption shows two strong periodicities, one at 6.14 h and a second at 1.44 h (Retter et al., 1998). Retter et al. (1998) associated the first periodicity with the orbital motion and the second with the spin of the

WD, implying that the system is likely an IP. However, a subsequent study by Worpel et al. (2020) was not able to detect any X-ray emission coming from the system, calling into question the possibly magnetic nature of the WD. Spectroscopic observations following the nova eruption reveal the presence of thin dust material, a dust-to-gas ratio of $< 10^{-3}$, evidence of clumpy structures within the shell, highly enhanced C, N, and O with respect to the solar abundance, FWHM consisten with $v_{\rm exp} \sim 1\,800$ km s^{-1}, and an ejected mass of the order of $2 - 4 \times 10^{-5}$ M$_\odot$ (Greeley et al., 1995; Mason et al., 1996; Kamath et al., 1997; Lyke et al., 2001). By comparing the abundances in the spectra against the models of classical nova eruptions from José & Hernanz (1998), a $M_{\rm WD} \sim 0.9$ M$_\odot$ was estimated (Sanad, 2014).

This CV and its expanding shell received little attention until Tappert et al. (2023) presented new Southern Gemini Multi-Object Spectrograph (GMOS-S) LS spectroscopic and NB photometric data of the system, revealing the expanding material to consist of apparently two distinct shells: an inner and outer shell. The inner shell is traced mainly by allowed transitions (Balmer, HeI and HeII, and NII) but also the forbidden lines of [OIII] and [NII], while the outer shell is observed only in the forbidden lines of [OIII] and [NII]. What calls the most attention to this nova shell is the evident differences in the spatial position of the two shells, with the inner one being symmetrically centred on the position of the binary and the outer one consisting of a cone of material expanding to a larger distance from the binary and exclusively in the south-west direction. The larger extension of the asymmetric shell suggests a higher expansion velocity, which was confirmed by the LSS data: the velocities of the inner shell are ~ 500 km s^{-1}, while the velocities of the outer shell reach up to ~ 1500 km s^{-1}. The differences observed in the [OIII]/[NII] ratio between the two shells, plus the absence of hydrogen in the outer shell, suggest significant differences in the abundances, electron densities and/or electron temperatures between the two. The shells appear to have originated during the same event (the 1995 eruption), although the uncertainties allow the possibility of a time difference of up to a couple of years between potentially individual ejections. This kind of asymmetry has not previously been reported in any other shell of a similar age; its origin is far from clear and could be either intrinsic or extrinsic.

V842 Cen

V842 Cen (Nova Centaurus 1986) was discovered by McNaught et al. (1986) in November 1986. Its light curve reached a maximum magnitude of ~ 4.7 mag, and

faded 3 magnitudes after the maximum in 45 d. The light curve showed a dip in brightness $\sim$ 130 days after the eruption (Bateson & McIntosh, 1986; Strope et al., 2010). Rapid photometric observations of the system revealed the constant presence of quasi-periodic flares with a typical magnitude variation of $\sim$ 0.25mag, and no evidence for eclipses, implying a low-inclination system (Woudt & Warner, 2003). High-speed photometry revealed a periodicity of $\sim$ 57 s which was attributed to the spin of the WD, thus classifying V842 Cen as an IP system (Woudt et al., 2009). From the presence of additional side-band periodicities, the authors conclude the orbital period of the system must be $\sim$ 3.94 h. Recent high-speed photometry from TESS refined these periodicities to 56.5 s and 3.555 h for the WD's spin and the orbital period, respectively (Rao et al., 2025).

The presence of a nova shell around the system was confirmed by Gill & O'Brien (1998), who detected a spherical shell with a radius $<$ 1.5 arcsec, based on NB Hα images taken in 1995. This size is inconsistent with the value measured three years later by Downes & Duerbeck (2000), who observed an incomplete circular shell with a size of 5×6 arcsec.

RR Cha

The nova eruption in RR Cha (Nova Chamaleon 1953) was reported by Hoffmeister (1959) who discovered it after examining old photographic plates. The maximum brightness of the eruption was not recorded, but it is estimated to have occurred between April and July 1953. Its nova shell was imaged by Gill & O'Brien (1998), who observed a prolate shell with a size of 3×2 arcsec.

BY Cir

A nova eruption was reported on BY Cir in January 1995 (Nova Circinus 1995, Liller et al., 1995). Its light curve reached a maximum magnitude of $\sim$ 7.4 mag in the visual, and a decline value t_3 of 124 d (Bateson & McIntosh, 1998; Strope et al., 2010). The shape of the light curve of the nova eruption showed a steeper decline in brightness during the first days ($t_2 = 35$ d), and then followed by a smooth and lower decrease in its brightness. Its spectrum after the eruption was dominated by carbon, nitrogen, and oxygen lines, showing emission profiles with FWHM between 1 600 and 2 700 km s^{-1} (Greeley et al., 1995). By contrasting the abundances of these elements against the nucleosynthesis models of classical novae provided by José & Hernanz (1998), a

$M_{WD} \sim 1.15\,M_\odot$ was estimated (Sanad, 2014). The light curve of the system evidences deep eclipses with an orbital period of 6.76 h (Woudt & Warner, 2003). Its nova shell was attempted to be observed by Downes & Duerbeck (2000) without success, with the authors claiming that the shell was too young at the time to be resolvable.

HR Del

A classical nova was observed in HR Del in July 1967 (Nova Delphinus 1967), reaching a maximum brightness of 3.5 mag in the visual, followed by a slow decline ($t_3 = 250$ d). The nova light curve was catalogued as a 'J'-type, showing a significant jittering 200 days after the eruption (Strope et al., 2010). Its light curve shows periodic dips of $\sim$ 0.2 mag related to an orbital period of 0.21416215 d ($\sim$5.14 h), while its inclination has been estimated to be close to 40° (Bruch, 1982; Schaefer, 2022). It was suggested that its WD should have a mass $\sim 0.6 - 0.7\,M_\odot$, based on radial velocity measurements and in the mass-radius relation for main-sequence stars (Kuerster & Barwig, 1988).

Its nova shell has been extensively studied in [OIII], Hα, [NII], revealing a prolate shape (Kohoutek, 1981; Slavin et al., 1994; Harman & O'Brien, 2003; Moraes & Diaz, 2009; Santamaría et al., 2022b). The axial ratio of the shell appears larger in [OIII] than in Hα and [NII], while the comparison between images from different epochs has demonstrated that this shell continues expanding freely.

BT Mon

A nova was observed in the Monoceros constellation in late December 1939 (Nova Monoceros 1939, Whipple, 1940). Photographic plates recorded a maximum brightness of 8.5 mag in the visual, but it could have reached a maximum brightness of 5 mag (Duerbeck, 1987a). There is no consensus in its t_3 value, with some authors arguing it was a slow nova ($t_3 \approx 190$ d; Schaefer & Patterson, 1983; Strope et al., 2010), and others that it was a fast nova ($t_3 = 42$ d; Duerbeck, 1981; Smith et al., 1998). The binary system presents deep ($\sim$ 0.4 mag) eclipses, from which an orbital period of 0.33381490 d ($\sim$ 8.01 h) and an inclination of 82.2 ± 3.2° have been measured (Robinson et al., 1982; Schaefer & Patterson, 1983; Smith et al., 1998; Schaefer, 2022). The system is also classified as a double spectroscopic binary. The masses of the components in the system have been measured to be 1.04 ± 0.06 and $0.87 \pm 0.06\,M_\odot$ for the WD and the secondary star, respectively (Smith et al., 1998).

Its nova shell was first detected by Marsh et al. (1983), who reported a ring-shaped

Hα nebula around the system with a radius of 7 arcsec, based on LS spectroscopy. Later NB images showed a clumpy and incomplete ring around the system, with a size of 10 arcsec (Gill & O'Brien, 1998).

V2214 Oph

V2214 Oph (Nova Ophiucus 1988) erupted as a nova in April 1988 (Kosai et al., 1988), reaching a maximum brightness of 8.5 mag and a $t_3 = 89$d (Strope et al., 2010). The orbital period of the system is 0.1175147 d ($\sim$ 2.8 h), and the system was catalogued as a possible magnetic system, based on the observed emission of HeII λ 4684 and 5412 Å(Baptista et al., 1993). Its nova shell has not been detected.

RR Pic

RR Pic (Nova Pictoris 1925) experienced a nova eruption in May 1925, reaching a maximum brightness of V = 1.0 mag and t_3-time of 122 days (Lunt, 1926). Its light curve presented a small jittering, which was particularly strong between days 60 and 70 after the eruption, which led Strope et al. (2010) to classify the system as a member of the J-type subclass. The light curve of the system in the optical wavelength shows shallow eclipses with a variable amplitude, which indicates an intermediate inclination of the system, estimated to be around 60° (Schmidtobreick et al., 2003; Sion et al., 2017). A tomographic study of the system allowed Schmidtobreick et al. (2003) to conclude that the eclipsing part corresponds to an emission source of the leading side of the accretion disc, but also that RR Pic shares many similarities with the SW Sextantis subclass of CVs. Its orbital period has been measured to be 3.48 hours (Schmidtobreick et al., 2008; Vogt et al., 2017). Sporadic positive superhumps associated with an eccentric accretion disc have also been detected in the system with a period of 3.79 hours (Schmidtobreick et al., 2008; Fuentes-Morales et al., 2018), as well as quasi-periodic oscillations around 13 min (Kubiak, 1984; Schmidtobreick et al., 2008). The mass of the WD has been estimated to be close to the solar mass, while the secondary star should have a mass between 0.3–0.4 $M_\odot$ (Haefner & Metz, 1982; Sion et al., 2017). Its systemic velocity has been measured to be 1.8 ± 0.2 km s^{-1} (Ribeiro & Diaz, 2006). From its well-constrained parallax of 1.996 ± 0.021 miliarcsec provided by *Gaia* DR3 (Gaia Collaboration et al., 2023), the distance to the system can be determined to be 501^{+6}_{-7} pc.

The nova shell around RR Pic was first detected 6 yr after the eruption by Spencer

Jones (1931), and has since been observed again between the late 1970s and the mid-1990s (Williams & Gallagher, 1979; Duerbeck, 1987c; Evans et al., 1992; Gill & O'Brien, 1998). Because of the proximity of the system, it was possible to resolve its shell from very early stages. The first spectroscopic observations carried out by (Spencer Jones, 1931) revealed two bright knots at opposite sides of the remnant. Posterior observations using Hα+[NII] NB filters showed that these knots have been expanding in the NE-SW direction with a position angle (PA) of $\sim$70 deg, while an additional structure appears in the SE-NW axis with a PA of $\sim$150 deg (Williams & Gallagher, 1979; Duerbeck, 1987c). These authors refer to these structures as the 'polar blobs or filaments' and the 'equatorial ring', respectively. The last Hα+[NII] NB image of the nova shell was obtained by Gill & O'Brien (1998) in February 1995. Their image shows that the aforementioned structures are still discernible, with extensions of 30 and 23 arcsec for the polar blobs and the equatorial ring, respectively. The authors concluded that both structures have been expanding at a constant rate since 1931. Spectral analysis of the nova shell in the optical and ultra-violet wavelength range has revealed a difference in the observed strength line of Carbon, Oxygen and Nitrogen between the polar blobs and the equatorial ring, with the former presenting higher C/O and O/N ratios compared with the equatorial ring (Williams & Gallagher, 1979; Duerbeck, 1987c; Evans et al., 1992)

CP Pup

A nova eruption was recorded in CP Pup during November 1942 (Nova Puppis 1942, Dawson & Shapley, 1942). The light curve of the eruption reached a minimum visual magnitude of 0.5 mag, followed by a fast decline, with a recorded t_3 of 8 days (Pettit, 1949; Strope et al., 2010). CP Pup is one of the most extensively studied classical novae and has been revealed as one of the most mysterious systems. Several spectroscopic and photometric studies have attempted to determine its orbital period, but the results are inconclusive, and sometimes, inconsistent between them (see Bruch, 2022, and references therein). The reported period varies between 0.06115 and 0.06834 d (1.47 and 1.64 h), and, even when they have been quoted in the literature as the orbital period of the system (see for example Schaefer, 2022), it must be pointed out that there is no consensus if this values correspond to the actual orbital period. Instead, it has been proposed that these periods, particularly the $\sim$ 1.47 h period correspond to the period spin of a magnetic WD, making CP Pup a member of the IP group (Mason et al., 2013), with the true orbital period possibly in the order of $\sim$ 5.7 h instead (Veresvarska

et al., 2024).

The idea of CP Pup corresponding to an IP system is supported by the report of X-ray emission from the system with a modulation close to 1.47 h. (Orio et al., 2009; Mason et al., 2013). The X-ray emission has been used as a basis to estimate the mass of the WD, assuming it is a magnetic WD. The derived mass for the WD varies between 1.16 ± 0.2 (Selvelli & Gilmozzi, 2019) and $0.73^{+0.12}_{-0.11}$ (Veresvarska et al., 2024) $M_\odot$.

The nova shell around CP Pup is composed of several clumps of material expanding in a spherical configuration (Seitter & Duerbeck, 1980; Williams, 1982; Cohen & Rosenthal, 1983; Gill & O'Brien, 1998; Downes & Duerbeck, 2000). Hubble Space Telescope images revealed a shell composed of approximately 30 different knots distributed across the shell, with some of them being interpreted as potential polar blobs, while the rest form an equatorial ring (Downes & Duerbeck, 2000). The different observation of the expanding shell indicates a constant expansion rate of ~ 0.25 arcsec yr^{-1}.

V351 Pup

A nova eruption (Nova Puppis 1991) was observed in late December 1991 (Camilleri et al., 1992), reaching a minimum V magnitude of 6.4 and a t_3 of 26 d (Strope et al., 2010). Photometric observations revealed an orbital period of 0.1182 d (~ 2.8 h) and a smooth light curve consisting of a single minimum of variable shape (Woudt & Warner, 2001).

The nova shell around V351 Pup consists of a ring without evident asphericities, and an expansion rate of 0.100 ± 0.003 arcsec yr^{-1} (Downes & Duerbeck, 2000; Wendeln et al., 2017). Spectral analysis of the nova revealed expansion velocities in the range of $2\,500 - 3\,000$ km s^{-1} (della Valle et al., 1992; Williams et al., 1994). The amount of mass ejected as a result of the eruption has been a topic of debate. From the analysis of UV spectroscopic data Saizar et al. (1996) estimated an ejected mass $M_{\rm ej} \sim 10^{-7}$ $M_\odot$, while Hjellming (1996) derived a significantly higher $M_{\rm ej} \sim 10^{-3}$ $M_\odot$ from the analysis of the radio light curve of the nova. A more recent reanalysis of this radio light curve yielded a $M_{\rm ej} \sim 10^{-5}$ $M_\odot$ (Wendeln et al., 2017). The detection of [NeIII] in the spectra of the nova eruption suggests the presence of a massive O/Ne WD in the system (Williams et al., 1994). An estimation of the WD's mass from models and the derived $M_{\rm ej}$ indicates a 1.25 $M_\odot$ WD, consistent with an O/Ne WD (Wendeln et al., 2017).

T Pyx

T Pyx is a well-studied RN in the galaxy. Six different eruptions have been recorded in the years 1890, 1902, 1920, 1944, 1966, and 2011. In addition, it has been proposed that the system experienced a classical nova eruption circa 1866 (Schaefer, 2010). From the photometric data recorded during the eruption of 1966, Strope et al. (2010) derived a $t_3 = 66$ d. The system has an orbital period of 0.07623361 d ($\sim$ 1.8 h) and a mass ratio $q = 0.20 \pm 0.03$ (Uthas et al., 2010; Schaefer, 2022). As a RN, T Pyx should host a massive WD. By fitting the spectra of T Pyx in the UV, Selvelli et al. (2008) estimated $M_{\rm WD} \sim 1.36$ M$_\odot$, on the other hand, Uthas et al. (2010) derived a significantly lower $M_{\rm WD} = 0.7 \pm 0.2$ M$_\odot$ from the period-density relation and theoretical main-sequence mass-radius relation for the secondary component. The latter value is incompatible with the recurrent nature of T Pyx, raising concerns about the relation used to estimate the mass of the secondary component by Uthas et al. (2010).

T Pyx is the only known RN with a large optical shell. NB images in Hα+[NII] reveal the presence of a complex ejecta around the system (e.g. Williams, 1982; Schaefer, 2010; Shara et al., 2015), while spectroscopic studies reveal clumpy ejecta (Williams, 1982; Shore et al., 2011). From the latter studies, an extinction $E_{\rm B-V} = 0.5 \pm 0.1$ was derived (Shore et al., 2011). The most recent MUSE IFS data revealed a shell consisting of a ring with an inclination $i \approx 52^\circ$ observed in Hα and Hβ, and several knots of material seen in [OIII] and [NII] which are joined by filaments (Izzo et al., 2024; Santamaría et al., 2024).

V3888 Sgr

A nova eruption was recorded in October 1974 (Nova Sagittarius 1974), subsequently associated with V3888 Sgr (Leibowitz et al., 1976). According to the authors, the nova experienced a fast decline corresponding to $t_3 = 10$ d. The distance to the system has been estimated from spectroscopic and photometric analysis, yielding different values: ≤ 6 kpc (Leibowitz et al., 1976), 3.5 kpc (Vogt & Maitzen, 1977), and 2.5 kpc (Downes & Duerbeck, 2000). The parallax provided by *Gaia* DR3 ($\pi = 0.0712 \pm 0.0894$) mas) leads to a distance of 5086^{+2227}_{-816} pc. Its shell was imaged by Downes & Duerbeck (2000), showing an extension of 5.2×4.6 arcsec^2

FV Sct

FV Sct (Nova Scutum 1960) erupted in June 1960 (Nassau & Stephenson, 1961). The spectrum of the post-nova shows Hα emission, and from its continuum, the presence of a dwarf secondary star of type K3-K5 may be inferred (Ringwald et al., 1996). Its light curve was not recorded, and in consequence, its t_3 or light curve class can not be known, and there has been no attempt to image its shell.

CT Ser

CT Ser was observed to erupt as a nova during April of 1948 (Nova Serpens 1948), potentially occurring during November 1947 while in conjunction with the Sun (Mclaughlin, 1948). No photometric follow-up was done for this system, and its t_3 and light curve class remain unknown. The system has an orbital period of 0.195 ± 0.002 d ($\sim$ 4.6 h), and an spectrum characterised by a blue continuum with significant emission lines from hydrogen and helium, while its light curve presented significant flickering without evidence for eclipses (Ringwald et al., 2005; Rodríguez-Gil & Torres, 2005). Its nova shell was detected by (Downes & Duerbeck, 2000), as a Hα circular shell of $\sim$ 4 arcsec radius.

FH Ser

The nova eruption of FH Ser was observed in February 1970 (Nova Serpens 1970; Hirose & Honda, 1970). The nova light curve showed a dip $\sim$ 100 days after the outburst and t_3 of 63 d (Rosino et al., 1986; Strope et al., 2010). The nova shell around FH Ser consists of an elliptical and clumpy shell with a clear equatorial ring (Duerbeck, 1992; Gill & O'Brien, 2000; Santamaría et al., 2020; Guerrero et al., 2025). The shell is dominated mainly by Hα and [NII] emission, from which a shell mass of 2.6×10^{-4} $M_\odot$ was determined (Guerrero et al., 2025).

X Ser

Nova Serpens 1903 was discovered in photographic plates by H.Leavitt (Duerbeck, 1987a). From the photographic plates from the date, it can be seen that the nova eruption presented a slow and steady decline in brightness since its maximum, which should have taken place between May and September of 1903. It is classified as a slow nova with $t_3 \approx 730$ days (Šimon, 2018; Schaefer, 2022). The orbital period of the system, corresponding to 1.47 days, puts it as one of the CVs with the longest orbital

period (Thorstensen & Taylor, 2000). There have been no attempts to resolve the nova shell that originated during the 1903 eruption.

XX Tau

XX Tau erupted as a nova in November 1927 (Nova Tauri 1927; Schwassmann & Wachmann, 1928). The nova eruption presented a $t_3 = 47$ days, and it is catalogued as a D-type light curve (Downes & Duerbeck, 2000; Schaefer, 2022). The light curve of the system presents two strong periodicities at 0.1293567 and 2.929974 days (Schaefer, 2022). The authors argued that the shortest periodicity corresponds to the orbital period of the system ($\sim$ 3.1 h), while the longest period has an unclear origin. An attempt to observe its nova shell was carried out by Gill & O'Brien (1998). Although they did not detect the shell, the data were included in the sample of Santamaría et al. (2025), who detected an irregular shell with an average radius of 1.9 arcsec.

NQ Vul

Nova Vulpecula 1976 corresponds to the nova eruption recorded in October 1976 and associated with the system NQ Vul (Duerbeck, 1987a). The nova light curve showed a dip around $\sim$ 80 days after the eruption, it is catalogued as a member of the D-type light curve class, and its $t_3 = 50$ days (Strope et al., 2010). The orbital period of the system was determined by Schaefer (2022) to be 0.1462568 d ($\sim$ 3.5 h). Its nova shell was first detected in Hα by Slavin et al. (1995), and later reobserved by Downes & Duerbeck (2000), with the shell consisting of an almost circular shell with sizes 7.0×7.3 arcsec.

QU Vul

QU Vul erupted as a nova in December 1984 (Nova Vulpecula 1984b; Collins et al., 1984). The nova reached a minimum magnitude of 5.3 mag, and $t_3 = 36$. It was catalogued as a member of the P-class light curve (Strope et al., 2010). The photometry of the system reveals eclipses, from which an orbital period of 0.1117648(9) d ($\sim$ 2.7 h) can be measured (Shafter et al., 1995). The spectroscopic data reveal the presence of Ne in the ejecta, from which it can be deduced that the system should host a massive ONe WD (Rosino & Iijima, 1987). Based on theoretical light curves for ONe novae, Hachisu & Kato (2016) argued for a WD mass of $0.82 - 0.96$ M$_\odot$ for QU Vul.

The first image of the shell around QU Vul was provided in Downes & Duerbeck

(2000), whose authors reported a circular shell of 5.6 arcsec diameter. This size is in contradiction with HST images obtained the same year, showing a smaller shell of 1.6×1.3 arcsec (Downes & Duerbeck, 2000). Later observations carried out during 2020 revealed a spherical shell with a radius ~ 2.1 arcsec, supporting the HST measurement (Santamaría et al., 2020). The shell of QU Vul was studied using IFS by Santamaría et al. (2022a), who determined that the shell has an axial ratio of 1.4 ± 0.2, which is higher than the axial ratio derived from the NB images. The ejected mass was estimated to be $\sim 2 \times 10^{-4}$ $M_{\odot}$ (Santamaría et al., 2022a).

2.4 On CVs parameters

2.4.1 Masses of WDs

The mass of the WD in a CV can be measured from radial velocity curves, by fitting the light curve of the system during an eclipse, or it can be estimated from other observables, as the X-ray emission in the case of magnetic WDs, for instance. The most reliable method consist on the solution of eclipsing system with accurate radial velocities, which are rare due to the restrictive inclination ranges required; by the use of spectral fitting, or by the measurement of the gravitational redshift effect, which both methods requiring high resolution spectra in the UV range (see for example Zorotovic et al., 2011; Pala et al., 2022). This led to only a small part of CVs having accurate measurements for $M_{\rm WD}$. The values presented in the literature and mentioned in Sect. 2.3 were obtained using several methods, in some cases under a considerable number of assumptions (e.g., HR Del). In some cases, such as the case of CP Pup, they yielded different values for $M_{\rm WD}$ across different studies. This reflects the overall difficulty of measuring $M_{\rm WD}$ in CVs, and the large scatter expected from these values.

Another possibility to estimate $M_{\rm WD}$ is from models. In this sense, it is worth mentioning the work of Shara et al. (2018), whose authors estimated the WD mass of 92 post-novae systems from their light curve parameters (maximum brightness amplitude and t_2) and the theoretical models for nova eruption from Hillman et al. (2016). The model used by the authors is strongly dependent on t_2; thus, it is expected that a tight correlation between both parameters is present in the data. Several of the systems in our samples were considered in the work of Shara et al. (2018), and even under the expected correlation with t_2, they are worth considering for further analysis to compare against the $M_{\rm WD}$ derived from other sources.

2.4.2 Distances to the systems

Measuring the distance to post-novae CVs is not a trivial problem. There are several techniques to achieve this goal, as expansion parallax of the expanding shell (e.g. Tappert et al., 2023), by using the maximum magnitude rate decline of nova eruptions (Della Valle & Izzo, 2020), or by considering the parallax of the system, ϖ. The last method is usually referred to as the most reliable one, especially when considering the parallaxes provided by the *Gaia* mission (Schaefer, 2018).

With the *Gaia* EDR3, distances to 1.5 billion stars were determined by Bailer-Jones et al. (2021), including a significant number of post-novae. A more comprehensive analysis of the distance to 402 galactic novae was done by Schaefer (2022). For this thesis, the distances to the different post-novae within the sample were computed using the parallax values provided by *Gaia* DR3. To compute the proper distance from the provided parallaxes, the Bayesian approach proposed by Luri et al. (2018) was used. The probability $P(d|\varpi)$ corresponds to the probability that a system is at a distance d given a certain ϖ, according to:

$$P(d|\varpi) = \frac{1}{Z} P(\varpi|d) P(d), \tag{2.1}$$

where $P(\varpi|d)$ is the likelihood of measuring the observed ϖ at a given distance, $P(d)$ is the prior information of the distance to the system (i.e. how likely is that the system is at a given distance), and Z is a normalisation constant. For the likelihood, a normal distribution with $\mu = \varpi$ and $\sigma = \varpi_{\rm err}$ was used, while for the prior, the one proposed by Luri et al. (2018) was used:

$$P(d) = \frac{1}{2L^3} d^2 e^{-d/L}, \tag{2.2}$$

where $d = 1/\varpi$, and L is the length-scale parameter equal to 1 kpc. For systems with low parallax uncertainty ($\varpi_{\rm err}/\varpi < 0.1$), this approach converges to the expected theoretical distance obtained from parallaxes, corresponding to $d = 1/\varpi$.

It must be noted that the posterior distribution is virtually independent of $P(d)$ when the fractional error of the parallax, $f_\varpi := \varpi_{\rm err}/\varpi$ is smaller than 0.3 (Bailer-Jones, 2015). If instead $f_\varpi > 0.3$, the resulting posterior distribution is strongly dependent on $P(d)$, and therefore, the derived distance will be biased by the prior considered. Within the sample, a total of 10 systems have $f_\varpi > 0.3$. This means that the distance derived for these systems and the subsequent analysis must be taken with a grain of salt.

2.5 Summary of targets

A summary of the targets considered in this work is presented in Table 2.2, including the position of the system in the sky, the year of the nova and the observation, the age of the nova, its parallax including its error and fractional error, the distance derived from the parallax, the light curve type and t_3, orbital period, and WD mass when reported. The last column indicates if the nova shell was detected in the datacubes. From the 21 systems observed with MUSE, only 17 shells were detected. Those systems for which no shell was detected were left out of the following analysis.

Table 2.1: Summary of targets.

Target	RA [J2000]	Dec [J2000]	Nova [yr]	Obs [yr]	$\Delta t_{\rm nova}$ [yr]	$\varpi(\varpi_{\rm err})$ [mas]	f_ϖ	d [pc]	lc(t_3) [d]	$P_{\rm orb}$ [h]	$M_{\rm WD}$ [$M_\odot$]	Shell?
DO Aql	19:31:25.88	-06:25:38.74	1925.7	2023.6	97.9	0.348(0.180)	0.52	2580^{+1440}_{-450}	F(900)	4.03[a]	0.62[b]	✓
V1229 Aql	19:24:44.60	+4:14:46.60	1970.3	2022.7	52.4	0.410(0.504)	1.23	2120^{+1775}_{-510}	P(32)	–	1.12[b]	✓
V1425 Aql	19:05:26.62	-1:42:03.42	1995.1	2021.6	26.5	–	–	3300^{+300c}_{-300}	S(79)	6.14[d]	0.9[e]	✓
											1.09[b]	
V842 Cen	14:35:52.57	-57:37:35.39	1986.9	2022.0	35.1	0.731(0.045)	0.06	1370^{+100}_{-70}	D(48)	3.56[f]	1.02[b]	✓
RR Cha	13:26:23.88	-82:19:43.43	1953.3	2022.4	69.1	0.533(0.179)	0.34	1860^{+770}_{-245}	–	–	–	✗
BY Cir	14:44:53.46	-63:53:55.97	1995.1	2024.6	29.5	0.356(0.128)	0.36	2615^{+1290}_{-380}	P(124)	6.76[g]	1.15[e]	✓
											1.04[b]	
HR Del	20:42:20.34	+19:09:39.16	1967.5	2023.3	55.8	1.116(0.021)	0.02	897^{+17}_{-16}	J(250)	5.14[h]	0.6-0.7[i]	✓
											0.84[b]	
BT Mon	06:43:47.24	-02:01:13.88	1940.0	2021.9	81.9	0.641(0.031)	0.05	1560^{+90}_{-65}	F(190)[j], 42[k]	8.01[h]	1.04 ± 0.06 [k]	✓
											0.95[b]	
V2214 Oph	17:12:01.69	-29:37:32.78	1988.3	2024.4	36.1	2.156(0.613)	0.28	540^{+1250}_{-30}	S(89)	2.82[l]	–	✗
											0.99[b]	
RR Pic	06:35:36.06	-62:38:24.29	1925.4	2022.0	96.6	1.996(0.021)	0.01	501^{+6}_{-5}	J(122)	3.48[m]	0.95[b]	✓
											0.62 ± 0.2 [n]	

References: [a] Shafter et al. (1994); [b] Shara et al. (2018); [c] Tappert et al. (2023); [d] Retter et al. (1998); [e] Sanad (2014); [f] Woudt et al. (2009); [g] Woudt & Warner (2003); [h] Schaefer (2022); [i] Kuerster & Barwig (1988); [j] Strope et al. (2010); [k] Smith et al. (1998); [l] Baptista et al. (1993); [m] Vogt et al. (2017); [n] Selvelli & Gilmozzi (2019).

Table 2.2: Continuation of Table 2.2.

Target	RA [J2000]	Dec [J2000]	Nova [yr]	Obs [yr]	$\Delta t_{\rm nova}$ [yr]	$\varpi(\varpi_{\rm err})$ [mas]	f_ϖ	d [pc]	lc(t_3) [d]	$P_{\rm orb}$ [h]	$M_{\rm WD}$ [$M_\odot$]	Shell?
CP Pup	08:11:46.06	-35:21:04.99	1942.9	2021.9	79.0	1.282(0.019)	0.01	780^{+12}_{-11}	P(8)	1.47-1.64[o]	$0.73^{+0.12}_{-0.11}$[p]	✓
											1.16 ± 0.2[n]	
V351 Pup	8:11:38.389	-35:07:30.305	1992.0	2021.9	29.9	0.519(0.399)	0.77	1970^{+1800}_{-400}	P(26)	2.84[q]	1.25[r]	✓
											1.19[b]	
T Pyx	09:04:41.50	-32:22:47.50	1866.0	2021.9	155.9	0.347(0.029)	0.08	2870^{+300}_{-180}	P(62)	1.83[h]	0.7 ± 0.2 [s]	✓
											1.23[b]	
											1.36[t]	
V3888 Sgr	17:48:41.47	-18:45:34.79	1974.8	2022.2	47.4	0.071(0.089)	1.26	5090^{+2230}_{-820}	-(10)	–	–	✗
FV Sct	18:34:51.676	-12:55:26.447	1960.5	2023.5	63.0	0.482(0.218)	0.45	2050^{+1580}_{-320}	–	–	–	✓
CT Ser	15:45:39.079	+14:22:31.402	1948.3	2023.6	75.3	0.292(0.054)	0.18	3290^{+810}_{-350}	–	4.68[u]	–	✓
FH Ser	18:30:47.04	+02:36:52.03	1970.1	2023.4	53.3	0.980(0.063)	0.06	1025^{+80}_{-55}	D(63)	–	1.02[b]	✓
X Ser	16:19:17.69	-02:29:29.53	1903.2	2023.2	120.0	0.196(0.083)	0.42	3090^{+750}_{-370}	-(730)	35.28[v]	–	✗
XX Tau	05:19:24.465	+16:43:00.426	1927.9	2023.6	95.7	0.628(0.227)	0.36	1670^{+1475}_{-215}	D(47)	3.10[h]	–	✓
NQ Vul	19:29:14.75	+20:27:59.56	1976.8	2022.5	45.7	0.839(0.074)	0.09	1200^{+140}_{-80}	D(50)	3.51[h]	1.10[b]	✓
QU Vul	20:26:46.02	+27:50:43.16	1985.0	2022.7	37.7	1.111(0.309)	0.31	985^{+1014}_{-102}	P(36)	2.68[w]	0.82-0.96[x]	✓
											1.12[b]	

References: [o] Bruch (2022); [p] Veresvarska et al. (2024); [q] Wendeln et al. (2017); [r] Woudt & Warner (2001); [s] Uthas et al. (2010); [t] Selvelli et al. (2008); [u] Rodríguez-Gil & Torres (2005); [v] Thorstensen & Taylor (2000); [w] Shafter et al. (1995); [x] Hachisu & Kato (2016)

CHAPTER 3

Unveiling the 3D structure of nova shells with MUSE: The case of RR Pic

Because of its closeness and age, the nova shell around the classical nova RR Pic (Nova Pic 1925) is an ideal target for studying the evolving morphology of nova shells. In this chapter, an IFS study of the RR Pic nova shell using the MUSE instrument is presented, with a particular emphasis on the extraction of the 3D morphology of the shell. By measuring the extension of the nova shell in these new observations and comparing it against previous measurements, the expansion history of the ejected material can be determined. This information can be combined with the distance to the system based on *Gaia* EDR3 parallaxes and the systemic velocity of the system reported in the literature, to obtain a physical 3D view of the shell. The MUSE data confirm the presence of the nova shell in Hα, Hβ and [OIII], and very faintly in [NII]. A comparison with previous observations suggests that the shell continues in its free-expansion phase, but with the different parts of the shell apparently expanding at different rates. The data analysis corroborates the previous vision that the shell is composed of an equatorial ring and polar filaments traced by Hα. At the same time, the new data also reveal that [OIII] is confined in gaps located in the tropical regions of the shell where no hydrogen

is observed. The flux measurements indicate that ∼99% of the shell flux is confined to the equatorial ring, while the polar filaments show a flux asymmetry between the NE and SW filaments, with the latter being $\sim$ 2.5 times brighter. The mass of the shell was estimated to be $\sim 5 \times 10^{-5}$ $M_\odot$. From the analysis of the 3D-extracted data, it was determined that the ring structure extends $\sim$ 8 000 au from the central binary, and has a position angle of $\sim$ 155 deg and an inclination of $\sim$ 74 deg. The analysis of the equatorial ring reveals it is composed of a main ring and several small clouds, extending up to a height of $\sim$ 4 000 au above and below the main plane of the equatorial ring. The radial profile of the whole ring structure is reminiscent of a bow shock. This analysis has proven the capabilities of observing nova shells using IFS, and how the nova shell around RR Pic is an interesting object of study. Further and continuous observations of the shell across the electromagnetic spectrum are required to confirm the results and ideas presented in this work. This chapter corresponds to a published paper in the Astronomy & Astrophysics Journal (Bibcode: 2024A&A...681A.106C).

3.1 Imaging and spectral analysis

The analysis of the MUSE datacube confirms the presence of the nova shell around RR Pic as well as the ring-like and polar filament structures previously observed. The nova shell was detected in the Balmer lines of Hα and Hβ, as well as in the forbidden line of [OIII] and very faintly in [NII]. In the following section, the analysis regarding the image and spectral features observed within the shell is presented.

3.1.1 Image

The top row of Fig. 3.1 presents narrow band images created from the MUSE datacube for all the detected emission lines from the nova shell. The images were created by integrating the observed emission lines within a range of velocities of $[-750, +750]$ km s^{-1} for Hα and Hβ, $[-500, +500]$ km s^{-1} for the [OIII] λ500.7 nm line and $[-250, +250]$ km s^{-1} in the case of the [NII] λ658.4 nm line. These velocity ranges were determined based on the observed velocity profile of the shell material, so we can include all the observed emissions while minimising the noise contribution (see Sect. 3.1.4).

These images corroborate the presence of a ring-like structure surrounding the CV, whose semi-major axis extends along the SE-NW direction, but also a series of polar

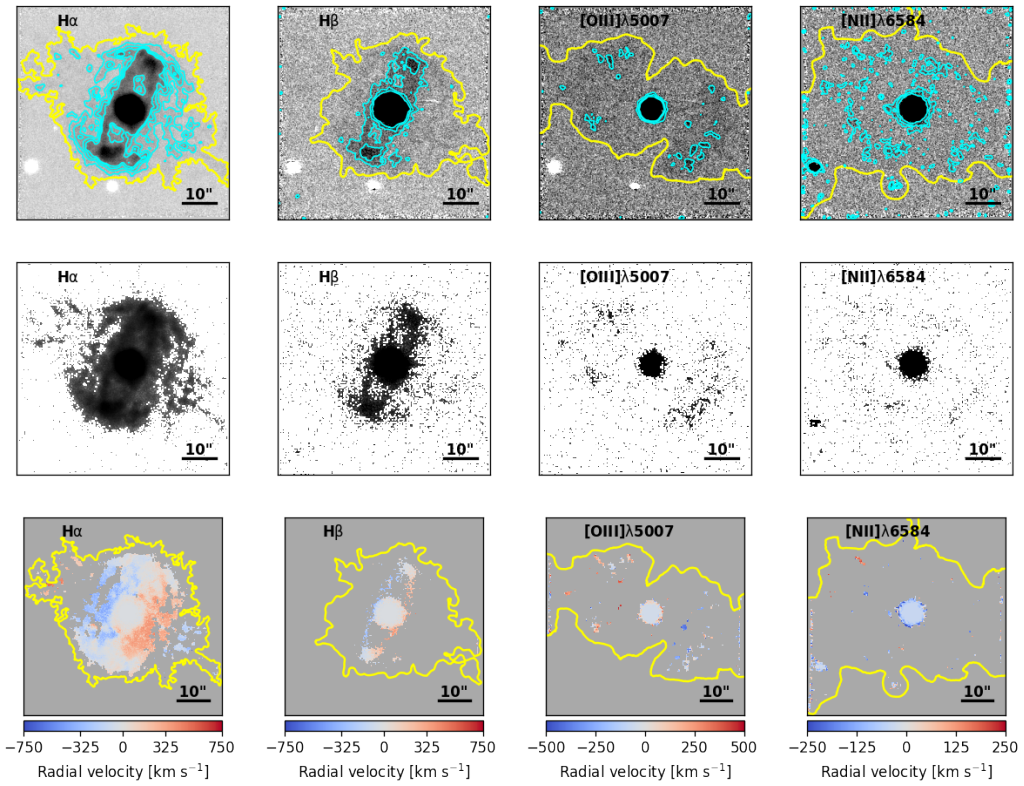

Figure 3.1: NB images and velocity maps of the RR Pic nova shell obtained from the MUSE datacube. Top row: flux images of the shell in Hα, Hβ, [OIII] and [NII]. The yellow contour level indicates the median background value, while the cyan levels indicate fluxes up to 1, 2, 3 and 10 sigma over the background median for Hα, 1, 2, and 3 for Hβ and [OIII] and 0.5, 1, and 2 for [NII]. Middle row: same images as top row but presented in logarithmic scale to appreciate the extension of the faintest part of the nova shell. The contours presented in the top row have been removed for clarity. The bottom row shows the radial velocity maps corresponding to each line. In all images, north is up and east to the left.

filaments expanding along the axis defined by the SW-NE direction. For better clarity, the background median value and its standard deviation were determined through a sigma clipping process on the images after applying a 5-arcsec circular mask around the central star. The 1-sigma contour level in the Hα image shows the equatorial ring also extending in the SW-NE direction, with several blobs of material in this direction. This overall structure, composed of a clear equatorial ring and polar filaments, was previously imaged by Gill & O'Brien (1998), GO98 from here on, using the 3.9 m Anglo-Australian Telescope. The comparison between the GO98 and MUSE image indicates that the nova shell has been expanding while preserving its geometry during the last $\sim$ 26 yr. These two components (ring and filaments) differ from each other in terms of their Hα flux, with the polar blobs being much fainter than the equatorial ring. For this structure, the brighter regions correspond to the zones located at each side of the ring in the SE and NW directions, which are traced by the 10-sigma contour level. The edges of the ring possess a bow shape, where it is also possible to identify regions of higher intensity. Overall, there are no significant differences between the SE and NW sections of the ring.

On the other hand, the polar filaments show a clear difference between the SW and NE regions, with the SW being brighter than its northern counterpart. Several blobs of material can be identified in the southern filament interconnected between them at a 1-sigma level, while for the northern filament, we can observe four isolated blobs only. The middle row in Fig. 3.1 shows the same images but using a logarithmic scale. The extension of the faintest part of the shell can be better appreciated. Besides the already mentioned structures, an additional faint tail of material can be observed leaving the system together with the SW filaments.

The distinction between the equatorial ring and the polar filament is evident when we look at their radial velocities. The bottom row of Fig. 3.1 shows the radial velocities corresponding to each one of the detected shell lines. These velocity maps reveal that the NE part of the equatorial ring has negative radial velocities, indicating that this part is moving towards us, while the opposite occurs in the SW part of the equatorial ring, which shows positive velocities. This confirms the idea of an equatorial ring around the system. In the case of the polar filaments, we have the opposite situation where the SW has negative velocities and the NE positive ones, suggesting that they are expanding in an apparent orthogonal direction with respect to the plane defined by the equatorial ring.

In the rest of the lines, only one of the components, the equatorial ring or polar

filaments, is present. The Hβ emission traces mainly the equatorial ring, as it is shown in Fig. 3.1. Faint fragments of Hβ emission can also be observed in the logarithmic image, being spatially coincident with the SW filaments observed in Hα. The polar filaments are traced by Hα but also by the forbidden line of [OIII]. In this line, we can observe several blobs at both the northern and southern filaments. Their velocity distribution shows the same pattern as the Hα blobs, with the southern blobs moving towards us. But it is also possible to observe some blobs with velocities close to zero, which indicates that they are expanding perpendicular to the observer. Lastly, the shell is also detectable in the forbidden line of [NII], but very faintly. The contour levels in the left, bottom row of Fig. 3.1 are set to 0.5 sigmas over the median background, for which it is possible to observe several blobs of material scattered throughout the field of view, but also coincident with the locations where the equatorial ring lobes are located in Hα and with the blobs observed in [OIII]. The brightest blob in this line is located at the NE filament, and its velocity is negative, following the behaviour of the rest of the lines.

3.1.2 Comparison with Gill&O'Brien 1998 image

A comparison with the GO98 image reveals that the shell has expanded considerably in the last 26 yr. It is expected that during the first decades after the nova event, the ejected material expands freely through the ISM, but after a certain time, it should start to show signals of deceleration, although it is not clear when this deceleration will start to become evident (Duerbeck, 1987b; Santamaría et al., 2020). To address this issue, two images taken at different times can be compared, identifying features within them and measuring the difference in position between the images. This approach was used to study the expansion of several knots that composed the nova shell around GK Per (Liimets et al., 2012) from which the authors conclude the knots are consistent with a free and radial expansion. Following this scheme, several knots of material were identified in the image published by GO98, together with their tentative counterparts in the Hα MUSE image. The astrometry in the GO98 image was determined from the stars present in the field, including RR Pic itself. This allows for a precise determination of the celestial position of the knots to compare against the MUSE data.

The top panel of Fig. 3.2 shows the nova shell observed in Hα by MUSE, in greyscale, with the contours of the narrow-band image published by GO98 overim-

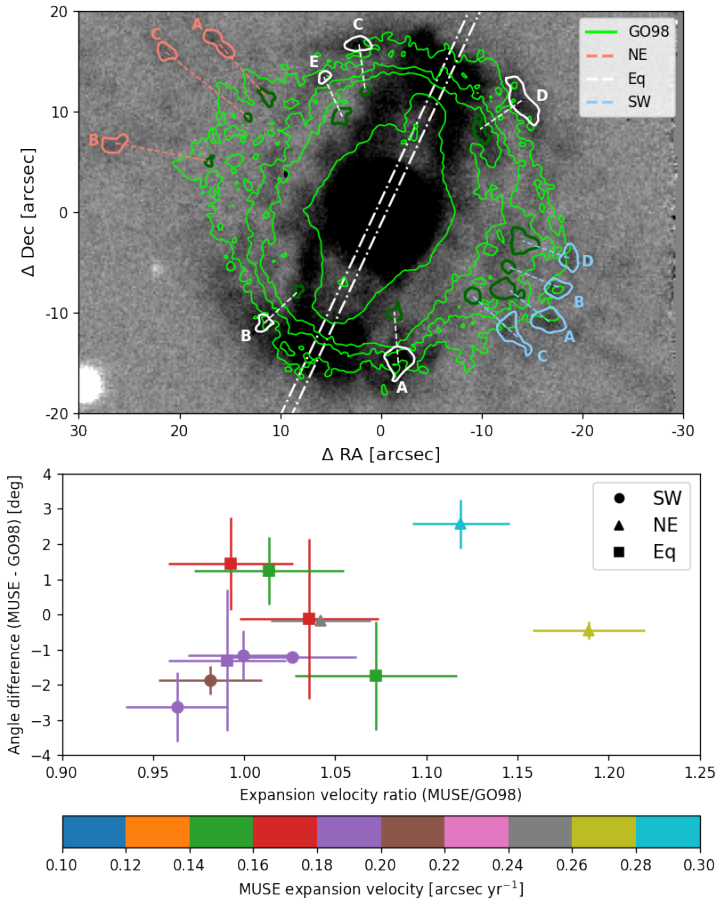

Figure 3.2: Comparison between MUSE and GO98 Hα images. The top panel shows the MUSE background-subtracted image (black-grey) with the GO98 image overimposed in green contours. Within the GO98 image, several knots of material were identified and marked with dark green contours. Their tentative counterparts in the MUSE image were also identified (joined through dashed lines). The different colours indicate if the knots belong to the NE or SW filaments, or to the equatorial ring. The white dotted dashed line indicates the rectangular section used to determine the extension of the equatorial ring. The bottom panel shows the ratio of expansion velocities between the MUSE and GO98 images versus the difference in position angle between MUSE and GO98 images for each knot identified in the top panel. The different markers indicate whether the knot belongs to the equatorial ring or a filament, while the colours show the expansion velocity measured from the MUSE image. Overall, the knots are consistent with a radial, free-expanding shell.

posed in green. Because the GO98 image does not contain physical units of flux, arbitrarily contour level values were chosen to highlight the several knots of material that appear to have remained relatively constant as the shell expanded.

These knots of materials are marked in dark green contours in Fig. 3.2 when referring to the GO98 image, and in red, white or blue colours in the case of the MUSE image. The distinction in colour in the case of the MUSE image was done to differentiate the knots belonging to the equatorial ring (white) from those of the NE (red) and SW (blue) filaments. In all cases, the knots identified in the GO98 image and the MUSE data are connected through dashed lines to illustrate their expansion.

The knots are labelled from the highest surface brightness observed in the MUSE Hα image, starting from A, and depending on which part of the shell they belong to. The celestial positions and surface brightness in the MUSE Hα image for each knot are presented in Table 3.1. The positions presented for each knot correspond to the average pixel position that composes the region, weighted by their flux. The uncertainties in the position of the knots were estimated by performing this procedure 10 000 times, each time adding a background noise following a normal distribution with μ equal to zero and σ equal to the previously determined background standard deviation.

The bandpass used by GO98 has a width of 54 Å centred on 655.5 nm, which is broader than the wavelength range that we used to create the Hα image from the MUSE datacube (33 Å centred at 656.3 nm). Because the wavelength range used to create the MUSE image is embedded within the GO98 bandpass, and most of the flux incoming from the shell is within the MUSE range, we do not expect significant differences in the incoming flux between the images. On the other hand, the seeing conditions in both images were similar, with GO98 reporting a seeing value of 1.1 arcsec during their RR Pic observations, which is comparable to the 1.2 arcsec seeing during the MUSE observations. The pixel scale of the GO98 image is 0.31 arcsec per pixel, a $\sim$ 50% worse than the MUSE pixel scale of 0.2 arcsec per pixel. Because in both cases the angular resolution is dominated by the similar seeing conditions together with the similarities in bandpass, a direct comparison is possible.

For each knot in the GO98 and MUSE images, the radial distance to the central star and the position angle were measured. The ratios of expansion velocity, derived from the measured radial distance and the time since the nova, were then compared to the differences in position angle for each knot pair. The results are shown in the bottom panel of Fig. 3.2. Assuming that the knots were correctly identified in both images

Table 3.1: Basic information for the knots identified in the MUSE Hα image. The columns show the celestial coordinates, radial extension and position angle measured from the central star, the expansion velocity and the surface brightness for each knot. The surface brightness is given in units of 10^{-19} erg s^{-1} cm^{-2} arcsec^{-2}.

Knot	RA (J200)	Dec (J2000)	r [arcsec]	PA [deg]	$v_{\rm exp}$ [arcsec yr^{-1}]	Surface brightness
NE-A	06:35:38.43(5)	-62:38:07.76(4)	23.25(6)	44.38(1)	0.2407(7)	218(2)
NE-B	06:35:39.94(5)	-62:38:17.80(3)	27.46(6)	76.12(4)	0.2842(6)	198(3)
NE-C	06:35:39.20(5)	-62:38:08.65(4)	26.66(6)	53.83(1)	0.2759(7)	188(3)
Eq-A	06:35:35.84(1)	-62:38:39.32(1)	15.03(1)	186.27(3)	0.1555(1)	787(4)
Eq-B	06:35:37.79(1)	-62:38:35.64(1)	16.31(2)	133.66(5)	0.1688(2)	649(5)
Eq-C	06:35:36.44(2)	-62:38:07.88(1)	16.69(2)	8.57(5)	0.1727(2)	721(6)
Eq-D	06:35:34.07(2)	-62:38:13.51(1)	17.61(3)	308.11(9)	0.1823(3)	476(2)
Eq-E	06:35:36.92(2)	-62:38:11.12(2)	14.49(2)	23.69(3)	0.1500(2)	450(6)
SW-A	06:35:33.69(3)	-62:38:35.39(2)	19.81(4)	236.24(1)	0.2051(4)	311(2)
SW-B	06:35:33.56(2)	-62:38:32.17(2)	19.02(4)	245.85(2)	0.1969(4)	289(3)
SW-C	06:35:34.22(2)	-62:38:36.42(3)	17.56(5)	226.72(2)	0.1817(5)	274(2)
SW-D	06:35:33.38(2)	-62:38:29.15(3)	19.17(4)	255.61(8)	0.1984(4)	271(3)

and that the material is expanding freely and radially, the ratio between the expansion velocities would be expected to scatter around one, while the difference in position angle would be expected to scatter around zero.

The bottom panel of Fig. 3.2 shows that the position angle differences are scattered symmetrically around zero with differences lower than $\pm$4 degrees, consistent with a radial expansion of the shell given the uncertainties. The velocity ratio, however, shows a systematic trend towards ratios greater than one. The most evident examples correspond to the NE filaments B and C with ratios of $\sim$ 1.12 and $\sim$ 1.19 respectively. These high-velocity ratios could, in principle, indicate an acceleration of the ejected material. This scenario is rather unlikely, although not impossible, as evidence for acceleration has been reported for knots in born-again planetary nebulae (Fang et al., 2014). Instead, a more likely explanation is a wrong identification of the knots of the NE filaments within the GO98 image due to a combination of intrinsic lower fluxes of the knots and the overall lower quality of the GO98 image compared with the MUSE image.

The colours in the markers of the bottom panel in Fig. 3.2 indicate the expansion velocity measured from the MUSE image, whose values are presented in Table 3.1. The

range of expansion depends on whether the knots belong to a filament, SW or NE, or the equatorial ring. This is not surprising as previous authors have already observed the polar filaments expanding faster than the equatorial ring (Williams & Gallagher, 1979; Gill & O'Brien, 1998). The SW knots have a range of expansion velocities close to $\sim$ 0.2 arcsec yr^{-1}, with the exception being SW-C, which shows a smaller expansion velocity of $\sim$ 0.18 arcsec yr^{-1}. In the case of the equatorial knots, the observed range of velocities is distributed approximately uniformly between $\sim$ 0.15 and $\sim$ 0.18 arcsec yr^{-1}. Lastly, the knots belonging to the NE filaments show the highest expansion velocities, reaching velocities between $\sim$ 0.24 and $\sim$ 0.28 arcsec yr^{-1}.

3.1.3 Expansion history

The previous section provided evidence for a free-expanding shell around RR Pic. However, to correctly quantify the expansion history of the ejected material, the shell extension must be measured in the same way as the previous authors did. They make a distinction between the equatorial ring and the polar filaments, finding that these regions expand at different velocities, consistent with the evidence presented in the previous section. The extension of the equatorial ring was measured from the separation between peaks across its semi-major axis. This separation was measured in the MUSE Hα image using a rectangular region of 1 arcsec width and position angle of 155 degrees centred on the central binary, thus covering the semi-major axis of the equatorial ring (top panel of Fig. 3.2) The presence of the shell is revealed as the two symmetric peaks observed at the sides of the central binary (Fig. 3.3). The separation of these peaks, based on the measurement of their centroid positions after fitting a Gaussian profile, is 29.8(2) arcsec.

In the case of the polar filaments, the previous authors estimated their extension as the separation between knots, but without specifying which knots they refer to (Spencer Jones, 1931; Williams & Gallagher, 1979; Gill & O'Brien, 1998). The average radial extension of the filaments is different for the NE and SW filaments, with the first one being more extended than its southern counterpart. This may induce an artificial acceleration or deceleration of the shell, depending on which filament is chosen to compare with the previous measurements. In the GO98 image, the authors reported an extension of the polar filaments to be 30 arcsec. This value is in good agreement with the average separation between the NE and SW knots in their image. Therefore, the average radial distance between the NE and SW knots in the MUSE image can be

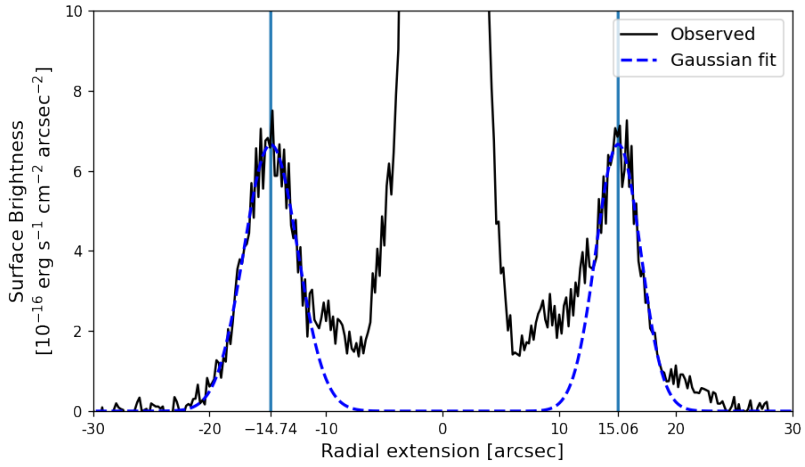

Figure 3.3: Surface brightness profile observed in the rectangular region presented in Fig. 3.2. Gaussian profiles were fitted to each one of the observed peaks (blue dashed lines) to determine the equatorial ring extension to be 29.8(2) arcsec. The positions of the Gaussian centres are marked with blue vertical lines. The radial distance is expressed with respect to the central binary with positive values towards the north.

compared with the GO98's measurement.

The radial extension of the shell around RR Pic as a function of the years since the nova is shown in Fig. 3.4. The shell extension measurements reported by the different previous authors are presented in black dots for the equatorial ring and black squares for the polar filaments. The first measurement was provided by Spencer Jones (1931) at a time when the shell structures were not resolvable. As the polar filaments are expanding faster, this measurement can be associated with the mentioned filaments. In the case of the other two authors, Williams & Gallagher (1979) and GO98, the shell structures were resolved and measurements of the extension of the equatorial ring and polar filaments were provided.

The new data are presented in colour squares for the polar filaments (red for the NE knots, blue for the SW knots, and grey for the average between the polar knots), while the equatorial ring measurements are presented in cyan and green dots for the slit measurement and the equatorial knots, respectively. In the case of the measurement from knots, the markers indicate the mean value, while the error bars correspond to the standard deviation of the sample. The expansion velocity rate for the polar and equatorial ejecta was determined after performing a linear fit to the data. The results indicate that the equatorial ring is expanding at a rate of 0.154(1) arcsec yr^{-1} (dashed line), while the polar filaments are expanding at a rate of 0.225(2) arcsec yr^{-1}

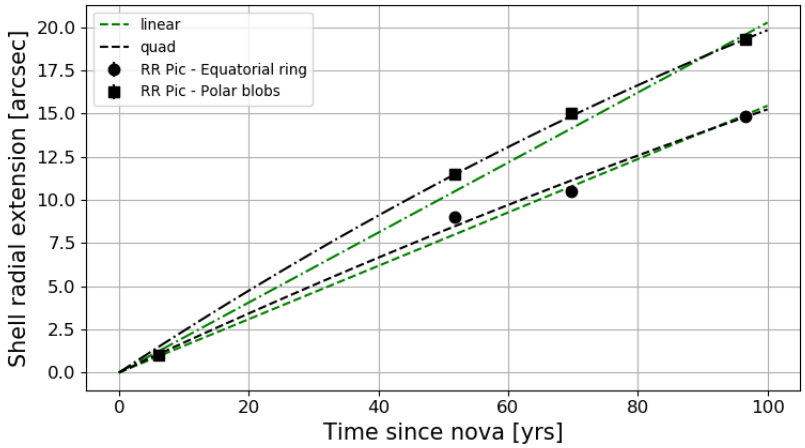

Figure 3.4: Radial extension of the nova shell around RR Pic as a function of the years since the nova eruption. Measurements provided by previous authors are presented in black dots for the equatorial ring and squares for the polar filaments. The new measurements from MUSE data are presented in colours. The best linear model indicates expansion rates of 0.154(1) and 0.225(2) arcsec yr^{-1} for the equatorial ring and the polar filaments, respectively.

(dotted line). In the case of the polar filaments, only the average value between the NE and SW knots was included. The derived expansion velocities are consistent with the previous expansion values of 0.159(1) and 0.217(3) arcsec yr^{-1} for the equatorial and polar filaments, supporting the free-expanding scenario proposed in Section 3.1.2. These projected expansion velocities can be converted to proper expansion velocities by considering the distance to the system ($d = 501$ pc; Table 2.2). This led to an expansion velocity of 368(4) km s^{-1} for the equatorial ring and 532(8) km s^{-1} for the polar filaments. These expansion velocities are consistent with the observed spectral profile (Fig. 3.5) in the case of the equatorial ring, but appear to be higher in the case of the polar filaments, as the spectra show velocities around $\sim$400 km s^{-1}. This is due to the filaments expanding orthogonally to us. When considering the NE and SW radial extension measured as independent measures, the average expansion of 0.199(5) arcsec yr^{-1} for the SW and 0.26(1) for the NE is found, which translates into an expansion velocity of 473(12) and 613(26) km s^{-1} respectively.

3.1.4 Description of the spectrum

For the spectral analysis of the nova shell, a distinction was made between the equatorial ring and polar filaments based on the contour levels and velocity maps presented

in Fig. 3.1. For the equatorial ring, a mask that considers the data within the 1-sigma level presented in the Hα image was applied. The filaments at the north and south were not considered due to the differences in their velocities with respect to the ring. Once this mask is defined, it can be applied to the datacube to obtain a single spectrum by summing all the flux contributions at each wavelength. To minimise the contamination from the stellar component, a circular mask of 5 arcsec radius centred on the position of RR Pic was applied. The radius of this mask was chosen as it offers a good equilibrium between removing the stellar flux and keeping most of the nova shell flux intact. Following the same procedure of applying this circular mask to the cube, a single spectrum for the CV can be obtained, which then can be subtracted from the equatorial spectrum to end up with a spectrum that represents mostly the contribution of the nova shell. In the case of the polar filaments, the Hα and [OIII] images at 1-sigma level with respect to the background were considered to create a mask which yields a spectrum in the same manner as the previous case.

The resulting spectra are presented in Fig. 3.5. The upper panels show the spectrum of the equatorial ring, the polar filaments and the CV itself, corresponding to the total flux inside their respective masks. The spectra of the equatorial ring and polar filaments presented were median binned by considering boxes of 8 pixels to reduce the noise within the data, while the spectrum of the CV was median binned using boxes of 2 pixels. The spectra reveal that Balmer lines dominate the equatorial ring, while the polar filaments show the Balmer lines and the [OIII] λ 495.9 and λ 500.7 nm lines. On the other hand, the stellar spectrum shows a blue continuum dominated by the accretion disc, with several emission lines that originate from it. These emission lines correspond to Balmer and Helium, including the HeI λ 492.1 nm, λ 501.5 nm, λ 587.5 nm, λ 667.8 nm and λ 702.1 nm lines, and the HeII λ 541.1 nm line. The CIV λ 580.0 nm line is also prominent, as well as the Paschen series. No evident absorption lines are detected. Additionally, in the equatorial and polar filament spectra, a blue continuum is also present. This is the result of the residual contribution of the CV flux into the background. Similarly, several features are observed beyond 700 nm in these two spectra. An examination of the datacube reveals that they are caused by the high background noise at these wavelengths.

The bottom panels of Fig. 3.5 present a close-up of the main, unbinned lines detected in the nova shell, in blue for the equatorial ring and orange for the polar filaments. The mean flux inside the mask, instead of the total flux, is presented to facilitate the comparison between spectra. All lines are presented in their respective velocity

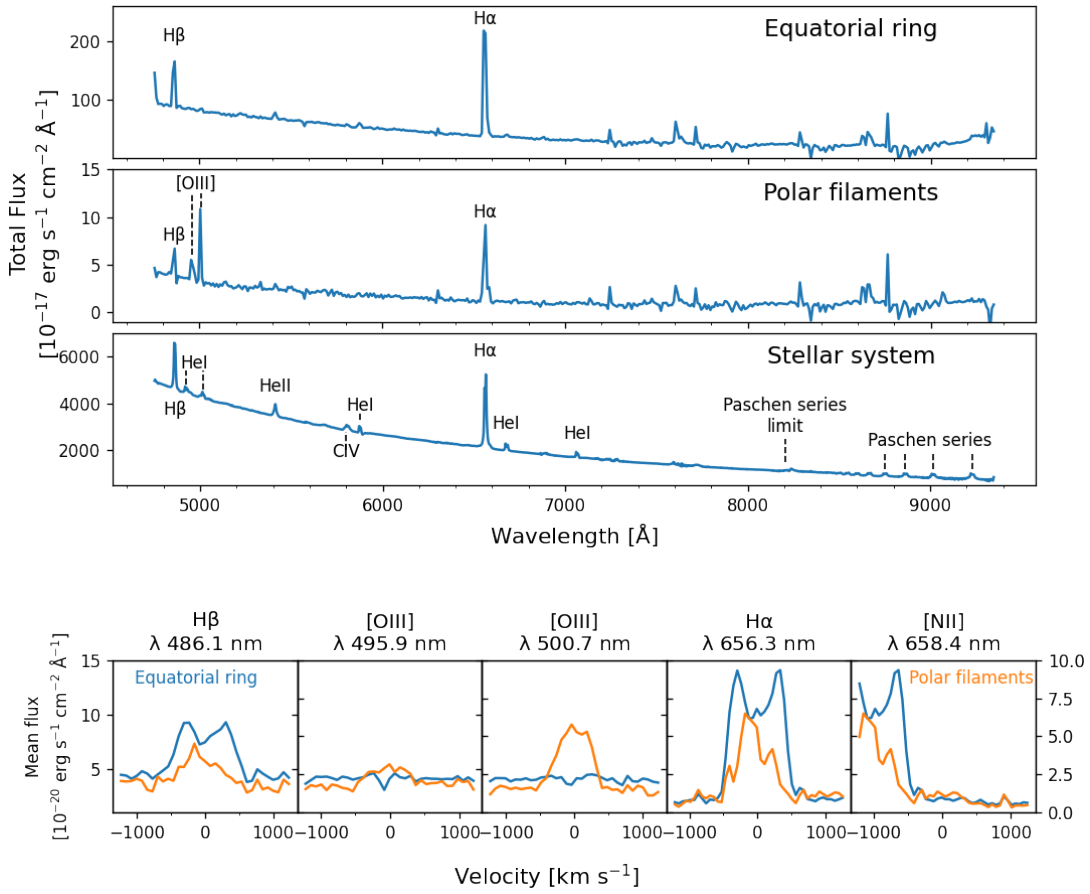

Figure 3.5: Spectra of the equatorial ring, polar filaments and the central binary (CV) of RR Pic. The top panels present the total spectrum of the equatorial ring, the polar filaments and the CV, with the observed main lines labelled in the spectra. The bottom panels show the average spectra of the equatorial ring (blue) and polar filaments (orange) for the lines observed within a velocity range between $-1\,250$ and $1\,250$ km s^{-1}. The flux scales are different, with the equatorial ring defined by the scale present on the left, and the polar filaments by the scale presented on the right.

space with a range between $-1\,250$ and $1\,250\ \mathrm{km\,s^{-1}}$. The Balmer lines in the equatorial ring present a double peak profile, which indicates the symmetry of the equatorial ring. In the case of the polar filaments, a more clumpy structure is observed around Hα, with one central peak and two minor ones on each side. The peak also appears to be blueshifted, which is consistent with the SW filaments having negative velocities and higher flux than their NE counterpart, as indicated in the images (Fig. 3.1). In the case of the forbidden oxygen lines, we only see one clumpy peak. A small bump is present in the polar filament at the [NII] line, but it is difficult to characterise it due to its low S/N.

3.2 3D reconstruction

The main goal of this work is to obtain a 3D view of the shell from the data, from which its geometry, luminosity, spatial extension, and other physical properties can be analysed. In the following, the methodology implemented to obtain the 3D view from the datacube, as well as the assumptions and considerations, are explained.

3.2.1 Extraction methodology

Shell extraction

As a first step to extract the shell's structure from the datacube, a suitable range in the spatial axes and wavelength is defined in which all the shell's flux for a given line is expected to be contained. These ranges are used to create a subcube from the original datacube. By linearly interpolating the average of the first three and last svoxels at each spaxel of this subcube, a continuum cube is created, which is then subtracted from the subcube data.

Once the background is subtracted from the subcube, the selection of svoxels that are likely to belong to the nova shell can be done. As it is shown in Figs. 3.1 and 3.5, the strongest lines in the nova shell are the Hα and Hβ emission, as well as the forbidden line of [OIII] λ 500.7 nm. Two selection criteria are defined to isolate the flux coming from these lines while avoiding the noise and artefacts present in the data. The first criterion is based on a minimum S/N, selecting only those svoxels whose fluxes exceed a certain threshold value. The S/N can be calculated at each svoxel from the variance cube provided by MUSE according to $\mathrm{S/N} = F/\sqrt{\sigma^2}$, where F and σ^2 are the flux and variance, respectively. A low threshold value will ensure that most of

the flux coming from the shell will be considered, but at the detriment of including a significant amount of noise.

That is where the second criterion comes into play. To get rid of most of the noise, a criterion based on a minimum number of adjacent svoxels was applied to all those svoxels that passed the first criterion. In that way, most of the pure random noise can be discarded, as this should appear as isolated svoxels across the entire datacube. The price paid for this criterion is to erase the outer parts of the shell. Lastly, a certain percentage of the svoxels that have passed the second criteria selection can be discarded based on their flux values, to be sure that most of, if not all, the noise in the subcube has been discarded. For the case of RR Pic, we set the values for these criteria to 2 for the minimum S/N value, having at least 3 adjacent svoxels, and the discard of the 10% of the faintest svoxels.

If necessary, the S/N can be increased prior to the application of these criteria by binning the subcube. This was the case when we extracted the line of [OIII], in which case the spatial axes were binned by a factor of two.

Position-position-velocity space

At this point, all those svoxels with a high flux contribution with respect to the continuum, including the nova shell and the CV itself, which, in turn, is dominated by the emission coming from its accretion disc, have been selected. The position of each svoxel is known, and so, its distance in arcsec from the central binary can be obtained from the pixel scale of the instrument. Similarly, the velocity with respect to the reference line for each svoxel can be derived from the classic Doppler effect. With that information, the Position-Position-Velocity (PPV) space for each emission line in the shell can be created, which can be used later to construct the physical 3D space.

As we are interested only in the nova shell, not the accretion disc, we proceed to remove its contribution from the PPV space. For that purpose, it is sufficient to apply a circular mask to the CV, as was the case in Sect. 3.1.4. If the shell has expanded enough to be spatially resolved from the central binary, then the mask should not present any problem for further analysis. But if this is not the case and it is not possible to spatially resolve the shell from the central binary, as could be the case for younger and/or distant nova shells, then masking it would be harmful, and therefore not recommended. In these cases, the analysis should go on with the inclusion of both sources of emission. In the case of RR Pic, the system falls into an intermediate point where the shell has expanded enough to be clearly distinguished from the central star, except for the

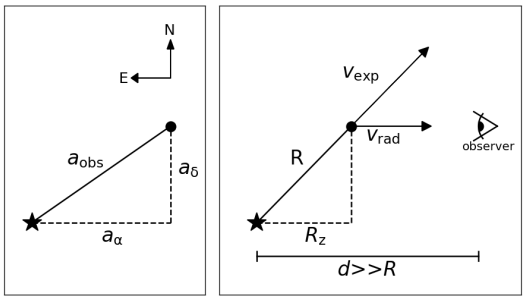

Figure 3.6: Schematic visualisation of the conversion of a single svoxel from PPV to PPP space. The left panel shows the situation in the plane of the sky, while the right panel presents the view perpendicular to it, that is, in the line of sight of the observer. The central binary is marked with a star, and the svoxel with a filled circle in both cases. See text for details.

most inner parts of the equatorial ring, where, due to the inclination angle of the ring, some parts appear to be projected very close to the central star. In the end, the central star was masked using a 5 arcsec aperture that removes almost all its flux, without carving too much the equatorial ring.

Conversion to physical space

Once the shell has been extracted, the PPV space can be converted into a proper physical 3D space, also called Position– Position–Position (PPP) space. To achieve that, however, additional information regarding the expansion of the ejecta and the distance and systemic velocity of the system is required. To illustrate the conversion from the PPV into the PPP, the position of a single svoxel in the plane of the sky (left) with respect to the position of the central binary is shown in Fig. 3.6. This svoxel is located at a projected distance $a_{\rm obs}$ from the central binary. This distance can be decomposed into its right ascension (a_α) and declination (a_δ) components. By knowing the distance from the observer to the binary, d, we can convert these projected coordinate differences into physical distances, $R_{\rm x}$ and $R_{\rm y}$, according to:

$$R_{\rm x} = a_\alpha\, d;\ R_{\rm y} = a_\delta\, d. \tag{3.1}$$

Here, it is assumed that the physical separation between the nova shell and the central binary is negligible compared to the distance between the central binary and the observer. Considering that the radial sizes of nova shells are of the order of $\sim 10^3$ au, while the distance between the observer and post-novae typically amounts to $10^2 - 10^3$ parsec, this is a very reasonable assumption.

In addition to the projected distance of each svoxel, its radial velocity is also known. The right panel of Fig. 3.6 shows the position of this svoxel on the z (line of sight) axis. The svoxel is located at a physical distance R from the central star and is moving away from it at an expanding velocity $v_{\rm exp}$. The observed can only measure the projected velocity of the expanding material, $v_{\rm rad}$, from which we must find the distance projected on the z-axis, $R_{\rm z}$. By assuming that the material is expanding radially from the central star, then the angle formed by $v_{\rm exp}$ and $v_{\rm obs}$ is identical to the one formed by R and $R_{\rm z}$, and thus is easy to see the given relation:

$$R_{\rm z} = \frac{R}{v_{\rm exp}}\, v_{\rm rad}. \tag{3.2}$$

It is worth noting that the assumption of the shell expanding radially does not necessarily imply a spherical geometry for it. Different sections can expand at different velocities, resulting in oblates, prolates, or more complex geometries.

To determine the quantities R and $v_{\rm exp}$, a function for the expanding history of the ejected material must be assumed, which we denote as $f_{\rm vexp}(t)$. The expressions for R and $v_{\rm exp}$ are then given by:

$$R = \int_0^{t_{\rm sn}} f_{\rm vexp}(t)\, dt;\ v_{\rm exp} = f_{\rm exp}(t_{\rm sn}), \tag{3.3}$$

where $t_{\rm sn}$ corresponds to the time that has passed since the nova event.

The factor $R/v_{\rm exp}$ in Eq. 3.2 has dimensions of time, and it acts like a correction factor for the current observed value of $v_{\rm rad}$. In the case of a constant expansion velocity, which is the expected case for young shells where the material is still in its free expansion phase, this correction factor becomes simply $t_{\rm sn}$ (linear expansion with time), and the value of $R_{\rm z}$ is obtained just by multiplying $v_{\rm rad}$ by the time since nova. In the case of older shells where deceleration starts to become evident, a function that represents this deceleration must be assumed, and the quantities for R and $v_{\rm exp}$ have to be computed accordingly. In this case, the factor $R/v_{\rm exp}$ will be a function of $t_{\rm sn}$ having units of time, but multiplied by a factor greater than one, compensating that way the underestimation in $R_{\rm z}$ if a linear expansion of the shell would be assumed istead. Because different regions of the shell could expand and decelerate at different rates, it is important that these differences are represented correctly within our function $f_{\rm vexp}(t)$, otherwise, a spherical expanding shell may be assumed, which is usually not the case in nova shells.

Lastly, it is important to mention that it is essential to correctly identify the tran-

sition corresponding to the observed emission. A misidentification would lead to an erroneous radial velocity and thus to improper values for R_z, which will negatively affect the recovered morphology of the shell. While this may seem trivial, strong blends are likely to occur for the lines of Hα and [NII], and can pose a serious problem for the recovery of the shell structure (e.g. the nova shell around V1425 Aql, Tappert et al., 2023). In the case of RR Pic, the contribution of the [NII] line is negligible compared to the Hα emission, as it was shown in Figs. 3.1 and 3.5, therefore that are not needs to worry about possible blends between these two lines. Last, but not least, the radial velocities also have to be corrected for the systemic velocity $v_{\rm sys}$ of the central binary.

3.2.2 RR Pic 3D reconstruction

After the extraction of the shell using the methodology described in Sect. 3.2.1, the study of its PPV space can begin. The top row of Fig. 3.7 shows a 3D view of the PPV space of the nova shell centred on the CV before the application of the circular mask, where the Hα and [OIII] emissions are presented in black-red-yellow and blue-green colours, respectively. The axes on the plane of the sky (X and Y) correspond to the observed projected separation in right ascension and declination, respectively, and the axis along the line-of-sight (Z) to the observed projected velocity.

The most evident structure observed in the PPV space is a biconical structure appreciable in Hα and centred at the position of the binary system. This structure is the result of the high velocities reached by the material in the accretion disc around the WD, showing the importance of its removal when properly analysing the nova shell. The shell itself appears as a ring structure surrounding the system, with additional cloudy features observable above and below the ring. The aforementioned filaments are also detectable in the PPV space as clouds of material located perpendicular to the central ring. Similar structures are also evident in [OIII], where they appear to occupy a different region in the space than the Hα emitters.

When converting to PPP after masking the central star, a free-expanding model for the shell was considered, based on the results presented in Sect. 3.1.3. Together with the *Gaia* EDR3 distance of 501 pc, and the reported systemic velocity of 1.8 km s^{-1} (Ribeiro & Diaz, 2006), the observed quantities can be converted into proper physical distances with confidence. The resulting 3D view of the nova shell in the PPP space is presented on the bottom row of Fig. 3.7. The ring structure is much clearer now after removing the contribution of the accretion disc. Similarly, the position of the

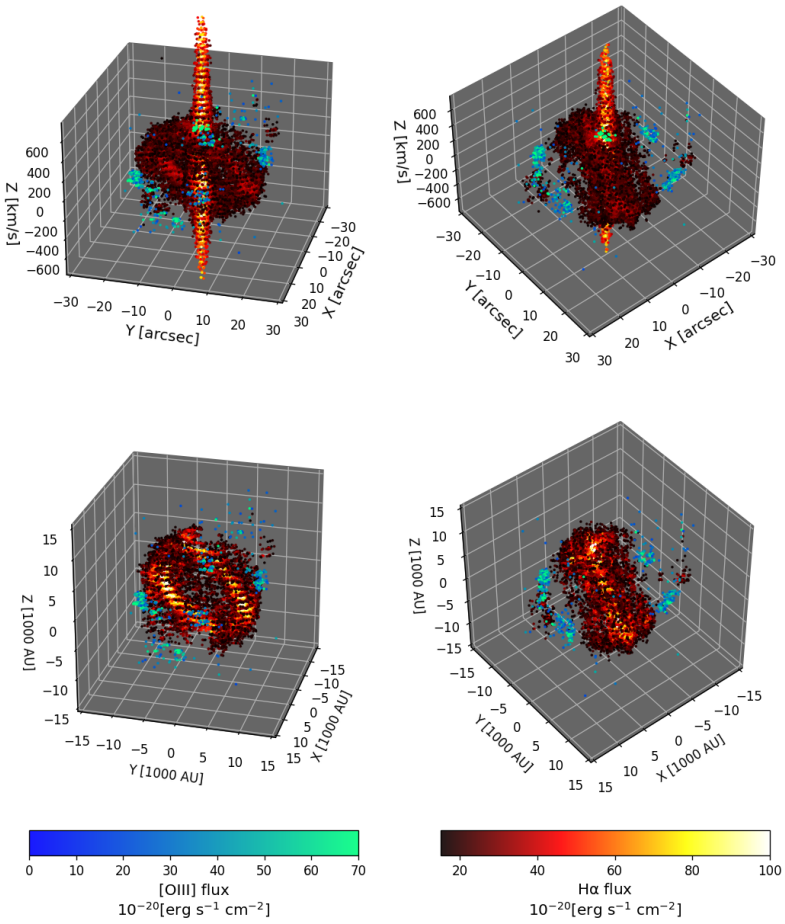

Figure 3.7: 3D view of the PPV (top row) and PPP (bottom row) spaces for the RR Pic nova shell. The Hα emission is presented in black-red-yellow colours, while [OIII] is presented in blue-green colours. In both cases, the brighter regions are presented in lighter colours. The angles of the frames were chosen so the circular ring (left column) and the polar filaments (right column) could be better appreciated.

Table 3.2: Best parameters from the circular fit to the equatorial ring.

Parameter	Value
Radial extension (au)	7890±60
Position angle (°)	155.0±0.2
Inclination (°)	73.6±0.3 height

polar filaments in Hα and [OIII] appears clearer, with the two emitters being spatially separated, confirming the impression from the PPV.

3.2.3 Measurements from 3D data

Geometrical measurements

The creation of a 3D frame for the nova shell allows the study of its geometry in great detail. The most evident structure within the shell is its equatorial ring, thus, it is natural to start the analysis by studying it. A circular fit to the ring was performed to obtain information about its radial size, inclination, and position angle. Only the 5% of the brightest points belonging to the equatorial ring were selected to trace the inner part of the ring in order to reduce the computational cost of the process. The fit was done via 3D space minimisation of the separation between the svoxels belonging to the equatorial ring in the PPP space and the circular ring itself. Uncertainties for the distance and systemic velocity were incorporated through a Montecarlo process by performing a thousand different fits, each one incorporating a distance and a systemic velocity value drawn from a normal distribution with mean and standard deviation being the value and its uncertainty for each one of the two aforementioned parameters. Each random sample was used to build the PPP space from the PPV as previously described, after which the best parameters to fit a circular ring to the created PPP were determined. The results of these thousand fits are presented in Table 3.2, where the given values and uncertainties correspond to the mean value and standard deviation for each one of the parameters. The results constrain very well all the ring parameters, up to the point that one could consider the given uncertainties as unrealistically low. The likely reason is the low number of points considered, corresponding only to the 5% brightest points. The inclusion of a high number of points and/or the inclusion of fainter points will likely impact the uncertainties derived.

The Aitoff projection of the nova shell is presented in Fig. 3.8 after transforming

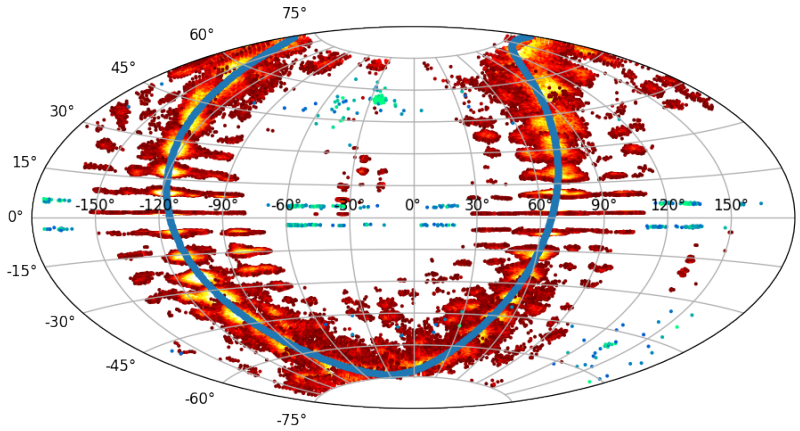

Figure 3.8: Aitoff projection of the RR Pic nova shell. The Hα and [OIII] emission are presented together with the best circular ring fitted to the observed equatorial ring shown in pale blue. The colour scale for Hα and [OIII] is the same as in Fig. 3.7.

the Cartesian coordinates of the 3D data into spherical coordinates. The Hα and [OIII] emissions are presented in black-red and cyan-blue colours, respectively, while the best fit for the circular ring is presented in blue points. The circular ring traces the observed distribution of the equatorial ring in Hα very well, which confirms the quality of the fit for the inclination and position angles. On the other hand, the observed distribution of the [OIII] line appears concentrated around the equator of the projection ($v_{\rm obs}$ $\sim$ zero) and the polar regions, emphasising once more the difference in spatial location between the two emitters.

Once the best circular ring has been determined, the resulting parameters can define a new reference frame in cylindrical coordinates where the circular ring, and therefore the equatorial ring of the shell, lies on the $\rho - \phi$ plane. This coordinate system allows for a better appreciation of the radial structure of the equatorial ring, its overall size, and the polar filaments. In the left panel of Fig. 3.9, the mean radial profile of the shell in the ρ-Z plane is presented. The equatorial ring extends up to $\rho \sim 10\,000$ au, a higher value than the one obtained after the ring fit to the equatorial ring of $\sim 8\,000$ au (Table 3.2). The reason is that the latter traces the inner and denser parts of the ring, and not the outer ones.

The equatorial ring shows a bow shock-like structure, with material above and below the main ring. To better highlight this structure in the image, we provided contour levels corresponding to 1, 2, and 3 sigmas over the Hα mean value in the plane. The cloudy structures, traced at the 1 level, appear as regions of higher flux around

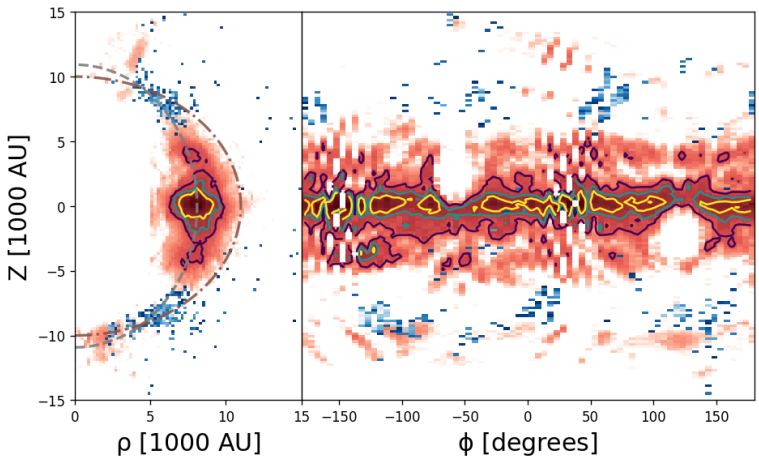

Figure 3.9: Projection of the nova shell in cylindrical coordinates. The system is presented in a way that the equatorial plane is located at Z = 0. Left: average view on the ρ–Z plane. Right: average view on the ϕ-Z plane. In both panels, the Hα emission is presented in red-black colour scale, while [OIII] is presented in blue. The contour levels indicate the flux corresponding to 1, 2, and 3 times the standard deviation value on each plane. The lines in the ρ–Z plane indicate an ellipse with an equatorial radius of 8 090 au and an axial ratio of 1.35 (grey dashed line), and an equatorial radius of 10 990 au and an axial ratio of 0.91 (brown dotted line).

3 900 au above and below the equatorial ring, and an opening angle of $\sim$ 30 deg with respect to the equatorial plane. It is also interesting to note that the [OIII] emission is located in the gaps between the equatorial ring and the polar filaments observed in Hα. The axial ratio between both emitters is also different. The lines plotted in the ρ-Z plane correspond to the ellipses that best fit the observed data in Hα (grey dotted line) and [OIII] (brown dashed line). The ellipse parameters (axial ratio and equatorial radius) were determined via least squares minimisation from the data presented in the plane, weighted by their fluxes. Both, Hα and [OIII] were fitted independently from each other. The results indicate a prolate ellipse for Hα with an equatorial radius of 8 090(20) au and axial ratio (defined as the polar over the equatorial radius) of 1.34(3), while for [OIII] the best fit indicates an oblate geometry with an equatorial radius of 11 000(30) au and axial ratio 0.92(3). In the case of the Hα data, the parameters found are in reasonable agreement with the ones determined through the equatorial ring fit (equatorial radius 7 890(60) versus 8 090(20) au) and the ratio between the equatorial and polar expansion rates (1.445(2) versus 1.34(3)).

The right panel of Fig. 3.9 shows the ϕ–Z plane. Several artefacts appear as results of the masking of the central star, like the holes at $\phi \sim -60$ and 120, but also the ones

produced by the sliced nature of the datacube, which generates observable gaps in the data at angles of ~ -150 and 30 degrees. Even so, the structure of the equatorial ring is still appreciable, and in particular, it is possible to appreciate that the cloudy structures above and below the main ring are not continuous but fragmented. This is also evident in the 3D view of the shell (Fig. 3.7). The polar filaments in Hα span a wide range of ϕ angles, which means they behave more like an extending ring than a bullet of material leaving the system. This does not seem to be the case for [OIII], where the emission appears to be concentrated within a narrow range of ϕ values.

Fluxes and masses

Together with their physical position, for each svoxel included in the final extracted 3D data, we also have their respective flux and associated uncertainty. This allows the determination of the total flux of the nova shell and its different components. The measured fluxes for Hα, Hβ and [OIII] are presented in Table 3.3. The fluxes were corrected for a reddening value of 0.034(17) mag, according to the 3D map of the interstellar medium provided by the Stilism website [1] (Capitanio et al., 2017). By using an extinction law parameter R equal to 3.1 and the reddening law from (Fitzpatrick, 1999), we determined correction factors of 1.08(4), 1.12(6), and 1.11(6) for the lines of Hα, Hβ, and [OIII] λ 500.7 nm respectively.

Together with the Balmer fluxes, rough estimates of the mass of the shell can be provided. The mass of a nova shell, $M_{\rm shell}$, can be estimated as:

$$M_{\rm shell} = \mu\, m_{\rm p}\, n_{\rm p}\, V_{\rm shell}\, \epsilon, \tag{3.4}$$

where μ corresponds to the mean molecular weight of the gas, $m_{\rm p}$ and $n_{\rm p}$ are the proton mass and density , respectively, $V_{\rm shell}$ is the volume of the shell and ϵ is its filling factor. This approximation can be applied to planetary nebulae and nova shells (Osterbrock & Ferland, 2006).

Our data do not provide enough lines to constraint the electron density $n_{\rm e}$, the electron temperature $T_{\rm e}$, or ϵ within the gas, and therefore an alternative method to determine the gas density must be used. Because only the fluxes corresponding to the Balmer transitions are in consideration, a gas composed purely of Hydrogen can be assumed, allowing to set $\mu = 1$ and $n_{\rm p} = n_{\rm e}$. The electron density and temperature can then be estimated by comparing the observed energy emitted by the shell against

[1] Stilism website

Table 3.3: Fluxes and masses measured for the nova shell around RR Pic. The mass values given correspond to an electron temperature of 5 000 K.

Shell	Flux [erg s^{-1} cm^{-2}]	Volume [cm^3]	Mass [M$_\odot$]
Hα			
Equatorial ring	$2.891(2)\times10^{-14}$	3.04×10^{51}	$5.119(4)\times10^{-5}$
SW filament	$3.66(2)\times10^{-16}$	5.32×10^{49}	$7.60(5)\times10^{-7}$
NE filament	$1.38(2)\times10^{-16}$	2.17×10^{49}	$2.92(3)\times10^{-7}$
Total	$2.941(2)\times10^{-14}$	3.12×10^{51}	$5.224(4)\times10^{-5}$
Hβ			
Equatorial ring	$4.42(5)\times10^{-16}$	4.99×10^{49}	$1.43(1)\times10^{-6}$
[OIII]			
SW filament	$1.47(1)\times10^{-16}$	5.72×10^{49}	
NE filament	$8.97(9)\times10^{-17}$	4.11×10^{49}	
Total	$2.37(1)\times10^{-16}$	9.83×10^{49}	

its expected energy according to:

$$4\pi d^2 F_{\rm obs} = \epsilon(\mathrm{j,i}|n_{\rm e}, T_{\rm e})\, n_{\rm e}\, n_{\rm p}\, V_{\rm shell}, \tag{3.5}$$

where d corresponds to the distance to the system, $F_{\rm obs}$ to the observed flux and $\epsilon(j,i|n_{\rm e},T_{\rm e})$ to the recombination emissivity for the hydrogen transition $j \rightarrow i$ given certain values of $n_{\rm e}$ and $T_{\rm e}$. For simplicity, a filling factor $\epsilon = 1$ has been assumed. An array of values for $T_{\rm e}$ ranging from 500 to 10 000 K in steps of 500 K was defined, for which for each value of $T_{\rm e}$ its corresponding value of $n_{\rm e}$ that best matches Eq. 3.5 was obtained. The PyNeb Python package (Luridiana et al., 2015) was implemented to determine the values of $\epsilon(j,i|n_{\rm e},T_{\rm e})$. These values correspond to the values published by Storey & Hummer (1995). The volume of the shell can be directly determined from the volume that each svoxel occupies in the physical space. Once the best value for $n_{\rm e}$ has been determined, the mass of the shell can be obtained using Eq. 3.4. The shell masses computed as a function of $T_{\rm e}$ are presented in Fig. 3.10, while the masses for an electron temperature of 5000 K, a representative value for the $T_{\rm e}$ in nova shells (e.g. Sahman et al., 2018; Tappert et al., 2023), are presented in Table 3.3.

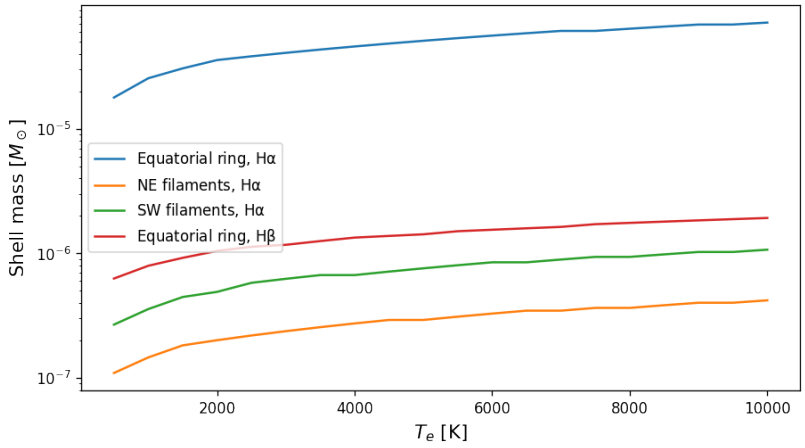

Figure 3.10: Shell masses as a function of electron temperature. The masses were determined by comparing the observed flux against theoretical values given a fixed electron temperature.

3.3 Discussion

Historically, the study of nova shells in the optical wavelengths has been limited to the use of narrow-band images and long-slit spectroscopy, either technique on its own or a combination of the two. There are very few works in the literature that carried out IFS observations, these concerning the nova shells around V723 Cassiopeiae (Lyke & Campbell, 2009), HR Delphinus (Moraes & Diaz, 2009), the Helium nova V445 Puppis (Macfarlane et al., 2014), V5668 Sagittarius (Takeda et al., 2022), and QU Vulpecula (Santamaría et al., 2022a). In these works, the capabilities of the IFS observations have been used to study the spatio-kinematics, chemical composition, and morphology characteristics of these nova shells. This work goes in the same direction, being the first one using MUSE data for the analysis of a nova shell.

3.3.1 Shell expansion

In the present study, to develop a 3D view of the shell around RR Pic, it was assumed that it is expanding radially from the central star. This assumption is supported by the comparison between the MUSE Hα image and the one published by Gill & O'Brien (1998), in which several knots of material were identified in both images, being consistent with a radial, uniform expansion of the ejected material. To our knowledge, there is currently no model for a non-radial expansion. One could, in principle, think that such non-radial expansion could be produced by strong magnetic fields and/or interaction with the secondary star, but to date, no evidence for such an expanding

shell has been reported. On the other hand, the assumption of radial expansion is supported by multi-epoch observations of several nova shells (e.g. Liimets et al., 2012; Harvey et al., 2016; Santamaría et al., 2020).

The assumption of a uniform, radially expanding shell was used by Takeda et al. (2022) to create a 3D view of the young shell around the system V5668 Sgr. When compared with our approach, the main difference is that we have left open the possibility of including different models for the expansion velocity history of the material, instead of the free expansion only. This, in principle, is useful for older shells where deceleration of the expanding material is expected to occur. Our test case, RR Pic, is one of the oldest novae recorded, so it was expected from our side to find some signals of deceleration within the shell.

The overall geometry of the RR Pic nova shell, previously reported as consisting of an equatorial ring around the system and polar filaments leaving the system in an orthogonal direction to the ring, is preserved, as can be seen in the MUSE Hα image (Fig. 3.2). From the measurements of the radial distance of the several knots identified in the image, in both MUSE and Gill & O'Brien (1998) images, we found that the shell is consistent with a still free-expanding phase (Fig. 3.4). It has been proposed that nova shells start to show signals of deceleration decades after the nova eruption, decreasing their initial expansion velocity by half after $\sim$ 75 (Duerbeck, 1987b). However, recent studies have contradicted this idea (Liimets et al., 2012; Santamaría et al., 2020). In particular, the recent studies on the nova shells around T Aur ($\sim$ 125 yr) and V476 Cyg ($\sim$ 100 yr) reveal that these shells are still expanding free (Santamaría et al., 2020), which together with the results on RR Pic ($\sim$ 96 yr), indicates that nova shells can expand freely for more than a century after the nova eruption.

3.3.2 Interaction with the ISM

In the study of supernova remnants, it is expected that the deceleration occurs when the material swept up by the expanding shell has a similar mass to the initially ejected one, the moment at which the expanding shell will enter a new phase called the Sedov-Taylor phase (Reynolds, 2008). By applying the same principle to nova shells, it could be possible to estimate the time required for the shell to reach this phase. From the mass estimated in Sect. 3.2.3 we conclude that most of the mass of the shell is confined to the equatorial ring. Using the mass estimated at T_e = 5000 K corresponding to $\sim 5 \times 10^{-5}$ $M_\odot$, and the opening angle of the ring of $\sim$ 30 deg, we can compute

the mass drag by the equatorial ring, assuming an ISM with homogeneous density. As RR Pic is relatively close to the Sun ($\sim$ 500 pc), for the density value of the ISM, we use a value representative of the local interstellar medium, $n_{\rm H} = 0.1$ cm^{-3} (Frisch et al., 2011). Assuming a spherical geometry corrected by the opening angle of the expanding equatorial ring, and a uniform expansion velocity of 370 km s^{-1}, the time required to drag a mass equivalent to the measured mass of the ring will be approximately $\sim$ 650 yr. If we increase (decrease) the ISM density by one order of magnitude, the time required would decrease (increase) up to a value of $\sim$ 300 ($\sim$ 1400) yr. These numbers indicate that the equatorial ring will last centuries expanding freely before reaching the Sedov-Taylor phase and starting to show signals of deceleration. This potentially has significant consequences for the determination of ages of the shells of unrecorded nova eruptions (see for example, Shara et al., 2017b; Santamaría et al., 2020).

The situation may be very different for the case of the polar filaments, as they present much lower masses than the equatorial ring. While these lower masses of the knots can be compensated with a smaller dragged volume, preventing an earlier deceleration compared to the equatorial ring, other possible interactions may take place. As the knot advances through a less dense medium, some processes like Rayleigh–Taylor instabilities could start to play a role in the evolution of the knot. It is unlikely that these instabilities will be able to change the direction of the advancing knot, but they could affect the knot's surface and its surface brightness, and perhaps being the cause behind the apparent acceleration observed in the NE filaments knots between the GO98 and MUSE images (Sect. 3.1.2).

To test this hypothesis, we checked the available data of the Wide-Field Infrared Explorer Survey, WISE (Wright et al., 2010). The WISE filter at 12 µm (WISE band 3) is sensitive to poly-aromatic hydrocarbures, ubiquitous tracer of the ISM material, while the WISE filter at 22 µm (WISE band 4) is sensitive to small and large dust grain particles. The normalised intensity map of the WISE bands 3 and 4 for a region of 80 arcsec size centred at the position of RR Pic is presented in Fig. 3.11, with the Hα MUSE image overimposed with blue contours. The data show that in the WISE band 3, there is a zone of higher intensity in the NE direction of the shell with respect to the intensities observed in the SW direction. This could indicate that the NE filament of the shell is entering a zone where the ISM has a relatively higher density. The WISE band 4, on the other hand, presents a difference in the intensity observed in the NE-SW (polar filament) axis with respect to the SE-NW (equatorial ring) direction. The intensity in the

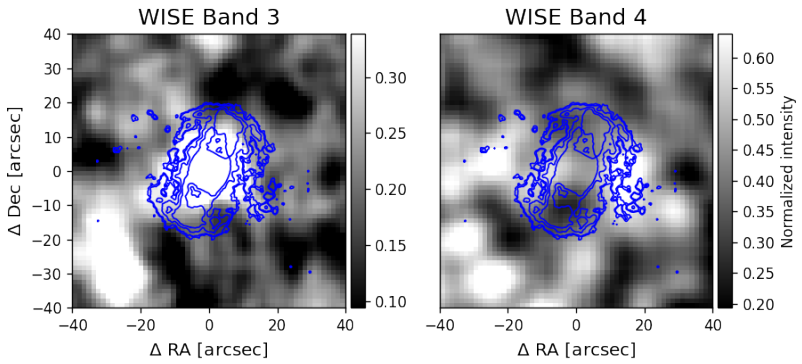

Figure 3.11: Normalised intensity maps of WISE bands 3 and 4 around the position of RR Pic. The nova shell observed with MUSE is presented with blue contours.

axis of the polar filament appears to be higher than the intensity across the equatorial ring, suggesting a higher amount of dust in the ISM in the direction of the expanding filaments. We must note however that in spite of the seductive coincidence observed between the equatorial ring and polar filaments observed in the WISE band 4 image, we do not have a way to estimate the distance to the features in the WISE images, and therefore, we cannot confirm whether the aforementioned possibilities are real or just the result of a projection effect.

Additional evidence for interaction between the nova shell and the ISM could come in the form of shock waves, which should increase the luminosity of the shell in X-rays and radio wavelengths (Chomiuk et al., 2021, and references there in). *Chandra* observations of the RR Pic's nova shell showed an extended X-ray emission source which follows the equatorial ring, indicating a shock between the ring and the surrounding ISM (Balman, 2006). The cloudy structures observed in the equatorial ring (Fig. 3.9) could find their origin as the result of the aforementioned interaction. No X-ray detection regarding the polar filaments has been reported.

3.3.3 Nova shell geometry

Our results indicate that the equatorial and polar materials are expanding at different velocities, with the polar filaments expanding faster. This is consistent with the idea of two-phase ejections proposed by Aydi et al. (2020), where the material in the poles of the CV leaves the system faster, as there is less material in this direction to oppose

the ejected material. The apparent chemical composition of these two regions is also different, with the equatorial ring traced by hydrogen mainly, and the polar filaments by hydrogen and [OIII] (Fig. 3.1). Weak traces of [NII] can also be observed in the NE polar filaments. These differences between the ring and filaments could be due to differences in abundances, but also to differences in the densities and temperatures of these environments. This latter scenario would imply a denser equatorial ring, which is in agreement with results provided by hydrodynamical simulations (Booth et al., 2016). What was previously unnoticed is that the NE filaments are apparently expanding faster than the SW filaments by a non-negligible factor ($\sim$ 40% faster). As we could not find strong evidence for interaction between these filaments and the surrounding ISM, we must consider the possibility that the observed differences in expansion velocity must come from the nova explosion itself. The observed asymmetry in the expansion velocity could be explained then by a difference in the ejected mass, a difference between the energy of the nova eruption on the poles of the WD, or a combination of both.

From our mass estimation, we can observe that there is a difference ratio of $\sim$ 2.5 between the SW and NE filament masses. This ratio is similar to the differences in the observed fluxes (Table 3.3). It is worth noting that the NE filament corresponds to the receding filament, and therefore its lower flux with respect to the SW filaments could be explained by self-absorption of the shell caused by the formation of grain dust (Shore et al., 2018). This idea has been proposed as a solution to explain the observed asymmetry in flux between blue and red peaks in the spectra of young, dusty classical novae. While a certain amount of self-absorption is possible within the system, it is very unlikely that this could explain the observed difference in flux between the NE and SW filaments, as the shell has expanded considerably, departing from the scenario proposed in Shore et al. (2018). Furthermore, the light curve of RR Pic did not show evidence for dust formation (Strope et al., 2010). Therefore, we can conclude that the differences in flux must be intrinsic to the filaments. We can compare the kinetic energy of both filaments by using the expansion velocities determined at the end of Sect. 3.1.3. This leads to kinetic energies of the order of $\sim 1.7 \times 10^{42}$ erg for the SW and $\sim 1.0 \times 10^{42}$ erg for the NE filament, giving a ratio between the SW and NE of 1.7. The observed differences in fluxes, masses and kinetic energies suggest an intrinsic origin for the observed asymmetry, the genesis for which could be found in the nova eruption itself. While the origin of such asymmetries is unclear, it has been hypothesised that they may be an important factor in the long-term evolution of CVs (Nelemans et al.,

2016; Schaefer et al., 2019).

From our 3D model, we can observe in Fig. 3.9 that the allowed and forbidden transitions trace different regions of the shell, with hydrogen tracing the equator and the polar regions of the system, while oxygen follows the tropical latitudes where a gap in hydrogen emission is observed. We noticed that the distribution of both emitters is best fitted in the ρ-Z plane by different ellipses, with the hydrogen being best fitted by a prolate ellipse with an axial ratio of 1.35(2), and the oxygen by a prolate ellipse with an axial ratio of 0.92(3). The morphology of nova shells correlates with their expansion speed, being more spherical for faster shells (Santamaría et al., 2022b). RR Pic was considered a slow nova, with expansion velocities of the order of 400 $\mathrm{km\,s^{-1}}$ and a t_3 of 122 days, the reason why we would expect the shell to have a prolate shape, which was confirmed by the Hα emission. However, the axial ratio differs when we use the data from the projected image (Fig. 3.1) or those from the 3D reconstruction (Fig. 3.9). In the first case, we can determine the axial ratio from the polar and equatorial radial extension (Fig. 3.4), which leads to an axial ratio of 1.445(2), while when we measured through the fit of the 3D data, we obtain a lower value of 1.35(3). Differences in the geometry derived from image and IFS have been reported before (Santamaría et al., 2022a), which highlights the importance and advantage of using IFS data. In the case of [OIII], the best fit suggests an oblate shape with an axial ratio smaller than one. Because the oxygen material is confined to the tropical latitudes of the shell only, the fit does not have any constraints in the equatorial region. As a consequence, it favours an oblate shape due to the aperture angle observed in the [OIII] emission.

3.3.4 CV properties from the nova shell

The 3D data also allow us to find the circular ring that best fits the geometry of the equatorial ring around the system, from which we could determine its inclination to be 73.6$\pm$0.3 deg. Assuming a coplanar geometry, we can extrapolate this result to the inclination of the system itself. The light curve of RR Pic shows an orbital hump of variable amplitude, and possibly also shallow eclipses, with the latter being dependent on the structure of the accretion disc (Schmidtobreick et al., 2008; Fuentes-Morales et al., 2018). This suggests that the inclination of the system must be at an intermediate angle that allows for shallow eclipses only at certain states of the accretion disc. Sion et al. (2017) used Far Ultraviolet Spectroscopic Explorer (FUSE) data to

estimate an inclination of 60 degrees for the accretion disc and a mass of 1 $M_\odot$ for the WD. These physical parameters were obtained by fitting the observed continuum of the disc and, as pointed out by the authors, would be different when fitting instead the absorption lines in the spectrum. This indicates that there is still room for improvement of the disc model implemented by the authors, which could be the reason behind the discrepancy between their and our value for the system inclination.

Another possibility is that the inclination of the shell and the inclination of the disc are actually different. However, a coplanar geometry between the orbital plane and the equatorial outflow is supported by hydrodynamical simulations of the ejected material around the symbiotic system RS Oph (Booth et al., 2016). If this were the case also in RR Pic, then a tilted disc would be required to explain the differences in inclination regarding the equatorial ring and the accretion disc. A tilted disc has been indicated to be the cause for negative superhumps, which correspond to periodic modulations of the CV light curves with a period shorter than the orbital, and have been observed in classical novae and nova-like systems (see for example Fuentes-Morales et al., 2018; Iłkiewicz et al., 2021). However, no negative superhumps have been reported on RR Pic (Fuentes-Morales et al., 2018), which argues against the possibility of a tilted disc within the system. For the mentioned reasons, we concluded that the inclination of the system should be closer to our result of ~ 70 degrees.

The 3D view of the data shows the equatorial ring in RR Pic nova shell to be composed of a continuous ring where most of the emission comes from, but also of several cloudy structures above and below the main ring, which extends to a height of $\pm 4\,000$ au, in a configuration that is reminiscent of a bow shock (Fig. 3.9, left panel). The origin of these clouds could be intrinsic to the nova eruption or the result of the interaction between the expanding material and the static ISM. In the first scenario, it is expected that the same structures are present in the image published by Gill & O'Brien (1998). Although the quality of the published image makes it difficult to appreciate the details of these clouds, it appears that some structures in the northern part of the shell have persisted throughout the years, with no significant change to their appearance, supporting an intrinsic formation scenario. According to the simulations of Porter et al. (1998), tropical rings could be formed in the shell, whose height with respect to the orbital plane depends on the WD rotation. Such tropical rings could present a potential place of origin for the observed clouds.

From Porter et al. (1998), the rotational velocity at the surface of the WD v_ϕ is given by:

Table 3.4: Tropical rings opening angle θ as a function of the factor $f(R_{\rm WD}, \pi/2)$. Extracted from Figure 1 of Porter et al. (1998).

θ [deg]	$f(R_{\rm WD}, \pi/2)$
25	0.0
37	0.5
77	0.7

$$v_{\text{Œ}} = f(R_{\rm WD}, \pi/2)\sqrt{\frac{GM_{\rm WD}}{R_{\rm WD}}} \tag{3.6}$$

where $M_{\rm WD}$ and $R_{\rm WD}$ are the mass and radius of the WD, respectively. The dimensionless factor $f(R_{\rm WD}, \pi/2)$ corresponds to the ratio between the WD rotation period and the Keplerian rotation period of a particle at the radius of the WD and can be related to the height of the tropical rings. While Porter et al. (1998) did not provide values of $f(R_{\rm WD}, \pi/2)$ as a function of the tropical rings opening angle θ, some information can be extracted from their Fig. 1. The extracted angles θ and their respective value for $f(R_{\rm WD}, \pi/2)$ are presented in Table 3.4.

Using the opening angle of 30 deg for the cloudy structures (Sect. 3.2.3) and by linear interpolating the data provided in Table 3.4, we obtain a value for $f(R_{\rm WD}, \pi/2)$ of 0.21. With a WD mass of 1 $M_\odot$ (Sion et al., 2017) and a WD radius of 0.008 $R_\odot$ that results from the theoretical mass-radius relation for WDs from (Fontaine et al., 2001), v_ϕ then results in 1 025 km s^{-1}, which translates into a spin period for the WD of 31 seconds. In most non-magnetic CVs, the reported value for the WD $v \sin(i)$ is below 400 km s^{-1} (Sion, 1999), while for RR Pic, our estimate would result in $\sim$ 980 km s^{-1}. This would place RR Pic in a row with intermediate polar systems like WZ Sge and CTCV J2056-3014, which possess spin periods of 28 s and 29 s, respectively (Lasota et al., 1999; Lopes de Oliveira et al., 2020).

3.3.5 Possible evolution of the nova shell

Understanding how the nova shells evolve is key to fully comprehending the origin of the ancient nova shells and their implications for the CV evolution. The luminosity evolution of nova shells in Hα and [OIII] as a function of the time since nova eruption was studied by Downes et al. (2001) and Tappert et al. (2020), with the latter using the light curve classification used in the work of Strope et al. (2010). RR Pic was classified

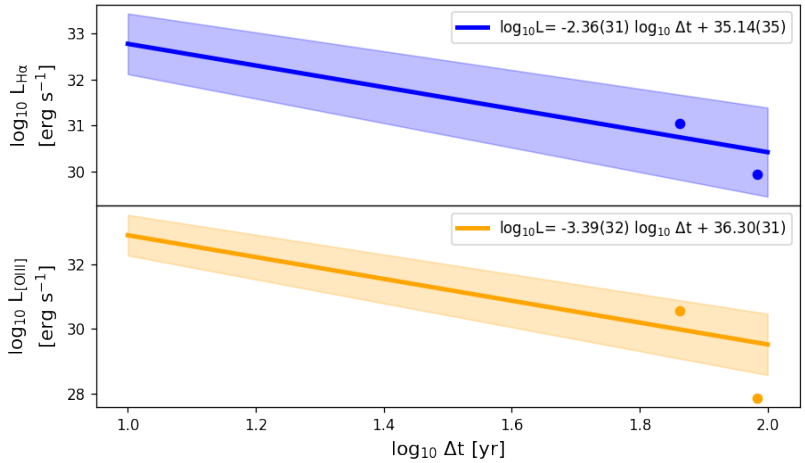

Figure 3.12: Expected Hα (blue) and [OIII] (orange) luminosity evolution for RR Pic according to Tappert et al. (2020). The dots represent the measured flux for RR Pic by Downes et al. (2001) and this work. The Hα luminosity is consistent with the expected value given the uncertainties, while the [OIII] luminosity appears to be fainter than expected.

as a member of the jitter (J) subgroup. The expected evolution for this group in the $\log L - \log \Delta t$ diagram is presented in Fig. 3.12, together with the luminosity reported in Downes et al. (2001) ($\Delta t \sim 74$ yrs) and from the MUSE data ($\Delta t \sim 96$ yrs).

The luminosity from MUSE in Hα is consistent with the expected decline within the given uncertainties, but the [OIII] luminosity appears to be fainter when compared to the expected value. From their Fig.3, it is clear that the fit proposed by Tappert et al. (2020) is dominated by the nova with the largest number of points (HR Del), while at least one other system in this group, PW Vul, appears to follow a steeper decline. It is therefore feasible that RR Pic follows a decline in [OIII] similar to PW Vul rather than the one followed by HR Del. Furthermore, Tappert et al. (2020) suggest that at the late stage of their evolution, nova shells reach an 'ancient nova valley', a region where the luminosity of ancient shells appears to maintain a constant value regarding the time since their eruption. It is not clear, however, whether or not all shells reach this stage, and if they do, at what time after the nova eruption. Future observations of RR Pic's nova shell during the next decades will help to answer these questions.

Focusing on the Hα flux, most of it is concentrated on the equatorial ring and just a minor fraction in the polar filaments. It is very likely then that in the future the filaments will disperse sooner than the ring, ending with a very similar geometry to the ancient shells of AT Cnc (Shara et al., 2017b) and IPHASX J210204.7+471015 (Guerrero et al., 2018; Santamaría et al., 2019). These ancient shells present incomplete ring

structures that have fragmented into several blobs of material, with both of them being dominated by forbidden transitions of [OIII] and [NII]. It is certainly possible that the equatorial ring currently observed in RR Pic evolves into a geometry similar to the ancient shells mentioned above. As the ring expands and interacts with the ISM, it should start to fragment while its density decreases, causing the ring to start transitioning towards being dominated by forbidden transitions. The ages of AT Cnc and IPHASX J210204.7+471015 are estimated to be 200 yr old and $\sim$ 170 yr old, respectively. Assuming the proposed evolution scenario for the equatorial ring of RR Pic is correct, then such a transition should happen within the next century.

3.4 Conclusions

This is the first work in which a nova shell has been studied using data from the MUSE instrument from Paranal, ESO. The methodology used to extract the 3D geometry of the nova shell from the datacube has been presented, including its analysis in the PPV and PPP spaces. As a test case for this kind of analysis, the observations of the classical nova RR Pictoris (Nova Pic 1925) and its expanding shell have been presented. The nova shell around the binary system was observed in the Hα and Hβ lines, as well as in the [OIII] λ 492.1 and λ 500.7 nm lines, and very faintly in the [NII] λ 658.4 nm line. The overall structure observed by Gill & O'Brien (1998) in their Hα narrow-band image, consisting of an equatorial ring and polar filaments, is still preserved. From a comparison with those previous observations, it can be concluded that the shell is likely to continue in its free-expansion phase. The expansion rates of the equatorial ring and the polar filaments differ, with the former expanding at a rate of 0.154(1) arcsec yr^{-1}, and the filaments expanding significantly faster. The rate at which the polar filaments expand varies for the NE and SW filaments, with the NE filaments expanding at 0.26(1) arcsec yr^{-1} and the SW filaments expanding at 0.199(5) arcsec yr^{-1}.

The observed spectrum shows that the equatorial ring is dominated by Balmer emission, while the polar filaments are observed mainly in the [OIII] lines, and only to a lesser extent in Balmer lines. The total Hα flux measured in the polar filaments corresponds to $\sim$ 1% of the equatorial ring's flux. The flux of the polar filaments is not equal, with the SW filaments being $\sim$ 2.5 and $\sim$ 1.7 times brighter than the NE filament for the lines of Hα and [OIII] λ 500.7 nm, respectively. From the total measured Hα flux, a mass of the shell of $\sim 5 \times 10^{-5}$ M$_\odot$ was estimated.

The extracted 3D view of the data allows for a better constraint of the geometry of the nova shell, in particular concerning its equatorial ring. A circular ring geometry was assumed to determine the radial extension, inclination, and position angle of the equatorial ring. The results indicate a ring with a radius of $\sim$ 8 000 au tracing the inner and denser parts of it, but extending between $\sim$ 6 000 and $\sim$ 10 000 au when considering the fainter regions of the ring. Its inclination and position angle are well constrained to $\sim$ 74 and $\sim$ 155 deg, respectively. We argue that the inclination value for the ring corresponds to the inclination of the binary.

The mean radial profile of the equatorial ring shows a shape that is reminiscent of a bow shock, with clouds of material extending up and below the equatorial ring, with a height of $\sim$ 4 000 au. The polar filaments extend asymmetrically, with the northern one extending further at a maximum distance of $\sim$ 15 000 au. The overall 3D structure of the shell observed in Hα is well fitted by an ellipsoid with an axial ratio of 1.34(3), with the semi-major axis following the polar axis. The Hα and [OIII] emissions trace different regions within the shell, with the latter tracing the gap between the equatorial ring and the polar material. This indicates a difference in density across the shell related to its polar angle.

Exploring the possibility that the nova shell is experiencing an interaction with the surrounding ISM, we have analysed the WISE public data in the search for evidence supporting this idea, but we find the results to be inconclusive. Theorising the origin of the observed cloudy material within the equatorial ring, we have explored the possibility that they correspond to the tropical rings predicted by the hydrodynamical simulations of Porter et al. (1998). Based on that assumption, we have estimated the spin period of the WD to be $\sim$ 31 s.

Lastly, we have speculated about the future of the nova shell around RR Pic. We compared the current observed luminosity with the expected values according to the luminosity evolution proposed by Tappert et al. (2020). The result is consistent for the Hα luminosity, but the decline observed in the [OIII] is steeper than expected. As the RR Pic's nova shell continues to evolve, we conjecture that the filaments will disperse into the ISM, leaving only the equatorial ring in a geometry that is similar to that currently observed in some ancient nova shells.

This work has shown the advantages of using IFS in the study of nova shells, while also pointing to the interesting features observed in the nova shell around RR Pic. Many of the results and ideas presented in this work can be tested with further and repeated observations of the shell.

Chapter 4

MUSE observations of V1425 Aql reveal an arc-shaped nova shell

A nova shell that challenges the current understanding of the processes that shape the nova shells is the one observed around V1425 Aql. It has at least two different components: an inner, symmetric shell and an outer, asymmetric shell, with the latter expanding faster than the former. The physical reason for the asymmetric ejecta is not clear. In this work, we aim to characterise the properties of and differences between these two components to understand the origin of the unusual shape. This is the continuation of the work carried out in Tappert et al. (2023), where this unusual shell was characterised using NB photometry and LSS spectroscopy. We acquired MUSE data to study the spatial position and kinematics of the expanding gas across the shell. Our analysis involved channel maps, position-velocity diagrams, and the reconstruction of the 3D geometry of the nova shell. Several emission lines are detected within the MUSE wavelength coverage, including but not limited to Balmer, oxygen, nitrogen, and helium lines. There are significant differences in the spectra of the inner and outer shells, with the latter being observed only in forbidden transitions, and the former in a mix of forbidden and allowed ones. Our analysis reveals that the outer shell has a geometry consistent with an arc-shaped structure that partially encircles the more spherical inner shell. Within the inner shell, clumpy structures start to be noticeable in the lines of Hα+[NII]. We have constrained the geometry of the outer shell to an arc-

shaped structure, although the physical reason for its origin still eludes us. Further monitoring of the evolution of both shells of this object might help clarify the mechanism behind this unusual configuration. This chapter corresponds to a published paper in the Astronomy & Astrophysics Journal (Bibcode: 2025A&A...694A.238C).

4.1 Data analysis

4.1.1 A general view of the shell

An overall view of the system is presented in Fig. 4.1, where a bandpass image corresponding to the Sloan Digital Sky Survey i-filter (i_SDSS, Doi et al., 2010) was created from the MUSE datacube using the available transmission for the GMOS-S telescope in the Spanish Virtual Observatory[1]. The contribution of the expanding shell in this filter is minimal if any, and therefore this emission defines the position of the binary. This is located at the centre of the field and is found to be within a relatively crowded field. Two stars in the field are very close to the position of the binary, at ~ 2 and ~ 3 arcsecs, so that their projected positions overlap with the expanding ejecta (red and blue contours). From the bandpass image, we determined the i_SDSS magnitude of V1425 Aql to be 20.5±0.1 mag.

To show the extension of the inner shell, we plot the contour levels at the rest wavelength of Hα after subtracting the flux of the continuum between 6620 and 6640 Å. The contour levels are defined as 0.1, 0.25, 0.5, and 0.75 times the maximum of the observed flux in the continuum-subtracted image. The projected geometry of the inner shell in the plane of the sky can be observed to be fairly circular, with a radius of ~ 2 arcsec. The flux increases towards the centre of the shell, where clumpy material starts to appear as a region of higher flux in the eastern part of the shell.

The extension of the outer shell is shown by the emission of [OIII] at 5007 Å with blue contours. Similar to the Hα contours, these were obtained after subtracting the continuum corresponding to the wavelength range between 5040 and 5050 Å, and the levels indicate 0.25, 0.5 and 0.75 times the maximum flux. To reduce the noise level in the contours, the [OIII] image was binned by a factor of two before drawing the contours. The region of strongest [OIII] emission is located in the south-west and appears to be composed of two smaller lobes. If we define the centre of emission as the middle point between these two smaller lobes, then it is located 2.84 ± 0.14 arcsec

[1] http://svo2.cab.inta-csic.es/theory/fps

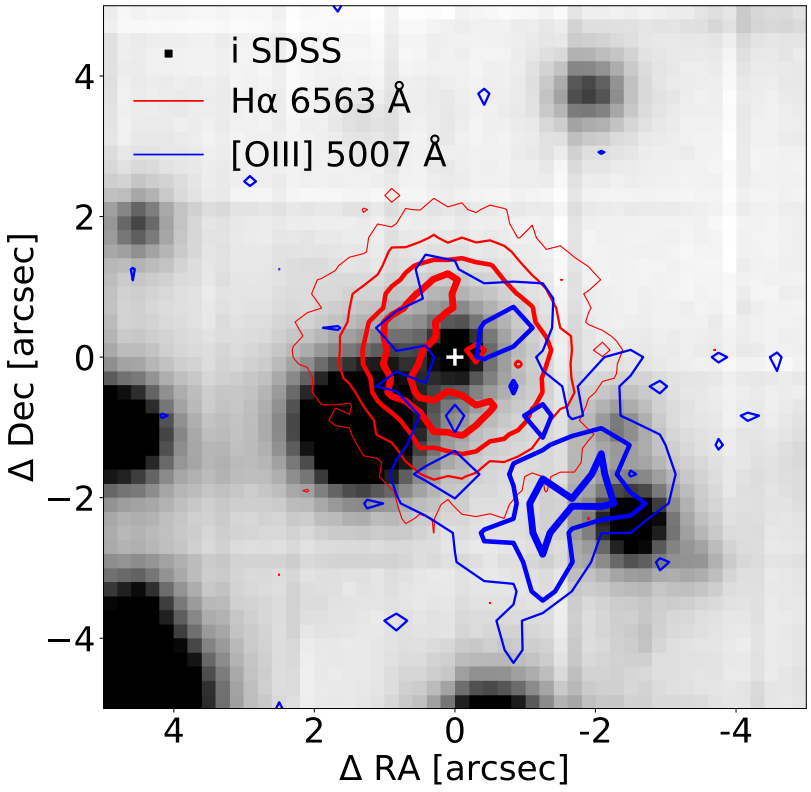

Figure 4.1: Bandpass image of 10×10 arcsec^2 centred at the position of V1425 Aql, showing the extension of the nova shell. The grey image corresponds to an i_SDSS image, and the contours show the extension of the inner and outer shell as seen at the Hα (red) and [OIII] λ 5007 Å (blue) wavelengths, respectively, with thicker lines denoting regions with higher emissivity. Both the image and the contours were obtained from the MUSE datacube. The difference in spatial extension between the two shells is evident, as is the asymmetry observed in the outer shell.

from the position of the binary, with the uncertainty indicating one-pixel uncertainty in the position.

We can compare this value with the previous measurements from Tappert et al. (2023). From the GMOS LSS data, the extension of the outer shell is 2.33 ± 0.08 arcsec, while from the GMOS NB image, the extension of the brightest region in the outer shell is 1.91 ± 0.10 arcsec. Both values are lower than our measurement from the MUSE data. In the case of the LSS measurement, the discrepancy can be explained by the fact that the angle of the used slit did not perfectly coincide with the angle of the outer shell. In the case of the NB image, the difference occurs because the contours are tracing only the material that is expanding orthogonally to us, while the GMOS NB image includes the blue and red components of the ejecta. This causes the brightest region in the GMOS NB image to be shifted closer to the binary.

In fact, if we compare the GMOS NB images from Tappert et al. (2023) with band-pass images from MUSE that mimic the GMOS NB images, we observe there are no major differences between them (Fig. 4.2). The figure shows the MUSE NB images for Hα and [OIII] $\lambda\,5007\,$Å in grey, with contour levels indicating the extension of both shells for the MUSE (red) and GMOS (cyan) data. The images were normalised in flux, with the total normalised flux in right ascension and declination presented at the top and right of the images. The levels correspond to 0.1, 0.5, and 0.8 times the maximum normalised flux value in the case of Hα, and 0.4, 0.6, and 0.8 times in the case of the [OIII] images. The [OIII] images were binned by a factor of two before drawing the contour levels to reduce the noise. The GMOS and MUSE data for the Hα images behave identically, with no significant differences. There are minor differences in the case of the [OIII] line, particularly in the region of the highest emission, which in the GMOS data appears slightly farther south than in the MUSE data. We attribute this spatial difference to the lower S/N in the GMOS data and we do not consider it to be significant. From the MUSE data, we determined the position of the highest emission observed in the [OIII] NB image to be located at 2.0 ± 0.2 arcsec and at an angle of 222 ± 6 degrees with respect to the centroid of the emission observed in Hα, in good agreement with the values derived in Tappert et al. (2023).

4.1.2 Channel maps

The MUSE capabilities allow us to observe the behaviour of the nebular structure in the inner and outer shell as a function of the velocity of the material. This can be seen

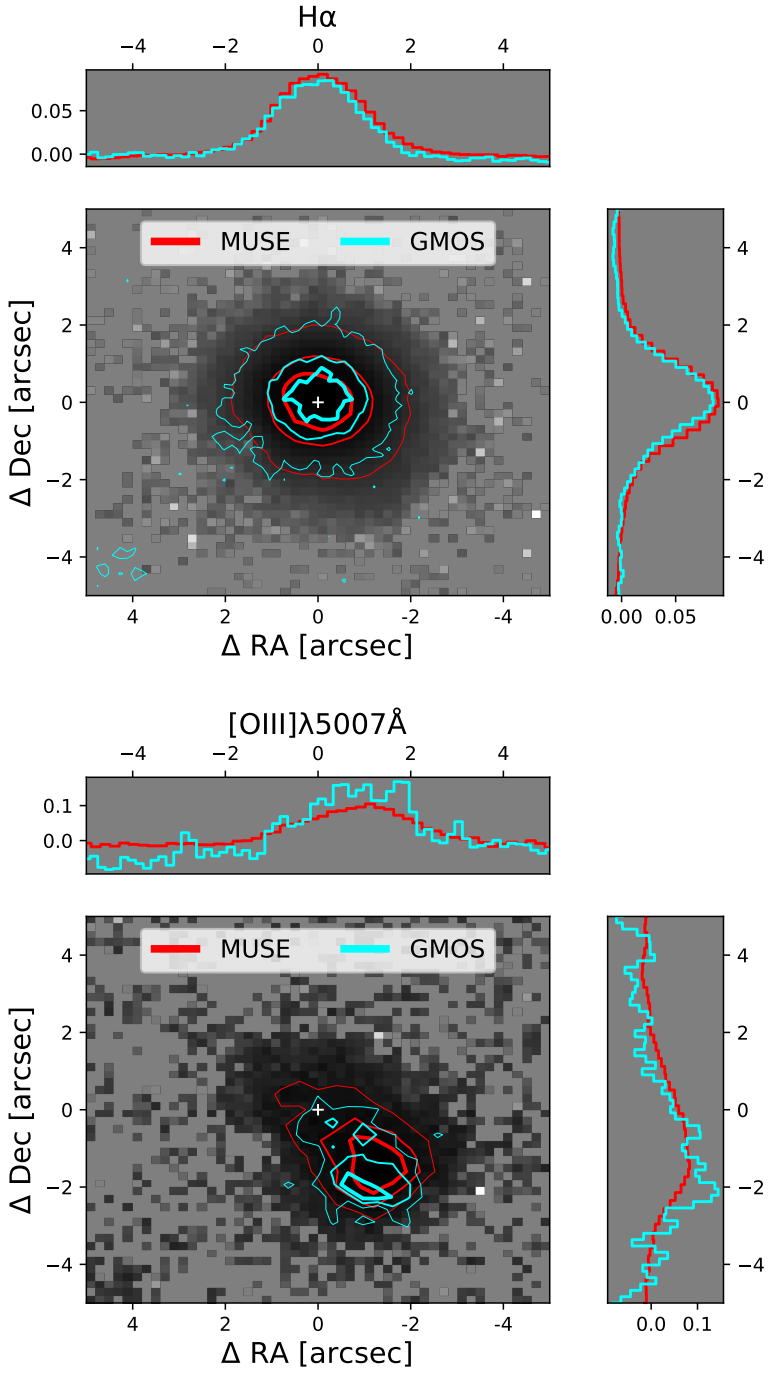

Figure 4.2: Comparison between the GMOS NB images presented in Tappert et al. (2023) and MUSE data for Hα (top) and [OIII] λ 5007 Å (bottom). The MUSE images (grey background) were obtained by mimicking the bandpass used in the GMOS images. The contour levels indicate the same normalised fluxes for MUSE (red) and GMOS (cyan), and the white cross marks the position of the binary. The contours presented in Hα indicate no major differences between GMOS and MUSE, while [OIII] shows differences in the location of the brightest region within the outer shell, although they can be attributed to the noise in the GMOS data.

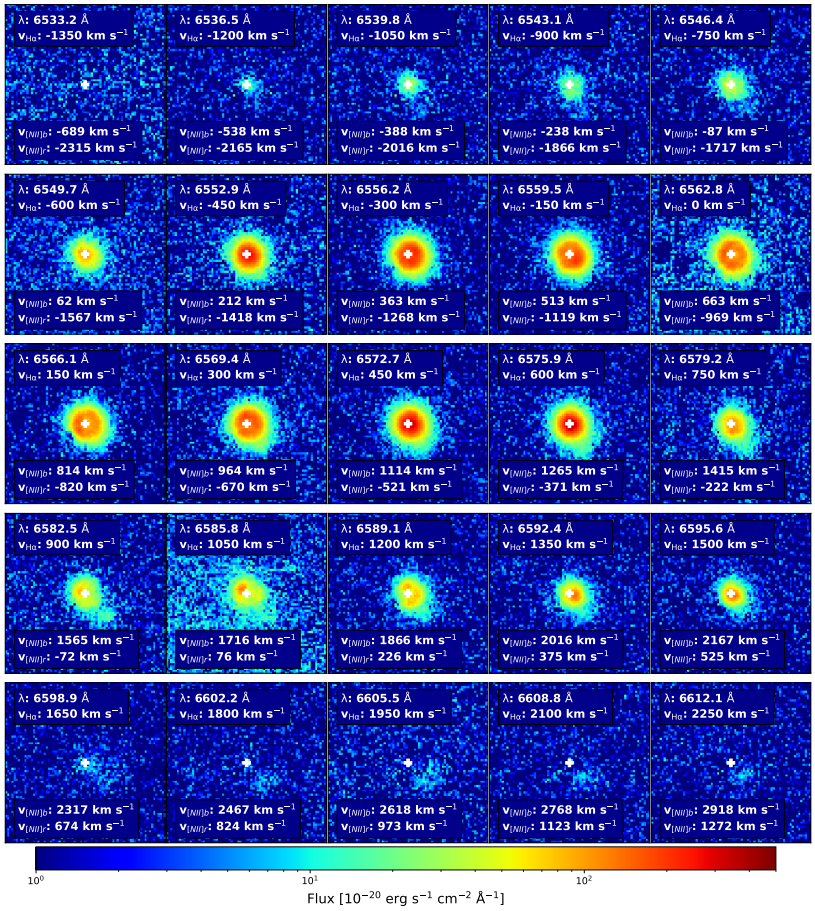

Figure 4.3: Channel maps of V1425 Aql for the lines of Hα+[NII] λ 6584 Å. Each channel map shows a region of 15 $\times$ 15 arcsec^2. In all cases, the fluxes are presented in linear scales, with their ranges defined in the colour bars and the position of the binary marked with a white cross.

in the channel maps of the lines of Hα and [NII] λ 6584 Å, (Fig. 4.3), and the [OIII] λ 5007 Å line (Fig. 4.4). They show the observed emission at a given wavelength after performing a continuum subtraction.

The inner shell traced by the Hα+[NII] emission shows a general symmetric distribution around the binary that also includes several regions of clumpy material that are distributed non-homogeneously across it. At velocities close to the Hα rest wavelength, a ring-like structure can be discerned, which, however, becomes disrupted both at redder and bluer velocities. Instead, regions of higher emission appear within the shell without a clear preferential axis or defined structure. Additional clumpiness, likely related to [NII] λ 6584 Å rather than Hα, can be observed at longer wavelengths. Some of these clumps appear to have a preferential axis that coincides with the axis of

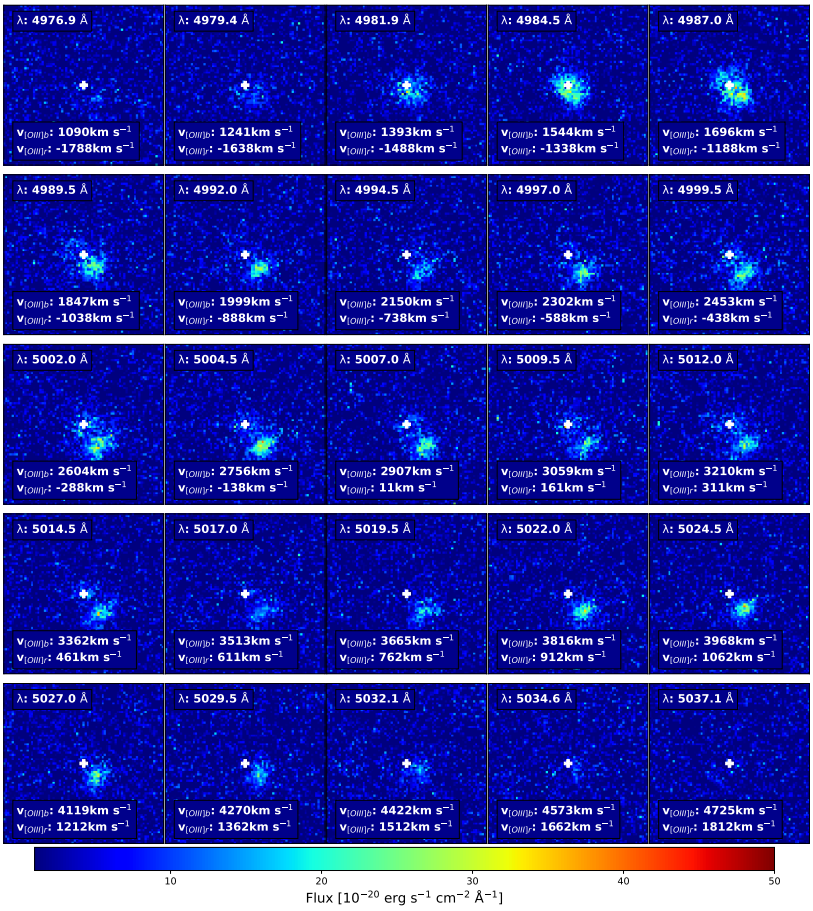

Figure 4.4: Same as Fig. 4.3 but for the [OIII] λ 5007 Å instead.

the outer ejecta (north-east to south-west), although the quality of the data does not allow us to claim this with confidence.

The outer shell is traced mainly by the line of [OIII] λ 5007 Å, but it is also possible to detect a faint tail associated with it in the [NII] λ 6584 Å line. The spatial position of the [OIII] emission strongly depends on its velocity, with the bluest and reddest parts being closer to the position of the binary, while its maximum extension occurs when its velocity is closer to zero. We also note that the flux observed at the position of the binary (white cross) lacks the flux of the red component, with only its blue component present. This behaviour is not consistent with a cone or plume structure and instead is more consistent with an arc-shaped structure that partially encloses the inner shell. Regarding the [NII] emission associated with the outer shell, this appears as a blob of material that shows signals of separation, with the main emission at the centre. The separation in question appears as a small region with a clear decrease in the observed flux. This confirms the idea that the inner and outer shells are in fact two different components.

4.1.3 Shell spectra

One of the advantages of MUSE is that we can select the spaxels within the datacube to maximise the signal from the different shells when extracting their spectrum, while also minimising unwanted contributions from other sources. We defined three different regions, each one chosen to maximise the contribution of the different components of the system (inner and outer shells, and the binary itself). We used the contour maps presented in Fig. 4.1 for the lines of Hα and [OIII] as a reference to define the extension of these regions. The spaxels inside each region were summed to create a spectrum that should be representative of the component in question, and they were smoothed by convolving them with a Gaussian profile with a full-width at half maximum (FWHM) of 3.75 Å (3 pixels) to reduce the noise.

The first region (region A) corresponds to a spectrum of the binary extracted using an aperture radius of 1.4 arcsec. We obtain this value by modelling the flux in the i_SDSS bandpass image using a Gaussian function from which we determined a $\sigma = 0.48$. The selected aperture corresponds to three times this value, therefore enclosing most of its flux. We must note that because the inner shell is also present in the line of sight of the binary, this will also include features from it. Lastly, we masked the nearby star in the south-east using a mask of 1 arcsec radius to avoid undesired

contamination. A total of 136 spaxels were used to extract this spectrum.

The second region (region B) was extracted considering the spaxels that are contained within the contour level corresponding to 0.1 times the maximum flux observed in Hα and outside the 1.4 arcsec aperture used in region A. As for the previous spectrum, we masked the contribution from the nearby star. As the stellar contribution of both the nearby star and the binary has been removed, this spectrum contains only emission from the inner shell but misses the emission from the ejecta in the line of sight. A total of 175 spaxels were selected.

The last region (region C), corresponding to the outer shell, was extracted from the spaxels within the 0.5 contour level observed in [OIII] and outside of the 0.1 contour level drawn from the Hα emission. The latter criterion was applied to minimise the contamination from the inner shell into the spectrum. In this case, a total of 49 spaxels meet our requirements.

The extracted spectra can be observed in Fig. 4.5, where the top panel shows the spectra across the full MUSE wavelength range, and the bottom panels show the differences between spectra for some emission lines. The spectrum corresponding to region A (orange) shows a bluer continuum compared with the other two spectra, which must come from the binary. It also shows several lines, the most prominent ones being the Balmer (Hα and Hβ) and [OIII] $\lambda\lambda$ 4959, 5007 Å lines, but also contributions from HeI λ 6678 Å and HeII λ 5411 Å, as well as nitrogen lines: [NI] $\lambda\lambda$ 5197, 5200 Å, [NII] λ 5755 Å, [NII] $\lambda\lambda$ 6548, 6584 Å, and NII λ 5679 Å. Compared with the spectra presented in Tappert et al. (2023), the MUSE data reach redder wavelengths, which allows us to detect the lines of [OII] λ 7320, 7330 Å and Paschen9 at 9229 Å. We also observe an emission feature at $\lambda \sim 8235$ Å that we were not able to identify. Its profile shape suggests a blend, with candidates being the lines of HeII λ 8237 Å, NI λ 8216, 8223 or 8242 Å, and [OI] λ 8222 Å. From here on, we refer to this emission as the U (for unidentified) emission.

Because the region A spectrum includes both the binary and the inner shell, all the observed forbidden emission in this spectrum must originate in the latter. This is supported by the spectrum of region B, which corresponds to the inner shell only, showing all the forbidden lines observed in the spectrum of region A. Allowed transitions such as Balmer or HeI, whose presence is not rare in nova shells, are also present in this spectrum. The HeII and Pa9 lines observed in the spectrum of region A are not observed here, which indicates that these two lines originated in the binary, likely from an accretion disk around the WD, and not from the inner shell. The unidentified

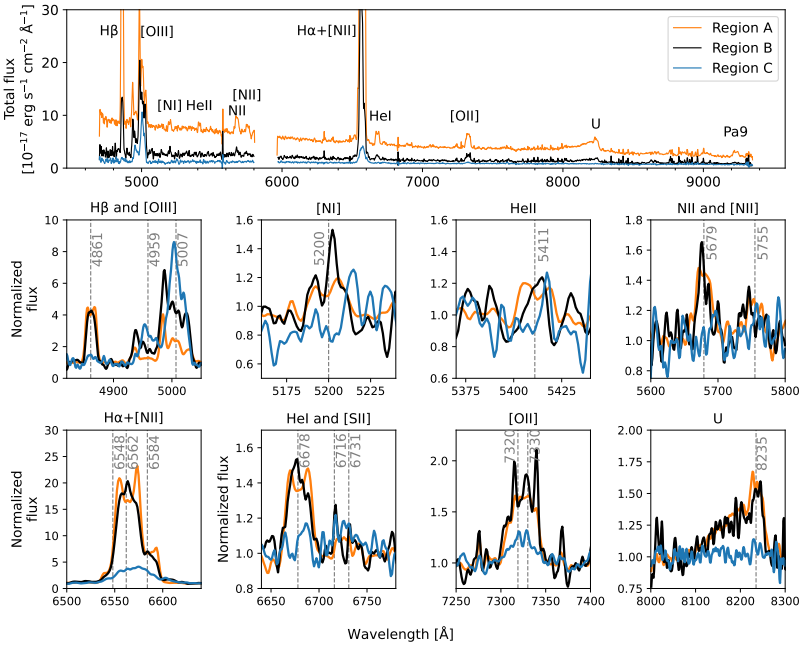

Figure 4.5: Extracted spectra of the three different regions defined: A (binary + inner shell), B (inner shell only), and C (outer shell). The top panel shows the extracted spectra to illustrate their differences along the whole MUSE wavelength coverage in terms of the continuum and emission lines. The bottom panels show a zoomed-in view of the differences between the three spectra for the different lines, including some weak lines that are not visible in the top panel spectra. All the bottom spectra have been normalised to the continuum for a better comparison.

emission is also present in this spectrum, implying its origin in the inner shell.

The outer shell from region C is dominated by the [OIII] emission instead of Hα+[NII] as is the case in the other two regions. As was described by Tappert et al. (2023), there is no significant contribution of Balmer lines in the outer shell, and this is also valid for the He and N lines with the exception of [NII] $\lambda\lambda$ 6548, 6584 Å. The newly observed line of [OII] shows a minor contribution only in this spectrum. Lastly, the spectrum of the inner shell (black) shows a weak continuum that is likely the residual from the masked nearby star, while the outer shell spectrum (blue) does not show any noticeable continuum contribution.

The bottom panels of Fig. 4.5 show a closer look at several lines. For a better visualisation of the differences in the spectral lines, they were normalised to the continuum. Although the spectra of regions A and B share many similarities, the inclusion of the outermost part of the inner shell in the later spectra causes differences in the shape of the different lines. This is noticeable in all lines, but particularly evident in the lines of Hα and HeI λ 6678 Å. In these cases, the spectrum corresponding to region A shows distinctive double-peak profiles originating from the expanding shell. When we consider only the material from the outer part of the inner shell instead (region B), the double peak is replaced with a single peak emission. The normalised spectra of N and He show similarities: both are absent from the outer shell spectra and show stronger normalised fluxes in the spectrum of region B, indicating that the two lines originate in the inner shell.

Right next to the HeI line, we can observe a weak emission that could tentatively be identified as [SII] $\lambda\lambda$ 6716, 6731 Å doublet, although it must be noted that the intensity at these wavelengths only barely exceeds the continuum noise, slightly more so in region C than in the other two. The profile observed in the [OII] $\lambda\lambda$ 7320, 7330 Å is present in the three spectra but shows significant differences among them. It appears stronger in the inner shell spectra where three distinct peaks are present, only the middle one coinciding with the rest wavelength. However, the continuum in this spectrum also shows similar peaks that we attribute to noise in the data, which sheds some doubt on the significance of the above structure in the emission line. In the case of region A, the line profile shows a single peak profile, while in the case of the outer shell, two small peaks at the rest wavelength can be observed. Lastly, the emission at $\lambda \sim 8235$ Å is present only in the binary and inner shell spectra with very similar profiles in both cases, which suggests that its origin can be found in the inner shell rather than in the binary.

4.1.4 Fluxes

The fluxes of the most prominent lines in the three spectra are presented in Table 4.1. They were obtained by integrating the spectra within a velocity range of $\pm 1\,500$ km s^{-1} after performing a subtraction of the continuum in the form of a one-degree polynomial. In the case of the lines of [OII] $\lambda\lambda$ 4959, 5997 Å and Hα+[NII] $\lambda\lambda$ 6549, 6584 Å the velocity range was increased to $\pm 2\,000$ km s^{-1} and the respective lines combined to incorporate all the flux. On the other hand, for the line of [SII] $\lambda\lambda$ 6716, 6731 Å, we reduce the spectral range up to ± 500 km s^{-1} to avoid contamination from the nearby HeI λ 6678 Å line. For the U emission, a spectral range between 8 000 and 8 300 Å was considered, as we were not able to identify the origin of this emission. Furthermore, we also measured the total incoming flux at each line, without distinguishing between spectra. For that purpose, we obtain an image from the datacube corresponding to the same spectral range used to determine the line fluxes. The image was obtained by subtracting the continuum and then summing the fluxes within a circular aperture of 5 arcsec. The results are also presented in Table 4.1. Not all the lines are present in all the spectra, so we present only the fluxes of the lines that have a S/N ≥ 5 in the case of the spectra and ≥ 10 for the images.

The extension of the shell in the different lines is presented in Fig. 4.6. Each presented image was smoothed by convolving it with a 2D symmetric Gaussian kernel of FWHM of 0.2 arcsecs (1-pixel size), and pixels whose flux is below the median level of the background plus its standard deviation were discarded. In all cases, a linear scale was used that, in combination with the exclusion of the faintest pixels, provides a good visualisation of the nova shell. The position of the binary is marked with a black cross, while the positions of the closest stars to V1425 Aql are indicated with white x marks.

The images are sorted from the highest (top left panel) to the lowest (bottom right panel) flux. As had been established in Tappert et al. (2023), the strongest lines are Hα+[NII] and [OIII], followed by the Hβ line. The MUSE data unveiled the presence of [OII] $\lambda\lambda$ 7320, 7330 Å lines and the U emission, both of which also present a significant flux. Both emission lines are observed tracing mainly the inner shell, with the [OII] emission also showing a small contribution to the outer shell. Next in flux are the previously detected allowed transitions of HeI λ 6678 Å and NII λ 5679 Å, which are observed to trace the inner shell only. The last line presented is [NII] λ 5755 Å showing only a spurious detection of the inner shell. This line also illustrates how the contri-

Table 4.1: Fluxes and S/N for the lines detected in the expanding shell. The values for lines in the different regions are presented, as well as for their corresponding images. All fluxes are given in units of erg s^{-1} cm^{-2} with the values in parentheses indicating the uncertainty in the last significant digit.

Line	Rest wavelength	Region A		Region B		Region C		Image	
	[Å]	Flux	S/N	Flux	S/N	Flux	S/N	Flux	S/N
Hβ	4861	$4.79(4) \times 10^{-15}$	128	$1.55(3) \times 10^{-15}$	48	–	–	$7.5(2) \times 10^{-15}$	39
[OIII]	4959,5007	$5.82(6) \times 10^{-15}$	102	$5.94(5) \times 10^{-15}$	119	$2.67(3) \times 10^{-15}$	96	$2.10(3) \times 10^{-14}$	78
[NI]	5197,5200	$9(2) \times 10^{-17}$	5	–	–	–	–	–	–
HeII	5411	$1.2(2) \times 10^{-16}$	6	–	–	–	–	–	–
NII	5679	$7.0(4) \times 10^{-16}$	18	$2.5(3) \times 10^{-16}$	8	–	–	$1.5(1) \times 10^{-15}$	14
[NII]	5755	$3.4(4) \times 10^{-16}$	9	$1.7(3) \times 10^{-16}$	5	–	–	$1.2(1) \times 10^{-15}$	11
Hα+[NII]	6562+6548,6584	$2.690(3) \times 10^{-14}$	961	$8.22(2) \times 10^{-15}$	369	$1.118(8) \times 10^{-15}$	140	$4.65(9) \times 10^{-14}$	495
HeI	6678	$4.7(2) \times 10^{-16}$	21	$1.8(2) \times 10^{-16}$	10	–	–	$9.7(6) \times 10^{-15}$	15
[SII]	6716,6731	–	–	–	–	$2.7(5) \times 10^{-17}$	6	–	–
[OII]	7320,7330	$7.7(1) \times 10^{-16}$	57	$3.2(1) \times 10^{-16}$	28	$5.2(5) \times 10^{-17}$	11	$1.49(5) \times 10^{-15}$	28
U	∼8235	$2.60(4) \times 10^{-15}$	66	$7.7(4) \times 10^{-16}$	21	–	–	$3.8(1) \times 10^{-15}$	24
Pa9	9229	$3.0(2) \times 10^{-16}$	15	–	–	–	–	–	–

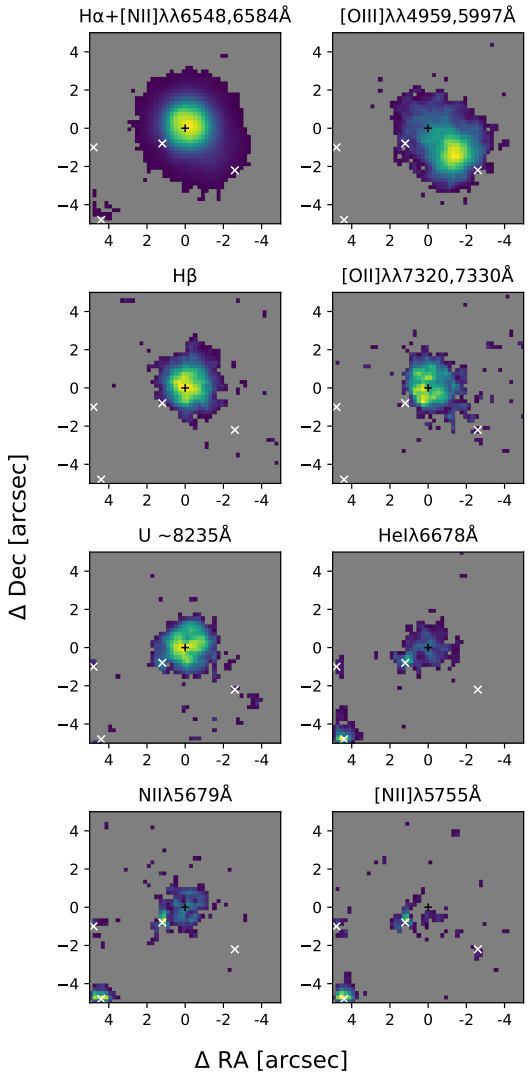

Figure 4.6: MUSE images of the strongest lines in the V1425 Aql nova shell. They were obtained by summing the flux within a certain spectral range after subtracting the continuum. They were smoothed using a Gaussian kernel, and the values below the background median value plus one sigma were masked. The position of the binary is marked with a black cross, and the white marks indicate the position of the nearby stars in the field. Most of the observed emission traces the inner shell, while the outer shell is observed only in [OIII], Hα+[NII], and [OII].

bution of the nearby stars starts to dominate as the flux of the emission line becomes fainter. For lines weaker than [NII], the images do not show any emission that can be related to the shell, inner or outer.

4.1.5 Shell geometry

The geometry of the nova shell around V1425 Aql appears to be complex, with the inner and outer shells showing evident differences in their geometries. The channel maps presented in Fig. 4.3 and 4.4 also indicate the presence of structures hidden within the inner shell. To discern the geometry of the shell, its position-position-velocity (PPV) space, and in particular the position-velocity (PV) planes can be studied. The PPV space corresponds to the three axes in the datacube: the equatorial coordinates (right ascension and declination), together with the spectral range. If the PPV space is collapsed into one of their equatorial coordinates, we end up with an image of one of the datacube's faces: a PV plane. The PPV space and the PV planes allow for visualising the spatial and spectral extension of the nova shell.

Additionally, the PPV can be converted into a proper physical space if we know the distance to the system, the time since the nova eruption, and its systemic velocity. We refer to this physical space as position-position-position (PPP) space. In Chapter 3, it was demonstrated that under the assumption of free and radial expansion, the conversion from the PPV to the PPP is a linear function. This allows us to determine the physical extension of the inner and outer shells.

PV planes

The PPV of the expanding shell was extracted from the datacube by following a similar procedure as for the images in Sect. 4.1.4. The same spectral ranges were considered, and the continuum was subtracted in the same way (by fitting a 1-degree polynomial). Once the shell has been extracted and the PPV obtained, the PV planes corresponding to the RA and Dec can be created. They were obtained by summing the PPV in the Dec and RA axes, respectively. To clean the PV planes and highlight the different structures within the shell, the resulting planes were smoothed by convolving them with a Gaussian kernel of FWHM equal to 2 pixels of the image. Those points in the plane whose fluxes are below the median value plus one standard deviation of the background were discarded for better clarity of the shell. We applied this extraction to the same lines as in Fig. 4.6. The resulting PV planes for right ascension and decli-

nation are presented in Fig. 4.7.

Each PV plane shows the observed flux using a square-root scale, with the dashed yellow lines indicating velocities of ± 500 km s^{-1} with respect to the rest wavelength. In case two or more lines are involved, they are represented by blue and red colours (two lines involved) or by blue, yellow, and red colours (three lines involved), from shorter to longer wavelengths. For each line, both planes are presented, the right ascension (upper row) and declination (lower row) planes. The position of the nearby stars is marked with dashed white lines, while the binary lies at position zero (black line).

The flux distribution observed in each plane for the different lines allows us to draw conclusions regarding its geometry. Starting with the strongest line, Hα shows a compact source with two prominent lobes at red and blue wavelengths. This structure can be better appreciated in the Hβ, where even a small ring structure starts to appear in the centre of the shell. The [NII] λ 6584 Å emission at its rest wavelength appears to be stronger in the north and east while it starts to appear closer to the binary position at redder and bluer wavelengths, in concordance with what is observed in the channel maps. This behaviour is similar to what is observed in the [OIII] emission tracing the outer shell, although in this case the emission at rest wavelength is observed in the south-west. It should be noted that the behaviour described for the [NII] emission is observed within the inner shell, which may indicate a common ejection mechanism for the two emissions. The inner shell can be observed in [OIII] λ 5007 Å as the central structure enclosed within ± 500 km s^{-1}. An asymmetric flux is evident in the inner shell, better seen in the Dec plane, where the blue part is stronger than its red counterpart. This is also noticeable in the outer shell, which appears as a 'banana' shape in the [OIII] planes. The [NII] also reveals a hint of the outer shell in the form of a little horn at the reddest wavelengths of the plane.

The rest of the planes are noisier, and the shell is not evident in all of them. The planes for the [OII] $\lambda\lambda$ 7320, 7330 Å lines show two evident artefacts, the product of wavelengths with high noise across the entire datacube. The inner shell can be observed as a compact source in the planes. Several components of the shell can be distinguished: the blue component of the λ 7320 Å line, the red part of the λ 7320 Å line, and the central region where both lines contribute. The emission related to the outer shell is not observed. This shows that the PV planes are less sensitive to the faintest part of the emission when compared with spectra or images from the datacube. The U emission is clearly observed, and in the same manner as the spectra showed, it starts to

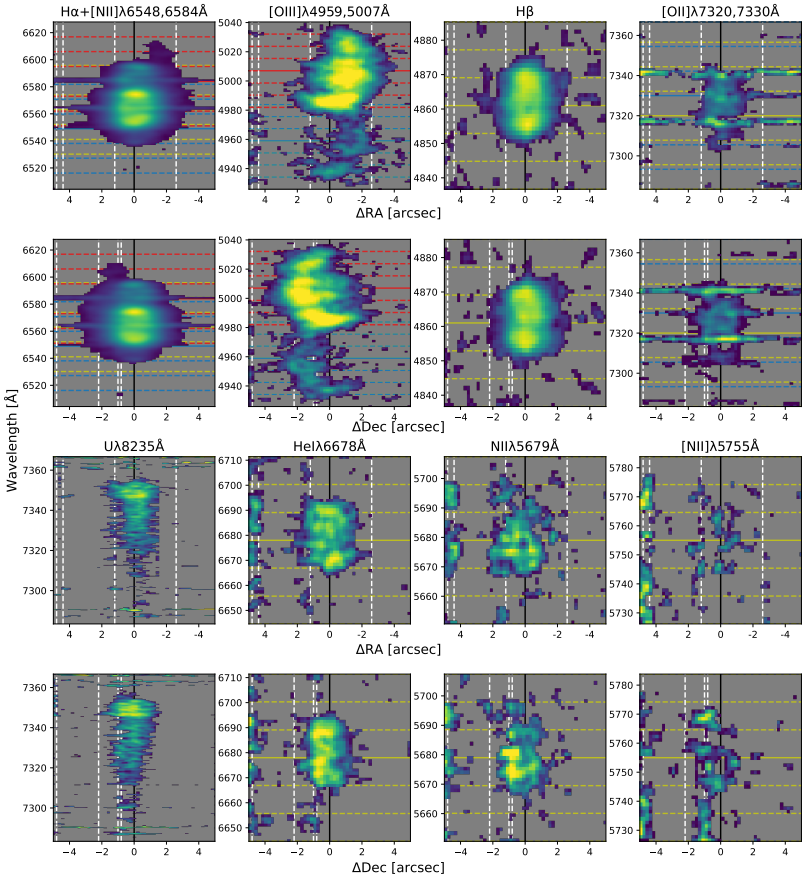

Figure 4.7: PV planes for RA and Dec showing the fluxes of Hα+[NII], [OIII], Hβ, the U emission, [OII], NII, HeI, and [NII]. In each plane, the horizontal dashed lines indicate velocities in steps of $\pm$500 km s^{-1} with respect to the rest line (solid line), while the positions of the stars near V1425 Aql are marked with vertical dashed white lines. In the RA planes, the east is to the left, while in the Dec planes, the north is to the right. To highlight the flux from the nova shell, the planes have been smoothed, and the pixels with low fluxes have been discarded. In all cases, the fluxes are presented using a square-root scale. All observed lines trace the inner shell, which appears as a compact, symmetric, and slow component ($v_{\rm exp} \lesssim 500$ km s^{-1}). The outer shell appears clearly in the [OIII] planes as an asymmetric component, but also in [NII] as a little horn in the red part of the Hα+[NII] planes.

increase its flux from blue to redder wavelengths until it reaches its peak at $\sim 8\,225$ Å. The feature does not show any remarkable asymmetry in the planes.

The inner shell can still be distinguished within the PV planes of the HeI λ 6678 Å and NII λ 5679 Å lines, but they also show a significant contribution in flux from the nearby stars. In both cases, the compact structure associated with the inner shell can still be recognised despite the stronger contamination from nearby stars whose positions in the planes are marked with dashed white lines. These stars are located mainly in the south (to the left in the Dec planes) and east (to the left in the RA planes) of the binary, leaving the north and west of the planes largely uncontaminated. The emission observed in these regions must thus come mainly from the inner shell. This is relevant for the plane of [NII] λ 5755 Å, which is the one that shows major contamination from nearby stars. Regardless, a faint emission is observed to be located close to the position of the binary, including some emission to the north and west.

Position-position-position

The PPP space was created for the lines of [OIII]λ 5007 Å and Hβ, from their respective PPVs. These lines were chosen as each one traces one of the shells (Hβ, the inner one and [OIII], the outer shell), they both have a good S/N, and they do not blend with other lines. The last point is of particular importance, as for blended lines, the line identification (and therefore the conversion to velocity) is not trivial, which could cause artefacts in the transformation to spatial position. For the transformation from PPV to PPP, we also need the distance and systemic velocity of the binary, corresponding to 3.3 kpc and 45 km s^{-1}, respectively (Tappert et al., 2023).

The resulting PPP is shown in Fig. 4.8. A projection of the 3D reconstruction is presented in the top panel of the figure, where the different shells are presented in different colour maps: red for [OIII] and blue for Hβ. The plot also includes the projection of the shell in the different planes. The 3D reconstruction of the outer shell indicates that it possesses an arc-shaped geometry that partially encircles the inner shell. This is consistent with what is observed in the channel maps (Fig. 4.4) and the PV space (Fig. 4.7) of the line of [OIII].

On the other hand, the Hβ emission presents a geometry that is closer to a sphere. This is supported by the behaviour observed in the histogram of the radial distances of the shell (middle panel), which was obtained after transforming the Cartesian coordinates of the PPP into spherical coordinates. To compare the observed distribution of the inner shell (blue) in the histogram, we recreated the behaviour that a perfect

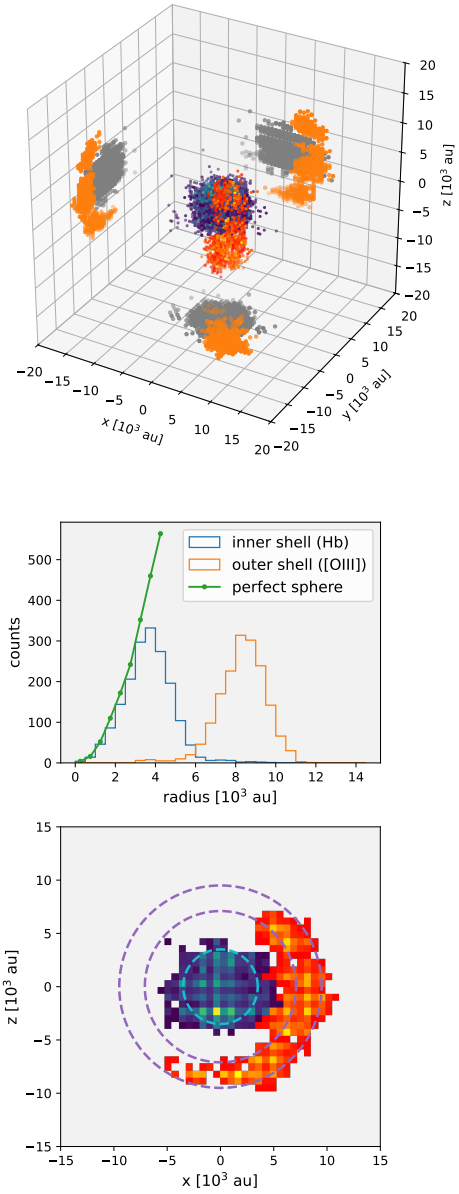

Figure 4.8: 3D reconstruction of the outer shell (red) traced by [OIII]λ 5007 Å, and the inner shell (blue) traced by the Hβ emission. Top panel: Projection of the inner and outer shells in the PPP space, together with their respective projections in each of the planes, shown in orange and grey, respectively. Middle panel: Histogram of the radial distance of both shells from the position of the central binary is presented in the middle panel. Bottom panel: Cut of both shells at the angle of the outer shell. The data were rotated and interpolated accordingly to present the structure of both shells. The data indicate a spherical inner shell that extends up to $\sim$ 3 500 au (dashed cyan line), while the outer shell shows an arc-like geometry that extends from $\sim$ 7 100 up to $\sim$ 9 500 au (dashed purple lines).

solid sphere (green) should have, that is, the number of counts as a function of the radius, given the same spatial distribution observed in the PPP. The comparison shows that the inner shell closely follows the distribution of a perfect sphere for radii lower than 3 500 au. Beyond this radius, the distribution starts to deviate significantly from a sphere, thus defining its outer limits. The outer shell shows a distribution close to a Gaussian, slightly skewed to lower radii, with the most likely reason being the contribution of the inner shell observed in [OIII]. The mean (μ) and standard deviation (σ) of this distribution are $\sim$ 8 300 and 1 200 au respectively.

The last panel in the figure presents a cross-section of 1 arcsec width of the expanding shell at the angle of the outer shell (222 degrees). The data were rotated to present a front view of this cross-section, with the PPP's z-axis (line-of-sight axis) presented in the y-axis of the plot, while the x-axis in the plot is a mixture of the PPP's x- and y-axis. The view of the shell from this angle confirms once more the arc-like structure of the outer shell, and how it spans an aperture angle of $\sim$ 180 degrees. The radius of 3 500 au determined for the inner shell is presented with a cyan dotted line. It encloses the inner shell well on the z-axis but not so well on the x-axis. This may be an indication of an overestimation of the distance used to obtain the PPP space. Similarly, the distribution of the [OIII] emission shows a bulk in the x-axis of the plot close to $z \sim 0$, but in this case, we could attribute it to the presence of the oxygen inner shell. In general, the outer shell is well confined within the radius defined by $\mu \pm \sigma$ (dashed purple lines).

4.2 Discussion

The main result of this work is the finding that the geometry of the outer shell corresponds to an arc-shaped structure that partially encircles the inner, and more spherical, shell. This is unexpected, as it was presumed that the most likely geometry for an isolated ejection should be a cone or a plume. A possible physical explanation for both the observed asymmetry and the arc-shaped geometry of the outer shell could be found in a magnetic WD. The presence of a magnetic WD in V1425 Aql was proposed by Retter et al. (1998) based on a photometric analysis of the system after the nova eruption. They found strong periodic signals at $\sim$ 6.1 and $\sim$ 1.4 h, allegedly corresponding to the orbital period and the WD spin, respectively. However, Worpel et al. (2020) did not detect any X-ray emission, thus challenging the previous idea. Therefore, the magnetic nature of the WD in V1425 Aql is not settled. Still, by assuming it is, we can speculate how the observed asymmetry could find its origin in a magnetic

WD.

In magnetic CVs where the magnetic and orbital axes of the WD are misaligned, the accretion rate on the magnetic poles may differ between them (Zhilkin et al., 2022). This will cause one of the poles to be hotter after the nova eruption, causing the thick winds that produce the fast outflow to be stronger at one of the poles. If the thick wind phase lasts for only half of the WD spin, this could, in principle, also explain the arc-like structure observed in the outer shell. Lastly, another piece of circumstantial evidence in favour of a magnetic WD is given by the spherical geometry of the inner shell. Porter et al. (1998) investigated the effect of the WD rotation in the shape of the nova shell, finding that slower rotating WDs produce more spherical shells. Assuming that the period of 1.44 hours modulation detected by Retter et al. (1998) corresponds to the spin period of the WD, this would classify the WD in V1425 Aql as a very slow rotator (Norton et al., 2004).

This idea, however, is not exempt from challenges. While an asymmetric accretion is possible under the circumstances discussed, one as strong as the one observed in the outer shell would require the WD to be a synchronous polar, so all the matter will be accreted on one pole only. This view is incompatible with the results of Retter et al. (1998) and Worpel et al. (2020). Furthermore, if the physical reason for the asymmetric ejecta lies in a magnetic WD, one should expect to observe similar features around other magnetic novae. This, however, is not the case (some famous magnetic novae are DQ Her Harvey et al. 2016 and GK Per Santamaría et al. 2020). However, we point out that the vast majority of nova shells have been observed using Hα NB filters only. Under these filters, the nova shell around V1425 Aql would appear as normal as any other shell. It is then plausible that some unexpected features have gone unnoticed in other magnetic novae. The Hα and [OIII] nova shell survey carried out by Downes & Duerbeck (2000) includes two, although doubtful, intermediate polars: CP Pup (Mason et al., 2013) and V842 Cen (Woudt et al., 2009; Luna et al., 2012; Sion et al., 2013). Neither of these systems showed ejecta with obvious asymmetric features.

On the other hand, a comparison between the GMOS and MUSE NB images has the potential to clarify the time of the ejection that gave rise to the outer shell, and provide hints about its origin. Unfortunately, due to the low S/N of the GMOS images, an evolution of the shell, and consequently its expansion rate in the plane of the sky, cannot be determined with any confidence. From the MUSE data, we derived a maximum extension of the outer shell of 2.84 ± 0.14 arcsec, which is higher than the value reported in Tappert et al. (2023) from the NB image (1.91 ± 0.1 arcsec) and

LSS (2.32 ± 0.11 arcsec). We attribute the differences to the wider transmission of the GMOS NB image and the angle of the used slit. From the measurements of Tappert et al. (2023), there is a margin of ± 2 years between the ejection of the inner and outer shell. With the new measurement, and using the same expansion velocities for the outer ejecta measured in Tappert et al. (2023) ($1\,500 \pm 20$ km s^{-1}), this value increases up to 4 ± 3 years, still compatible with a simultaneous ejection of the shells within two sigmas.

The MUSE spectral range allows us to study lines at redder wavelengths compared to Tappert et al. (2023), adding the lines of [OII] $\lambda\lambda$ 7320, 7330 Å and the feature observed at $\lambda \sim 8225$ Å. The [OII] lines were previously measured by Lyke et al. (2001). About 2.5 years after the nova eruption, these lines were significantly weaker compared with the rest of the lines in their spectrum, such as [OIII] λ 5007 Å. From the fluxes they reported, we can determine the ratio [OIII] $\lambda\lambda$ 4959, 5007 Å/ [OII] $\lambda\lambda$ 7320, 7330 Å to be ~ 180. In contrast, our data indicate a much lower value for the same lines, corresponding to ~ 14 from the flux obtained from the images (Table 4.1). The ratio [OIII]/[OII] is sensitive to the ionisation parameter and the ionisation field (e.g Kewley et al., 2006; Nakajima & Ouchi, 2014), and therefore, the drastic reduction in ratio between the Lyke et al. (2001) observations and ours indicates a significant decrease in the overall radiation field. This is not surprising as the major source of ionising photons should be the WD, which will cool with time.

We were not able to identify the emission observed at ~ 8235 Å. Possible candidates for this emission are the lines corresponding to HeII λ 8237 Å, NI λ 8216, 8223 or 8242 Å, and [OI] λ 8222 Å. From the spectra (Fig. 4.5) and images (Fig. 4.6), it appears clear that the observed emission originates in the inner shell, which implies that the nitrogen and oxygen lines are plausible candidates. The HeII is a less likely candidate as the inner shell does not show any emission from the HeII λ 5411 Å observed in the spectrum of the region A. The shape of the observed unidentified emission suggests a blend of lines, and therefore, several of the mentioned lines could be contributors. It is also interesting to note that in the spectrum published by Lyke et al. (2001), there is no clear emission around this spectral region, although the line of HeII was detected. Similar to the case of the [OII] lines, this illustrates the evolution of the nova shell with time.

4.3 Summary and conclussion

Our analysis of the nova shell around V1425 Aql has clarified the geometry of the outer and asymmetric ejecta, revealing an unexpected arc-like structure instead of the presumed cone or plume geometry. This unusual geometry is revealed by the data presented in the channel maps, the PV planes, and the 3D reconstruction. The physical reason for it is still unclear, but we have speculated how it may be due to a magnetic WD. However, the ambiguous evidence regarding the magnetic nature of the WD in V1425 Aql prevents us from conclusively identifying a magnetic WD as the true reason behind the asymmetric ejecta.

By selecting different spaxels in the datacube, we were able to better characterise the differences between the inner and outer shell, and between the shells and the binary itself. The outer shell is only visible in forbidden lines ([OIII], [NII], and [OII]), while the inner shell shows a mix of allowed and forbidden transitions. An interesting emission, likely a blend, appears in the red part of the spectrum, near 8235 Å; we were not able to identify it but were able to constrain its origin to the inner shell.

On the other hand, the strongest lines observed in the inner shell, the blend between Hα and [NII], start to reveal clumpy structures within the shell. These clumps are observed closer to the [NII] rest wavelength and appear to share the same axes in the sky as the outer ejecta, although with the current data we cannot discern if this is actually the case. As the shell expands, these clumps should become more evident; future observations should thus be able to discern if the clumps share a common axis with the outer ejecta or not.

Overall, while our study provides important progress with respect to the first report on the outer ejecta by Tappert et al. (2023), it raises additional questions regarding its shape, the physical reason for it, and the unidentified emission blend near 8235 Å. This should provide sufficient motivation for further detailed studies on this interesting nova and its peculiar shells.

CHAPTER 5

Geometry of nova shells: from axial ratio to their hidden shape

MUSE data of several nova shells have been collected over the last years, and a preliminary analysis of the data is presented in this chapter by applying the methodology presented in Chapters 3 and 4. The datacubes revealed the different shells emitting mainly in Hα, with significant contributions of [NII] and [OIII] emission in some cases. A variety of geometries are observed, including two new asymmetric shells dominated by forbidden emission (V1229 Aql and FV Sct). From the Hα emission, the axial ratio of the shells was measured by fitting an ellipse to the shell. Most of the shells present an axial ratio lower than 1.15, with the most extreme case being 1.46 (DO Aql). The axial ratio was used to search for correlations with t_3, expansion velocity, shell age, and $M_{\rm WD}$, finding a strong correlation only between the axial ratio and t_3, and also between the expansion velocity and the shell's age. Position-Position-Velocity (PPV) data were extracted from the datacube, revealing that many, apparently spherical, shells consist of equatorial ring and polar material, which were hidden behind projection effects. The results indicate that some nova shells have geometries more complex than the usual ellipsoidal configuration, with asymmetric shells not being as rare as previously thought. This has implications for our understanding of the ejection mechanism and the ISM interaction. The PPV diagrams, on the other hand, show that the geometry derived from the NB images can be significantly affected by

projection effects, having consequences for the measurements of axial ratio for certain shells. This, in turn, may have implications for the correlation between axial ratio and other parameters of interest. The results presented here are preliminary for what will be a future publication, which will expand on the outcome and discussion shown in this chapter.

5.1 Results

5.1.1 Narrow-band images

To confirm the presence of a nova shell around the 21 different targets presented in Chapter 2, Hα+[NII] images were obtained from the datacubes. These images were created by selecting the slices from the cube corresponding to the wavelength range between 6504.0 and 6628.0 Å. This corresponds approximately to the range defined by the [NII] λ 6548 Å and [NII] λ 6584 Å lines being blue and red shifted by 2 000 km s^{-1} respectively. This allows for most of the flux of the shell to be incorporated, including the Hα line. The actual images were obtained after incorporating all the flux within this range, after applying a subtraction of the continuum. To reduce the noise level in the resulting images, a convolution with a Gaussian kernel with $\sigma = 0.2$ arcsec (1 pixel) was applied. The resulting images are presented in Fig. 5.1.

The shells present a variety of geometries, with some of them being compact sources that can not be differentiated from the post-novae, while others present ellipsoidal and ringed geometries. Within the compact shells, we can include the shells around BY Cir, V1425 Aql, V842 Cen and QU Vul. These shells do not show any characteristic geometry besides their almost spherical appearance. This is expected for younger and distant shells where there has not been enough time for the shell to expand to the point where we can clearly separate it from the post-novae. It is not a surprise, then, that these shells are among the youngest within the sample, with ages of 29.5, 26.5, 35.1, and 37.7 years for BY Cir, V1425 Aql, V842 Cen and QU Vul, respectively.

As the shell expands, its geometry starts to be unveiled; that is, specific structures like rings or clumps can be resolved by MUSE. For instance, for the shells presented in Fig. 5.1, we can distinguish ringed, ellipsoidal, and clumpy geometries. For the first group, we can mention the shells around V351 Pup, BT Mon, CT Ser, XX Tau, and NQ Vul. In these shells, a ring that can be complete or incomplete can be observed. In the

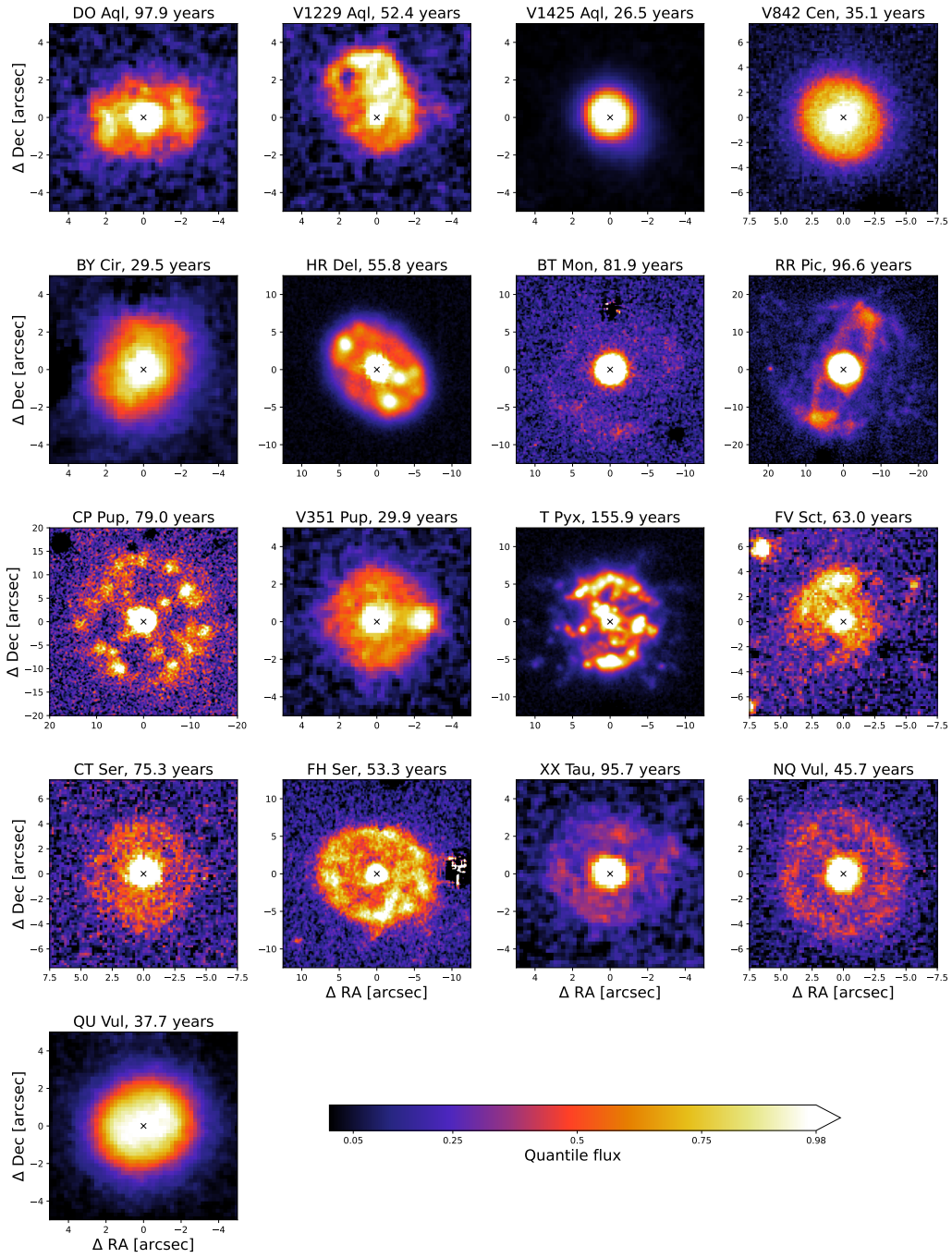

Figure 5.1: Hα+[NII] images for the 17 shells in the sample. All images are centred on the position of the CV (black cross), present the age of the shell at the top of each image. The orientation is such that north is up and east is to the left. The flux in all images is presented using a linear scale defined between the quantiles 5 and 98 of the flux distribution.

cases of V351 Pup, CT Ser, and XX Tau, the ring is filled with emission, which makes it difficult to discern its radius, but the amount of flux from this emission is low enough to distinguish the flux from the post-novae and their shell. The shell around BT Mon consists of an incomplete ring where most of the flux comes from the south and north-west of the position of the post-nova, consistent with the previous observations (Gill & O'Brien, 1998). The best example for a ringed shell is NQ Vul, which shows a complete and circular ring with a radius of $\sim$ 4 arcsec. The apparent sphericity of the shell may be deceptive, as was pointed out by Santamaría et al. (2022a), who studied this shell using IFS data, and found a prolate geometry instead, exemplifying the effects of the shell inclination in its apparent geometry.

This classification between compact and ringed shells is arbitrary and based solely on visual inspection. This may lead to systems with a more ambiguous classification, such as BY Cir. This system shows characteristics of both classifications, being compact and unresolved, but surrounded by a 'halo' that looks more similar to V351 Pup or CT Ser.

Much less ambiguous is the classification of the ellipsoidal shells, which correspond to the shells around DO Aql, HR Del, RR Pic, and FH Ser. They are characterised by a prolate geometry, with diverse substructures within them, such as rings, filaments, and clumps. In the case of DO Aql, two lobes of material stand out over the rest of the shell, which are located close to the edges of the prolate shell. Similarly, within the shell of HR Del, several ($\sim$ 5) bright knots of material can be observed at both poles of the shell. As was pointed out in Chapter 3, the previously reported structure of RR Pic, consisting of an equatorial ring and polar filaments, has remained unchanged. In the case of FH Ser, there is an arc to the west of the post-nova which appears to be orthogonal to the main axis of the prolate shell and can be associated with an equatorial ring, as was already noted by Guerrero et al. (2025).

Two shells appear more clumpy than the rest: CP Pup and T Pyx. The CP Pup shell consists of several knots, with Downes & Duerbeck (2000) counting 11 different blobs. The higher resolution of the MUSE data reveals a spherical shell composed of at least 25 different knots distributed mainly at the outside part of the ejecta. T Pyx, on the other hand, shows a more complex geometry with several knots and filaments forming an incomplete ring around the system. The filaments and knots observed in the Hα+[NII] image presented in Fig. 5.1 can be associated with [NII] solely, as the Hβ image presented in Izzo et al. (2024) shows only a ring.

More interestingly, there are two shells that show distinct and evident asymmetric

shells, these being V1229 Aql and FV Sct. In both cases, an emission is observed at the north of the system for which no counterpart is observed at the south. For V1229 Aql, the observed geometry appears relatively complex, with the shell composed of an apparent ring around the system, while the asymmetric material appears to consist of several filaments and arcs. In the case of FV Sct, the presence of an arc in the north is evident, while the shell surrounding the system is diffuse and without evident structures within it.

5.1.2 Kinematics of the shells

The main advantage of the IFS observations over the use of images only is the characterisation of the kinematics of the gas that forms the expanding shell. From the Hα+[NII] images obtained from the datacube, and presented in Sect. 5.1.1, it is clear that some of them present a more complex structure than others. These differences in complexity are more obvious after analysing the kinematics of the shells. Four different lines were studied for this purpose, including Hα, Hβ, [OIII]λ 5007 Å, and [NII]λ 6584 Å. These lines are the most common ones in nova shells, tracing different temperatures and densities across the shell, and therefore a good starting point to characterise the kinematics of the different shells in the sample. The analysis and methodology used are similar to the work done in Chapters 3 and 4.

The subsequent analysis focuses mainly on the asymmetric shells around V1229 Aql and FV Sct, the ellipsoidal shells of HR Del and FH Ser, and the clumpy shells around CP Pup and the RN T Pyx. A correct characterisation of the different structures within these shells may shed light on the different processes that play a role in shaping the nova shells. The shells around RR Pic and V1425 Aql are also complex and worth mentioning, but the analysis of their data was done in Chapters 3 and 4, respectively, and will not be repeated in this chapter. The rest of the systems present shells with less noticeable structures. This lack of remarkable features can be intrinsic to the shell (CT Ser, for example) or the result of being young and distant, and in consequence, harder to resolve (e.g. BY Cir).

Velocity maps

As a first characterisation of the shell's kinematics, fluxes and velocity maps were created from the datacubes. The flux maps were obtained following the same procedure as for the images in Sect. 5.1.1. The wavelength was restricted to a smaller

range compared to the Hα+[NII] images, to be able to discern between the two different emissions. For the lines of Hα and [NII] λ 6584 Å, a wavelength range of 13.75 Å (11 datacube slices) was considered, equivalent to a velocity range of $\sim \pm 300$ km s^{-1} with respect to their rest wavelength. Regardless of this restriction, it is expected that a certain degree of contamination between Hα and [NII] originates for material with velocities higher than $\sim$ 600 km s^{-1}, as at this velocity the blue part of the [NII] line will enter within the wavelength range for the Hα image (and the same case for the red part of the Hα line). Such contamination, if present, can be identified by comparing the velocity maps of both lines for a proper interpretation.

For the lines of Hβ and [OIII], on the other hand, a larger wavelength range was chosen. These two lines are relatively free from contamination by other lines, allowing for the exploration of a large wavelength range in search of material expanding at higher velocities. A wavelength range of 26.25 Å (21 datacube's slices) was considered to explore a velocity range between $\sim \pm 750$ km s^{-1}.

The resulting flux and velocity maps for the six shells previously mentioned (V1229 Aql, HR Del, CP Pup, T Pyx, FV Sct, and FH Ser) are presented in the top panels of Figs. 5.2 to 5.7. The smaller velocity range used to construct these maps makes the differences between Hα and [NII] emissions evident, both spatially and kinematically. In the case of the velocity maps, they were constructed from the flux map by computing the mean velocity at each spaxel of the datacube weighted by the flux values.

The maps show shells dominated by Hα emission, consisting mainly of rings, with some of them clumpier than the rest. Most of the shells also show a significant [NII], whose geometry presents significant differences with the one observed in Hα in some cases. Some of the shells also show emission in Hβ, and/or [OIII]. The velocity maps confirm the ellipsoidal geometry observed in the images by revealing a dipole pattern in the velocities of the ejecta, but they also reveal features previously unnoticed in the images.

In the case of the HR Del (Fig. 5.2), the shell is observed in all four lines, with the Balmer lines showing an ellipsoidal geometry, with the north-east axis having redder velocities. The Hα emission shows the presence of an equatorial ring within the shell, which is revealed in the velocity maps as a dipole pattern that is inverted with respect to the pattern observed in the ellipsoidal geometry, that is, the equatorial ring is observed showing blue velocities at the north-east. The [NII] emission also shows an ellipsoidal geometry with the same velocity pattern seen in the Balmer emission, with-

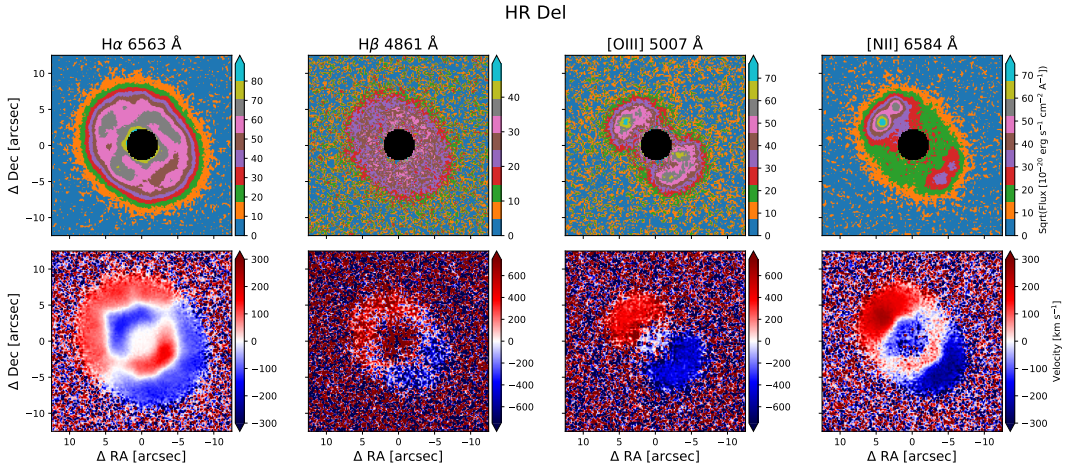

Figure 5.2: Flux and velocity maps for HR Del's nova shell. Top: flux maps for the lines of Hα, Hβ, [OIII], and [NII]. The flux is presented using a square-root scale to highlight fainter regions within the shell. Bottom: velocity maps for the same lines. The dipole pattern characteristic of an ellipsoid or a ring is present in the velocity maps of all lines, while the flux maps show the clumpiness within the ejecta, particularly strong in forbidden emission.

out a signal of the equatorial ring observed in Hα. There are two lobes of emission, with the north-east one showing higher fluxes and at least two different clumps of material at each lobe. The lobes are embedded within a fainter and more regular emission (green region in Fig. 5.2), which may be the residual of Hα, as it shares the same spatial region as the Balmer emission. A similar two-lobe geometry is observed in [OIII], although in this case the flux between lobes is similar, and there is no evidence for the faint emission surrounding the lobes, resulting in a more elongated (higher axial ratio) geometry. This difference in axial ratio between [OIII] and Hα+[NII] was already noticed by Slavin et al. (1994).

The only other shell that shows emission in the four lines is T Pyx (Fig. 5.3). The remnant of this RN shows an incomplete ring in the Balmer lines whose major axis is in the north-south direction. This is more evident in the velocity map of Hβ rather than Hα. In the latter, a significant number of filaments and knots are observed, whose main axis is orthogonal to the Balmer ring. This is more evident in the [NII] and [OIII] maps. In [NII], the emission is concentrated in a ring around the system, while [OIII] appears more clumpy. This is also revealed by its respective velocity map, which does not show the dipole pattern as clearly as Hα and [NII], and instead, a more complex pattern is observed. The [OIII] emission is stronger close to the system, showing a clear dipole pattern in this case, which may indicate material ejected from a recent

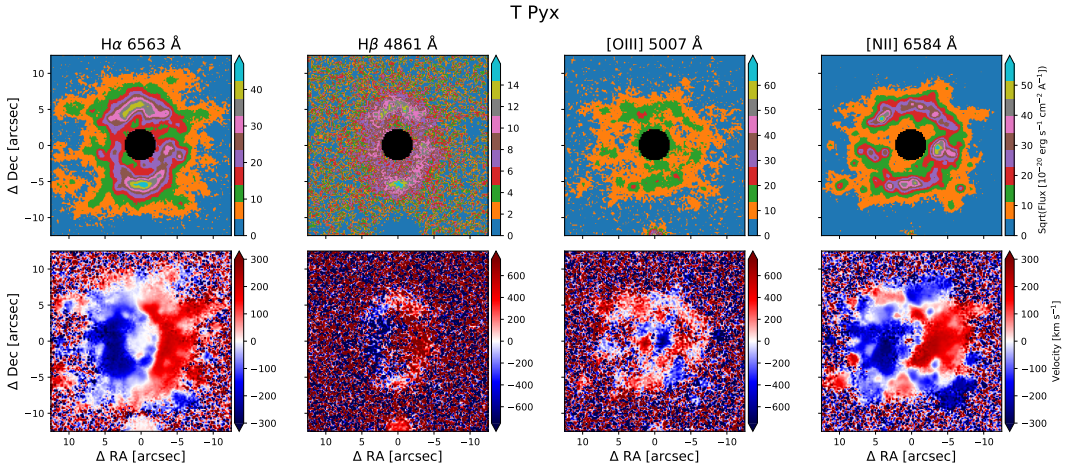

Figure 5.3: Same as Fig. 5.2 but for T Pyx. The simplicity of the equatorial ring observed in Hβ contrasts with the complex kinematics observed in the other lines, particularly the forbidden ones, where a mix between blue and red velocities is imposed over a more general dipole pattern.

eruption.

FH Ser (Fig. 5.4) is another interesting example of a shell, simple in appearance but actually complex. The Hα emission shows a ring structure with some clumpy material around the system. Its velocity map reveals a more intricate structure, with two superposed dipole patterns, indicating the presence of an equatorial ring and polar material. The arc observed in the Hα+[NII] image is not so evident in the flux map, but is still noticeable in the velocity map. Its red-shifted velocity suggests it is related to [NII]. The [NII] image shows the ring observed in Hα, but also a 'tail' of emission at the south of the system. The velocity map confirms that the material related to this tail comes from the shell, as its blue velocity clearly stands out from the background noise. The confirmation of the blue-shift velocity of this faint tail of material comes from the image and velocity maps of the [OIII] line. Here, the arc observed in Hα is also present, showing blue-shifted velocities. An additional arc of material to the south-west with similar characteristics is also observed.

The asymmetric shells of V1229 Aql and FV Sct (Figs. 5.5 and 5.6) are observed in Hα, [NII], and [OIII], although the latter is barely detectable in FV Sct. No traces of Hβ emission are observed in any of the shells. The Hα images show compact shells, with V1229 Aql hosting a spherical shell with a higher flux to the west of the system. Its velocity map is dominated by redder velocities, indicating a significant contribution from [NII], and/or a significant systemic velocity from the system. The flux of FV Sct,

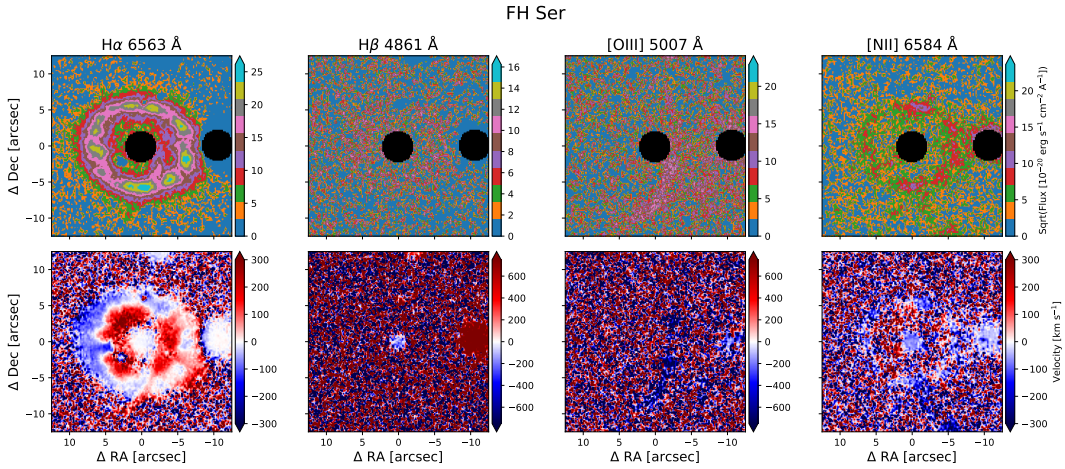

Figure 5.4: Same as Fig. 5.2 but for FH Ser. The ellipsoidal structure observed in Hα and the dipole pattern similar to the one observed in HR Del indicate the presence of an equatorial ring and polar material expanding orthogonally. The [NII] maps show an ellipsoidal geometry dominated by blue velocities. The arc observed in the Hα+[NII] image is dominated by red velocities in the Hα map, and by blue velocities in the [NII] and [OIII]. This indicates the arc originates from blue-shifted forbidden emission.

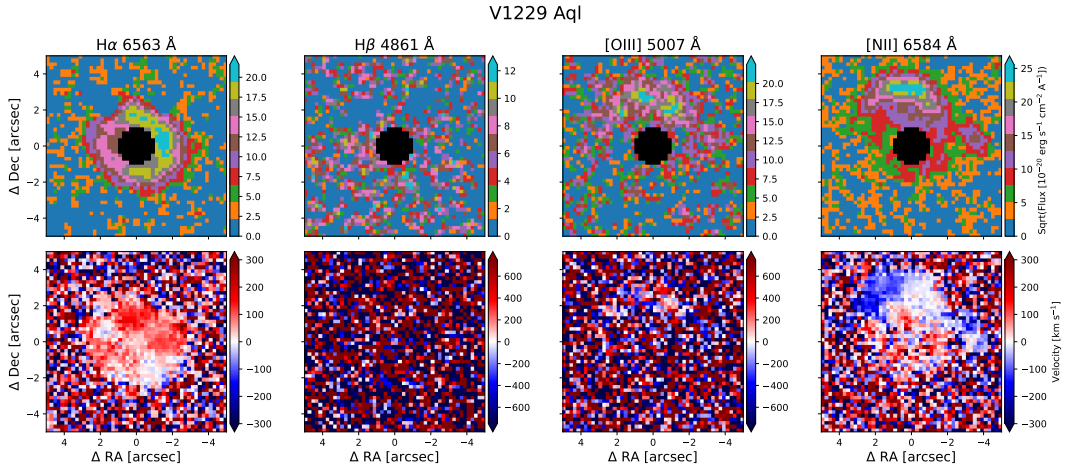

Figure 5.5: Same as Fig. 5.2 but for V1229 Aql. The spherical shell observed in Hα is dominated by red velocities, suggesting a significant systemic velocity. In the forbidden emission, the asymmetric ejecta observed north of the binary stand out. The flux is stronger for [NII], it is dominated by blue-shifted velocities, and extends beyond the Hα emission.

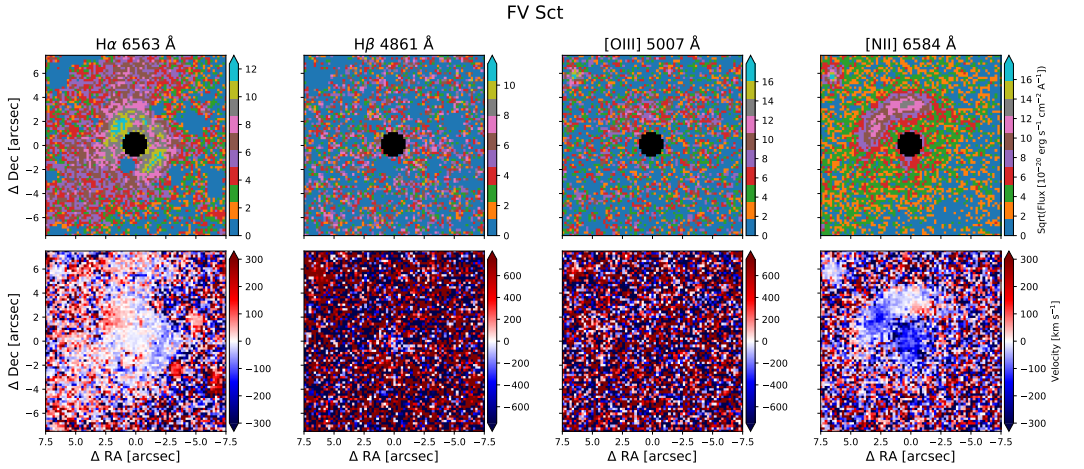

Figure 5.6: Same as Fig. 5.2 but for FV Sct. Similar to V1229 Aql, FV Sct presents an asymmetric ejecta to the north, dominated mainly by [NII]. The hydrogen shell presents two lobes of stronger emission, which also display a dipole pattern.

on the other hand, shows a dumbbell-like shell with a dipole pattern in the velocity map. Its main axis is in the northeast-southwest direction, with the north-east showing redder velocities. In both systems, the asymmetric feature is dominated by the [NII] emission, revealed as an arc-like structure located at the north. The velocity map of both systems shows that this arc is dominated by bluer velocities. The observed arc in [OIII] shares the same kinematics as [NII].

The last shell of this subsample, CP Pup (Fig. 5.7), is detected only in Hα, showing several clumps arranged forming a ring structure. The velocity map shows a dipole pattern with the east part of the ring dominated by bluer velocities, and the west by redder velocities. Some of the clumps present the opposite behaviour, which may indicate a structure composed of an equatorial ring and polar material.

The flux and velocity maps of the rest of the shells are presented in Appendix A. In general, these shells show compact geometries in Hα, sometimes showing rings or knots with higher fluxes, with many of them presenting a dipole pattern in their respective velocity map. Several of the shells also present [NII] emission showing a blue velocity, suggesting that it could be related to Hα rather than [NII].

The shells around BY Cir (Fig. A.5) and NQ Vul (Fig. A.16) share the characteristic of being compact, without clear geometries, and dominated by blue-shifted velocities. They are both young shells with small angular sizes, which can explain the lack of clear geometry, while the blue velocities can be explained by the systemic velocity of the system. An intrinsic blue-shifted systemic velocity is supported by the velocity

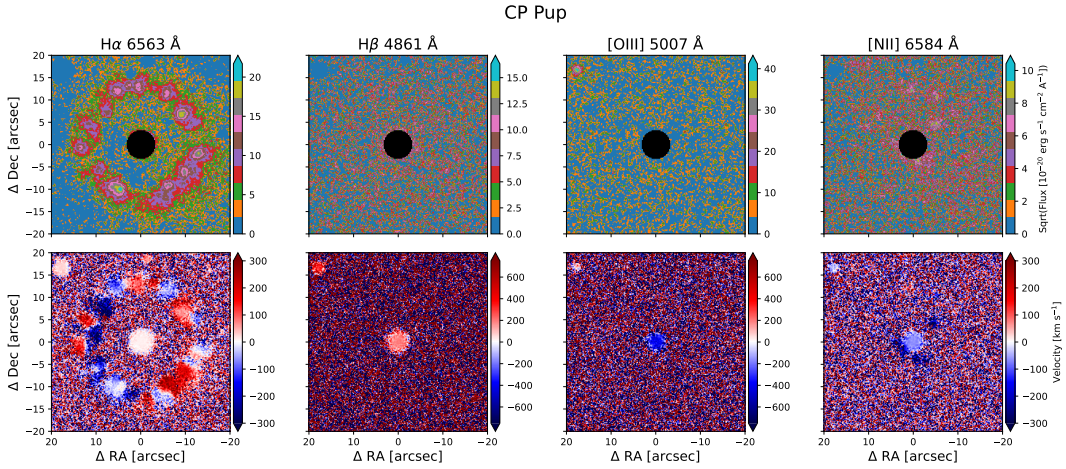

Figure 5.7: Same as Fig. 5.2 but for CP Pup. The clumpy ejecta of CP Pup are observed only in Hα, showing a clear dipole pattern. This indicates that the material is not expanding spherically, but instead, there is a ringed or ellipsoidal geometry behind.

maps of [NII], which are also blue. However, the apparent velocity may be the result of a complex shell, as is the case of V1425 Aql (Fig. A.3), which also appears dominated by blue velocities, but whose systemic velocity is red-shifted (Tappert et al., 2023).

Another system showing a small angular extension ($<$ 5 arcsec radius) is DO Aql (Fig. A.1). This shell is one of the oldest in the sample ($\sim$ 98 years), while its distance is not significantly larger than other shells in the sample, like V1425 Aql, for instance. This indicates a very low velocity expansion of the ejecta, consistent with the high t_3 value of its nova eruption. The shell in question shows two lobes of high fluxes in Hα and [NII]. The velocity map for the latter line shows red colours, confirming they originate from this forbidden line. The velocity map of Hα shows that the centre has blue velocities while the outer parts of the shell show red velocities instead. This can be explained if the systemic velocity of the system is positive, which causes the shell to have a red velocity, while in the centre, the velocity map is dominated by the blue peak of the accretion disc instead. Depending on the separation of the peaks of the accretion disc and the systemic velocity, the red peak of the disc may lie beyond the $\sim$ 300 km s^{-1} range used to create the velocity map.

The nova shells of CT Ser (Fig. A.13), NQ Vul (Fig. A.16), V351 Pup (Fig. A.10), and XX Tau (Fig. A.15) show Hα ring-like shells. Their velocity maps in all except for V351 Pup show a mix between blue and red velocities within the ring, indicating the presence of additional material expanding at different angles, which in turn suggests the presence of polar material. For V351 Pup, only the single dipole pattern is observed,

indicating a ring or ellipsoid geometry. Only V351 Pup shows the shell in [NII], but its blue velocity suggest it may be related to Hα instead.

The old shell around BT Mon (Fig. A.7) is observed only in Hα, being composed of an incomplete and clumpy ring. The distribution of clumps is clearer in the velocity map, which shows a homogeneous distribution of clumps across the whole ring. This is different from the distribution of clumps observed in CP Pup, in which they are distributed within a circle rather than only a ring. Lastly, in the case of V842 Cen (Fig. A.4), a spherical shell is observed in Hα and [NII]. In both lines, the velocity map shows a dipole pattern with the south-west having bluer velocities. While the Hα flux map appears symmetric, the [NII] map shows a higher flux in the north-east. The [NII] velocity map shows redder velocities in this region, discarding the possibility of contamination from the Hα emission. This opens the possibility that the shell of V842 Cen is an asymmetric one, similar to the cases of V1229 Aql and FV Sct. In this case, however, the potential asymmetry is not as evident as, and there is no [OIII] emission to confirm that this is the case.

5.1.3 Axial ratio correlations

It has been well documented that the axial ratio of nova shells correlates with their t_3 (see for example Slavin et al., 1995; Santamaría et al., 2025). It has been proposed that the physical origin of this correlation lies in the interaction between the expanding ejecta and the secondary star. Novae with shorter t_3 are supposedly less affected by this interaction, appearing more spherical (axial ratio closer to one). To test whether or not this correlation appears within our sample, we proceed to measure the axial ratio of the shell in Hα, and correlate these values with different novae and system parameters, such as t_3 or $M_{\rm WD}$.

Ellipse fitting

To measure the axial ratio of the shells within our sample, an ellipse fitting procedure was applied to each one of the Hα images presented in Sect. 5.1.2. Each Hα image is first smoothed using a Gaussian kernel with $\sigma = 1$ pixel, followed by a selection of pixels based on flux. The outer pixels of the image are used to determine the background mean and standard deviation, which values are used to select those pixels whose flux is n times the standard deviation above the background. A value of $n = 5$ was selected for all shells following the methodology used by Santamaría et al. (2025),

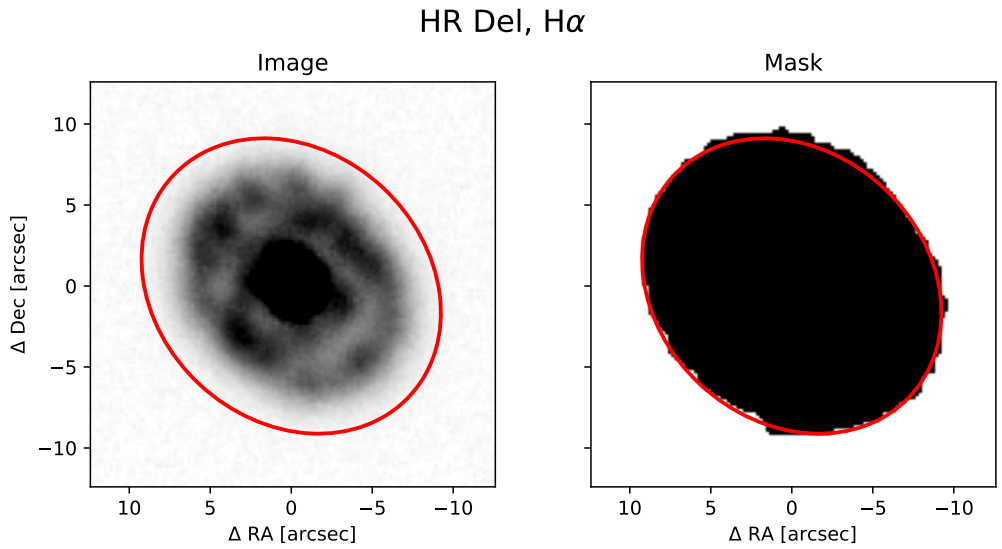

Figure 5.8: Ellipse fitting for HR Del. A mask of the data was created by selecting pixels that have a flux higher than 5σ with respect to the background (right). The ellipse that best fits the contour of this mask was determined using a least-squares minimisation method, and it is presented in red in both columns. The Hα image on the left shows that the method fits well the overall shape of the shell, although it is more sensitive to the outer parts of the shell.

with the exception of FV Sct, for which a value $n = 3$ was selected due to the noisier image. This selection process creates a mask where pixels above the flux threshold are selected. To find the ellipse parameters that best fit the mask, the ellipse equation is applied to the contour of the mask. The centre of the ellipse is imposed to be at the position of the system, thus leaving the ellipse axis and position angle as the free parameters to fit.

An example of the obtained mask and ellipse fitting is presented in Fig. 5.8, where the shell around HR Del is shown. The Hα image of the shell is presented in the left column, while the mask derived by the procedure previously mentioned is shown in the right column, with those pixels that passed the flux threshold in black. The ellipse that best fits the contour of the mask is presented in red in both cases. In the left plot, the ellipse appears to extend beyond the shell, which shows the problem of defining the boundaries of an extended source. It is clear that the ellipse is not tracing the brightest parts of the shell, but instead is tracing the outer and fainter parts. Although the axial ratio of the shell should not vary significantly if we consider its fainter or brighter regions, this may not be the case for all shells, with the consequent difference in axial ratio. This can be particularly significant for shells that show a clear equatorial

ring as T Pyx or RR Pic.

This uncertainty could be quantified by considering the overall uncertainty in the fitting process for these ellipses. This, however, is far from trivial. The datacubes include the variance of the flux at each svoxel, which can be propagated to the images from which the mask was created. This can be used to determine the statistical errors in the parameters of the ellipse. These uncertainties, however, are less relevant than those derived from the methodology. How much does the shape of the shell change as a function of the wavelength range? How much does the 5σ threshold impact the resulting axial ratio? It is likely that these factors significantly affect the results more than the variance within the datacube. At the moment of writing this text, the answer to these questions is not clear, and for the subsequent analysis, the uncertainties in the ellipse fitting will not be taken into account.

The images of the shells with their best ellipse fitting are shown in Figs. 5.9 and 5.10, while the ellipse parameters are presented in Table 5.1. These parameters include the major (a) and minor (b) axes of the ellipse measured in arcsec, the position angle of the ellipse measured in degrees with the usual convention (from north in anti-clockwise sense), as well as the projected axial ratio which is defined as the ratio between the major and minor axes. The resulting projected axial ratio values span between 1.03 (V351 Pup) and 1.46 (DO Aql). The histogram of the distribution (Fig. 5.11) shows the mode between 1.05 and 1.10, where the distribution starts to decay until reaching the value of 1.25. The shell of DO Aql deviates significantly from the rest of the distribution, showing an unusually high axial ratio. This correlates well with DO Aql being the nova that presented the highest t_3.

Correlation of parameters

The measured projected axial ratios were correlated against t_3. The results are presented in Fig. 5.12, where a clear correlation appears between the axial ratio and t_3. To test whether the correlation is significant or not, a Kendall's τ test was performed using the `Scipy Python` implementation. This test searches for a monotonic increase in the data, without concerning whether the data is distributed linearly, logarithmically, or by another function (Kendall & Stuart, 1977). It is also robust even when small samples are considered, which is an advantage over other tests like the Spearman correlation test. On the downside, the method does not consider the uncertainty associated with the variables, which means the result must be taken with caution in the presence of significant uncertainties. The Kendall's test yields a τ value of 0.52,

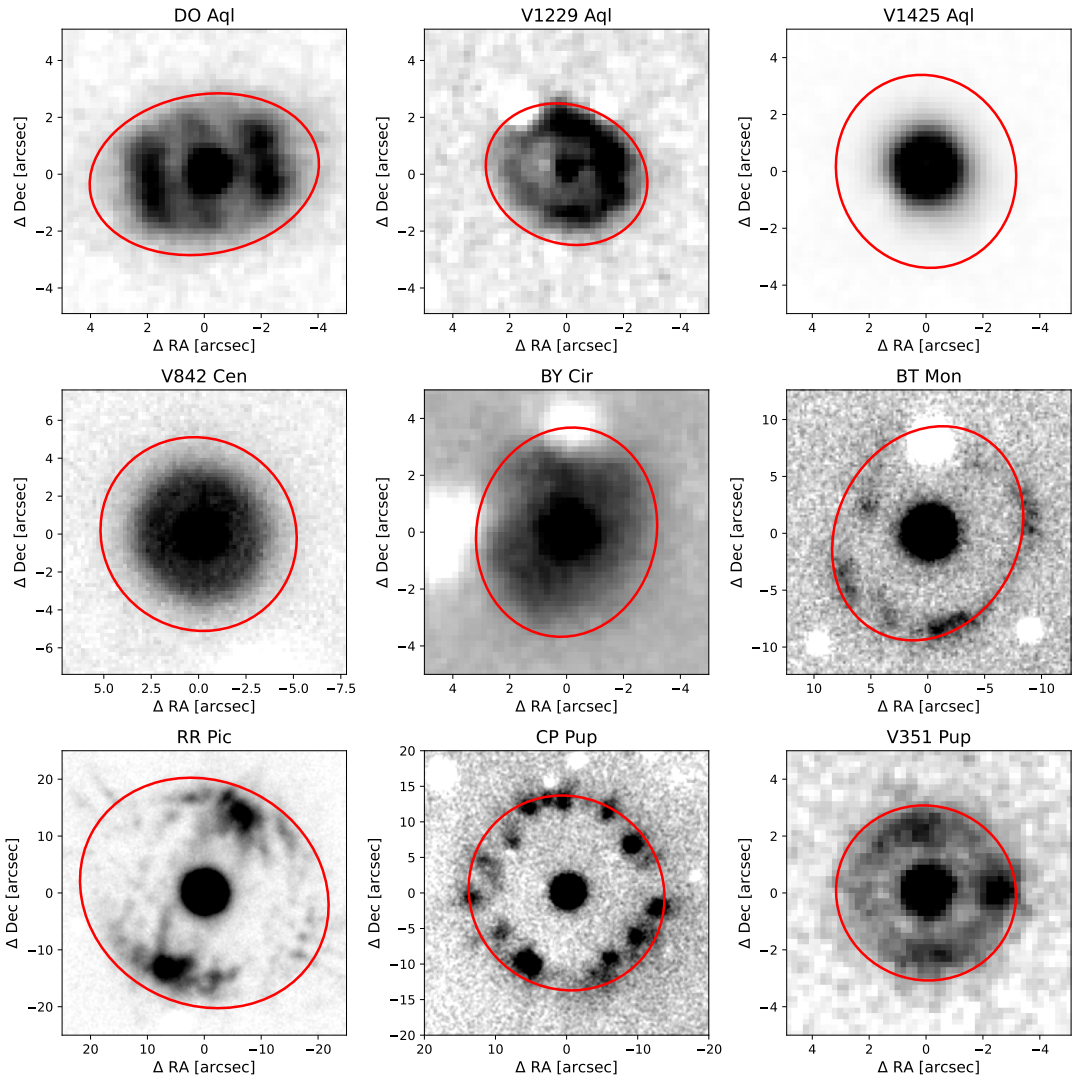

Figure 5.9: Best fitted ellipses (red line) for the different Hα shells presented in this study. The nova shells are presented in grey using a linear scale with values between the 0.05 and 0.97 quantiles of the flux distribution.

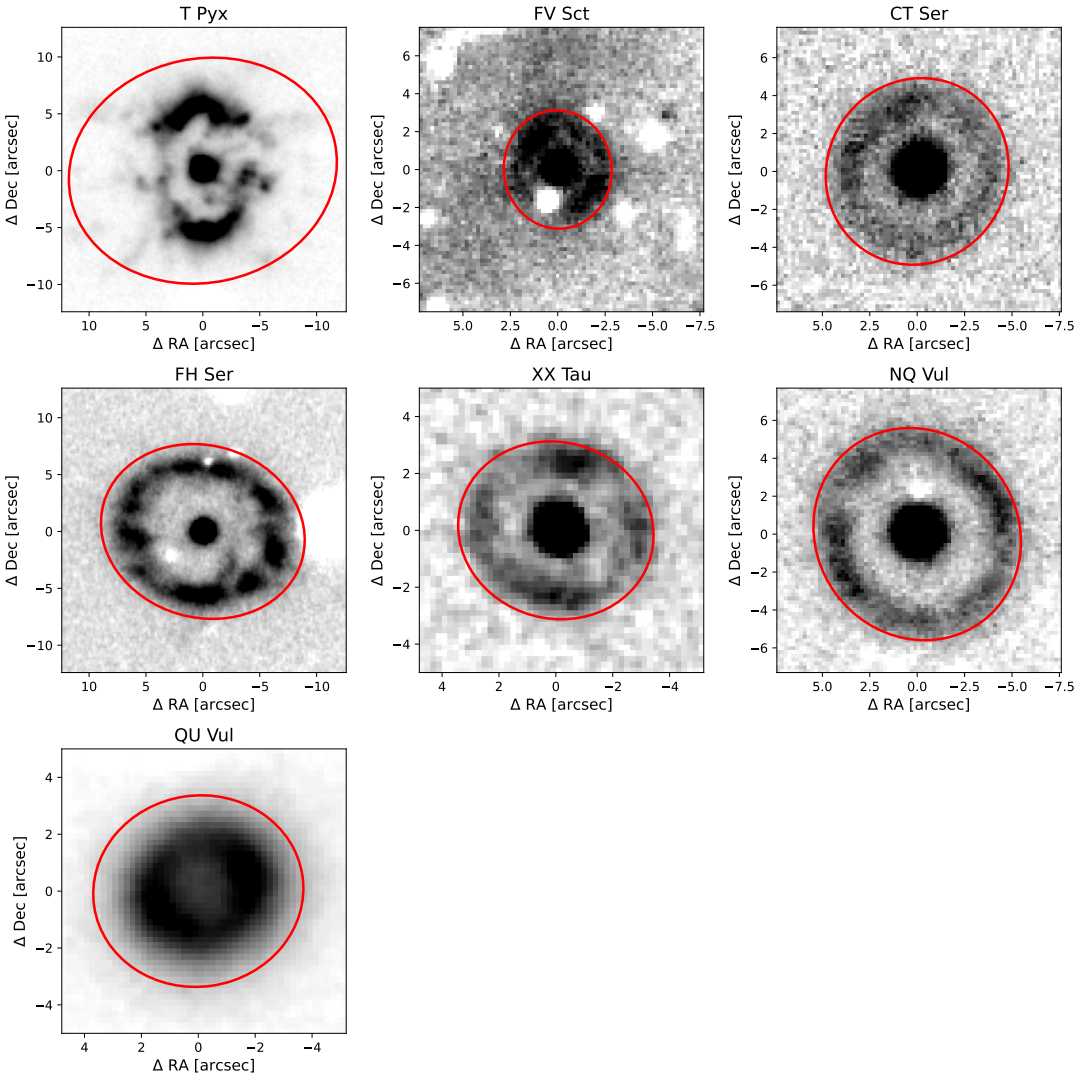

Figure 5.10: Same as Fig. 5.9 for the rest of shells.

Table 5.1: Parameters of the best ellipse fit for the nova shells in the sample.

System	a [arcsec]	b [arcsec]	PA [°]	Axial ratio	lc(t_3) [d]
DO Aql	4.1	2.8	100	1.46	F(900)
V1229 Aql	2.9	2.4	69	1.21	P(32)
V1425 Aql	3.4	3.1	27	1.10	S(79)
V842 Cen	5.3	5.0	53	1.06	D(48)
BY Cir	3.7	3.2	168	1.16	P(124)
HR Del	10.0	8.3	43	1.20	J(250)
BT Mon	9.7	8.0	153	1.21	F(190)
RR Pic	22.4	19.6	63	1.14	J(122)
CP Pup	14.1	13.4	48	1.05	P(8)
V351 Pup	3.2	3.1	68	1.03	P(26)
T Pyx	11.9	9.8	102	1.21	P(62)
FV Sct	3.1	2.8	6	1.11	–
CT Ser	5.0	4.7	75	1.06	–
FH Ser	9.1	7.6	74	1.20	D(63)
XX Tau	3.5	3.1	75	1.13	D(47)
NQ Vul	5.7	5.3	36	1.08	D(50)
QU Vul	3.7	3.4	98	1.09	P(36)

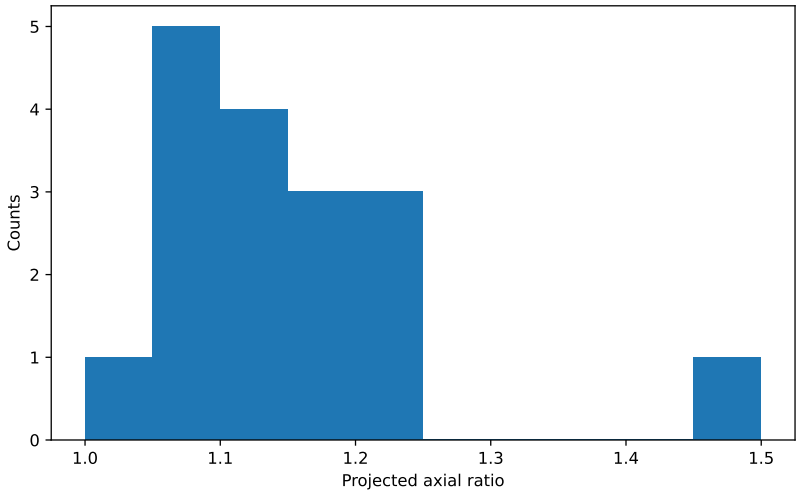

Figure 5.11: Histogram of the projected axial ratio derived from the ellipse fitting of the Hα shell images. The mode of the shell is around 1.05, while the median is close to 1.15. The extreme case of 1.46 belongs to DO Aql, which is also the slowest shell in the sample.

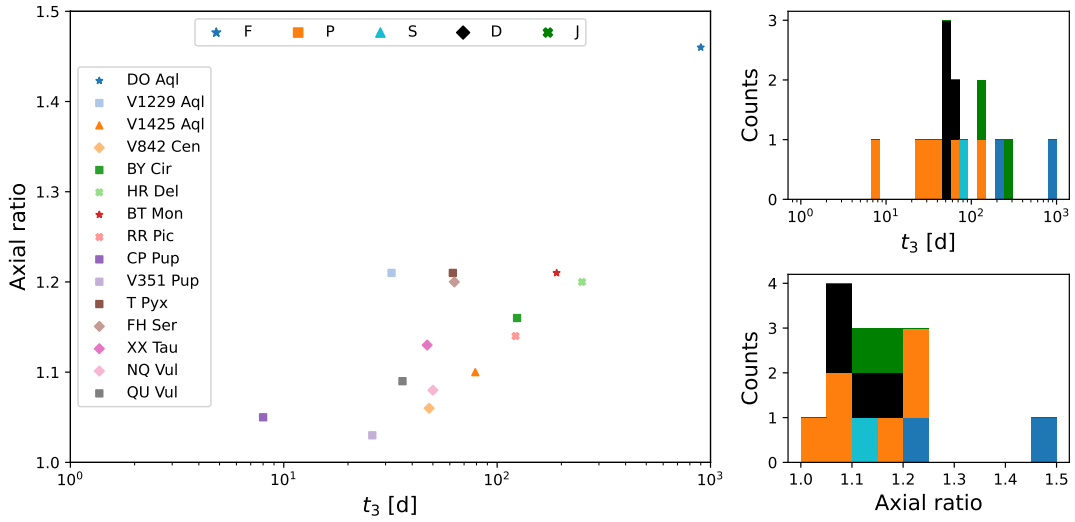

Figure 5.12: Projected axial ratio and t_3 for the different nova shells. A correlation between the axial ratio and t_3 is observed in the data ($\tau = 0.5$, p-value=0.008). The distribution of t_3 as a function of the light-curve class (top-right panel) indicates that the J and F classes are the fastest, while the P class is the slowest, in line with the results from Strope et al. (2010). When considering the axial ratio of the shells as a function of the light-curve class, the distribution is more mixed, which may indicate a hidden correlation between light-curve class and axial ratio.

indicating a positive correlation in the data. The p-value for the data is 0.008, which rejects the null hypothesis of both quantities being uncorrelated, and instead, indicates that both variables, t_3 and the axial ratio, are strongly correlated.

In Fig. 5.12, different markers represent the light curve class of each nova, showing that the flat-topped (F) class presents higher t_3 and axial ratios than the rest. It is followed by the jitter (J) class. On the other extreme, the plateau (P) class is the one that presents the lowest t_3 and axial ratios. The dust-dip (D) class appear to be restricted to a narrow range of $t_3 \approx 30 - 60$ days. This is more evident in the histogram of t_3 presented in the right-top panel, where the different light curve classes are shown with different colours. The histogram of the axial ratio is presented in the right-bottom panel, showing differences with the histogram in Fig. 5.11 due to two systems, FV Sct and CT Ser, not having a reported t_3 or light-curve class.

From the measured semi-major axis of each shell, its expansion velocity can be determined by using its age and the distance to the system. This velocity corresponds to the velocity of the ejecta if it has not experienced any deceleration since its ejection. Studies on old nova shells indicate that they can expand freely even a century after the

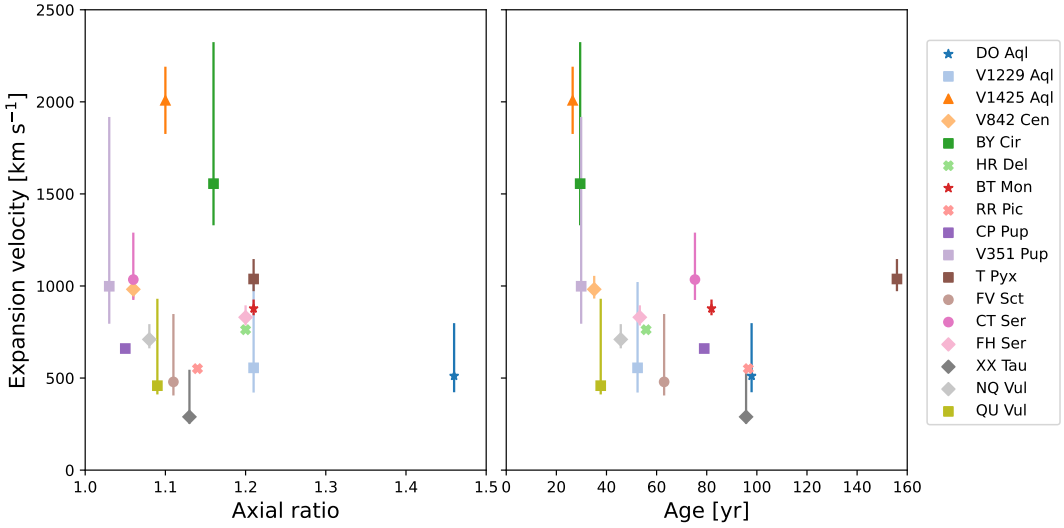

Figure 5.13: Expansion velocity of nova shells against their projected axial ratio (left column) and age (right column). No significant correlation is found between the expansion velocity of the shells and their axial ratio, although a subgroup of systems (lower axial ratio and expansion velocities) shows a clear anti-correlation between the parameters. If the data points corresponding to V1425 Aql and T Pyx are removed, a mild anti-correlation between age and expansion velocity appears in the data (see text for details and discussion).

nova eruption (e.g. Liimets et al., 2012; Santamaría et al., 2019, 2024). If we consider that two of the oldest shells within the sample show evidence that indicates a free expansion of the ejecta, the velocity derived from the semi-major axis of the shell should be representative of the actual expansion velocity of the ejecta.

The derived expansion velocity is presented in Fig. 5.13 as a function of the axial ratio and age of the shells. At first glance, the expansion velocity presents an apparent anti-correlation with the axial ratio, where shells with a smaller axial ratio present higher expansion velocities. However, the Kendall's tau analysis gives $\tau = -0.07$ with a p-value of 0.71, revealing that no correlation is present in the data. In the case of the age of the shells, a mild anti-correlation is observed, with the Kendall's τ test giving $\tau = -0.31$ and a p-value of 0.09.

The mean and median velocity of the sample are $\approx$ 840 and 760 km s^{-1}, respectively. There are two shells that show particularly high velocities: V1425 Aql with $v_{\rm exp} \approx 2\,000$ km s^{-1}, and BY Cir with $v_{\rm exp} \approx 1\,500$ km s^{-1}. In the case of V1425 Aql, the derived velocity is higher than the velocity of the outer ejecta ($v_{\rm exp} \approx 1\,500$ km s^{-1}; Tappert et al., 2023) or the FWHM of the spectral lines observed after the eruption

($v_{\rm FWHM} \approx 1\,700$ km s^{-1}; Greeley et al., 1995; Lyke et al., 2001). This suggests a likely overestimation of the shell by the employed methodology and/or distance. In the case of BY Cir, the derived expansion velocity is lower than the velocity derived from the FWHM emission lines ($v_{\rm FWHM} \approx 2\,100 - 2\,700$ km s^{-1}; Greeley et al., 1995).

Regarding the age of the shell, a mild anti-correlation with the expansion velocity of the shell is observed. However, if we discard the anomalous cases of V1425 Aql and T Pyx, with the latter discarded based on its RN nature, a stronger anti-correlation appears in the data ($\tau = -0.37$ and a p-value=0.06). This potential anti-correlation should be interpreted with caution, as the obtained p-value is still above the usual threshold of 0.05 used to claim strong correlation, and more importantly, the Kendall's tau test does not account for the uncertainties present in the data, which are significant for several systems. Similarly, if the systems of V1425 Aql and T Pyx are removed from the velocity and axial ratio data, a small improvement in the statistics is achieved ($\tau = -0.14$ and a p-value=0.49), but it is still insufficient to claim a confident correlation in the data.

The last parameter of interest analysed in this work is the WD mass, the most crucial parameter for nova eruptions. A distinction was made between the masses provided by Shara et al. (2018, ; S18 hereafter) and from other sources. As was mentioned in Chapter 2, the masses derived by S18 strongly depend on the t_2 parameter of the nova eruption, and in consequence, it is expected a tight correlation between $M_{\rm WD}$ and t_3 for this dataset. The WD masses from S18 and from other sources were correlated against the derived expansion velocity, axial ratio, and t_3 associated with the shells. The results are shown in Fig. 5.14, where the left column shows the results considering the masses of S18, and the right column the masses from other sources. From a visual inspection, it is evident the presence of the (expected) anti-correlation between the S18 masses and t_3 (bottom-left panel; $\tau = -0.69$ and a p-value=0.001), but when considering the other two variables, or $M_{\rm WD}$ from other sources, the situation is different.

In the case of $M_{\rm WD}$ from S18 and the expansion velocity (top left panel), the data suggest a weak correlation where systems hosting lower $M_{\rm WD}$ show lower expansion velocities ($\tau = 0.25$ and a p-value=0.24). Similarly to the behaviour observed in Fig. 5.13, the systems of V1425 Aql and BY Cir deviate from the rest of the data. When considering the axial ratio (mid left panel), the data suggest an anti-correlation where more massive WDs lead to smaller axial ratios ($\tau = -0.31$ and a p-value=0.16). The behaviour observed is, unsurprisingly, very similar to the distribution of datapoints

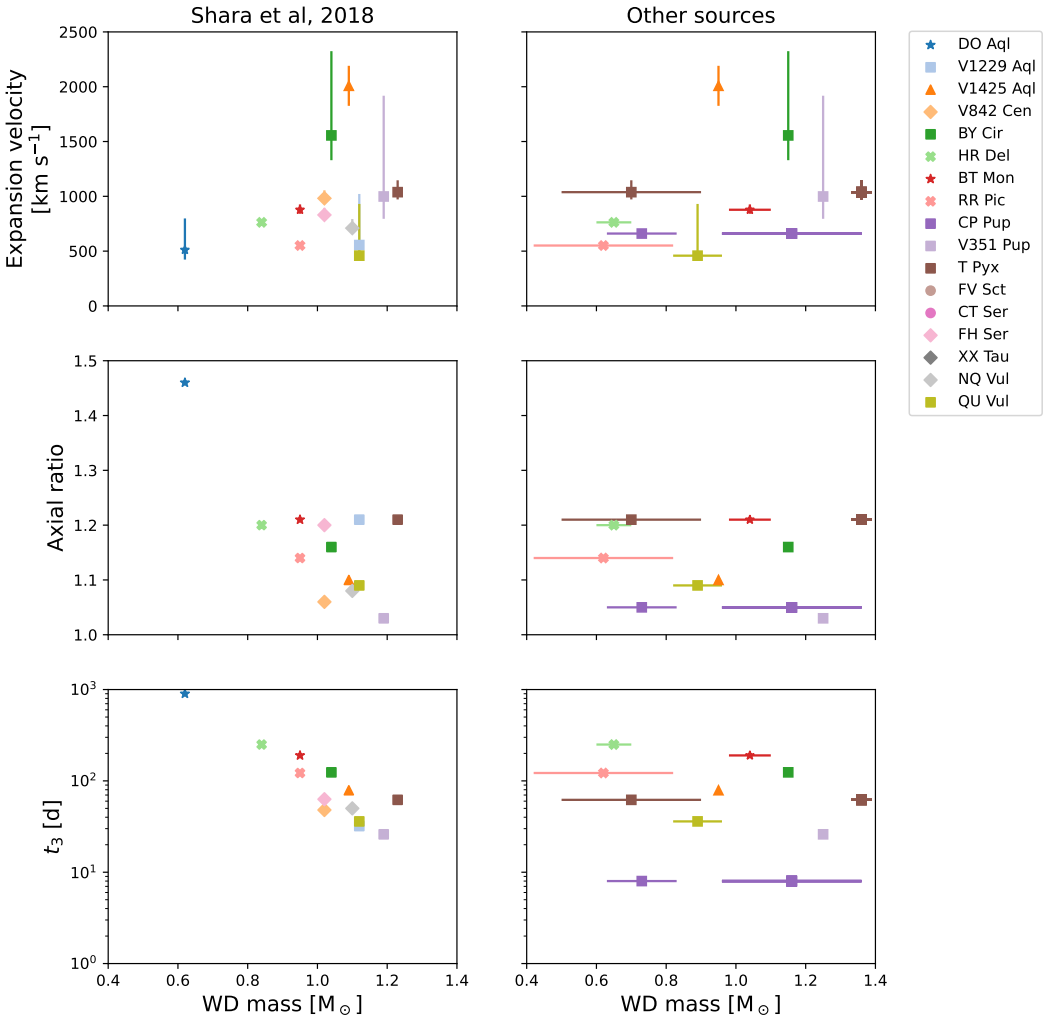

Figure 5.14: Behaviour of expansion velocity (top), axial ratio (mid), and t_3 (bottom) as a function of $M_{\rm WD}$. $M_{\rm WD}$ is separated between Shara et al. (2018) (left) and from other sources (right). In the first case, a strong correlation between $M_{\rm WD}$ and t_3 reveals the strong dependence of the model employed by Shara et al. (2018) on t_3. No strong correlations were found with other parameters.

in Fig. 5.12.

When considering $M_{\rm WD}$ from different sources rather than S18, the data appear more scattered, without showing evident correlations. The two different $M_{\rm WD}$ reported for CP Pup and T Pyx can be distinguished. By favouring one or another value, we can test under which combination of $M_{\rm WD}$ a strong correlation might appear. When considering $M_{\rm WD} = 0.73$ for CP Pup and $M_{\rm WD} = 1.36$ for T Pyx, a mild correlation between $M_{\rm WD}$ and the expansion velocity appears ($\tau = 0.44$ and a p-value=0.12). If instead, $M_{\rm WD} = 1.16$ and $M_{\rm WD} = 0.7$ are considered for CP Pup and T Pyx, respectively, a mild anti-correlation appears with the axial ratio ($\tau = -0.37$ and a p-value=0.17). No correlation appears with t_3 independent of which $M_{\rm WD}$ are considered for CP Pup and T Pyx (resulting p-values > 0.26).

5.1.4 Shells in 3D

As it was already established in Chapters 3 and 4, one of the main advantages of IFS is the possibility to infer and reconstruct the 3D geometry of the nova shell directly from the datacube. The analysis of the position-position-velocity (PPV) diagram provides a direct view of the shell geometry, allowing for the distinction of rings, filaments and clumps within the shell.

PPV diagrams

The PPV diagrams were obtained in the same manner as in previous chapters, including a small improvement for the background subtraction, in that the wavelength region considered for that purpose can be provided by the user and does not depend on the region selected for the PPV extraction, as was previously the case. For all shells, the region between 6513 and 6613 was selected for the extraction, which includes the Hα+[NII] emission. To reduce the noise in the datacube, this was smoothed using a 3D Gaussian kernel with $\sigma = 1$ pixel in each axis. After the smoothing process, the selection of svoxels was done by considering a flux threshold corresponding to 10 MUSE flux units (1 MUSE flux unit $= 10^{-20}$ erg s^{-1} cm^{-2} Å^{-1}). This threshold was applied to most of the shells, with some exceptions (e.g. HR Del), which presented higher background flux values, and so the threshold value was increased up to 30 MUSE units to avoid the inclusion of unnecessary background. Other parameters, like the number of adjacent svoxels and the discard of the faintest quantile, were set to one and zero, respectively, to incorporate as much of the shells as possible.

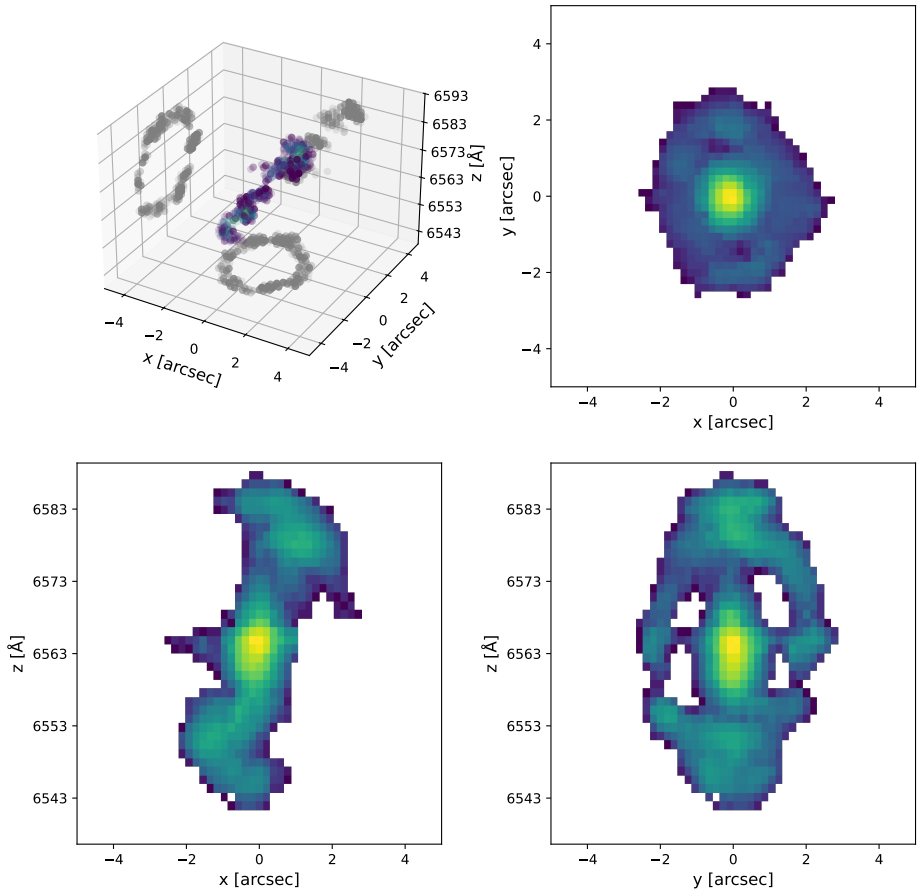

Figure 5.15: PPV diagrams for Hα for the shell around V351 Pup. Top left: the brightest points within the shell are presented in a 3D view with their projections in each plane displayed in grey to better appreciate the shell geometry in the PPV space. Top right: the sum of the total flux of the extracted shell in the xy plane (the plane of the sky), presenting the shell flux using a square-root scale. Bottom left: same as top-right but presenting the xz plane instead to appreciate the behaviour of the shell in this axis as a function of the wavelength. Bottom right: same as the bottom-left but for the yz plane instead. The shell around V351 Pup consists of a single ring surrounding the system.

As examples of the resulting PPVs, the shells around V351 Pup, FH Ser, and T Pyx are presented in Figs. 5.15 to 5.17. The advantage of presenting the shell using these diagrams is that it allows for discerning the different structures that form the nova shell. In the case of V351 Pup (Fig. 5.15), the shell consists of a sole equatorial ring, which is clearly visible in the top left corner of the figure. This panel presents a 3D view in three axes that form the PPV plane –x corresponding to the RA, y to the declination, and z to the wavelength– of the brightest 10% data points of the shell after masking the central star. The projection of the data points in the different planes of the PPV space is presented in grey. It is easy to identify the ring geometry in these projection planes, which appear as a circle in the xy plane (the plane of the sky) and the yz plane, while in the xz plane, its projection is more similar to a line. Depending on the inclination of the ring, the projection in the different planes will vary, but in general, there will be a plane where it will look more similar to a line than a ring. This marks the distinction with an ellipsoid, which will appear as a ring in all the projections, despite its inclination.

The projection of the whole nova shell in the different planes, including the emission from the post-novae, is presented in the remaining three panels of the figure. In these cases, the panels display the flux corresponding to the 'collapse' of the PPV in each plane, that is, the sum of the data in the x,y, and z axes. In the xy plane, the shell appears as it is in the NB images. In the case of V351 Pup, it appears with a circular shape, as already discussed in Sections 5.1.1 and 5.1.2. The other two planes, xz and yz, show the distribution of the shell's material as a function of the wavelength (and thus, velocity). The contribution of the post-novae emission dominates the central part of the planes ($x, y \sim 0$) due to the emission coming from the accretion disc within the system. In this case, the extension in velocity of the emission from the post-nova is not particularly high, which allows for a clear identification of the emission coming from the surrounding shell. As was already mentioned, in these planes the ring appears as a line in the xz plane and as a circle in the yz plane.

Many of the shells also present polar material, which in the PPV diagrams appears as 'clouds' clearly distinguishable from the equatorial ring. As an example, the PPV of the shell around FH Ser, whose images and velocity maps show the presence of polar material and an equatorial ring, is presented in Fig. 5.16. The equatorial ring in the shell is noticeable in the 3D view presented in the figure, and particularly evident in the xz projection, where the ring appears separated from the polar material towards the east and west of the system. The ring is not clear in the xy plane presented in the

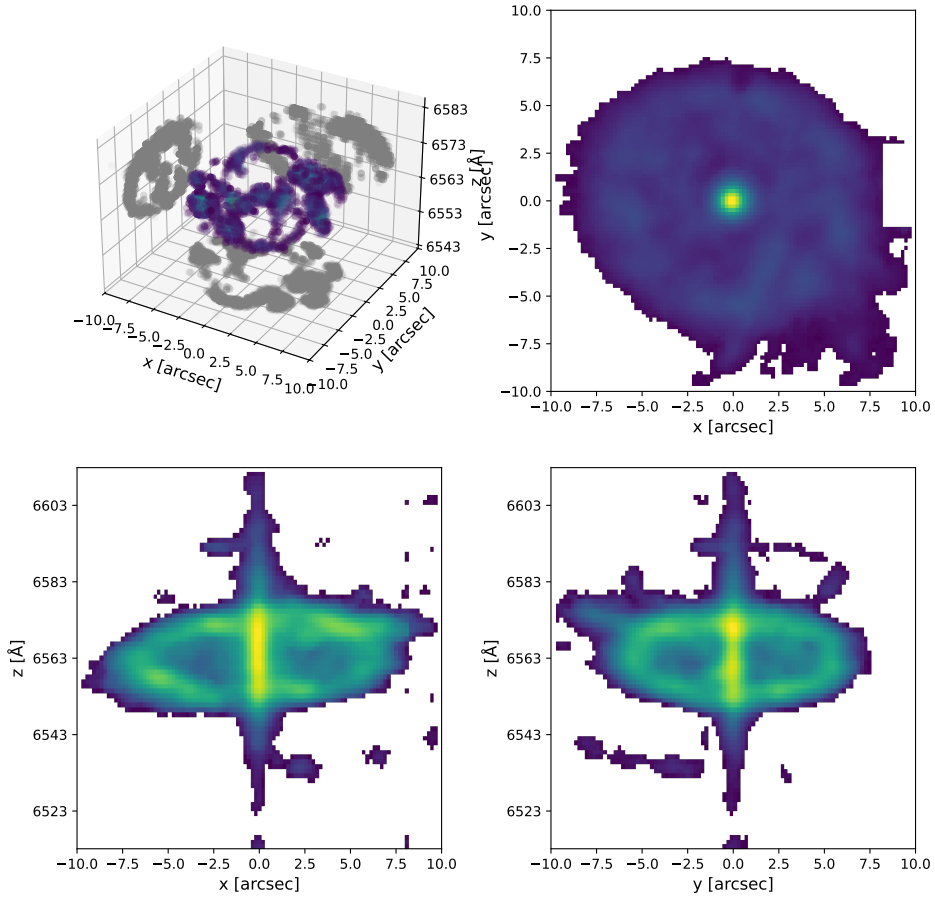

Figure 5.16: Same as Fig. 5.15 but for the shell around FH Ser. In the case of FH Ser, the equatorial ring can still be distinguished from the polar material in the xz plane, but in the rest of the planes, the contributions of all the structures are mixed and can not be discerned.

top right panel, but it can be distinguished in the xz plane at the bottom left, as an emission that crosses the post-nova at $x \sim 0$. The polar filaments can also be distinguished as emissions at the extreme x values, positive (west) and negative (east) of the system. In the yz plane, the emission of all the sources mixes, making the distinction between sources a very difficult task. The overall geometry of the shell can be described as an ellipse in the three planes, which is consistent with an overall ellipsoidal geometry of the shell.

In addition, the presence of [NII] λ 6548 and λ 6584 Å emission in the yz plane can be noticed, which likely originates close to the polar material. In some shells, the contribution of [NII] is significant, which makes the identification of the different elements of the shell a more difficult task. A good example of this is the shell around T Pyx, whose PPVs diagrams are presented in Fig. 5.17. Here, the hydrogen equatorial ring described by Izzo et al. (2024) can be detected as the straight emission crossing the $x \sim 0$ at $z \sim 6563$ in an apparent 45° angle, while in the yz plane, it appears as a ring around $z \sim 6563$. The polar material in this shell is dominated by [NII], as the velocity maps indicate (Section 5.1.2), and this is also reflected in the PPV diagrams. The [NII] emission dominates the xz and yz planes for $z > 6563$. In the xz plane, two lines can be seen at a negative angle, which corresponds to the polar material of the shell. In the yz plane, they appear to form a ring structure around the system.

The PPV diagrams for the rest of the shell are presented in Appendix B, and in the following, a brief description of the properties displayed by each shell is given.

- **DO Aql** (Fig. B.1): A ring appears in the xz plane with two 'lobes' of higher emission located at the east and west of the system, while no other clear structures are discernible. The orientation suggests that we are seeing the ring edge-on. Some [NII] emission is observed sharing the spatial position of the 'lobes' observed in Hα. The Hα emission is redshifted, indicating a systemic velocity $v_{\rm sys} \sim 140$ km s^{-1}.

- **V1229 Aql** (Fig. B.2): The emission is dominated by the [NII] arc in the north. The Hα shell consists of a spherical structure centred at 6563 Å, and extending up to velocities of $\sim \pm 740$ km s^{-1} ($\sim$ 25 slices). The [NII] arc is more evident at the yz plane, being observed at λ6584 and λ6548 Å. Two additional [NII] blobs are present, being discernible from the rest of the shell in the xz plane.

- **V1425 Aql** (Fig. B.3): A compact shell with Hα and [NII] emission, plus an asymmetric shell dominated by [OIII] emission. A more detailed analysis of the data

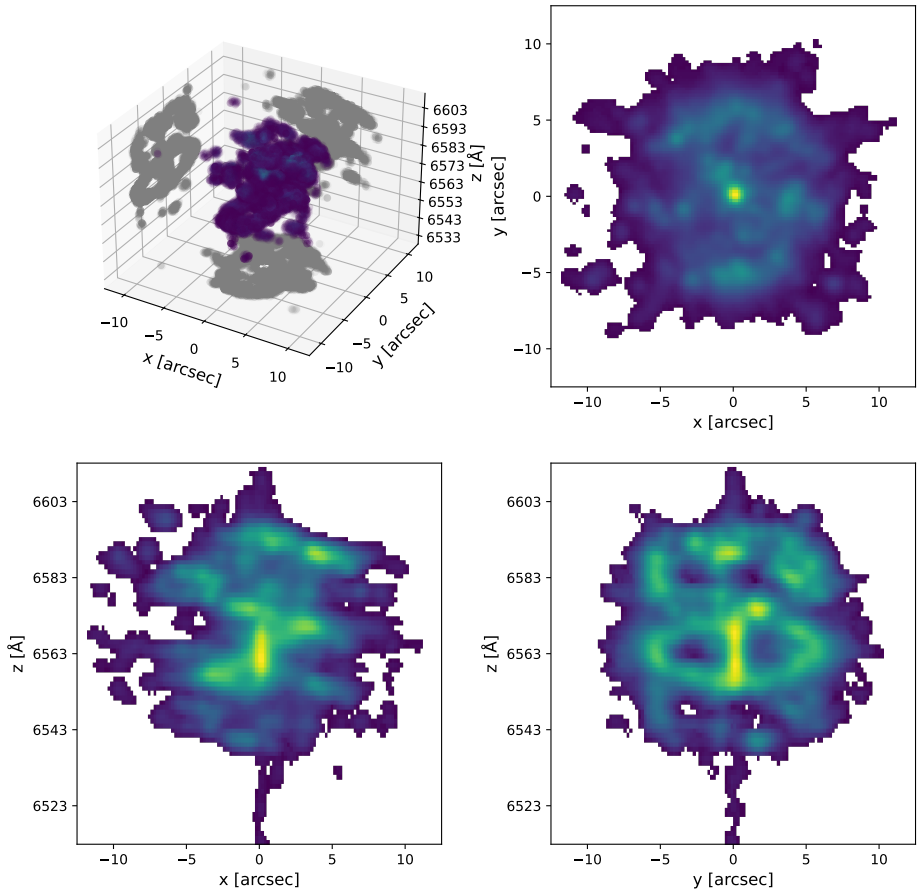

Figure 5.17: Same as Fig. 5.15 but for the shell around T Pyx. In addition to the equatorial ring and polar material observed in Hα, this shell presents a significant contribution of [NII] emission, which also mixes with Hα. Despite the mixing of emissions, the equatorial ring can be identified within the planes, as well as the polar material observed in [NII].

is provided in Chapter 4.

- **V842 Cen** (Fig. B.4): A compact Hα shell with significant contribution of [NII] emission. A certain ringed structure starts to be distinguishable within the Hα shell. The [NII] shell shows two bright emissions at blue and red wavelengths, with the λ6548 Å blue-shifted emission and the λ6584 Å red-shifted mixed with the Hα emission.

- **BY Cir** (Fig. B.5): The shell appears as a compact Hα emission with no discernible structure within it, besides certain regions showing a higher flux. The shell shows similar characteristics to the inner shell of V1425 Aql.

- **HR Del** (Fig. B.6): This shell shows Hα emission consisting of an equatorial ring and polar material, which is evident in the three plane projections. The [NII] emission is mixed with hydrogen, but its structure as a polar material is discernible, particularly for the λ6584 emission.

- **BT Mon** (Fig. B.7): The shell around this old shell consists of clumps of Hα, but some geometry can still be recognised. The clumps at the south and north both have red and blue shifted velocities, which argues against a ring structure, and instead, an ellipsoid geometry is favoured. This implies that the observed clumps correspond to polar material with no presence of an equatorial ring.

- **RR Pic** (Fig. B.8): This shell is dominated by an Hα equatorial ring, which is discernible in all the projection planes. A more detailed analysis of the geometry of this shell was done in Chapter 3.

- **CP Pup** (Fig. B.9): The shell consists of dozens of clumps arranged over an ellipsoidal geometry. The arrangement of the clumps in the xz planes, particularly the appearance of a 'bar' inside the ellipse formed by the clumps, suggests the presence of a ring within the shell.

- **FV Sct** (Fig. B.12): The flux at λ6563 Å is significantly stronger than at other wavelengths, which introduces additional noise and makes the determination of the shell geometry difficult. A potential Hα ring structure is revealed in the xz plane in the form of an incomplete ellipse. The [NII] asymmetric emission shows two lobes of higher flux, and its geometry is consistent with an arc that expands in the plane of the sky (no major variation in wavelength).

- **CT Ser** (Fig. B.13): The PPV of this apparent ringed and circular shell in the plane of the sky shows an equatorial ring and polar material in Hα. This is particularly evident in the projection of the brightest points on the yz plane, where the ring and polar material are discernible from each other.

- **XX Tau** (Fig. B.15): This shell presents an Hα equatorial ring with some material that can be associated with polar material. No [NII] is detected for this shell.

- **NQ Vul** (Fig. B.16): Another shell that shows a clear Hα equatorial ring with polar material, without [NII] emission. The polar material was hidden behind projection effects, giving the appearance of a spherical shell.

- **QU Vul** (Fig. B.17): A compact shell whose geometry is not evident in the MUSE data. The brightest points in the PPV diagram correspond to two lobes of emission at $\sim \pm 450$ km s^{-1} ($\sim$10 Å from Hα rest line), which show a certain inclination in the xz plane.

5.2 Discussion

5.2.1 Nova shells geometry and kinematics

The Hα+[NII] images presented in Fig. 5.1 show that the nova shells in the sample have a variety of geometries. If we consider the planetary nebulae classification proposed by Parker et al. (2006), and applied to nova shells by Santamaría et al. (2025, , S25 from here on), we can conclude that most of the shells in the sample present geometries consistent with ellipses and spheres. By applying the arbitrary selection used by S25 that shells with axial ratio < 1.05 are classified as rounds (spherical), then only V351 Pup is classified as such, with the rest classified as elliptical. This proportion is in contradiction with the distribution presented in S25, where the number of round shells is $\sim 50\%$ of the number of elliptical shells. It is important to consider the methodology used to measure the best ellipse parameters for each shell, from which the axial ratio is derived. In both works, this thesis and S25, a 5σ criterion was used to select the pixels corresponding to the shell, but the method used to fit the actual ellipse may differ. This difference is later reflected in the axial ratio of each shell, and consequently, in the aforementioned differences. This also illustrates the difficulty in determining the boundaries of an extended source, such as a nova shell.

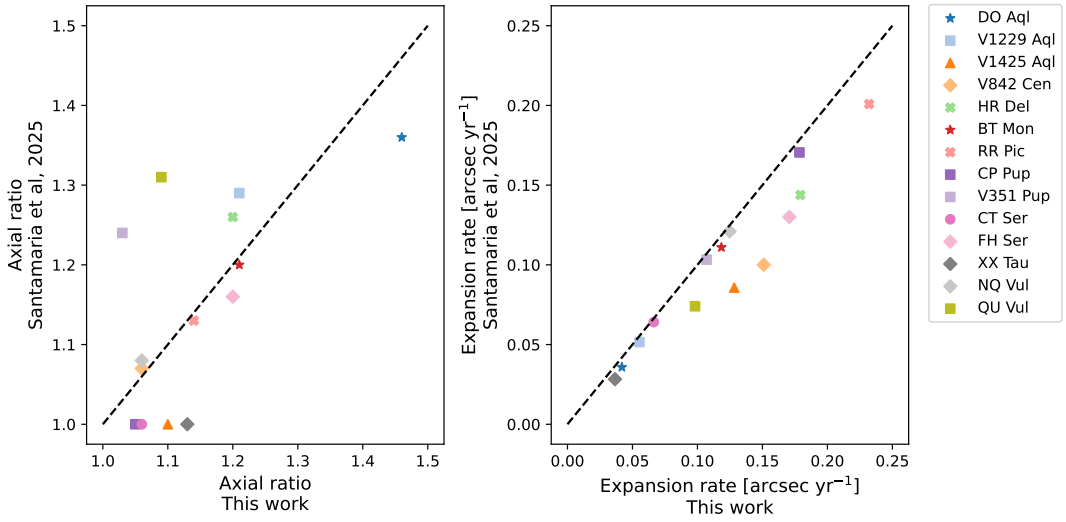

Figure 5.18: Comparison of axial ratio (left) and expansion rate (right) between this work and S25. The expansion rate differences indicate a systematic difference in this work, where larger shells are preferred with respect to the values derived by S25. The differences in axial ratio do not show systematics, but indicate differences in the methodology used to measure the ellipse parameters.

These differences are illustrated in the left panel of Fig. 5.18, where the axial ratios are compared. There are significant discrepancies between the axial ratio derived in this work and from S25, with only a few of them showing a similar axial ratio (black dashed line). The right panel of the figure shows the expansion rates derived from the semi-major axis. It shows a systematic trend where the semi-major axes derived in this work are larger than in S25. Because the expansion rate considers the age of the shell, the trend can not be explained by the fact that we are analysing more recent data (thus older ages for the shells), but instead reveals a difference in the methodology. From the images and ellipses presented in Figs. 5.9 and 5.10, we can claim that our methodology fits well the axial ratio of shells, but is most sensitive to the outer parts of the shell, as the differences in expansion rates indicate.

The Hα+[NII] NB images and their respective PPV diagram revealed the intrinsic geometry of nova shells. Several shells presented evidence for polar material either in their images (HR Del, RR Pic, T Pyx, and FH Ser) or in their PPV (XX Tau, CT Ser, NQ Vul). The latter are particularly interesting as they appear as round shells in the NB images, with the polar material hidden by projection effects. This has implications for the axial ratio correlations. On the other hand, two shells only show the presence of

equatorial rings (DO Aql and V351 Pup). The absence of polar material in these ones may be a result of the observations not going deep enough to detect it. On the opposite case, there is the clumpy and fragmented shell around BT Mon. The PPV suggest the observed clumps correspond to polar material, which leads to the absence of an equatorial ring in this shell. If this is the case, it will imply that polar material presents a higher luminosity than the equatorial ring, explaining the absence of the latter by not going deep enough to detect it. This scenario will make BT Mon an unusual nova shell, and in a certain sense, similar to the helium nova V445 Pup, whose remnant is dominated by polar material (Macfarlane et al., 2014).

Some shells (V1425 Aql, V842 Cen, and BY Cir) appear as a compact shell in the PPV diagram, without discernible geometries. The possibility that they appear like that because of low resolution can be discarded, as other shells of similar size present recognisable geometries (V351 Pup and XX Tau). An additional answer comes from considering the age of these shells. They are, together with V351 Pup, the youngest shells in the sample, which suggests that these shells may be embedded in a diffuse cocoon of hydrogen which will dissipate with time, allowing for the observation of the proper shell geometry. In the case of V351 Pup, which presents a similar age but also a recognisable geometry, its t_3 may provide an explanation, as this shell is the second fastest in the sample ($t_3 = 26$ days), only surpassed by CP Pup ($t_3 = 8$ days). In consequence, the shell should evolve faster, revealing its geometry more quickly.

A possible physical origin for this hypothetical hydrogen cocoon may lie in the fast wind blowing from the WD after the TNR. This wind blows in all directions (with allegedly fewer obstacles in the polar directions; Aydi et al., 2020), which, in combination with its high ejection velocity, may explain the presence of this hydrogen coccon surrounding the system. The slow ejecta, on the other hand, is embedded within the cocoon, and its geometry can not be resolved by MUSE at this time.

Additional peculiarities are observed in the irregular shells of V1229 Aql and FV Sct, whose geometries show evidence for asymmetric ejecta. These make them particularly interesting as asymmetric shells are not common, with V1425 Aql the most evident exponent of this sub-classification (Chapter 4, Tappert et al. (2023)). The flux, velocity maps, and PPV of these three shells reveal that the asymmetric component is entirely dominated by forbidden emissions, either [NII] in the case of V1229 Aql (Fig. 5.5) and FV Sct (Fig. 5.6), or by [OIII] in the case of V1425 Aql (Fig. A.3). In all cases, the asymmetric ejecta are further away from the system than the Hα emission, implying a faster ejection velocity (assuming it was ejected at a similar time as the hy-

drogen). This, together with the emission being dominated by forbidden transitions (implying a less dense environment), is consistent with the ejecta originating from the 'polar wind' that is thought to appear days after the nova eruption (Aydi et al., 2020).

The origin of the asymmetry is far from clear, though. In Tappert et al. (2023) and Chapter 4, the possible intrinsic and extrinsic origins for the shell geometry were discussed. From an extrinsic point of view, a possible interaction with the ISM appears as the most reasonable origin for the asymmetries in these shells. The three systems are located within the galactic plane (b = -5.4, -3.9, and -2.2 deg for V1229 Aql, V1425 Aql, and FV Sct, respectively), and thus a denser ISM environment is expected (e.g. Capitanio et al., 2017). A denser environment will inhibit the formation of forbidden emission, resulting in an asymmetry in the ejecta if the ISM surrounding the system is also asymmetric in density, as has already been discussed. An additional possibility is that the asymmetries are the result of bow shocks (e.g. V341 Ara, Castro Segura et al., 2021). A bow shock originates when an outflow moves supersonically through a dense environment, but when the source that originates the outflow also does (del Palacio et al., 2018). If the observed asymmetries are the result of a bow shock, then the proper motion of the system should point in the direction of the asymmetry. Fig. 5.19 shows the three asymmetric shells in Hα (grey image), [NII]λ6584 Å(red contours), and [OIII]λ5007 Å(blue contours). The *Gaia* DR3 proper motion of each system is presented with white arrows, with their size proportional to their motion. From here, it is clear that the asymmetries in V1229 Aql and FV Sct can not have a bow shock origin, as the system's proper motion does not match the direction of the ejecta. In the case of V1425 Aql, the proper motion direction is similar to the direction of the outer ejecta; however, other characteristic features of bow shocks, such as radio and high-energy ($>$ 1 keV) emission, have not been reported. Furthermore, the derived geometry of the outer ejecta in V1425 Aql (Chapter 4) does not match the expected conical geometry of a bow shock (del Palacio et al., 2018), ruling out this possibility. As an intrinsic origin for the asymmetric ejecta in V1425 Aql, the possible role of a magnetic WD was proposed. The presence of a magnetic WD in V1425 Aql has not been conclusively addressed, giving space for some speculation (see Sections 2.3 and 4.2 for a more detailed explanation). The basic physical parameters of the system for V1229 Aql and FV Sct are unknown, as well as their nova eruption properties. This prevents the identification of common features within these 3 systems that may shed light on a common physical mechanism responsible for the asymmetric ejecta.

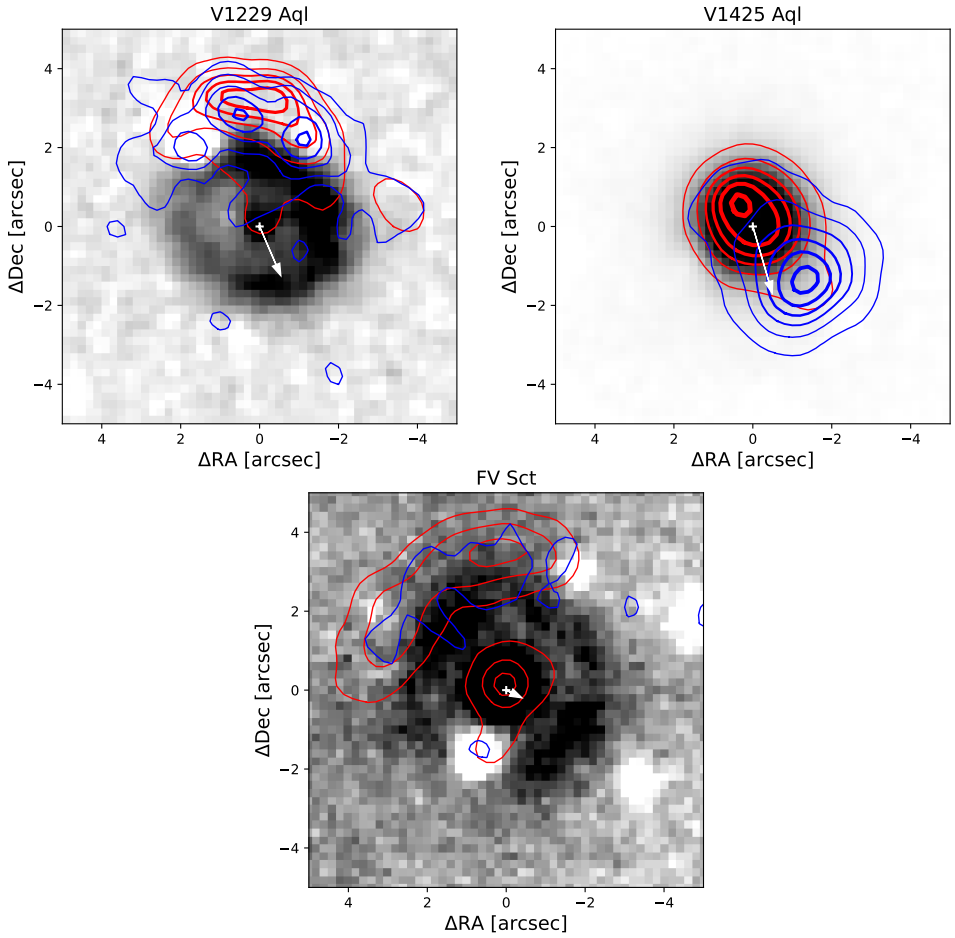

Figure 5.19: Hα (grey background), [NII] (red contours), and [OIII] (blue contours) images of the asymmetric shells of V1229 Aql, V1425 Aql, and FV Sct. The position of the systems is indicated with a white cross, while the white arrow indicates the direction of the proper motion of the system (according to *Gaia*), with the size being proportional to the motion velocity. For V1229 Aql and FV Sct, there is no indication that the proper motion is related to the asymmetric ejecta, while for V1425 Aql, the proper motion of the system is very close to the direction of the ejecta.

5.2.2 Correlation between nova parameters, system, and shell properties

Our measurements of the shell's projected axial ratios show a strong correlation with t_3, in a similar way as for previous works (Slavin et al., 1995; Santamaría et al., 2022b). The distribution of t_3 as a function of the light curve type shows that light curve types 'F' and 'J' are the ones with the highest t_3, while the P-type light curves are the fastest (lowest t_3). As expected, this distribution is the same as that derived from Strope et al. (2010). When considering the axial ratio instead of t_3, the aforementioned distribution is lost, and the different light curve types are more mixed. The differences in the distribution of the light-curve classes when considering the axial ratio or t_3 may hint at the existence of additional factors that may play different roles in the shell geometry depending on the light-curve class. It must be acknowledged, however, that the low number of systems involved in this analysis may lead to an overinterpretation of the data. The aforementioned distribution and possible differences related to the light curve class could be the result of random variation and, in any case, represent the distribution of the overall population. It is necessary to continue increasing the amount of data to draw a firm conclusion.

The theory states that the most crucial parameter that determines the properties of the nova eruption and the subsequent shell geometry is $M_{\rm WD}$. Systems hosting WDs with higher mass should cause nova eruptions that evolve faster (smaller t_3) and consequently, originate nova shells with higher ejection velocities and rounder geometries (lower axial ratios). All these parameters should display a clear correlation between them. We tested this by analysing the aforementioned relations from our measurements and literature values. The velocity of the expanding shell, derived from its semi-major axis and distance, does not show the anti-correlation expected from the theory (left panel of Fig. 5.13).

However, two suggestive populations appear in the data, each one presenting strong anti-correlations. The first population corresponds to the systems V351 Pup, CT Ser, V842 Cen, CP Pup, NQ Vul, QU Vul, FV Sct, RR Pic, and XX Tau, which are grouped at the bottom left of the figure. The Kendall's τ and p-value for this group of shells are -0.54 and 0.05, respectively, indicating the presence of an anti-correlation in the data. The second group, composed of the rest of the shells (V1425 Aql, BY Cir, T Pyx, BT Mon, FH Ser, HR Del, V1229 Aql, and DO Aql), also show the presence of an anti-correlation ($\tau = -0.62$ and p-value $= 0.04$). There are no evident differences

between these two tentative groups (in, for example, their light-curve class) to claim that they reflect two different populations of nova shells, and that they are not the result of simply low-number statistics.

On the other hand, an interesting but doubtful anti-correlation appeared when comparing the expansion velocity of the shells against their age (right panel of Fig. 5.13). This anti-correlation appears after removing the shells of V1425 Aql, which presented an unusually high velocity, and T Pyx, arguing that its RN nature may have affected the ejecta's kinematics. It must be emphasised that Kendall's tau test does not consider the uncertainties associated with the data, which are significant for many data points in the sample. These uncertainties may lead to a larger scatter of p-values, putting in question the resilience of the observed anti-correlation.

But assuming that such anti-correlation between velocity and age is real, it could, in principle, be explained by deceleration of the ejecta in older shells. However, this possibility could be ruled out by the analysis of old nova shells like RR Pic ($\sim$ 97 years old; Chapter 3), T Aur ($\sim$ 125 years old; Santamaría et al., 2020), or GK Per ($\sim$ 110 years old; Liimets et al., 2012), which conclude that these century-old nova shell are still expanding freely. Unless these cases are revealed as exceptional, and most of the shells start to show signs of deceleration before their first century, an additional explanation must be considered.

Such an explanation could be a systematic effect. The implemented method is sensitive to the outer, fainter regions of the shells. Since a nova shell is not a single structure but rather composed of several layers expanding at different velocities, the outer regions will expand and dilute more rapidly into the ISM. For this reason, older shells expanding at higher velocities should be harder to detect, potentially introducing a bias toward the detection of shells with lower expansion velocities. In the first case, the outcome is a systematic effect in which older shells are traced primarily by their inner regions, while in the second case, a bias toward slower-expanding shells is produced. Together, these two phenomena could account for the apparent anti-correlation without invoking shell deceleration.

Lastly, it should be emphasised that both parameters, the expansion velocity and the axial ratio, are subject to additional sources of noise. The derived expansion velocity directly depends on the distance estimated from *Gaia* parallaxes, many of which have uncertainties exceeding the 30% threshold typically adopted to classify them as reliable (Luridiana et al., 2015). In addition, the expansion velocity also depends on the semi-major axis of the shell, whose uncertainty was not even considered in this

work due to the challenges that this present (See Sect. 5.1.3). The axial ratio, meanwhile, corresponds to a projected value, which in some cases may differ from the true intrinsic ratio. The scatter introduced by these factors may compromise the robustness of the results; therefore, they should be interpreted with caution.

In the case of the WD masses, we searched for available information in the literature, from which we made a distinction between the masses published by S18 and those from other sources. The argument to make this distinction was that the models used by S18 are strongly dependent on t_2 (and thus, t_3), which is reflected in the correlation with this parameter (Fig. 5.14). In consequence, the observed weak correlation between $M_{\rm WD}$ and expansion velocity can be considered a result of this dependence.

On the other hand, when considering the WD masses from other sources, no clear correlation is observed. In this case, the system CP Pup and T Pyx has two (very) different reported values for their $M_{\rm WD}$. By testing the different combinations of $M_{\rm WD}$ available, it was found that a mild correlation appears between $M_{\rm WD}$ and the shell expansion velocity when the less massive value for CP Pup ($\sim$ 0.73 $M_\odot$; Veresvarska et al., 2024) and the most massive value for T Pyx ($\sim$ 1.36 $M_\odot$; Selvelli et al., 2008) are chosen. On the other hand, when the opposite situation is considered: most massive WD for CP Pup ($\sim$ 1.16 $M_\odot$; Selvelli & Gilmozzi, 2019) and less massive WD for T Pyx ($\sim$ 0.7 $M_\odot$; Uthas et al., 2010), a weak anti-correlation with the axial ratio is observed. Although both correlations are in line with the predicted theory: the correlation between $M_{\rm WD}$ and expansion velocity and the anti-correlation between $M_{\rm WD}$ and axial ratio; they do not appear simultaneously in the data. The appearance of these correlations depends on the combination of $M_{\rm WD}$ for CP Pup and T Pyx, resulting in mutually exclusive combinations. In consequence, the analysis does not allow us to favour one reported $M_{\rm WD}$ over the other.

The expected anti-correlation between $M_{\rm WD}$ and t_3 was not observed in any case. A likely reason for not observing any obvious correlation between $M_{\rm WD}$ and the three parameters analysed: expansion velocity, axial ratio, and t_3, is the scatter that originates from the difficulty of measuring $M_{\rm WD}$. As was already mentioned, the expansion velocity and axial ratio used are subject to hidden factors which might induce additional noise in the data, resulting in a lack of correlations. Another possibility is that $M_{\rm WD}$ does not correlate with these parameters, at least in the way that the theory predicts. This possibility sheds doubts about the models used by S18 and points to some additional, unknown factors playing a role during the ejection of the nova shell. With the current data, it is not possible to favour one possibility over the other.

It is also worth noting that these correlations were done using the projected axial ratio. This ratio, however, may not reflect the actual ratio of the nova shell. The PPV diagrams presented show that some shells that appear rounded contain equatorial rings and polar material (e.g. CT Ser). This implies that, after the respective conversion of the PPV into the proper physical PPP space, the true axial ratio may differ significantly from the projected axial ratio. This will have significant consequences for those shells that consist only of an equatorial ring (V351 Pup and DO Aql), as the lack of polar material precludes the determination of an axial ratio.

The determination of the true axial ratio for the shells will help to determine their true distribution. An attempt to clarify this was made by S25, who used the projected distribution of ellipsoidal shells and assumed a that the true distribution follows a Gaussian distribution, concluding that most of the nova shells (95%) have true axial ratios lower than 1.30, thus explaining the relatively high fraction of round shells in their sample as the result of projection effects. The axial ratio of 1.30 derived seems to be an underestimation of the true value, however, as the author's sample has $\sim$ 10% of shells with projected axial ratios greater than 1.30 [1]. The MUSE data have the potential to better clarify this topic by studying the axial ratio of the shells after the conversion to the PPP space.

5.2.3 Future prospects

The results presented in this chapter are preliminary for what will be a future, more detailed study. Already indirectly mentioned was the investigation regarding the deceleration of nova shells. In Section 5.1.3, the semi-major axis of nova shells was determined, from which evidence for a possible deceleration of nova shells might be inferred by comparing the derived semi-major axis against the age of their respective shell. In Chapter 3, a more detailed study of the expansion of the different knots observed in the shell around RR Pic was done. By comparing the position of these knots with the image in Gill & O'Brien (1998), it was concluded that the shell continues expanding freely through the ISM. A similar analysis can be performed for the different shells within this sample, particularly for those old shells already imaged in previous studies (e.g. CP Pup, BT Mon, or HR Del). Such analysis will clarify whether these shells are decelerating or not, providing further evidence for the discussion of when

[1] the axial ratio of the projection of an ellipsoid can only be equal to or smaller than the axial ratio of the ellipsoid.

and how shells decelerate.

On the other hand, the tentative deceleration inferred from Fig. 5.13 is affected by several uncertainties. The expansion velocity was calculated from the semi-major axis obtained through ellipse fitting and from the distance to the system derived from *Gaia* parallaxes, both of which introduce significant uncertainties. An alternative approach would be to adopt velocities derived from spectroscopic analyses, which may provide a more accurate characterisation of the ejecta velocity and, consequently, a more reliable assessment than that presented here.

The presented analysis of the PPV maps can be expanded. They can be used to measure the expansion velocity of the ejecta, providing a point of comparison with the velocities determined from the axial ratio measurements. The PPVs can be used to better establish the different geometries and structures within the shell. Several shells present clear equatorial rings in their PPVs for which their inclination can be obtained. That information can be used to find the ellipsoid that best fits the data in the PPV space. After transforming the PPV space into the PPP, using the distances to the systems, the true axial ratio of the shells can be derived from the ellipsoid. This will help to clarify the distribution of axial ratios of nova shells, and whether or not this correlates with physical parameters such as $M_{\rm WD}$ or $v_{\rm ej}$. Additionally, it will provide an independent indicator of the distance to the systems. In the case that the distance used to obtain the PPP is close to the true distance to the system, the equatorial ring should correspond to a circular ring. If the resulting ring shows instead an evident ellipticity, likely, the distance was incorrect. Furthermore, the conversion to the PPP will provide a new view for the different shells, which may lead to the characterisation of unnoticed features. A similar exercise was done in Chapter 3 for the shell around RR Pic, where its 3D view revealed cloudy structures above and below the main equatorial ring.

The 3D view of the shells resulting from the PPP is useful to investigate the spatial differences between allowed and forbidden emissions within the shell. This is particularly interesting for the asymmetric shells where the forbidden emission extends further beyond the limits of the Hα emission, or for shells where both kinds of emissions are mixed in a complex manner (e.g. HR Del or T Pyx). This, however, presents the additional challenge of disentangling the Hα from the [NII] emission. This is not a trivial task when the red part of Hα overlaps with the blue part of [NII], but the problem can be mitigated by examining the PPV of the shell carefully, or when there is Hβ emission.

5.3 Conclusion

In this chapter, the analysis of 17 nova shells was presented, focusing mainly on the geometry of these shells from NB Hα+[NII] images. The images showed the variety of geometries within the sample, including ellipsoidal (12), clumpy (2), round (1), and asymmetrical (2). Standing out are the asymmetric shells around V1229 Aql and FV Sct, whose NB images revealed peculiar ejecta to the north of the systems. The flux images and velocity maps revealed that these asymmetric ejecta are dominated by forbidden emission, similar to the case observed in V1425 Aql. The origin of the asymmetries is still unclear. The lack of certainties about the physical parameters of the binary system in general and the WD in particular for these systems prevents us from supporting or ruling out the possibility of an intrinsic origin. On the other hand, the analysis of the proper motion of these systems rules out a possible bow-shock origin for these asymmetries in V1229 Aql and FV Sct, but not necessarily for V1425 Aql.

Additionally, from the Hα image, the projected axial ratio of the shells was measured by fitting an ellipse to the contour defined by selecting pixels whose flux is 5σ above the background value. The results show that most of the shells (10 of 17) have an axial ratio lower than 1.15, while the most extreme case is DO Aql with a value of 1.46. The resulting values were used to search for correlation parameters against t_3, expansion velocity, age of the shell, and $M_{\rm WD}$. A strong correlation was found between axial ratio and t_3, following the results of previous works. Another, unexpected but doubtful, anti-correlation appeared between the expansion velocity of the shell and its age. This may be interpreted as evidence for deceleration if we consider the case of RR Pic (whose shell is still expanding freely) as a special case, but it could also reflect biases in the methodology used.

In the case of $M_{\rm WD}$, the values provided by Shara et al. (2018) were used separately from the values reported in other works in the literature. As expected, there is a strong correlation between $M_{\rm WD}$ from Shara et al. (2018) and t_3, resulting from the strong dependence of t_2 in the model used by the authors to determine $M_{\rm WD}$. When considering $M_{\rm WD}$ from other sources in the literature, no strong correlation appeared with any parameter, besides a mild suggestion of an anti-correlation with the axial ratio of the shell, as expected from the theory. The lack of clear correlations in this case can be explained by the intrinsic difficulties of measuring $M_{\rm WD}$ in CVs, or may be an indication that $M_{\rm WD}$ does not correlate with these parameters as we should expect.

With the current data is not possible to confidently choose one option over the other.

The analysis of the PPV diagrams revealed that many of the apparently round shells have polar material hidden by projection effects. This may have strong implications for the analysis of the axial ratio correlations in this thesis and other works. The same PPV diagrams reveal that most of the shells consist of an equatorial ring with polar material, but there is one example of a shell showing only polar material (BT Mon), while others consist only of an equatorial ring (DO Aql and V351 Pup). Three of the four youngest shells in the sample (V1425 Aql, BY Cir, and V842 Cen) appear as compact sources without clear geometries, and it is expected that the latter will be revealed in the future as they continue expanding.

CHAPTER 6

Overall discussion and conclusions

This thesis has focused on showcasing the advantages that IFS observations have for the analysis of nova shells and how they provide new insights into their study. The detailed study of the shell around RR Pic (Chapter 3) demonstrated the power that MUSE has as a diagnostic tool for the study of nova shells, as well as introducing the methods required for such analysis. The following research on the unusual shell that surrounds V1425 Aql (Chapter 4) provided a deep analysis of a shell that challenges our understanding of the shell's ejection mechanisms. The preliminary results of the comparative study of 17 nova shells (Chapter 5) focused on characterising common features among them, including their geometry and kinematics, and how they relate to certain parameters of the nova eruption and from the underlying CV. Some of the shells present unusual features, which make them good candidates for a more detailed analysis than the one carried out in this current thesis.

Across the different chapters, it has been emphasised how the MUSE data allows for a much better characterisation of the overall shell geometry, including spatial geometry and kinematics, when compared with other techniques. This has provided a better comprehension of the geometry of nova shells, how they evolve, and how they correlate with other parameters from the nova eruption or from the binary.

6.1 Advantages of IFS observations

For many years, the study of nova shells was limited to the use of NB images and/or LS spectroscopy. The use of IFS data represents a significant improvement over these techniques, providing a more comprehensive view of the nova shells. This was demonstrated throughout this thesis, as well as in some recent studies (e.g., Santamaría et al., 2022b; Izzo et al., 2024; Guerrero et al., 2025). The capabilities of MUSE, in particular, allow a simultaneous observation of a shell in some of their strongest lines, such as the Balmer, [NII] or [OIII] lines, and a complete kinematic characterisation of the ejecta at each one. This alone is a massive advantage of the instrument compared to the use of classic NB images, where only one line (or two in the case of a blend) can be studied simultaneously. This was demonstrated in Chapter 3 where the shell around RR Pic was firstly imaged in Hβ. Similarly, many of the shells presented in Chapter 5 were observed for the first time at an emission different from Hα, providing new insights into their properties.

Furthermore, the kinematic information provided by MUSE is key to resolving the geometry of nova shells. When using LS spectroscopy, it was necessary to extrapolate the information contained within the slit to the entire shell, which relies on assumptions about its geometry. MUSE, on the other hand, does not require any assumption, as the totality of the shell can be analysed. The advantages that MUSE offers largely surpass its limitations: a low spectral resolution and a limited FoV. They, however, may still present some difficulties for shells expanding at low velocities ($\sim 100 - 200$ km s^{-1}) or whose angular sizes are larger than 1 arcmin.

This provided new possibilities compared with the previous techniques, such as the analysis of the PPV and PPP spaces. In Chapter 3, an introduction to the PPV space and its conversion to the PPP was provided. For the latter, two assumptions were made: first, the material must be expanding radially, that is, it must have originated at the centre of the shell (the central binary) and should not have changed its direction since then. This is a safe assumption, as it is hard to think of a mechanism that deviates the ejecta from its original radial expansion. The second assumption comes from considering that the material has not decelerated since its ejection. This may not necessarily be true for old shells, but it is expected for the younger ones (see discussion in Section 6.3). If these two assumptions are met, the conversion of the PPV into the PPP space is linear and directly proportional to the distance to the system. In systems where the distance is well constrained, the resulting PPP is reliable, but in

cases where this is not the case, the resulting PPP may present distortions in the z-axis (line-of-sight axis) which may indicate an erroneous distance. This presents an opportunity to determine the distance of the systems in an independent and alternative manner.

In the case of the shell around RR Pic, the accurate distance ($d = 501^{+6}_{-5}$ pc) allows for a reliable PPP space (Chapter 3). The analysis of the shell in this 3D space led to a determination of the shell size, but more relevant, it allows for a clear differentiation between emission regions. The PPP revealed that most of the Hα emission is concentrated in the equatorial ring ($\sim$ 99% of the shell total flux), with a minor fraction in the polar regions as filaments of material. In the regions between the equatorial ring and the filaments, [OIII] emission is located, revealing the difference in densities across the shell. Similarly, the PPP analysis of the asymmetric shell in V1425 Aql (Chapter 4) also revealed unexpected features when the geometry of the outer ejecta was unveiled. The inner and symmetric shell, traced by Hβ emission, corresponds to an approximately spherical shell, which is surrounded by the outer ejecta whose geometry, traced by [OIII], consists of a semi-arc and not a plume or a cone, as one may think from the NB images. These results show the significant capabilities of MUSE for the study of nova shells and should encourage the scientific community to continue these kinds of studies.

6.2 Unusual shell geometries

The geometry of nova shells encoded the physical processes that played a role during its ejection. The current model states that the ejection mechanism consists of at least an ejection within the orbital plane of the binary and an ejection in the polar direction, giving the shells their characteristic prolate geometry. The observations supporting this model are numerous (see Aydi et al., 2020, and references therein) but incomplete in the sense that not the entire shell is analysed. In contrast, MUSE has revealed shells with geometries that escaped from the common picture presented before.

The first case of a shell showing an unusual geometry was V1425 Aql (Nova Aquila 1995). Tappert et al. (2023) observed a normal, symmetric, inner shell in Hα and Hβ, but also in [OIII] and [NII]. More interestingly, an extended and asymmetric outer shell was detected in [OIII] and [NII] only, whose origin defies the usual concept of ejecta in nova shells. Although an intrinsic origin for this asymmetric ejecta can not be confirmed, the possibility opens new challenges for the usual model of ejecta. Even

more, what was supposedly an unusual and rare kind of nova shell appeared to be not so rare, with the additional examples of V1229 Aql (Nova Aquila 1970) and FV Sct (Nova Scutum 1960), which also show evident asymmetries in their ejecta (Chapter 5). Similar to V1425 Aql, the asymmetric ejection in these shells is extended beyond the Hα shell, implying a faster ejection velocity than their symmetric counterpart; and they are all dominated by forbidden emission. These similarities suggest a similar origin for the asymmetric ejection in these three systems.

The physical origin of the asymmetric ejecta is far from clear, though. In Tappert et al. (2023) and Chapter 4, it was proposed that the origin may lie in the presence of a magnetic WD. The argument behind relies on the idea that the asymmetric ejecta is the result of an asymmetric accretion onto the WD surface, with the magnetic-funnelled accretion as the most promising mechanism to originate this phenomenon, although the physical reason behind the asymmetric accretion is not clear. The ambiguous evidence regarding the presence of a magnetic WD in V1425 Aql opened the door to this possibility. In the case of V1229 Aql and FV Sct, the properties of the binary system and the nature of their WDs are unknown, prohibiting us from further constraining the possible intrinsic origin for the asymmetric ejecta. In that regard, more studies are required to further constrain the physical properties of these systems in search of common patterns that provide hints of the origin of these unusual shells. Lastly, the possibility that the origin of these ejecta is the result of the interaction with the ISM can not be discarded. But this possibility also raises additional questions. If the fast asymmetric ejecta were originally symmetric, why do we not see fast (symmetric) ejecta in other shells? Why was the ISM asymmetric around the system to begin with? In all the other shells analysed in Chapter 5, the Hα and forbidden emission, either [NII] or [OIII], have similar projected spatial extensions. Age can not be a significant factor, as other shells of similar age to Nova Aquila 1995, Nova Aquila 1970, and Nova Scutum 1960 do not show unusual features. This places the three novae in question as significant cases of analysis for future studies.

6.3 Evolution of nova shells

The evolution of nova shells, regarding their expansion and luminosity, can be addressed with MUSE. As the nova shells expand, it is expected that their luminosity and geometry change, but how exactly is not clear. The deceleration of nova shells, for example, is a topic that has not been clarified. Duerbeck (1987b) proposed that the

expansion velocity decreases by a factor of two every $\sim$ 57 years, but was refuted by the studies of the old shells around T Aur (Nova Auriga 1891) and V476 Cyg (Nova Cygnus 1920), which are continuing to expand without signals of deceleration (Santamaría et al., 2020). In the same line, the study of the expansion rate of the different knots observed in the nova shell around RR Pic (Nova Pic 1925) is consistent with a free expansion of the shell, as was concluded in Chapter 3. Therefore, it can be concluded that shells younger than $\sim$ 100 years should still be expanding freely through the ISM.

On the other hand, the analysis presented in Chapter 5 suggests a potential deceleration of shells based on the appearance of an anti-correlation ($\tau = -0.37$ and p-value=0.06) between the shells' expansion rate and their age. The p-value in question may be deceptive, as the method used does not consider the (significant) uncertainties in the expansion rate, and could also be the result of the methodology used. To determine the expansion velocity of the shells in Chapter 5, an ellipse was fitted to each one, and from the extension of its semi-major axis and the distance to the system, therefore deducing an indirect expansion velocity was deduced, as was discussed in Sect. 5.2.2. A more detailed analysis that considers the expansion of discernible parts of the shell across different images at different times, such as clumps or filaments as was done for RR Pic (Chapter 3), or a comparison with the velocity derived from the spectroscopic data instead, will help to clarify the deceleration effect in nova shells.

As the shell expands, it will fade into the ISM while decreasing its luminosity. Studies of the luminosity evolution of nova shells show that they decrease their Hα and [OIII] luminosity in the decades after the eruption, following a power law, possibly reaching a valley of constant luminosity (Downes et al., 2001; Tappert et al., 2020). The MUSE data provide new measurements of the shell's fluxes, helping to clarify how the flux changes with time. The analysis of the flux of RR Pic indicates that the measured flux is below the expected value according to the power-law index provided by Tappert et al. (2020). The measured flux comes from the derived PPV space, which suggests that the difference can be explained in terms of the difference in the way of measuring the flux (from the PPV versus NB images). A detailed analysis of the flux of the different shells can be useful to clarify how the luminosity of shells varies in time.

6.4 Nova shell properties

Key parameters to describe nova shells are their axial ratio and their expansion velocity. In theory, both parameters are directly correlated to the nova eruption's t_n parameter, which in turn, is widely assumed to depend mainly on $M_{\rm WD}$. This opens the possibility to estimate some physical parameters of the system from the study of the nova shell. To achieve this, it is necessary first to determine the axial ratio and expansion velocity of nova shells with precision, and then search for an empirical correlation with their $M_{\rm WD}$. This presents diverse challenges, including the correct characterisation of the shell and overcoming the projection effects, and the determination of $M_{\rm WD}$ with precision.

The first problem can be addressed using MUSE data, as it allows us to study the nova shell from the PPV space, overcoming the projection effects. It can also provide us with the expansion velocity of the shells, either from the spectral information within the datacube, or by combining the axial ratio of the shell with the distance to the system. An attempt to correlate these parameters was done in Chapter 5, although the projected axial ratio was used instead of the true axial ratio. The results do not show any significant correlation beyond the projected axial ratio of the shells and their nova eruptions t_3, in line with previous studies (Slavin et al., 1995; Santamaría et al., 2022b). No significant correlation was found when considering $M_{\rm WD}$. The lack of results can be attributed to the significant scatter in the values of $M_{\rm WD}$, which limits the analysis, but also to the discrepancies between the projected and true axial ratio of nova shells. A good example is the shell of RR Pic, for which the projected axial ratio derived in Chapter 5 was 1.12, while the true axial ratio derived from the PPP in Chapter 3 was 1.35. Similar differences can be expected for the remaining shells, which will impact the overall analysis. Unfortunately, the difficulty of measuring precise $M_{\rm WD}$ in CVs makes obtaining an empirical law a difficult task.

On the other hand, the WD may print its physical properties in the shell in other forms. Porter et al. (1998) proposed that the spin of WDs in CVs is directly correlated to the formation of tropical rings. According to their simulations, WDs rotating faster will originate spherical shells with a tropical ring at lower angles (closer to the plane of the binary). This opens the possibility of obtaining some insight into the WD properties by studying the structure of the nova shells, particularly these tropical rings. The shell around RR Pic presents some cloudy structures above and below the equatorial ring. By assuming that these cloudy structures correspond to tropical rings, and

following the results of Porter et al. (1998), in Chapter 3 we derived a rotation period for the WD of $\sim$ 31 seconds. The exercise considered several assumptions that may have led to an erroneous result; however, it illustrates how nova shells can be used to estimate the physical parameters of the binary.

Last but not least, it is possible to obtain insights from the CV inclination from the nova shell. With the identification of the equatorial ring, it is possible to measure its inclination. The inclination of the equatorial ring in the shell should be similar to the orbital plane of the binary. Therefore, the latter can be obtained from the nova shell. This was done for the shell around RR Pic, for which the inclination of its equatorial ring was measured to be 74°, consistent with the previous estimation for the inclination of the system. A similar exercise can be done for the rest of the shells presented in Chapter 5 for which an equatorial ring can be observed. The determination of the inclination angle in a CV is essential to obtain some of its physical parameters with precision, like the mass of the components from radial velocity studies. In that way, nova shells can have a significant impact on characterising the physical properties of CVs.

6.5 Future research

In addition to the prospects presented in Section 5.2.3 to finish the study presented in Chapter 5, the study of nova shells will require additional effort to answer the different questions that remain. The most obvious strategy is the continued monitoring of the shells presented in this thesis. Future observations will allow us to draw compelling conclusions about how and when deceleration occurs, clarifying the contradictory results between Duerbeck (1987b) and Santamaría et al. (2020). The future data will also provide information on how the shell flux evolves in the different emission lines presented, expanding and complementing the research of Downes et al. (2001) and Tappert et al. (2020).

For future observations, the sister instrument of MUSE, BlueMUSE, will be key (Richard et al., 2019). BlueMUSE will be an IFS instrument that aims to provide similar spatial and spectral resolution to MUSE, but optimised for bluer wavelengths, covering the region between 350 and 600 nm. This will give access to important lines for nebular diagnosis such as [OIII]λ4363 Å [OII]$\lambda\lambda$3726, 3729 Å, or [SII]$\lambda\lambda$4069, 4076 Å(Osterbrock & Ferland, 2006; Draine, 2011). These lines, in combination with the lines observed in the MUSE wavelength coverage, will provide a

characterisation of the ejecta temperature and densities, and, in consequence, a more complete view of the ejecta.

Nova shells present a variety of geometries, as was shown across this thesis. The main physical parameter that governs this variety is not clear, and it has been proposed that the WD within the system plays a major role in shaping shells. Although $M_{\rm WD}$ should correlate directly with the ejected mass and the expansion velocity of the shell, there is no convincing observational evidence that supports this premise. The main reason is the difficulty of determining physical parameters of CVs with precision, as was discussed in Chapter 5. To determine the physical properties of post-novae with enough precision, so that the correlations with the shell properties can lead to meaningful conclusions, it would be necessary to combine the efforts of spectral and photometric studies. This will lead to, in the best of the cases, a dynamic mass of the WD in the system. Another possibility would be to model the WD mass and accretion rate from UV spectra (e.g. Pala et al., 2022). Interesting targets to do this kind of analysis are the systems of V1425 Aql, V1229 Aql, and FV Sct. A better characterisation of the physical properties of these systems may lead to a common mechanism that can explain a potential intrinsic asymmetric ejecta.

In addition to continuing the study of the systems and their shells presented in this thesis, the focus can be shifted to other post-novae and their shells. The number of detected novae increased significantly during the last decades, and with it, the number of potential shells to study (Santamaría et al., 2025). Young shells that have been imaged at early stages, such as the case of V5668 Sgr (Diaz et al., 2018), may offer a step toward a better understanding of the evolution of nova shells during their first decades.

Some of the observed systems did not show evidence for a shell, imposing an upper limit to their flux. Even when a shell is not detected, the MUSE data allow for studies of the post-nova. The effect that a nova eruption has on the CV is not understood. The spectra extracted from MUSE may provide some clues when compared with spectra previously reported. Even further, the spectra of the post-novae in the whole sample can be used to determine the colours that best highlight the post-novae from the rest of the field stars. This can be useful when searching for post-novae with ambiguous identification.

6.6 Conclusions

This thesis has explored a new way of studying nova shells: through the use of IFS data from MUSE. It has shown the significant advantages and capabilities of using this kind of data, encouraging the community to use this type of observation. The results support this statement, revealing an unprecedented view of several nova shells. The main results of this thesis are summarised as follows:

- A new methodology has been implemented to obtain a 3D view of nova shells from the MUSE data, under the assumption of radial and free expansion. The derived 3D geometry provides new insights into the nova shell's true geometry and axial ratio. Additionally, it provides a way to study how different emissions occupy different spatial extensions within the shell, allowing for obtaining insights into the shell density and composition.

- An in-depth analysis of the shell around RR Pic was published, confirming the ring and polar structures deduced from images and spectroscopic data. The 3D analysis revealed a more complex shell with a dense hydrogen equatorial ring and cloudy structures and polar filaments, and forbidden oxygen emission coming from the gaps where no hydrogen is present. The analysis also provides compelling evidence that supports a free expansion of this old shell, in line with the results of other old shells. From the flux measurements, the total ionised mass of the shell was estimated to be $\sim 5 \times 10^{-5}$ $M_{\odot}$. The overall analysis of this shell only strengthens the numerous possibilities that IFS data offers for the study of nova shells.

- The presence of asymmetric shells that challenge the usual ejection mechanisms was first observed through this study. The first example of V1425 Aql was later joined by the shells around V1229 Aql and FV Sct. In these three cases, the asymmetric ejecta correspond to a fast ejecta dominated by forbidden lines only. The origin of this asymmetry is not clear; it could be intrinsic or extrinsic to the shell. In any case, these special cases are hints of an unknown mechanism operating during the nova eruption and/or during the interaction between the expanding shell and the surrounding ISM. The analysis of the shell around V1425 Aql indicates an arc-shaped geometry for the outer shell, implying a more complex ejection mechanism than the stated polar wind. The analysis of the 3D geometry of the other two shells remains to be done.

- A total of 17 shells have been studied with MUSE, providing the largest sample of shells observed with this instrument to date. The preliminary results for this sample indicate no significant correlation with the published $M_{\rm WD}$, contrary to the expected behaviour from the theory. Although the likely explanation for this lack of correlation can be attributed to the large scatter in the data rather than a subyacent problem with the theory, it is not possible to provide a conclusion with the present data. Part of the scatter is due to the use of the projected axial ratio instead of the true one derived from the 3D model, which must be considered in future analysis. The latter will aim to provide a better characterisation of the shell parameters from their 3D structure, to find an empirical relation between the shell geometry and the underlying WD in the CV.

Appendix A

Velocity maps

Fluxes and velocity maps as presented in Sect. 5.1.2, for all the 17 shells.

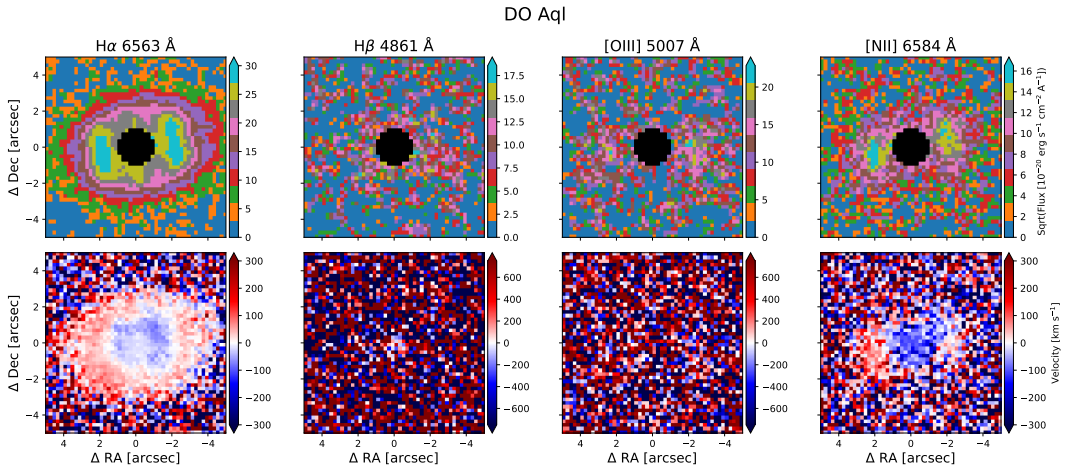

Figure A.1: Flux and velocity maps for DO Aql

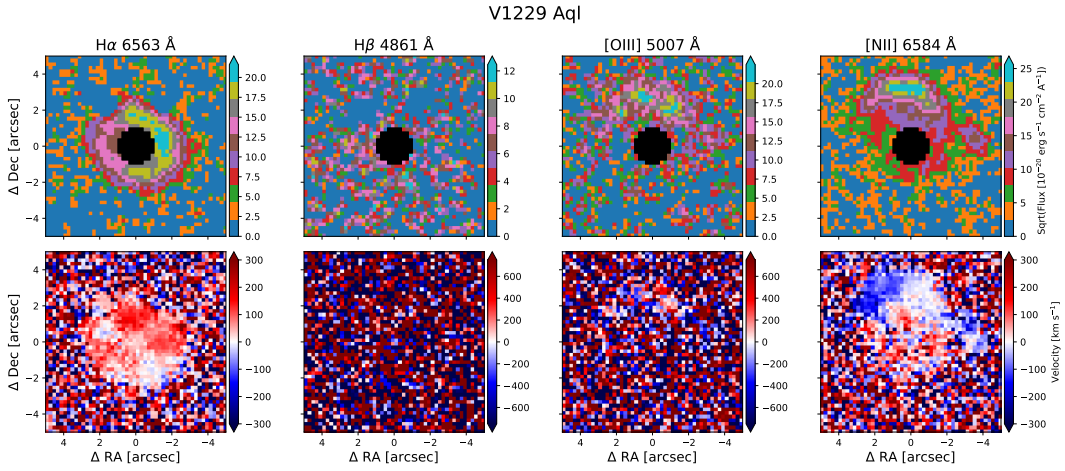

Figure A.2: Flux and velocity maps for V1229 Aql

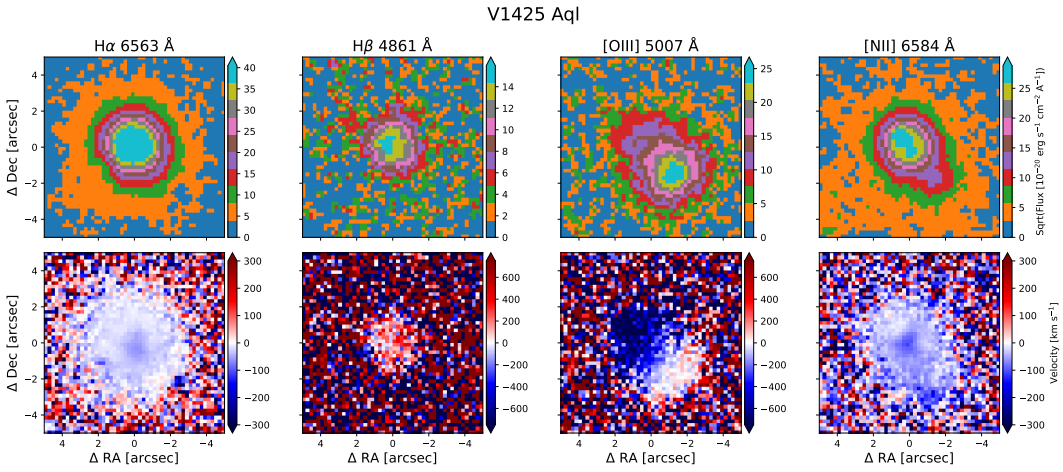

Figure A.3: Flux and velocity maps for V1425 Aql

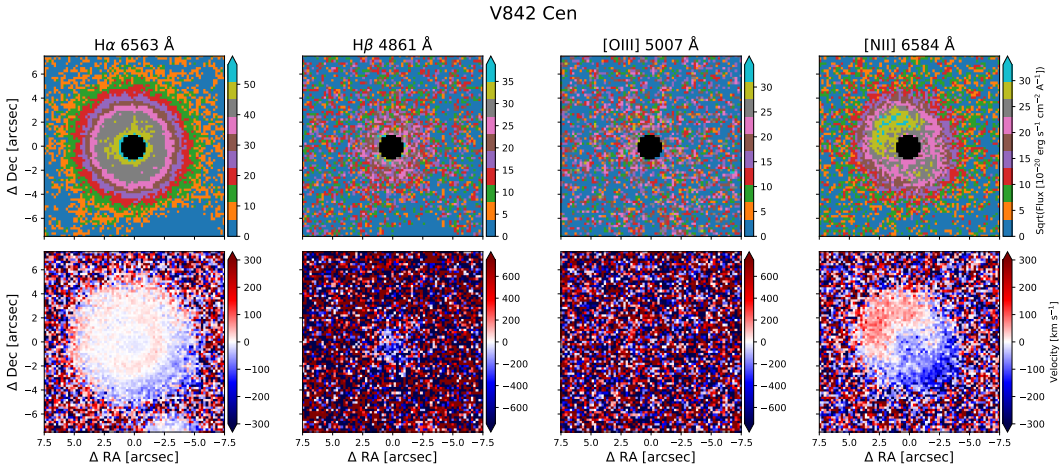

Figure A.4: Flux and velocity maps for V842 Cen

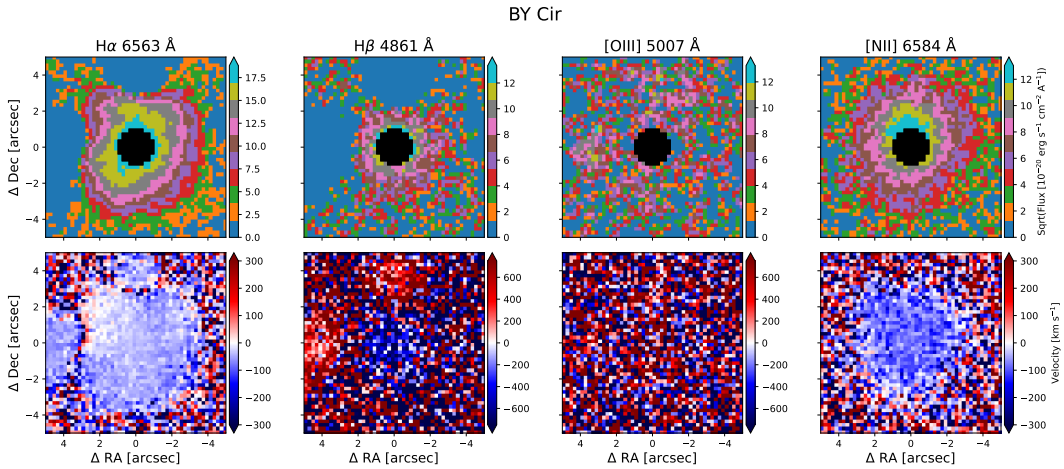

Figure A.5: Flux and velocity maps for BY Cir

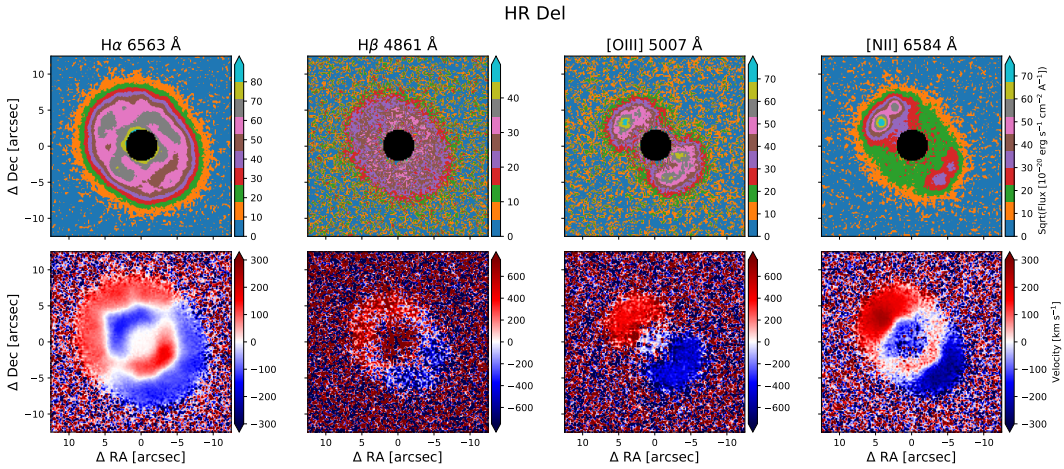

Figure A.6: Flux and velocity maps for HR Del

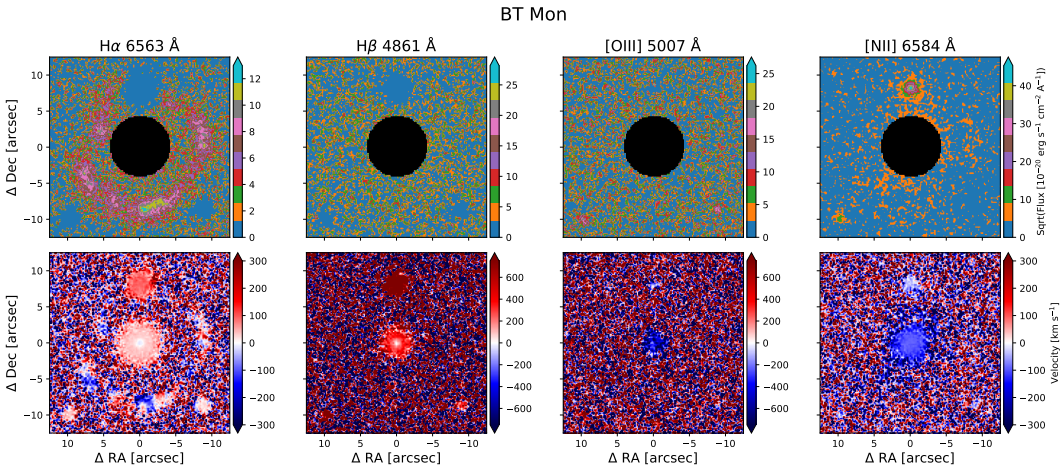

Figure A.7: Flux and velocity maps for BT Mon

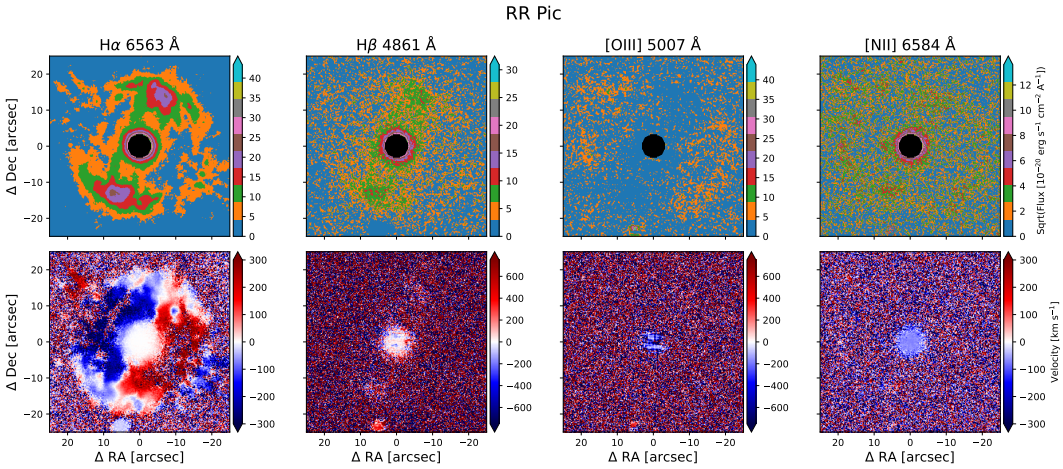

Figure A.8: Flux and velocity maps for RR Pic

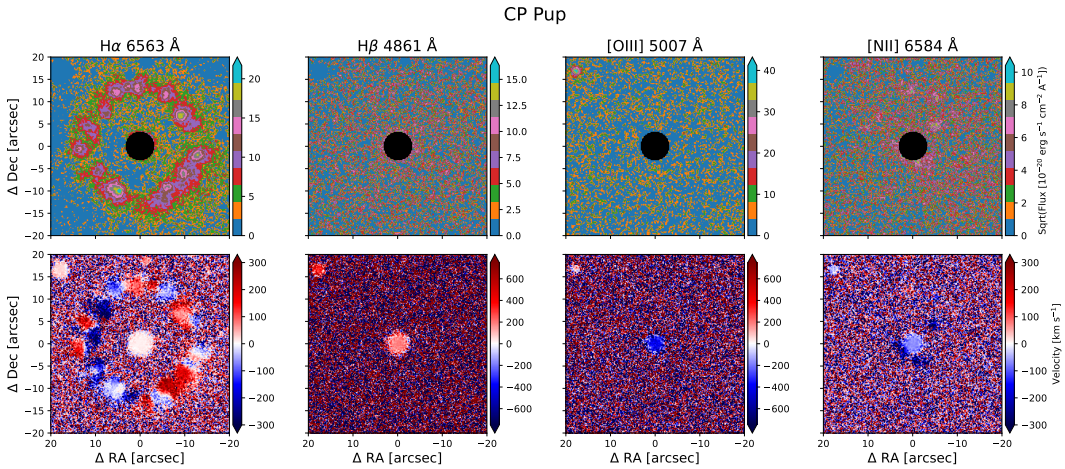

Figure A.9: Flux and velocity maps for CP Pup

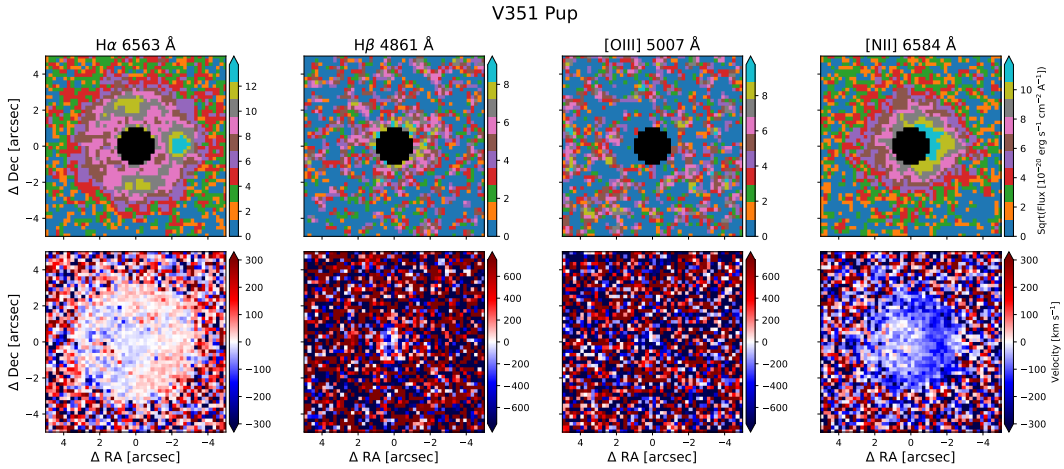

Figure A.10: Flux and velocity maps for V351 Pup

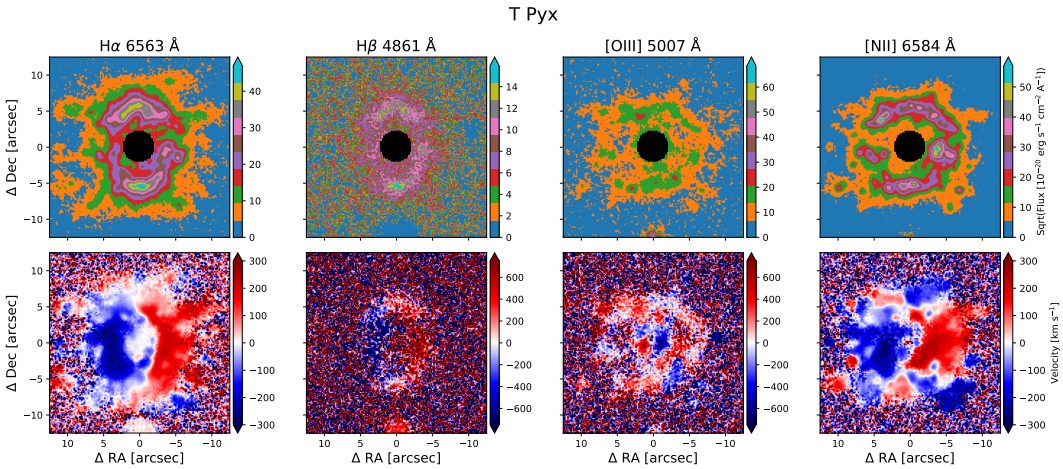

Figure A.11: Flux and velocity maps for T Pyx

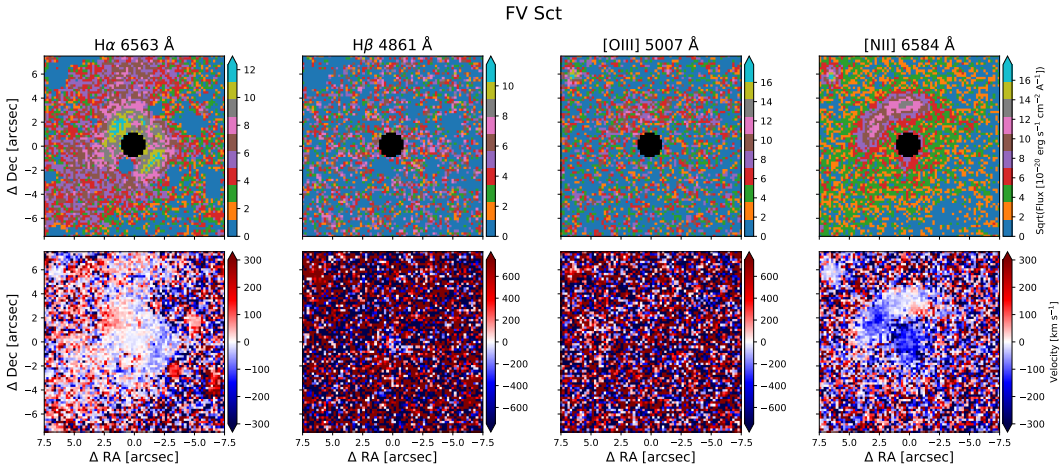

Figure A.12: Flux and velocity maps for FV Sct

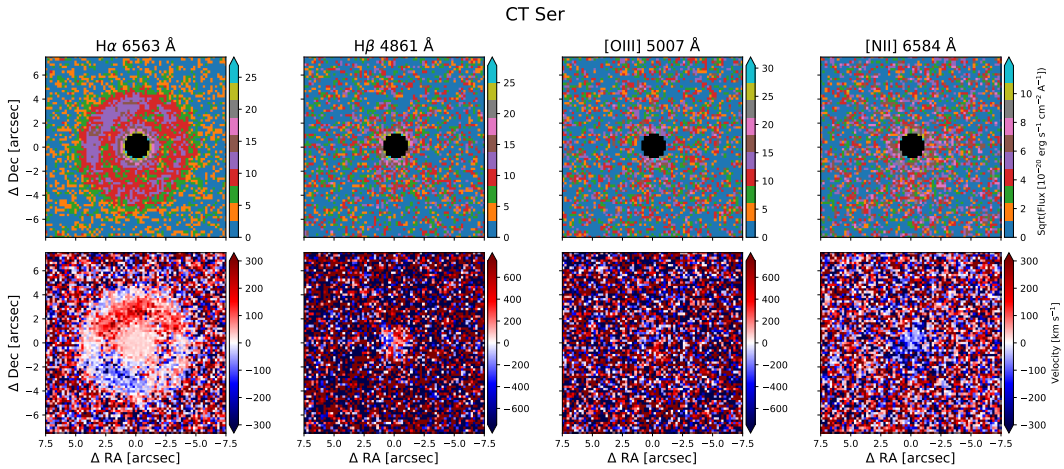

Figure A.13: Flux and velocity maps for CT Ser

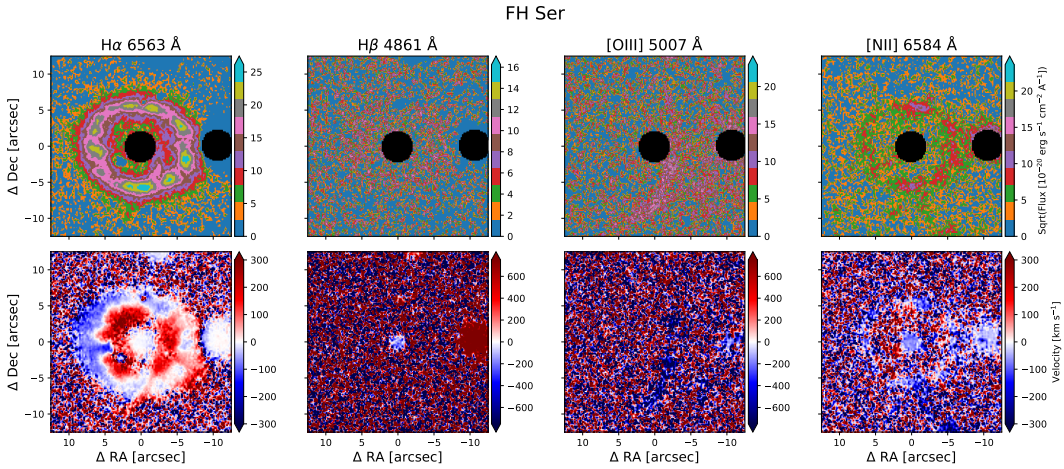

Figure A.14: Flux and velocity maps for FH Ser

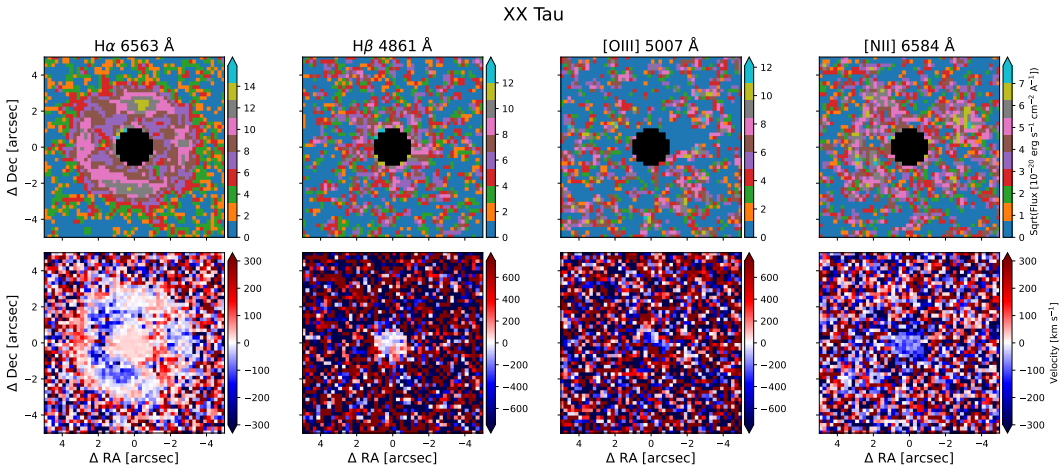

Figure A.15: Flux and velocity maps for XX Tau

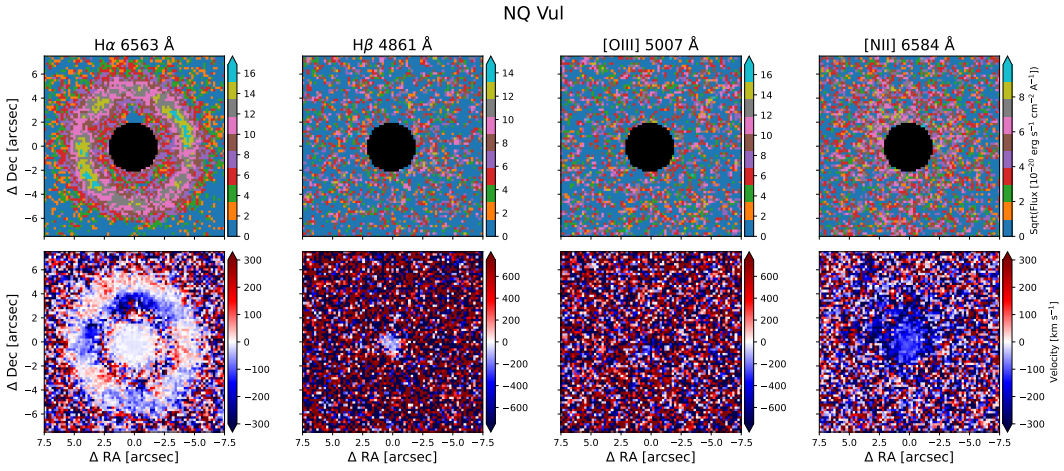

Figure A.16: Flux and velocity maps for NQ Vul

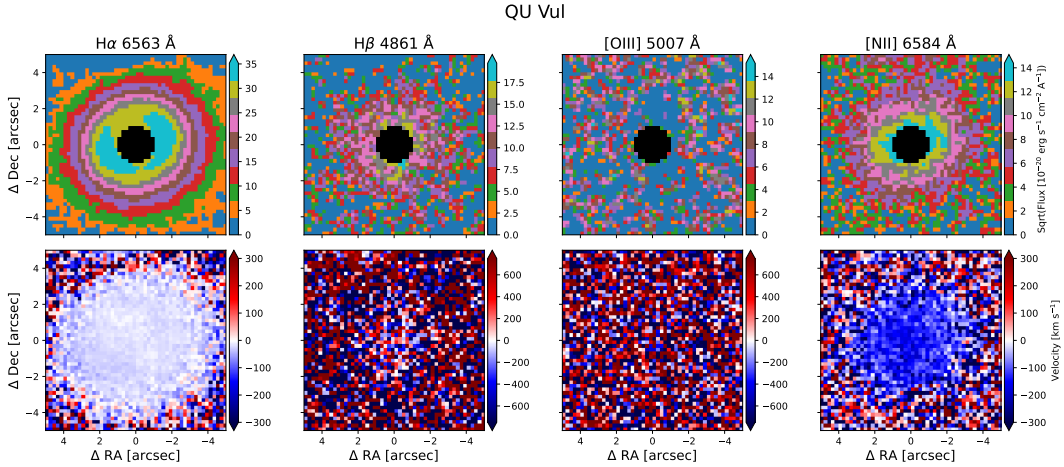

Figure A.17: Flux and velocity maps for QU Vul

APPENDIX B

PPV diagrams

PPV diagrams for the 17 nova shells described in Sect. 5.1.4 are presented in this Appendix.

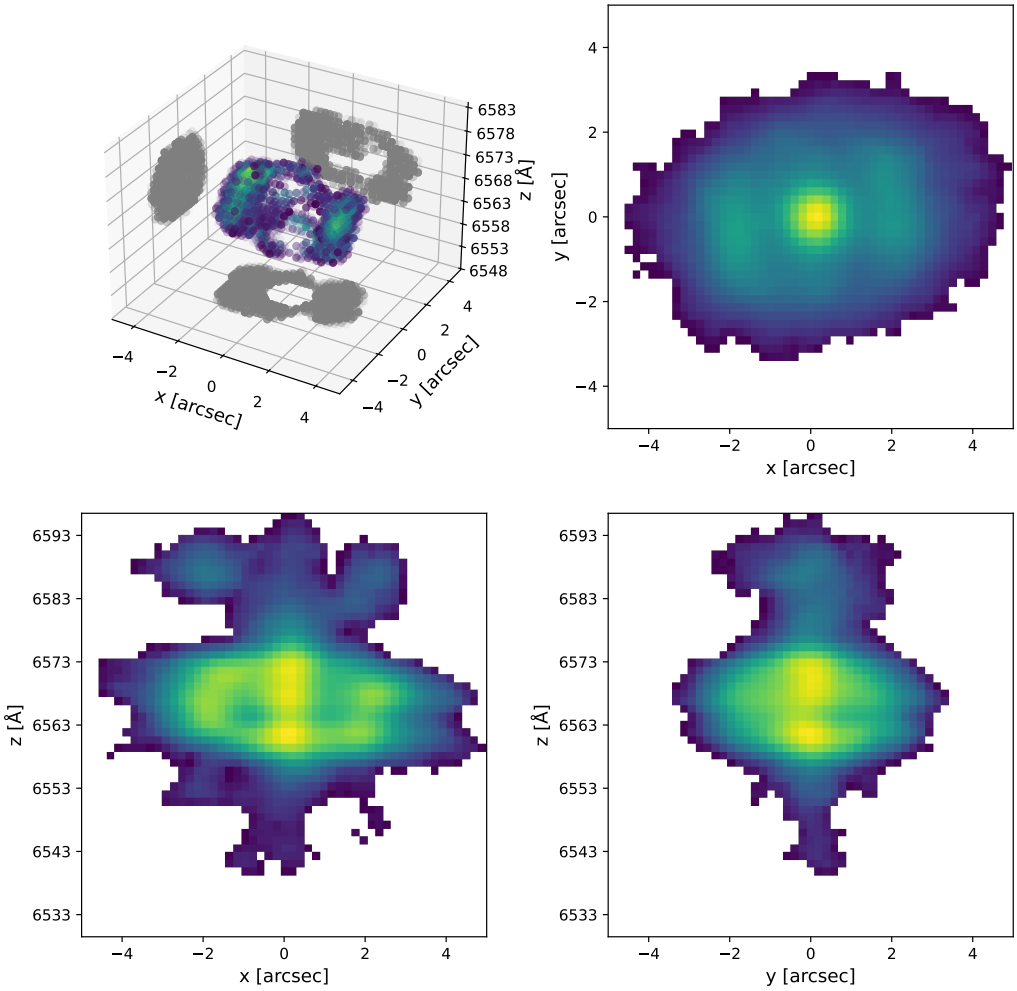

Figure B.1: PPV of DO Aql.

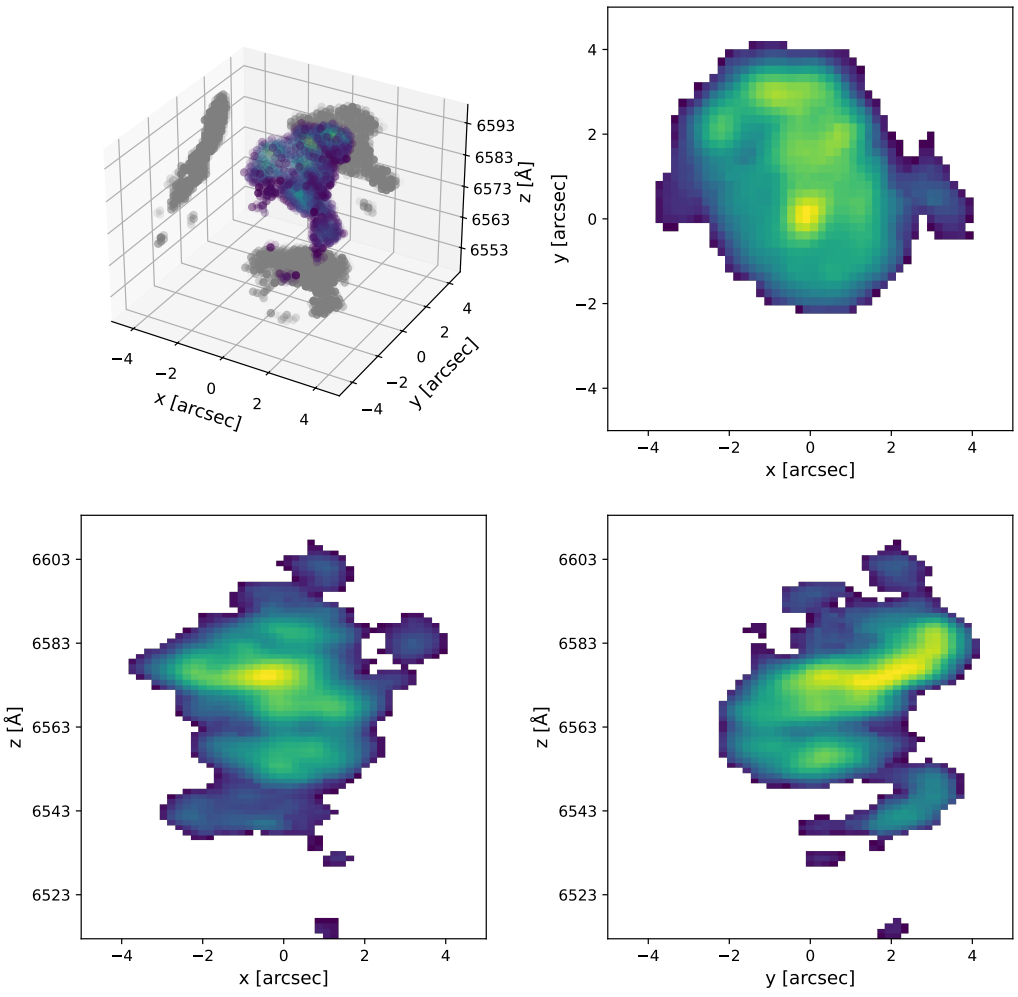

Figure B.2: PPV of V1229 Aql.

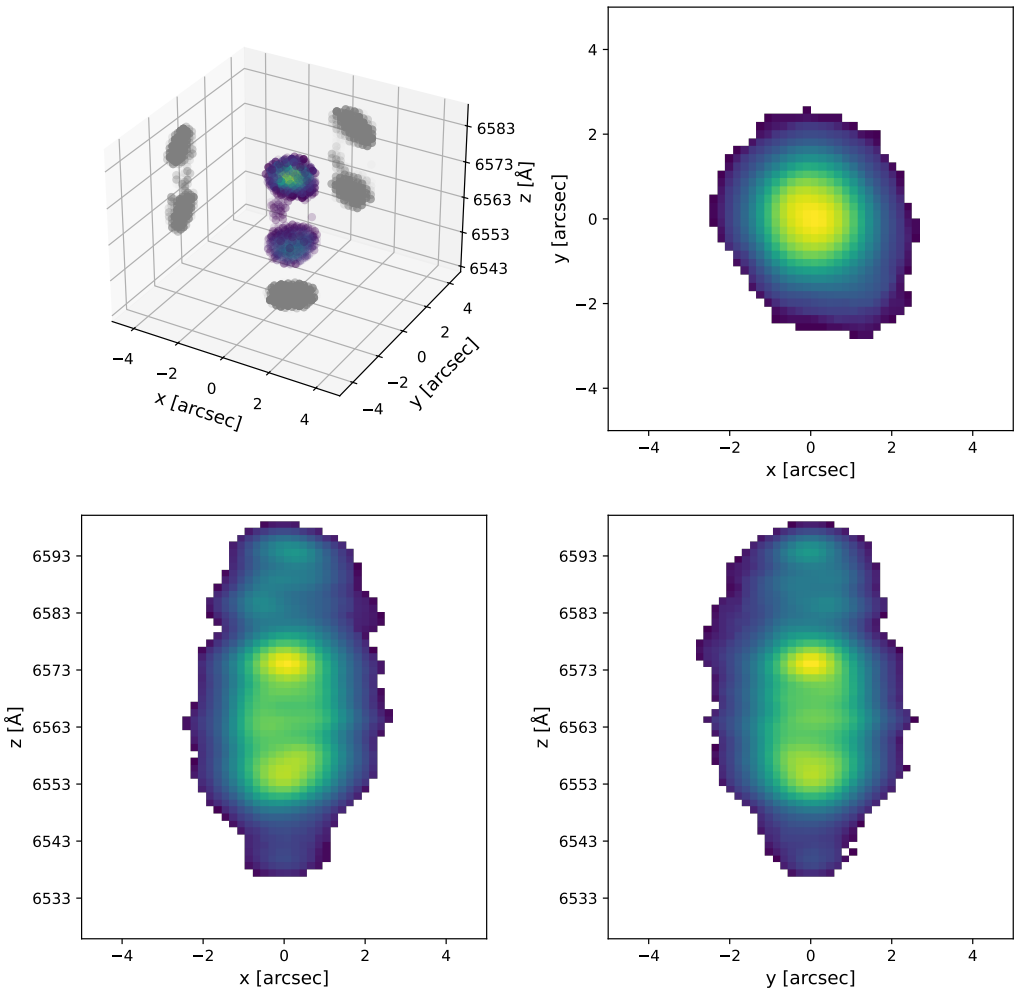

Figure B.3: PPV of V1425 Aql.

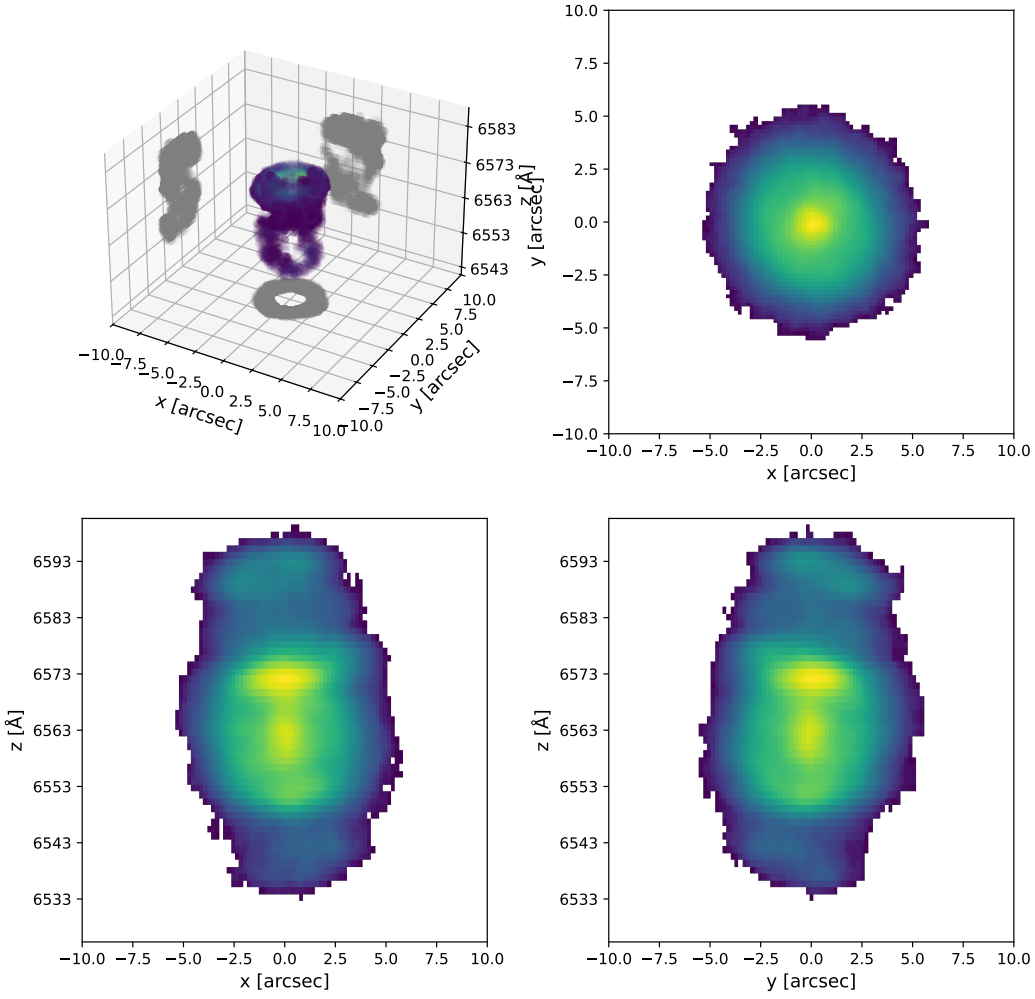

Figure B.4: PPV of V842 Cen.

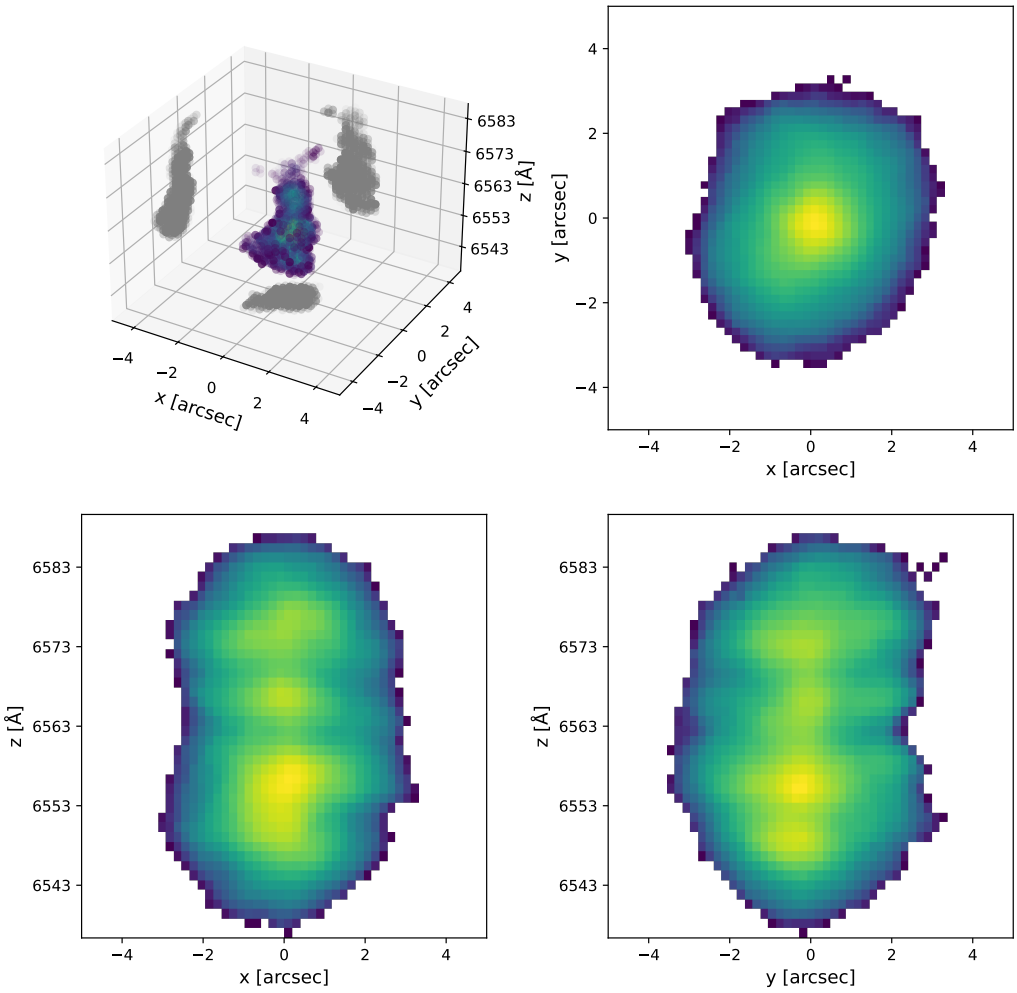

Figure B.5: PPV of BY Cir.

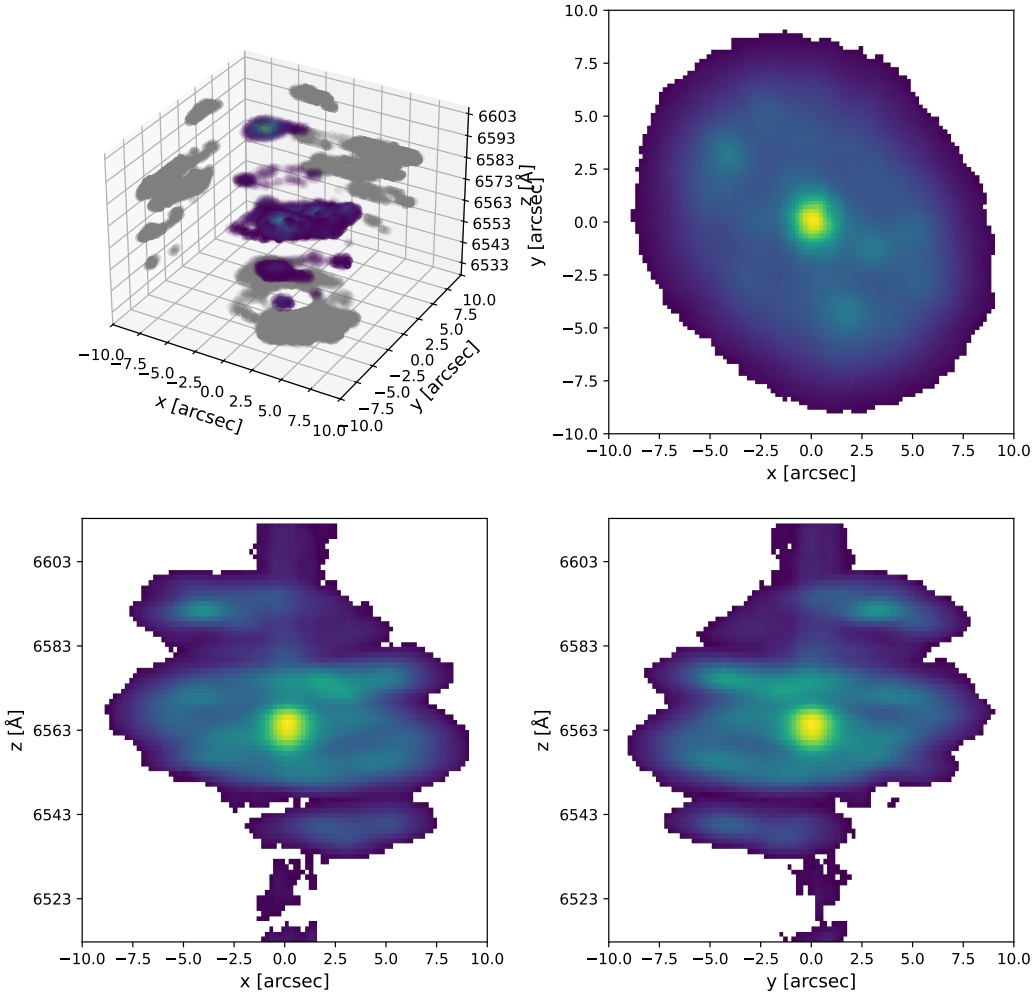

Figure B.6: PPV of HR Del.

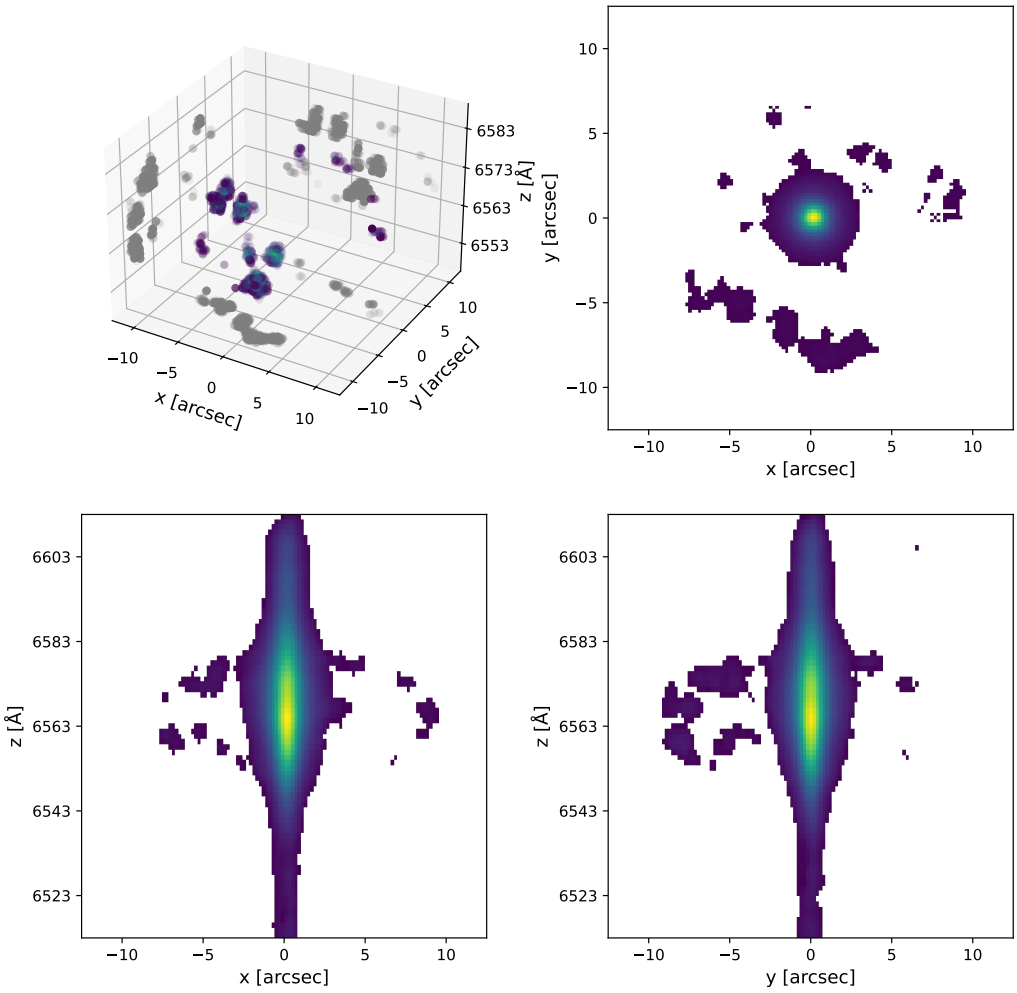

Figure B.7: PPV of BT Mon.

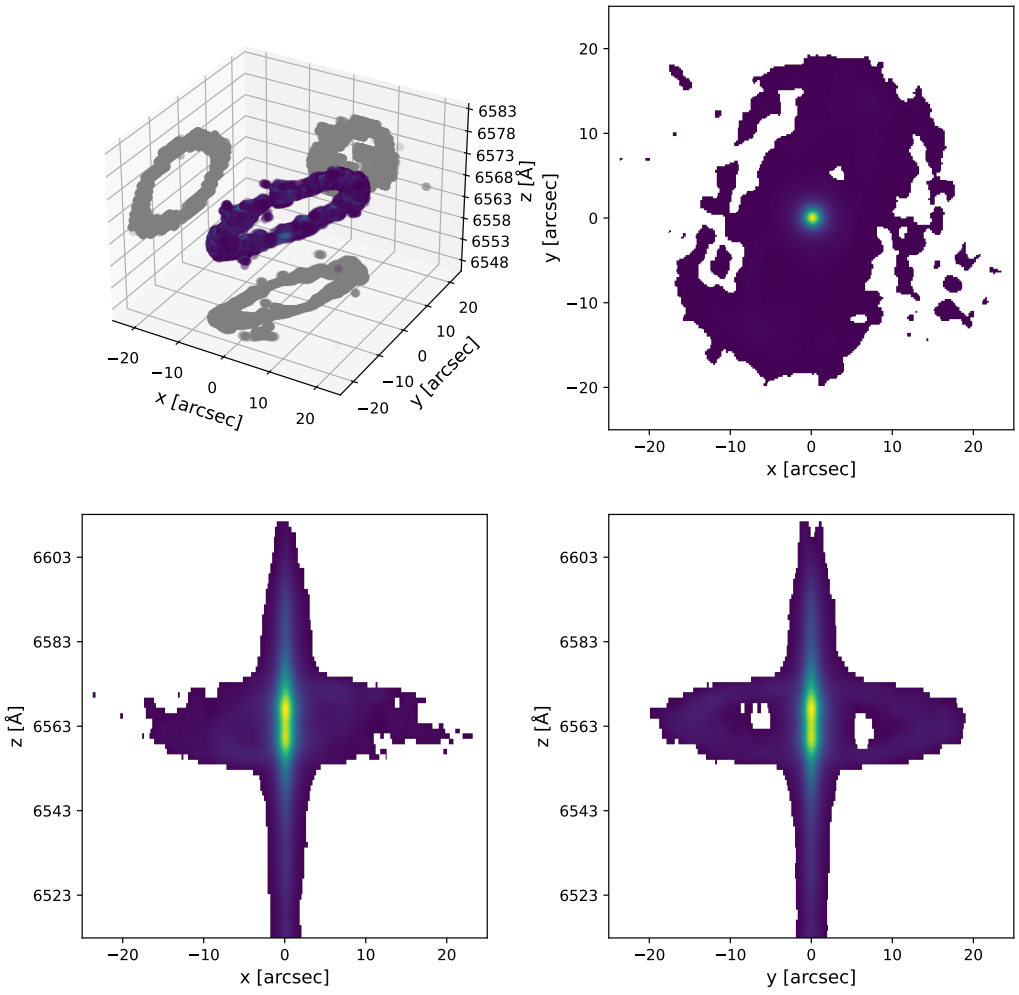

Figure B.8: PPV of RR Pic.

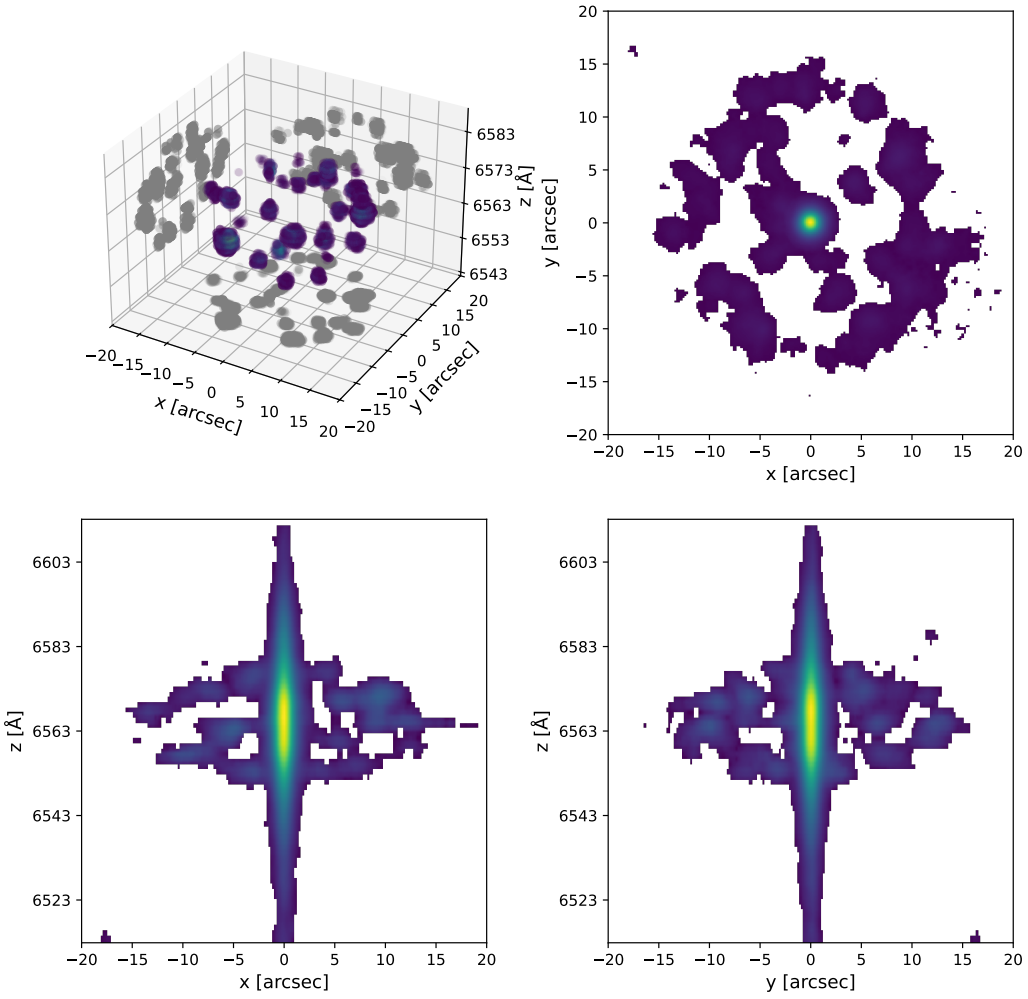

Figure B.9: PPV of CP Pup.

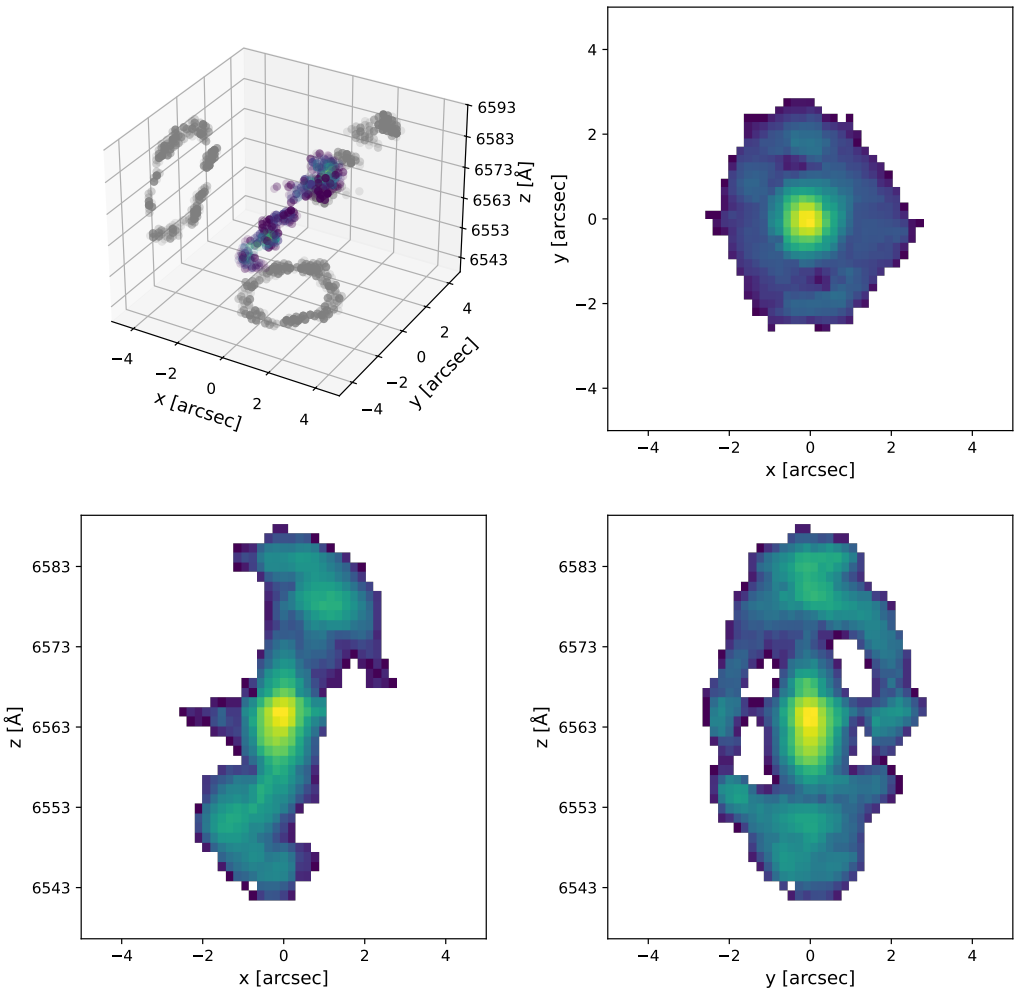

Figure B.10: PPV of V351 Pup.

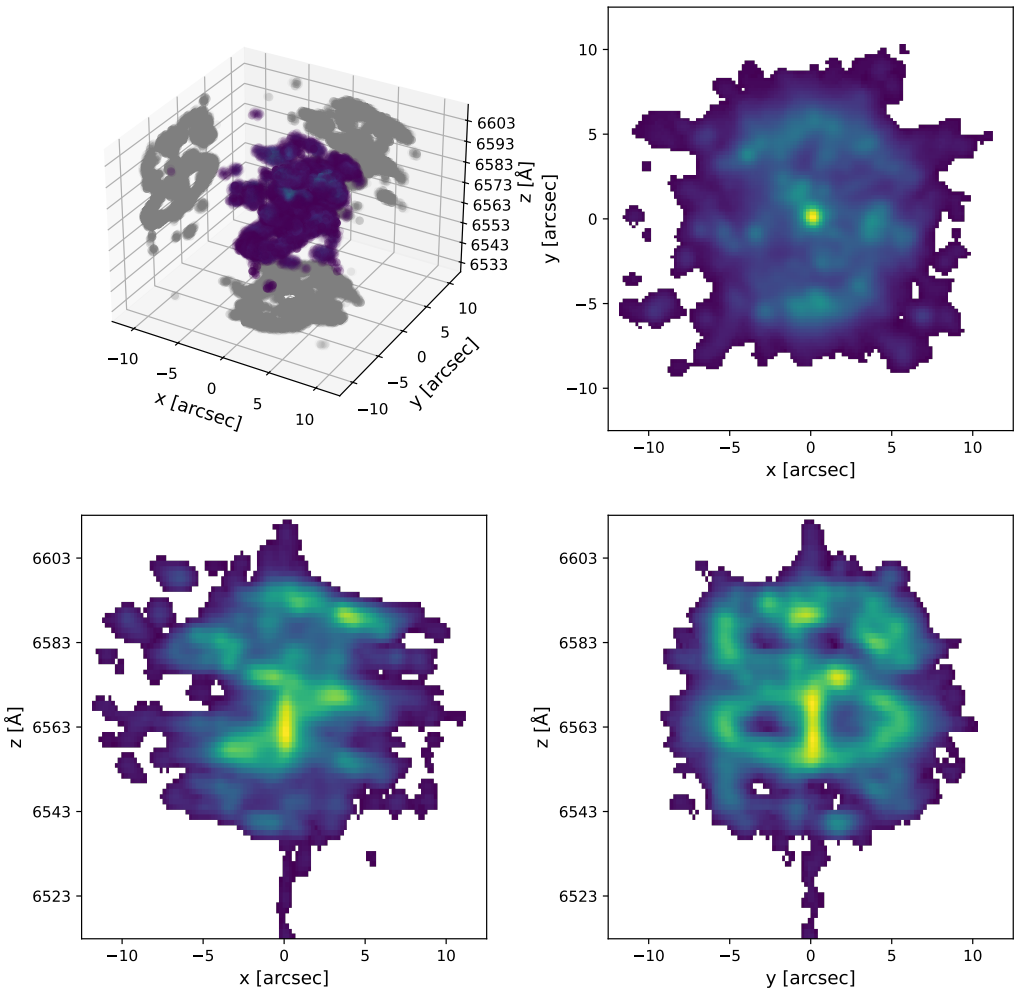

Figure B.11: PPV of T Pyx.

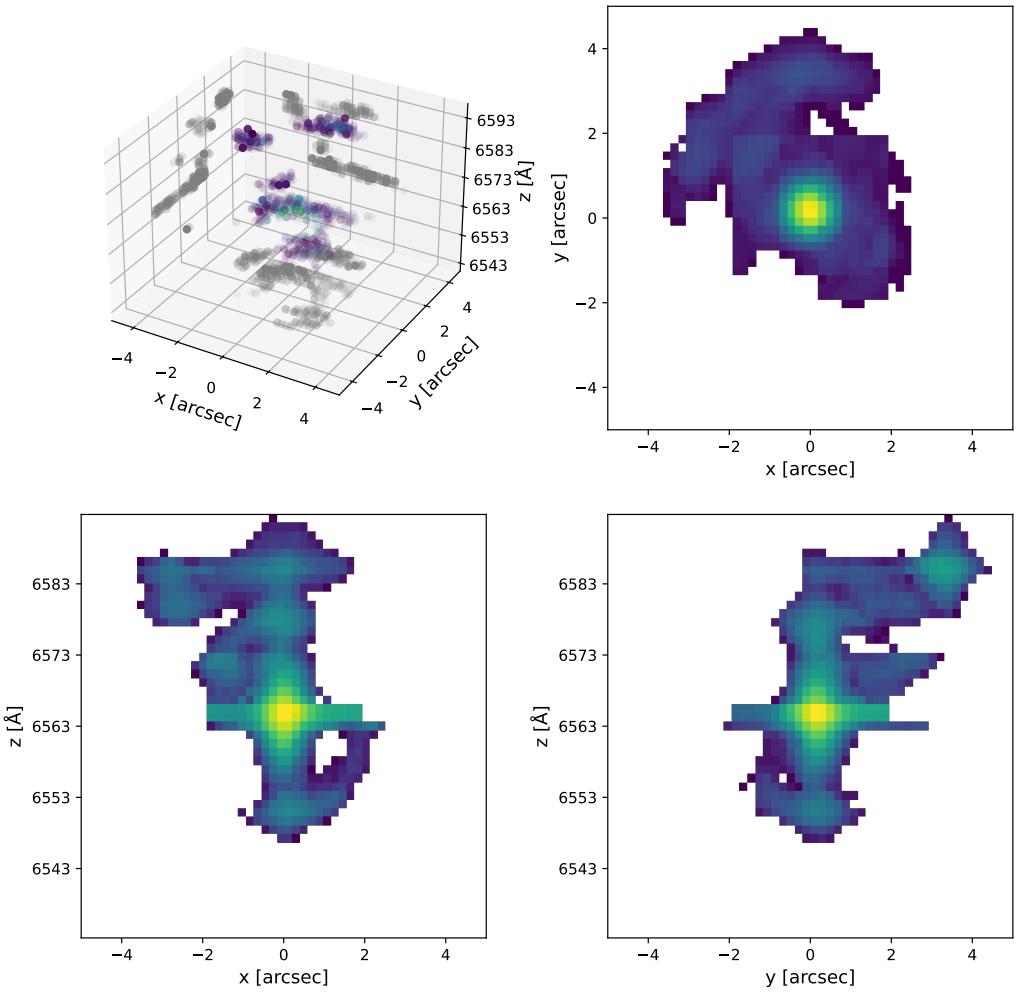

Figure B.12: PPV of FV Sct.

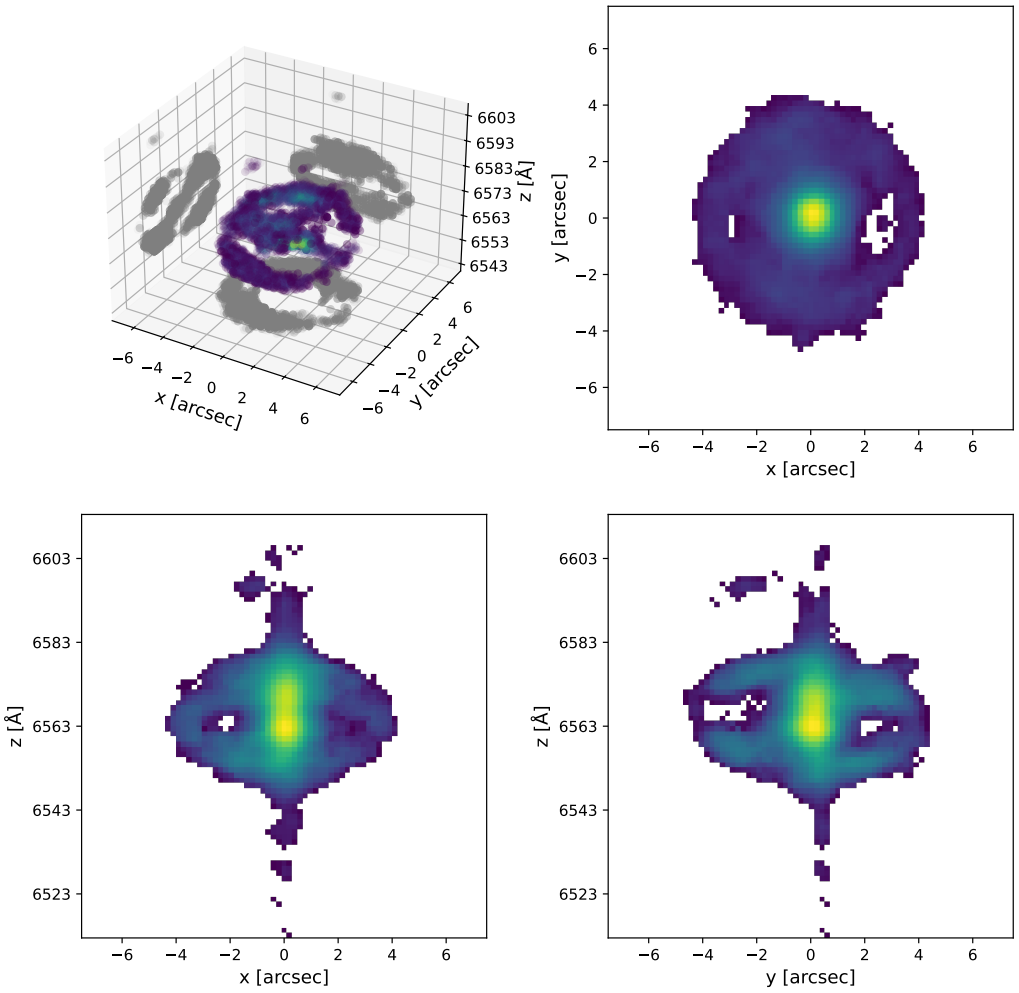

Figure B.13: PPV of CT Ser.

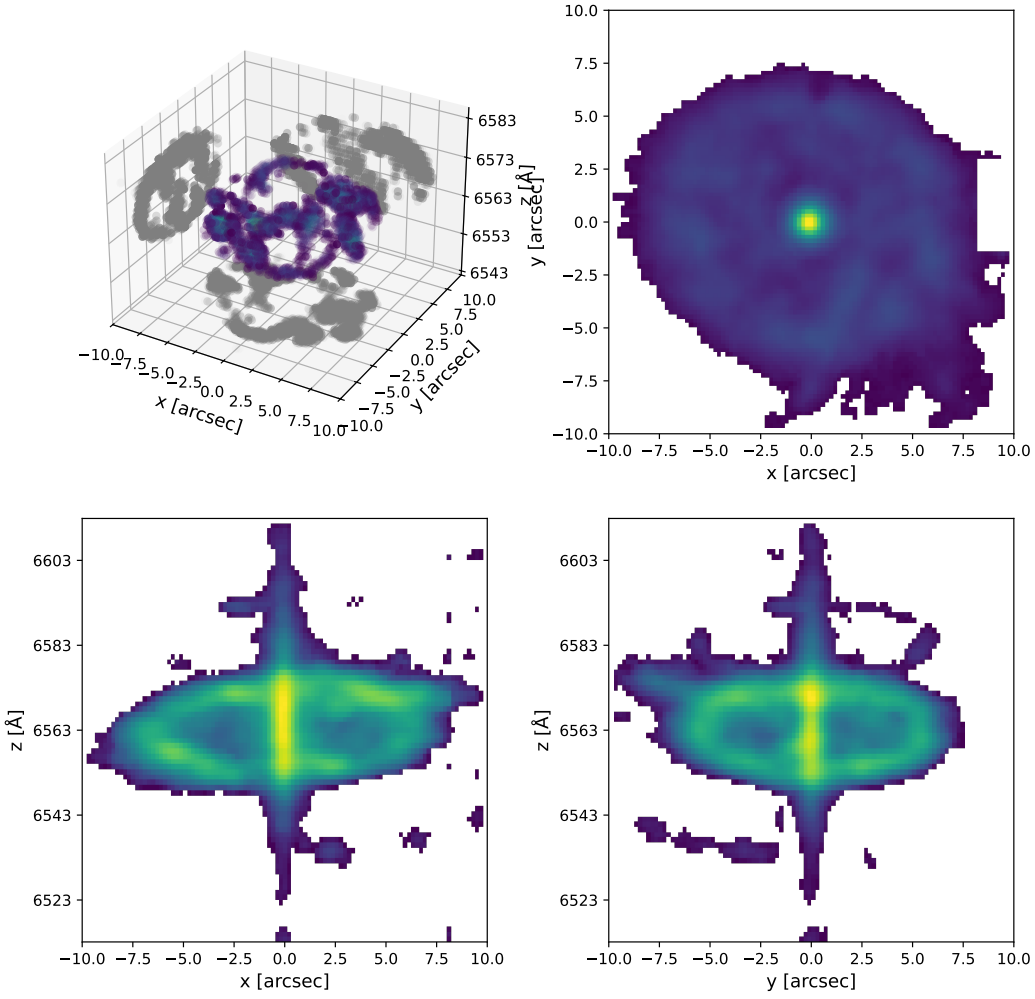

Figure B.14: PPV of FH Ser.

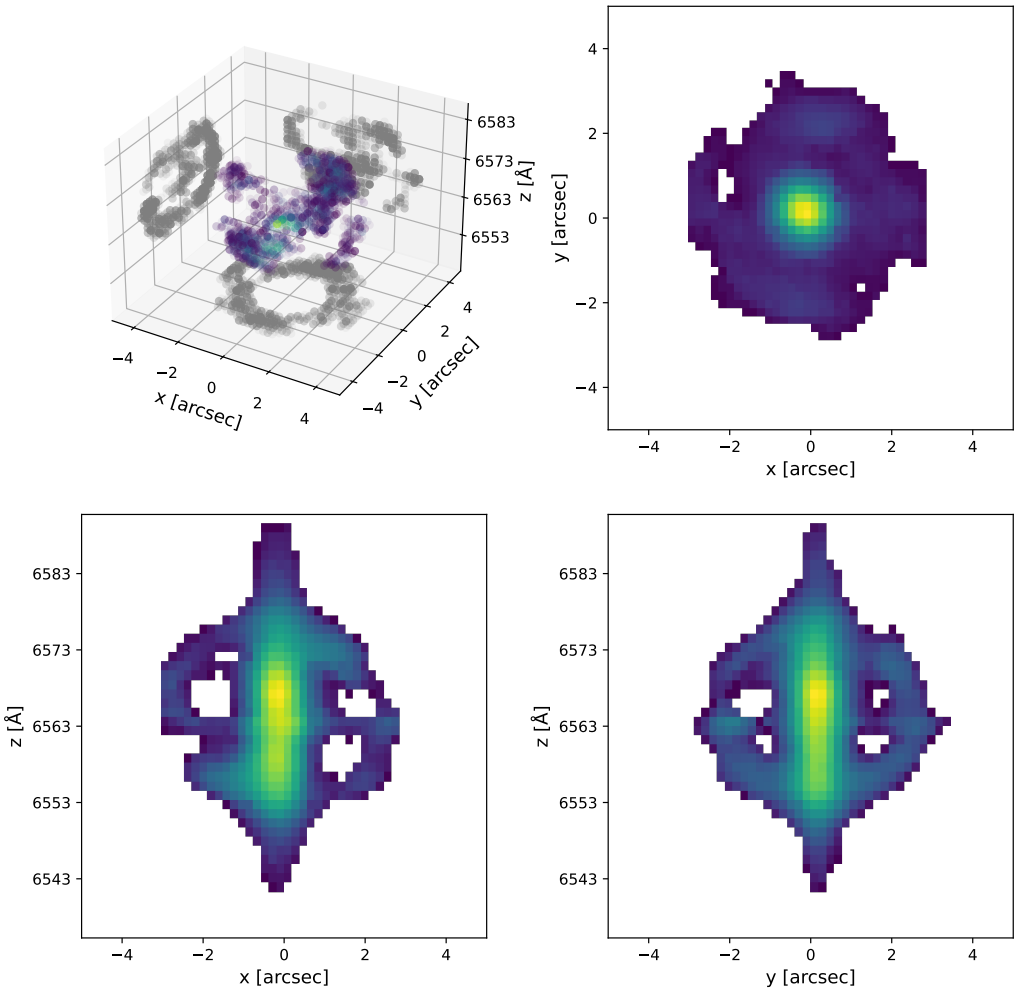

Figure B.15: PPV of XX Tau.

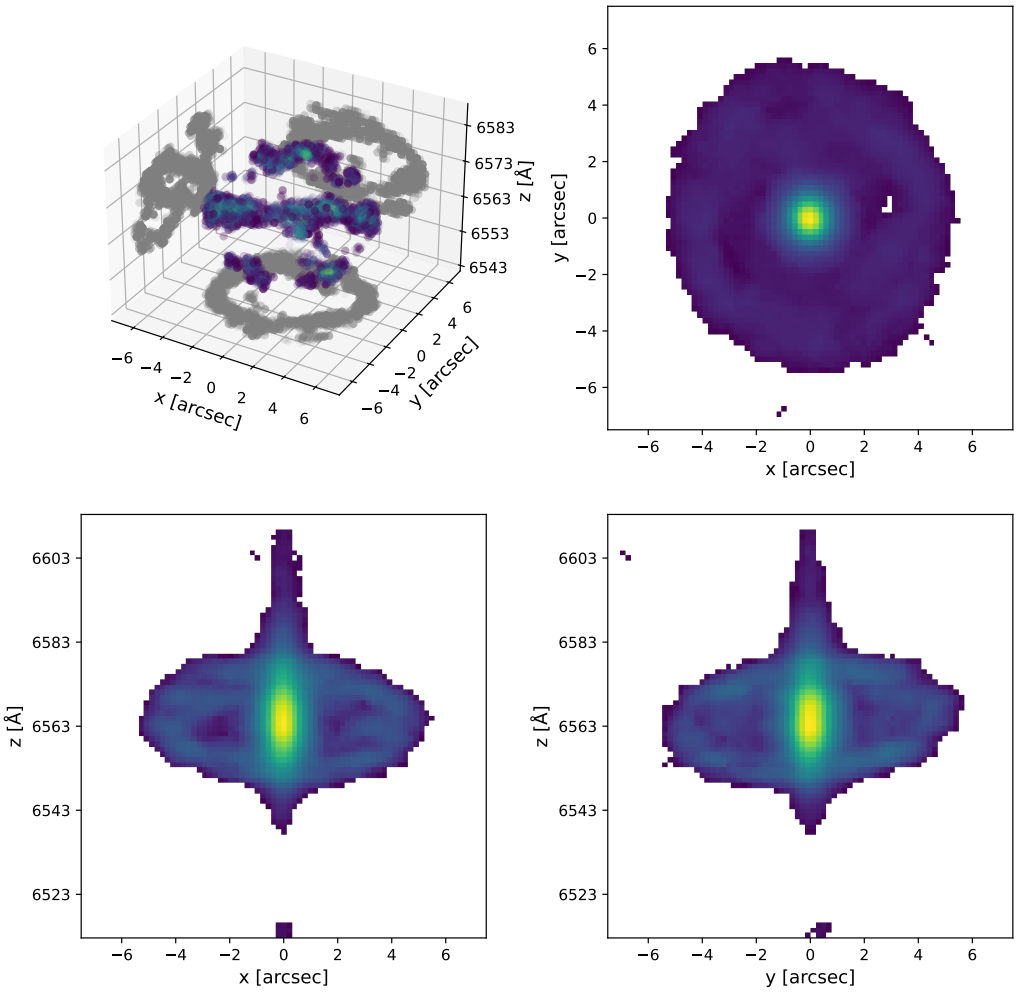

Figure B.16: PPV of NQ Vul.

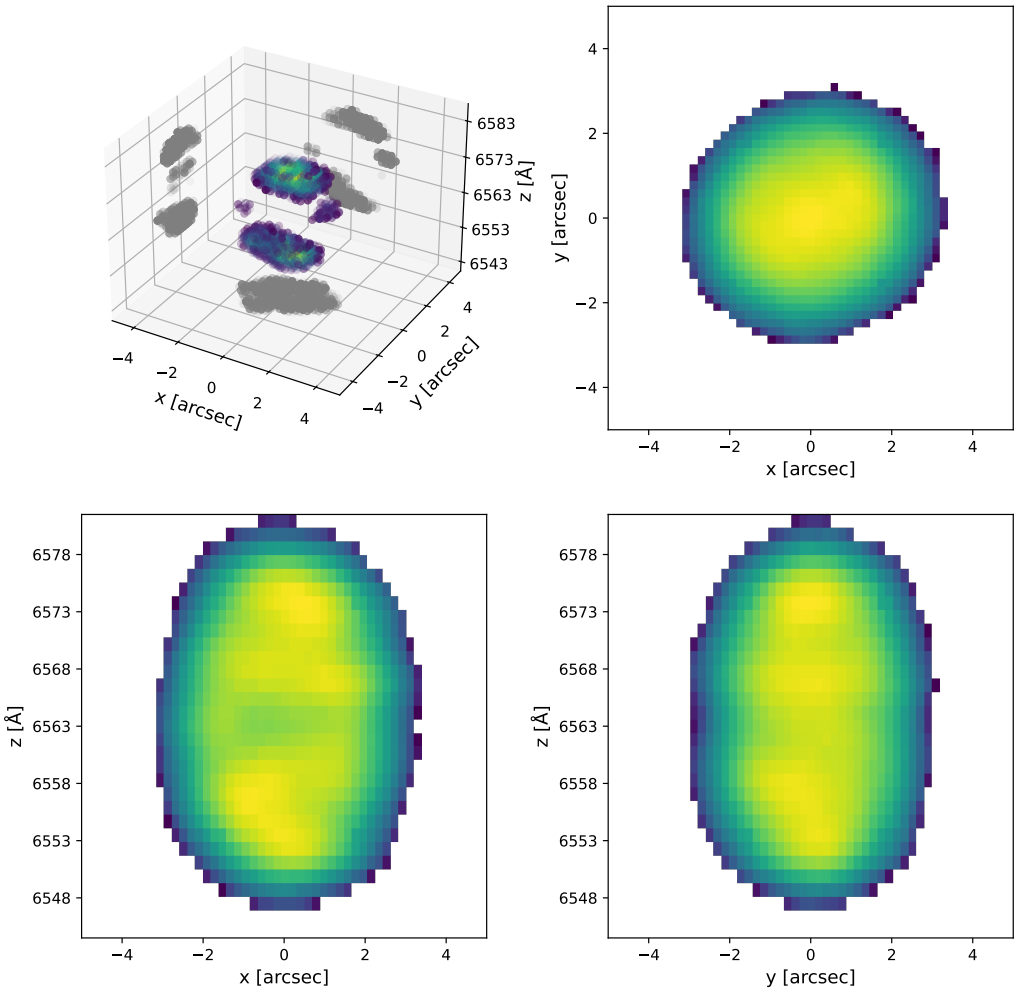

Figure B.17: PPV of QU Vul.

Appendix C

List of abbreviations and acronyms

To facilitate the reading of this manuscript, several acronyms and abbreviations are used after being introduced in the text. The following list aims to help the reader recall the meaning of those abbreviations and acronyms used in more than one section.

Angular momentum loss	AML
Cataclysmic variable	CV
Classical nova	CN
Declination	Dec
Dwarf nova	DN
Full width at half maximum	FWHM
Gravitational wave radiation	GWR
Integral field spectroscopy	IFS
Intermediate polar	IP
Interstellar medium	ISM
Long-slit (spectroscopy)	LS
Magnetic braking	MB
Multi-Unit Spectrograph Explorer	MUSE
Narrow-band (photometry)	NB
Nova like	NL
Position-position-position	PPP
Position-position-velocity	PPV
Recurrent nova	RN
Right ascension	RA
Thermonuclear runaway	TNR
White dwarf	WD

Bibliography

Ackermann M. et al., 2014, Science, 345, 554

Arp H. C., 1956, AJ, 61, 15

Aydi E. et al., 2020, ApJ, 905, 62

Aydi E. et al., 2024, MNRAS, 527, 9303

Bacon R. et al., 2010, in Society of Photo-Optical Instrumentation Engineers (SPIE) Conference Series, Vol. 7735, McLean I. S., Ramsay S. K., Takami H., eds, Ground-based and Airborne Instrumentation for Astronomy III, p. 773508

Bacon R., Piqueras L., Conseil S., Richard J., Shepherd M., 2016, MPDAF: MUSE Python Data Analysis Framework, Astrophysics Source Code Library, record ascl:1611.003

Bailer-Jones C. A. L., 2015, PASP, 127, 994

Bailer-Jones C. A. L., Rybizki J., Fouesneau M., Demleitner M., Andrae R., 2021, AJ, 161, 147

Balbus S. A., Hawley J. F., 1991, ApJ, 376, 214

Balman Ş., 2006, Advances in Space Research, 38, 2840

Baptista R., Jablonski F. J., Cieslinski D., Steiner J. E., 1993, ApJ, 406, L67

Bateson F. M., McIntosh R., 1986, Royal Astronomical Society of New Zealand Publications of Variable Star Section, 14, 59

Bateson F. M., McIntosh R., 1998, Royal Astronomical Society of New Zealand Publications of Variable Star Section, 23, 18

Bond H. E., Carter C., Elmore D. F., Goodhew P., Patchick D., Talbot J., 2024, AJ, 168, 249

Booth R. A., Mohamed S., Podsiadlowski P., 2016, MNRAS, 457, 822

Bruch A., 1982, PASP, 94, 916

Bruch A., 2022, MNRAS, 514, 4718

Camilleri P., McNaught R. H., Gilmore A. C., Kilmartin P. M., 1992, IAU Circ., 5422, 1

Capitanio L., Lallement R., Vergely J. L., Elyajouri M., Monreal-Ibero A., 2017, A&A, 606, A65

Carroll B. W., Ostlie D. A., 2017, An introduction to modern astrophysics, Second Edition

Casanova J., José J., García-Berro E., Shore S. N., 2016, A&A, 595, A28

Castro Segura N. et al., 2021, MNRAS, 501, 1951

Chomiuk L. et al., 2021, ApJS, 257, 49

Chomiuk L. et al., 2014, Nature, 514, 339

Chomiuk L., Metzger B. D., Shen K. J., 2021, ARA&A, 59, 391

Chong A. et al., 2025, MNRAS, 541, 980

Cohen J. G., 1985, ApJ, 292, 90

Cohen J. G., Rosenthal A. J., 1983, ApJ, 268, 689

Collins P. et al., 1984, IAU Circ., 4023, 1

Darnley M. J. et al., 2016, ApJ, 833, 149

Darnley M. J. et al., 2015, A&A, 580, A45

Darnley M. J. et al., 2019, Nature, 565, 460

Darnley M. J., Williams S. C., Bode M. F., Henze M., Ness J. U., Shafter A. W., Hornoch K., Votruba V., 2014, A&A, 563, L9

Davidson P. A., 2001, An Introduction to Magnetohydrodynamics

Dawson B. H., Shapley H., 1942, Harvard College Observatory Announcement Card, 637, 2

del Palacio S., Bosch-Ramon V., Müller A. L., Romero G. E., 2018, A&A, 617, A13

della Valle M., Duerbeck H. W., 1993, A&A, 275, 239

Della Valle M., Izzo L., 2020, A&A Rev., 28, 3

della Valle M., Livio M., 1995, ApJ, 452, 704

della Valle M., Reinsch K., Thomas H., Rampazzo R., 1992, IAU Circ., 5427, 1

Diaz M. P., Abraham Z., Ribeiro V. A. R. M., Beaklini P. P. B., Takeda L., 2018, MNRAS, 480, L54

Doi M. et al., 2010, AJ, 139, 1628

Downen L. N., Iliadis C., José J., Starrfield S., 2013, ApJ, 762, 105

Downes R. A., Duerbeck H. W., 2000, AJ, 120, 2007

Downes R. A., Duerbeck H. W., Delahodde C. E., 2001, Journal of Astronomical Data, 7, 6

Draine B. T., 2011, Physics of the Interstellar and Intergalactic Medium

Duerbeck H. W., 1981, PASP, 93, 165

Duerbeck H. W., 1987a, Space Sci. Rev., 45, 1

Duerbeck H. W., 1987b, Ap&SS, 131, 461

Duerbeck H. W., 1987c, The Messenger, 50, 8

Duerbeck H. W., 1992, , 42, 85

Eggleton P. P., 1983, ApJ, 268, 368

Evans A., Bode M. F., Duerbeck H. W., Seitter W. C., 1992, MNRAS, 258, 7P

Evans A., Gehrz R. D., 2012, Bulletin of the Astronomical Society of India, 40, 213

Fang X. et al., 2014, ApJ, 797, 100

Fitzpatrick E. L., 1999, PASP, 111, 63

Fontaine G., Brassard P., Bergeron P., 2001, PASP, 113, 409

Frank J., King A., Raine D. J., 2002, Accretion Power in Astrophysics: Third Edition

Frisch P. C., Redfield S., Slavin J. D., 2011, ARA&A, 49, 237

Fuentes-Morales I., Vogt N., Tappert C., Schmidtobreick L., Hambsch F. J., Vučković M., 2018, MNRAS, 474, 2493

Fujimoto M. Y., 1982, ApJ, 257, 767

Gaia Collaboration et al., 2016, A&A, 595, A1

Gaia Collaboration et al., 2023, A&A, 674, A1

Gänsicke B. T. et al., 2009, MNRAS, 397, 2170

Gehrz R. D., Truran J. W., Williams R. E., Starrfield S., 1998, PASP, 110, 3

Gill C. D., O'Brien T. J., 1998, MNRAS, 300, 221

Gill C. D., O'Brien T. J., 2000, MNRAS, 314, 175

Göttgens F. et al., 2019, A&A, 626, A69

Greeley B. W., Blair W. P., Long K. S., 1995, ApJ, 454, L43

Guerrero M. A. et al., 2018, ApJ, 857, 80

Guerrero M. A., Santamaría E., Takeda L., González-Carbajal J. I., Cazzoli S., Ederoclite A., Toalá J. A., 2025, A&A, 694, A144

Hachisu I., Kato M., 2016, ApJ, 816, 26

Haefner R., Metz K., 1982, A&A, 109, 171

Harman D. J., O'Brien T. J., 2003, MNRAS, 344, 1219

Harvey E., Redman M. P., Boumis P., Akras S., 2016, A&A, 595, A64

Harvey É. J. et al., 2023, MNRAS, 521, 4750

Harvey E. J. et al., 2020, MNRAS, 499, 2959

Hellier C., 2001, Cataclysmic Variable Stars

Hilditch R. W., 2001, An Introduction to Close Binary Stars

Hillman Y., Prialnik D., Kovetz A., Shara M. M., 2016, ApJ, 819, 168

Hillman Y., Shara M. M., Prialnik D., Kovetz A., 2020, Nature Astronomy, 4, 886

Hirose H., Honda M., 1970, IAU Circ., 2212, 1

Hjellming M. S., Webbink R. F., 1987, ApJ, 318, 794

Hjellming R. M., 1996, in Astronomical Society of the Pacific Conference Series, Vol. 93, Taylor A. R., Paredes J. M., eds, Radio Emission from the Stars and the Sun, p. 174

Hoffmeister C., 1959, Astronomische Nachrichten, 285, 149

Honda M., Kosai H., Jacchia L., Ashbrook J., 1970, IAU Circ., 2233, 1

Iłkiewicz K. et al., 2021, MNRAS, 503, 4050

Inight K. et al., 2023a, MNRAS, 524, 4867

Inight K., Gänsicke B. T., Breedt E., Marsh T. R., Pala A. F., Raddi R., 2021, MNRAS, 504, 2420

Inight K. et al., 2023b, MNRAS, 525, 3597

Ivanova N. et al., 2013, A&A Rev., 21, 59

Izzo L. et al., 2024, A&A, 686, A72

José J., 2012, Bulletin of the Astronomical Society of India, 40, 443

José J., Hernanz M., 1998, ApJ, 494, 680

Kamath U. S., Anupama G. C., Ashok N. M., Chandrasekhar T., 1997, AJ, 114, 2671

Kasliwal M. M., Cenko S. B., Kulkarni S. R., Ofek E. O., Quimby R., Rau A., 2011, ApJ, 735, 94

Kato M., Saio H., Hachisu I., Nomoto K., 2014, ApJ, 793, 136

Kendall M., Stuart A., 1977, The advanced theory of statistics. Vol.1: Distribution theory

Kewley L. J., Groves B., Kauffmann G., Heckman T., 2006, MNRAS, 372, 961

Kim C. H., Kreiner J. M., Zakrzewski B., Ogłoza W., Kim H. W., Jeong M. J., 2018, ApJS, 235, 41

Knigge C., 2006, MNRAS, 373, 484

Knigge C., Baraffe I., Patterson J., 2011, ApJS, 194, 28

Kohoutek L., 1981, MNRAS, 196, 87P

Kolb U., 1993, A&A, 271, 149

Kolb U., Baraffe I., 1999, MNRAS, 309, 1034

König O. et al., 2022, Nature, 605, 248

Konstantinou L. et al., 2025, A&A, 697, A227

Kosai H., Wakuda M., McNaught R. H., Morel M., 1988, IAU Circ., 4582, 1

Kreiner J. M., 2004, , 54, 207

Kubiak M., 1984, , 34, 331

Kuerster M., Barwig H., 1988, A&A, 199, 201

Lanzetta K. M., Gromoll S., Shara M. M., Berg S., Valls-Gabaud D., Walter F. M., Webb J. K., 2023, PASP, 135, 015002

Lasota J.-P., Kuulkers E., Charles P., 1999, MNRAS, 305, 473

LeBlanc F., 2010, An Introduction to Stellar Astrophysics

Leibowitz E. M., Wyckoff S., Vidal N. V., 1976, PASP, 88, 750

Liimets T., Corradi R. L. M., Santander-García M., Villaver E., Rodríguez-Gil P., Verro K., Kolka I., 2012, ApJ, 761, 34

Liller W., Benetti S., Cappellaro E., Gilmore A. C., Nelson P., Stubbings R., 1995, IAU Circ., 6130, 1

Lloyd H. M., O'Brien T. J., Bode M. F., 1997, MNRAS, 284, 137

Lopes de Oliveira R., Bruch A., Rodrigues C. V., Oliveira A. S., Mukai K., 2020, ApJ, 898, L40

Luna G. J. M., Diaz M. P., Brickhouse N. S., Moraes M., 2012, MNRAS, 423, L75

Lunt J., 1926, MNRAS, 86, 498

Luri X. et al., 2018, A&A, 616, A9

Luridiana V., Morisset C., Shaw R. A., 2015, A&A, 573, A42

Lyke J. E., Campbell R. D., 2009, AJ, 138, 1090

Lyke J. E. et al., 2001, AJ, 122, 3305

MacDonald J., 1983, ApJ, 267, 732

Macfarlane S., Steeghs D., Woudt P., 2014, in Astronomical Society of the Pacific Conference Series, Vol. 490, Woudt P. A., Ribeiro V. A. R. M., eds, Stellar Novae: Past and Future Decades, p. 115

Mari M. B., Gonçalves D. R., Akras S., 2023, MNRAS, 518, 3908

Marsh T. R., Wade R. A., Oke J. B., 1983, MNRAS, 205, 33P

Martin P., Dubus G., Jean P., Tatischeff V., Dosne C., 2018, A&A, 612, A38

Mason C. G., Gehrz R. D., Woodward C. E., Smilowitz J. B., Greenhouse M. A., Hayward T. L., Houck J. R., 1996, ApJ, 470, 577

Mason E. et al., 2013, MNRAS, 436, 212

McLaughlin D. B., 1943, Publications of Michigan Observatory, 8, 149

Mclaughlin D. B., 1948, PASP, 60, 265

McNaught R. H., Feast M. W., Carter B. S., Laing J. D., 1986, IAU Circ., 4274, 1

Miszalski B. et al., 2016, MNRAS, 456, 633

Montez R., Luna G. J. M., Mukai K., Sokoloski J. L., Kastner J. H., 2022, ApJ, 926, 100

Moraes M., Diaz M., 2009, AJ, 138, 1541

Nakajima K., Ouchi M., 2014, MNRAS, 442, 900

Nakano S., Takamizawa K., Kushida Y., Waagen E., Scovil C., Collins P., 1995, IAU Circ., 6133, 1

Nassau J. J., Stephenson C. B., 1961, PASP, 73, 256

Nelemans G., Siess L., Repetto S., Toonen S., Phinney E. S., 2016, ApJ, 817, 69

Norton A. J., Somerscales R. V., Wynn G. A., 2004, in Astronomical Society of the Pacific Conference Series, Vol. 315, Vrielmann S., Cropper M., eds, IAU Colloq. 190: Magnetic Cataclysmic Variables, p. 216

Orio M., Mukai K., Bianchini A., de Martino D., Howell S., 2009, ApJ, 690, 1753

Orio M., Shaviv G., 1993, Ap&SS, 202, 273

Osaki Y., 1974, PASJ, 26, 429

Osterbrock D. E., Ferland G. J., 2006, Astrophysics of gaseous nebulae and active galactic nuclei

Paczyński B., 1967, , 17, 287

Pagnotta A., Schaefer B. E., 2014, ApJ, 788, 164

Pala A. F. et al., 2022, MNRAS, 510, 6110

Pala A. F. et al., 2020, MNRAS, 494, 3799

Parker Q. A. et al., 2006, MNRAS, 373, 79

Patterson J., 1998, PASP, 110, 1132

Pettit E., 1949, PASP, 61, 41

Porter J. M., O'Brien T. J., Bode M. F., 1998, MNRAS, 296, 943

Potter S. B., Buckley D. A. H., 2018, MNRAS, 473, 4692

Rao S. M., Pandey J. C., Rawat N., Joshi A., Singh A. K., 2025, arXiv e-prints, arXiv:2506.04371

Rappaport S., Verbunt F., Joss P. C., 1983, ApJ, 275, 713

Retter A., Leibowitz E. M., Kovo-Kariti O., 1998, MNRAS, 293, 145

Reynolds S. P., 2008, ARA&A, 46, 89

Ribeiro F. M. A., Diaz M. P., 2006, PASP, 118, 84

Richard J. et al., 2019, arXiv e-prints, arXiv:1906.01657

Ringwald F. A., Chase D. W., Reynolds D. S., 2005, PASP, 117, 1223

Ringwald F. A., Naylor T., Mukai K., 1996, MNRAS, 281, 192

Ritter H., Kolb U., 2003, A&A, 404, 301

Robinson E. L., Nather R. E., Kepler S. O., 1982, ApJ, 254, 646

Rodríguez-Gil P., Torres M. A. P., 2005, A&A, 431, 289

Rosino L., Ciatti F., della Valle M., 1986, A&A, 158, 34

Rosino L., Iijima T., 1987, Ap&SS, 130, 157

Sahman D. I., Dhillon V. S., Knigge C., Marsh T. R., 2015, MNRAS, 451, 2863

Sahman D. I., Dhillon V. S., Littlefair S. P., Hallinan G., 2018, MNRAS, 477, 4483

Saizar P., Pachoulakis I., Shore S. N., Starrfield S., Williams R. E., Rothschild E., Sonneborn G., 1996, MNRAS, 279, 280

Sanad M. R., 2014, Journal of Astrophysics and Astronomy, 35, 715

Santamaría E., Guerrero M. A., Ramos-Larios G., Sabin L., Vázquez R., Gómez-Muñoz M. A., Toalá J. A., 2019, MNRAS, 483, 3773

Santamaría E., Guerrero M. A., Ramos-Larios G., Toalá J. A., Sabin L., 2025, MNRAS, 539, 246

Santamaría E., Guerrero M. A., Ramos-Larios G., Toalá J. A., Sabin L., Rubio G., Quino-Mendoza J. A., 2020, ApJ, 892, 60

Santamaría E., Guerrero M. A., Toalá J. A., Ramos-Larios G., Sabin L., 2022a, MNRAS, 517, 2567

Santamaría E., Guerrero M. A., Zavala S., Ramos-Larios G., Toalá J. A., Sabin L., 2022b, MNRAS, 512, 2003

Santamaría E., Toalá J. A., Guerrero M. A., Ramos-Larios G., Sabin L., 2024, MNRAS, 530, 4531

Scaringi S. et al., 2022a, Nature, 604, 447

Scaringi S., Groot P. J., Knigge C., Lasota J. P., de Martino D., Cavecchi Y., Buckley D. A. H., Camisassa M. E., 2022b, MNRAS, 514, L11

Schaefer B. E., 2010, ApJS, 187, 275

Schaefer B. E., 2018, MNRAS, 481, 3033

Schaefer B. E., 2022, MNRAS, 517, 3640

Schaefer B. E., 2023, MNRAS, 525, 785

Schaefer B. E., 2024, ApJ, 966, 155

Schaefer B. E. et al., 2019, MNRAS, 487, 1120

Schaefer B. E., Patterson J., 1983, ApJ, 268, 710

Schenker K., Kolb U., Ritter H., 1998, MNRAS, 297, 633

Schmidtobreick L., Papadaki C., Tappert C., Ederoclite A., 2008, MNRAS, 389, 1345

Schmidtobreick L., Tappert C., Saviane I., 2003, MNRAS, 342, 145

Schreiber M. R., Belloni D., Schwope A. D., 2024, A&A, 682, L7

Schreiber M. R., Zorotovic M., Wijnen T. P. G., 2016, MNRAS, 455, L16

Schwassmann A., Wachmann A., 1928, Astronomische Nachrichten, 232, 273

Sedov L. I., 1959, Similarity and Dimensional Methods in Mechanics

Seitter W. C., Duerbeck H. W., 1980, Mitteilungen der Astronomischen Gesellschaft Hamburg, 50, 70

Selvelli P., Cassatella A., Gilmozzi R., González-Riestra R., 2008, A&A, 492, 787

Selvelli P., Gilmozzi R., 2019, A&A, 622, A186

Shafter A. W., Misselt K. A., Szkody P., Politano M., 1995, ApJ, 448, L33

Shafter A. W., Misselt K. A., Veal J. M., 1994, in Astronomical Society of the Pacific Conference Series, Vol. 56, Shafter A. W., ed, Interacting Binary Stars, p. 302

Shakura N. I., Sunyaev R. A., 1973, A&A, 24, 337

Shara M. M., 1982, ApJ, 261, 649

Shara M. M. et al., 2017a, ApJ, 839, 109

Shara M. M., Drissen L., Martin T., Alarie A., Stephenson F. R., 2017b, MNRAS, 465, 739

Shara M. M. et al., 2024a, MNRAS, 529, 224

Shara M. M. et al., 2024b, MNRAS, 529, 212

Shara M. M. et al., 2024c, ApJ, 977, L48

Shara M. M., Livio M., Moffat A. F. J., Orio M., 1986, ApJ, 311, 163

Shara M. M. et al., 2007, Nature, 446, 159

Shara M. M., Mizusawa T., Wehinger P., Zurek D., Martin C. D., Neill J. D., Forster K., Seibert M., 2012a, ApJ, 758, 121

Shara M. M., Mizusawa T., Zurek D., Martin C. D., Neill J. D., Seibert M., 2012b, ApJ, 756, 107

Shara M. M., Prialnik D., Hillman Y., Kovetz A., 2018, ApJ, 860, 110

Shara M. M. et al., 2015, ApJ, 805, 148

Shore S. N., Augusteijn T., Ederoclite A., Uthas H., 2011, A&A, 533, L8

Shore S. N., Kuin N. P., Mason E., De Gennaro Aquino I., 2018, A&A, 619, A104

Sion E. M., 1999, PASP, 111, 532

Sion E. M., Godon P., Jones L., 2017, AJ, 153, 109

Sion E. M., Szkody P., Mukadam A., Warner B., Woudt P., Walter F., Henden A., Godon P., 2013, ApJ, 772, 116

Slavin A. J., O'Brien T. J., Dunlop J. S., 1994, MNRAS, 266, L55

Slavin A. J., O'Brien T. J., Dunlop J. S., 1995, MNRAS, 276, 353

Smith D. A., Dhillon V. S., Marsh T. R., 1998, MNRAS, 296, 465

Spencer Jones H., 1931, Annals of the Cape Observatory, 10, 9.1

Spruit H. C., Ritter H., 1983, A&A, 124, 267

Starrfield S., Bose M., Iliadis C., Hix W. R., Woodward C. E., Wagner R. M., 2020, ApJ, 895, 70

Starrfield S., Bose M., Iliadis C., Hix W. R., Woodward C. E., Wagner R. M., 2024, ApJ, 962, 191

Starrfield S., Iliadis C., Hix W. R., 2016, PASP, 128, 051001

Starrfield S., Iliadis C., Hix W. R., Timmes F. X., Sparks W. M., 2009, ApJ, 692, 1532

Starrfield S., Truran J. W., Sparks W. M., Kutter G. S., 1972, ApJ, 176, 169

Steffen W., Koning N., Wenger S., Morisset C., Magnor M., 2011, IEEE Transactions on Visualization and Computer Graphics, 17, 454

Storey P. J., Hummer D. G., 1995, MNRAS, 272, 41

Strope R. J., Schaefer B. E., Henden A. A., 2010, AJ, 140, 34

Takeda L., Diaz M., Campbell R. D., Lyke J. E., Lawrence S. S., Linford J. D., Sokolovsky K. V., 2022, MNRAS, 511, 1591

Tappert C., Celedón L., Schmidtobreick L., 2023, A&A, 679, A40

Tappert C., Vogt N., Ederoclite A., Schmidtobreick L., Vučković M., Becegato L. L., 2020, A&A, 641, A122

Tassoul J.-L., 1987, ApJ, 322, 856

Tassoul J.-L., 1988, ApJ, 324, L71

Taylor G., 1950, Proceedings of the Royal Society of London Series A, 201, 175

Thorstensen J. R., Taylor C. J., 2000, MNRAS, 312, 629

Uthas H., Knigge C., Steeghs D., 2010, MNRAS, 409, 237

Verbunt F., 1993, ARA&A, 31, 93

Verbunt F., Zwaan C., 1981, A&A, 100, L7

Veresvarska M., Scaringi S., Hagen S., De Martino D., Done C., Ilkiewicz K., Knigge C., Littlefield C., 2024, MNRAS, 529, 664

Vogt N., 1982, ApJ, 252, 653

Vogt N., Maitzen H. M., 1977, A&A, 61, 601

Vogt N., Schreiber M. R., Hambsch F. J., Retamales G., Tappert C., Schmidtobreick L., Fuentes-Morales I., 2017, PASP, 129, 014201

Šimon V., 2018, A&A, 614, A141

Warner B., 1995, Cataclysmic variable stars, Vol. 28

Warner B., van Citters G. W., 1974, The Observatory, 94, 116

Weilbacher P. M. et al., 2020, A&A, 641, A28

Weilbacher P. M., Streicher O., Palsa R., 2016, MUSE-DRP: MUSE Data Reduction Pipeline, Astrophysics Source Code Library, record ascl:1610.004

Wendeln C., Chomiuk L., Finzell T., Linford J. D., Strader J., 2017, ApJ, 840, 110

Whipple F. L., 1940, Harvard College Observatory Bulletin, 912, 5

Whitehurst R., 1988, MNRAS, 232, 35

Williams R., 2012, AJ, 144, 98

Williams R. E., 1982, ApJ, 261, 170

Williams R. E., 1992, AJ, 104, 725

Williams R. E., Gallagher J. S., 1979, ApJ, 228, 482

Williams R. E., Phillips M. M., Hamuy M., 1994, ApJS, 90, 297

Williams R. E., Woolf N. J., Hege E. K., Moore R. L., Kopriva D. A., 1978, ApJ, 224, 171

Wolf M., 1925, Astronomische Nachrichten, 225, 335

Worpel H., Schwope A. D., Traulsen I., Mukai K., Ok S., 2020, A&A, 639, A17

Woudt P. A., Warner B., 2001, MNRAS, 328, 159

Woudt P. A., Warner B., 2003, MNRAS, 340, 1011

Woudt P. A., Warner B., Osborne J., Page K., 2009, MNRAS, 395, 2177

Wright E. L. et al., 2010, AJ, 140, 1868

Zahn J. P., 1975, A&A, 41, 329

Zahn J. P., 1977, A&A, 57, 383

Zahn J. P., 1989, A&A, 220, 112

Zhilkin A., Sobolev A., Bisikalo D., 2022, Galaxies, 10, 110

Zorotovic M., Schreiber M. R., Gänsicke B. T., 2011, A&A, 536, A42